FABRICATION OF ZEIN-BASED BIODEGRADABLE SURFACE ENHANCED RAMAN SPECTROSCOPY BIOSENSOR PLATFORMS FOR THE DETECTION OF FOOD TOXINS

by

Hazal Turasan

A Dissertation

Submitted to the Faculty of Purdue University

In Partial Fulfillment of the Requirements for the degree of

Doctor of Philosophy

Department of Food Science

West Lafayette, Indiana

August 2020

THE PURDUE UNIVERSITY GRADUATE SCHOOL
STATEMENT OF COMMITTEE APPROVAL

Dr. Jozef Kokini, Chair

Department of Food Science

Dr. Lisa Mauer

Department of Food Science

Dr. Yuan Yao

Department of Food Science

Dr. Andrea Liceaga

Department of Food Science

Dr. Miko Cakmak

Departments of Materials & Mechanical Engineering

Approved by:

Dr. Arun Bhunia

To my family...

ACKNOWLEDGMENTS

First, I would like to thank my adviser, Dr. Jozef Kokini for his support, guidance, and encouragement during my PhD program. He has given me an incredible opportunity to develop myself both professionally and personally. I am very grateful for his mentorship. I also would like to express my gratitude to my committee members, Dr. Lisa Mauer, Dr. Yuan Yao, Dr. Andrea Liceaga and Dr. Miko Cakmak who always helped me with such valuable contributions during the last six years. I especially want to thank Dr. Miko Cakmak for always making his lab available to me and making me feel welcomed in his lab. I also would like to thank Fulbright Program for financially supporting me during the first two years of my PhD program.

I am also very grateful for the best lab mates anybody could ever have. It was a great experience to work and grow in such a friendly environment with friends who always helped and motivated me through every aspect of life. I would like to thank each and every lab mate I had a chance to work with but especially I would like to thank Gamze, Jose, Morgan, Merve, Tahrima, Luis, Menglu, Fifi and Nia for their unique friendship. I have also had a chance to collaborate with many colleagues from around the world and author publications together. I would like to thank all my co-authors for their great work.

Finally, I would like to express deepest gratitude to my amazing family, my father Tufan Turasan who always supported me in all my decisions and constantly gave me strength, to my sister Eylül Turasan who is the only person that knows me in and out and can make me smile no matter what, and to my mother Nazan Turasan, who I miss every second of every day and will always have a huge place in my heart. It has not been easy to be away from my family to complete this work and I hope I can make them proud. Lastly, I would like to thank my husband Oğuz Kaan Öztürk for being the rock of my life. I would not be able to complete my degree without his presence, his constant support, love and encouragement. Thank you for always believing in me more than myself and thank you for this amazing life and many other adventures we are about to have.

TABLE OF CONTENTS

LIST OF TABLES

LIST OF FIGURES

ABSTRACT

Identifying and detecting health hazards in food products, especially contaminants and toxic substances such as allergens, food toxins and agricultural residues from pesticides, remains a challenge. Increasing demand for food products and growing health consciousness necessitate rapid and accurate measurements which can be easily conducted on-site without long measurement times and high costs. Due to their ease of use, accuracy sample preparation and rapidity, biosensors have started to outcompete time-consuming lab-scale analytical devices. However, as the use of biosensors increase, a concern of the amount of plastics and synthetic polymers used in the fabrication of these biosensors rises. In this dissertation, new ways to create biodegradable and eco-friendly plant-based SERS biosensor platforms from corn protein, zein, are presented. Its higher hydrophobicity and film forming capability make zein a very suitable biopolymer for fabricating biosensors. In the first part of this dissertation, chemical crosslinking was tested to improve the surface hydrophobicity, surface roughness (using AFM), mechanical properties, kinetics of gelation and film formation of zein films, and as a result zein-film based SERS platforms with fewer defects could be fabricated. In the second part, the detection sensitivity of the zein film-based SERS platforms was increased with metallic nanoparticle decoration (gold, silver or silver-shelled-gold). The addition of all three types of nanoparticles significantly increased the SERS enhancement factors of the platforms, with silver-shelled-gold nanoparticles giving the highest enhancement factor of 10^5. In the last part of this thesis, a novel approach was tested, where electrospun zein nanofibers decorated with metallic nanoparticles were used as a SERS biosensor platform. Due to their higher surface area-to-volume ratios, electrospun zein nanofibers gave a higher SERS enhancement factor (10^6). This enhancement factor enabled the detection of acrylamide, a food carcinogen, with a 10^4 times lower detection limit than nanophotonic based nanoimprinted zein, acrylamide sensor platform. Overall, this dissertation successfully shows the fabrication of biodegradable and eco-friendly SERS sensor platforms that have comparable detection sensitivities to those of non-biodegradable ones.

CHAPTER 1. INTRODUCTION

1.1 Importance of biosensors in food and agricultural industries

The rapidity of testing, specificity, ease of mass fabrication, low cost and field applicability of biosensors, make them one of the foremost relevant diagnostic techniques used in many fields like medicine, environmental monitoring, food safety and quality monitoring and agricultural applications (Thakur and Ragavan, 2013). The applications of biosensors in the food industry are gaining a great deal of importance due to the increasing incidences of food-borne illnesses, which are commonly due to food-borne pathogens and microorganisms or food toxins (Kumar et al., 2012). Also, consumers are becoming more health conscious and this requires production of foods without certain ingredients, such as allergens or natural contaminants. All these require detailed screening of food products in each step of handling, processing, storage, distribution and transportation (Thakur and Ragavan, 2013). Additionally, with new research we are gaining more knowledge on the effects of pesticides and insecticides that have been used for decades and this brings in new regulations against these pesticides, which require reliable detection techniques in the agricultural industry with fast screening methods.

This is why there is an increasing amount of studies focusing on fabricating biosensors in the literature. However, one of the challenges about fabrication of biosensors is that they do not have high sensitivity compared with high-tech analytical tools. That is why researchers are always looking for ways to increase sensitivity and to lower the limits of detection. In addition, for biosensors to replace high-tech analytical tools, they need to be able to do rapid measurements without losing their precision.

1.2 Surface enhanced Raman spectroscopy based (SERS) biosensors

Surface enhanced Raman spectroscopy (SERS) is a commonly used technique for molecular detection and characterization. It benefits from the enhanced Raman scattering of the molecules of interest that are adsorbed on, or near, SERS-active surfaces, such as nanostructured metals (Lal et al., 2008). These nanoscale features on a metallic surface can support strong fields that are significantly enhanced relative to the incident laser fields that are shone on to the surface. This

enhanced near field gives much higher Raman signals observed from molecules located within the enhanced near field (Lal et al., 2008). These highly localized regions (hot spots) of intense local field enhancement are formed within the interstitial crevices present in metallic nanostructures and are believed to be caused by local surface plasmon resonances (Maher, 2012). Even though hot spots are claimed to provide extraordinary enhancements of up to 10^{15} orders of magnitude to the SERS signals, the understanding of why this phenomenon is occurring is not completely understood. There are two mechanisms proposed for this signal enhancement. The electromagnetic mechanism is considered to provide the majority of the enhanced signals in SERS. It occurs due to the presence of enhanced electromagnetic fields localized within a few nanometers of nanostructured metallic surfaces formed by surface plasmon resonances. This enhanced electromagnetic fields decay exponentially from the surface and therefore enhances the optical processes within those molecules in close proximity to the surface (Maher, 2012).

The other mechanism, chemical or charge transfer mechanism, results from resonant charge transfer effects between a molecule that is strongly chemically adsorbed onto the surface and the metal itself. This mechanism is believed to contribute 10^2 –10^3 to the total enhancement. Thus, the chemical or charge transfer mechanism is believed to be only active for systems where molecules are strongly interacting with the surfaces (Maher, 2012).

Benefiting from these high enhancement factors, SERS is a widely used tool in a variety of fields such as electrochemistry, life sciences, biomedical engineering, environmental sciences, and public security (Ding et al., 2006). In food science, SERS technique is used for the detection of microorganisms (Duan et al., 2016), toxins (Marks et al., 2014) or for colorimetric assays where the interactions between nanoparticles or between nanoparticles and targets were investigated using SERS (Pang and He, 2016). Other applications include intracellular monitoring of drug release, detection of cancer markers, detection and imaging of biological cells for tumor targeting (Ding et al., 2006).

1.3 Zein-based surface enhanced Raman spectroscopy (SERS) biosensor platforms

Zein is the most abundant protein found in corn and is a byproduct of ethanol production from corn. It is a prolamin and has a high proline content and serves as the storage protein of corn. Since

zein is a prolamin, it is insoluble in pure water and soluble in alcohol solutions. It contains high amounts of glutamine, leucine, proline, alanine and phenyl alanine. However since it lacks the essential amino acids such as lysine or tryptophan, it has no nutritional value for humans. It has a yellow color, which comes from high lutein content. The structural organization of the amino acids in zein has been studied by many through the years (Argos et al., 1982; Cabra et al., 2005; Matsushima et al., 1997; Tatham et al., 1993). Even though there are many different suggestions of the configuration of zein and there has not been a consensus made on the exact model. Usually in studies, either the model of Argos et al. (1982) or Matsushima et al. (1997) is taken as the reference model, where antiparallel helices are stacking linearly through the hydrophilic glutamine bonds residing at the bottom and the top of the helices, forming rod-shaped structures.

Zein has many unique properties which makes it a sought-after protein for various applications. It has an amphiphilic structure, which makes it comparably more hydrophobic than other proteins. This property becomes useful in food packaging and drug coating applications. Its film forming ability makes zein one of the most commonly chosen plant-based materials for creating platforms. Zein has been shown to have a good biocompatibility, biodegradability and compostability in soil when it was used as an environmentally friendly plant pot (Dong et al., 2004; Helgeson et al., 2009; Lin et al., 2010). Due to its biodegradable and biocompatible nature, many studies focus on producing zein nanoparticles for drug and nutrition delivery. Films produced from zein also found many applications in the literature, such as antimicrobial coatings (Kashiri et al., 2016). Probably the most commonly used technique to produce zein film is the solvent casting method which includes dissolving zein in a solvent and then evaporating the solvent from the solution. Resin formation (Lai and Padua, 1998), extrusion (Selling, 2010), and electrospinning (Torres-Giner, Gimenez, & Lagarona, 2008) are some other techniques used to create zein products in the literature.

SERS sensors have been developed from cast zein films for the detection of acrylamide, a carcinogenic toxin, and Ara h1, the main peanut allergen protein (Gezer et al., 2016a, 2016b). In the fabrication of these sensors, soft lithography was used to transfer inverted pyramid nano/microstructures from PDMS molds onto the zein films surfaces (Figure 1). In order to obtain the SERS enhancement, gold layer was deposited onto the PDMS molds. The results showed that,

the fabrication of these biodegradable sensors were successful, where an enhancement signal of 10^4 was obtained (Gezer et al., 2016).

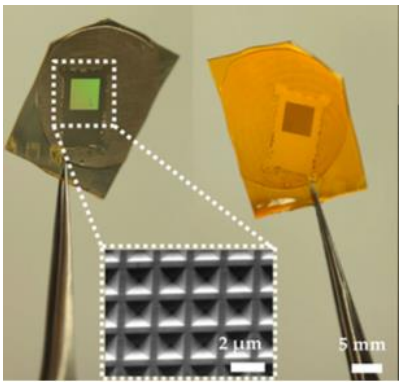

Figure 1. Zein-based SERS sensors with microstructures. Reprinted from Gezer et al. (2016) with permissions from Springer Nature.

In another study, zein was used to coat three types of nanoparticles, gold, silver and lead sulfide, to test how protein aggregation affects the SERS signals of the nanoparticles (Navdeep et al., 2016). Even though the results showed that SERS experiments were successful in characterizing zein, no enhancement factor was reported in this study. Clearly this is a curious but useful study since zein blocks the ability of the noble metals to generate hot spots.

Even though the detection of samples were successful in these studies, it is clear that the enhancement factors obtained from these sensors are much lower than to those obtained from other metallic, carbon-based SERS based sensors. One way to increase the enhancement factors is to increase the electromagnetic enhancement by creating more hotspots on the surface. In this dissertation, different approaches were tested to increase the sensitivity of zein-based SERS sensor platforms. These approaches include decorating the surface of nano/micro-structured zein film platforms with different types of metallic nanoparticles or fabricating metallic nanoparticle decorated zein-based SERS platforms from electrospun nanofibers.

1.4 Nanofiber fabrication with electrospinning

Nanofibers are a unique class of materials due to their advantages which come from their nanoscale diameters and large aspect ratio (Ahmed et al., 2015). They show superior mechanical properties

facilitating modification of surface properties useful in creating biosensors (Papkov et al., 2013). There are many ways to create nanofibers including drawing, template synthesis, phase separation or self-assembly. However, electrospinning has more advantages over these techniques such as making ultra-thin fibers or blending different polymers to make fibers with desired properties (Zhang et al., 2005). Electrical forces are used to produce polymer fibers whose diameter can range between 2 nm to micrometers (Bhardwaj and Kundu, 2010). Electrical potential difference causes a rapid acceleration of stretching in the polymer solution, leading to a fluid stream drawn out from the spinneret. Solvent evaporation from this stream leads to solidification and fiber formation. By creating nanofiber mats, a unique highly porous structure is obtained. This unique structure offers an ideal platform for SERS applications since the target analyte molecules are at or very close to the hotspots forming on the surface of these nanofibers as the surface to volume ratio is exceptionally large.

In order for electrospinning to be successful, several factors in precursor material design has to be considered. One is the solution properties: specifically the solution viscosity must be optimized and become sufficiently high to avoid electrospraying into droplets that typically occurs at low solid contents (hence viscosities) (Li et al., 2009). In addition, the solvent or solvent mixture has to be chosen such that boiling points are not too high or too low. If too high solvent is chosen, the fibers may not have a chance to dry before they land on the grounded target. If the boiling point of the solvent is too low then sometimes processing them may be difficult as the material may solidify near the nozzle exit creating processing issues.

Of all the parameters affecting the physical properties of the electrospun fibers, polymer molecular weight/concentration plays a key role in the formation of uniform bead-free fibers. The number of chain entanglements between the polymer molecules increases with increasing concentration or the molecular weight, and directly affects the structure of the fibers (Shenoy et al., 2005). As the concentration increases, the polymer forms different phases. These include 1) nanoparticles as a result of electrospraying in the dilute solution region, 2) nanoparticles with a few fibers in the mildly concentrated region, 3) fibers with beads with further increase in concentration, 4) beadless uniform fibers, and 5) globular fibers with large particles. So, for the formation of thin uniform fibers, there is an optimum concentration window. For the formation of beadless uniform

electrospun fibers, the empirical rule is to have 2-2.5 times the entanglement concentration (C_e) of the polymer (Klossner et al., 2008; McKee et al., 2004; Zhang et al., 2018). The entanglement concentration depends on the molecular weight of the polymer. For example while for poly(ethylene oxide) with a molecular weight of 4000 kDa C_e was found as 0.5% (Zhao et al., 2015), for zein (MW=22 kDa) the C_e was 11-12%. Therefore, for the preparation of electrospun fibers, the polymer's scaling behavior as a function of concentration is an important parameter to be studied.

1.5 Objective

The overall objective of this project is to develop biodegradable zein-based SERS biosensor platforms with higher sensitivities than already existing zein-based sensor platforms and to test the new zein-based SERS sensor platforms on detecting food toxins. In order to accomplish these objectives six different studies were conducted and are presented in this dissertation. In these studies, first, zein structure in different solvents were characterized and the effects of chemical crosslinking were analyzed. Then, new knowledge on zein crosslinking was used to fabricate improved nanostructured zein film-based SERS biosensor platforms. Lastly, a new approach was tested, where electrospun zein nanofibers were used as a new SERS biosensor platform. These new zein nanofiber-based SERS platforms were optimized for higher sensitivity and were tested on a food toxin for detection validation.

1.6 Hypothesis

The main hypothesis of this dissertation is that more sensitive biodegradable SERS biosensor platforms with increased enhancement factors can be fabricated from zein with 1) the use of chemical crosslinking for improved properties, 2) the addition of metallic nanoparticles onto the existing zein-based SERS platforms and 3) the fabrication of a new electrospun zein nanofiber SERS platform that has a very high surface to volume ratio. This way more sensitive, biodegradable and renewable biosensors with lower limits of detection can be fabricated which would serve as greener alternatives for non-biodegradable plastic-based sensor platforms.

1.7 References

Ahmed, F. E., Lalia, B. S., & Hashaikeh, R. (2015). A review on electrospinning for membrane fabrication: Challenges and applications. *Desalination*, *356*(Supplement C), 15–30. https://doi.org/10.1016/j.desal.2014.09.033

Argos, P., Pedersen, K., Marks, M., & Larkins, B. (1982). A Structural Model for Maize Zein Proteins. *Journal of Biological Chemistry*, *257*(17), 9984–9990.

Bhardwaj, N., & Kundu, S. C. (2010). Electrospinning: A fascinating fiber fabrication technique. *Biotechnology Advances*, *28*(3), 325–347. https://doi.org/10.1016/j.biotechadv.2010.01.004

Cabra, V., Arreguin, R., Galvez, A., Quirasco, M., Vazquez-Duhalt, R., & Farres, A. (2005). Characterization of a 19 kDa alpha-zein of high purity. *Journal of Agricultural and Food Chemistry*, *53*(3), 725–729. https://doi.org/10.1021/jf048530s

Ding, S.-Y., Zhang, X.-M., Ren, B., & Tian, Z.-Q. (2006). Surface-Enhanced Raman Spectroscopy (SERS): General Introduction. In *Encyclopedia of Analytical Chemistry*. John Wiley & Sons, Ltd. https://doi.org/10.1002/9780470027318.a9276

Dong, J., Sun, Q., & Wang, J.-Y. (2004). Basic study of corn protein, zein, as a biomaterial in tissue engineering, surface morphology and biocompatibility. Biomaterials, 25(19), 4691–4697. https://doi.org/10.1016/j.biomaterials.2003.10.084

Duan, N., Chang, B., Zhang, H., Wang, Z., & Wu, S. (2016). Salmonella typhimurium detection using a surface-enhanced Raman scattering-based aptasensor. *International Journal of Food Microbiology*, *218*, 38–43. https://doi.org/10.1016/j.ijfoodmicro.2015.11.006

Gezer, P. G., Hsiao, A., Kokini, J. L., & Liu, G. L. (2016). Simultaneous transfer of noble metals and three-dimensional micro- and nanopatterns onto zein for fabrication of nanophotonic platforms. *Journal of Materials Science*, *51*(8), 3806–3816. https://doi.org/10.1007/s10853-015-9699-0

Gezer, P. G., Liu, G. L., & Kokini, J. L. (2016a). Development of a biodegradable sensor platform from gold coated zein nanophotonic films to detect peanut allergen, Ara h1, using surface enhanced raman spectroscopy. *Talanta*, *150*, 224–232. https://doi.org/10.1016/j.talanta.2015.12.034

Gezer, P. G., Liu, G. L., & Kokini, J. L. (2016b). Detection of acrylamide using a biodegradable zein-based sensor with surface enhanced Raman spectroscopy. *Food Control*, *68*, 7–13. https://doi.org/10.1016/j.foodcont.2016.03.002

Helgeson, M. S., Graves, W. R., Grewell, D., & Srinivasan, G. (2009). Degradation and Nitrogen Release of Zein-based Bioplastic Containers. Journal of Environmental Horticulture, 27(2), 123–127. https://doi.org/10.24266/0738-2898-27.2.123

Kashiri, M., Cerisuelo, J. P., Dominguez, I., Lopez-Carballo, G., Hernandez-Munoz, P., & Gavara, R. (2016). Novel antimicrobial zein film for controlled release of lauroyl arginate (LAE). *Food Hydrocolloids*, *61*, 547–554. https://doi.org/10.1016/j.foodhyd.2016.06.012

Klossner, R. R., Queen, H. A., Coughlin, A. J., & Krause, W. E. (2008). Correlation of Chitosan's Rheological Properties and Its Ability to Electrospin. *Biomacromolecules*, *9*(10), 2947–2953. https://doi.org/10.1021/bm800738u

Kumar, S., Dilbaghi, N., Barnela, M., Bhanjana, G., & Kumar, R. (2012). Biosensors as Novel Platforms for Detection of Food Pathogens and Allergens. *BioNanoScience*, *2*(4), 196–217. https://doi.org/10.1007/s12668-012-0057-2

Lai, H.-M., & Padua, G. W. (1998). Water Vapor Barrier Properties of Zein Films Plasticized with Oleic Acid. *Cereal Chemistry Journal*, *75*(2), 194–199. https://doi.org/10.1094/CCHEM.1998.75.2.194

Lal, S., Grady, N. K., Kundu, J., Levin, C. S., Lassiter, J. B., & Halas, N. J. (2008). Tailoring plasmonic substrates for surface enhanced spectroscopies. *Chemical Society Reviews*, *37*(5), 898–911. https://doi.org/10.1039/B705969H

Li, L., Yalcin, B., Nguyen, B. N., Meador, M. A. B., & Cakmak, M. (2009). Flexible Nanofiber-Reinforced Aerogel (Xerogel) Synthesis, Manufacture, and Characterization. *ACS Applied Materials & Interfaces*, *1*(11), 2491–2501. https://doi.org/10.1021/am900451x

Lin, T., Lu, C., Zhu, L., & Lu, T. (2010). The Biodegradation of Zein In Vitro and In Vivo and its Application in Implants. AAPS PharmSciTech, 12(1), 172–176. https://doi.org/10.1208/s12249-010-9565-y

Maher, R. C. (2012). SERS Hot Spots. In C. S. S. R. Kumar (Ed.), *Raman Spectroscopy for Nanomaterials Characterization* (pp. 215–260). Springer Berlin Heidelberg. https://doi.org/10.1007/978-3-642-20620-7_10

Marks, H. L., Pishko, M. V., Jackson, G. W., & Coté, G. L. (2014). Rational Design of a Bisphenol A Aptamer Selective Surface-Enhanced Raman Scattering Nanoprobe. *Analytical Chemistry*, *86*(23), 11614–11619. https://doi.org/10.1021/ac502541v

Matsushima, N., Danno, G., Takezawa, H., & Izumi, Y. (1997). Three-dimensional structure of maize alpha-zein proteins studied by small-angle X-ray scattering. *Biochimica Et Biophysica Acta-Protein Structure and Molecular Enzymology*, *1339*(1), 14–22. https://doi.org/10.1016/S0167-4838(96)00212-9

McKee, M. G., Wilkes, G. L., Colby, Ralph. H., & Long, T. E. (2004). Correlations of Solution Rheology with Electrospun Fiber Formation of Linear and Branched Polyesters. *Macromolecules*, *37*(5), 1760–1767. https://doi.org/10.1021/ma035689h

Navdeep, Banipal, T. S., Kaur, G., & Bakshi, M. S. (2016). Nanoparticle Surface Specific Adsorption of Zein and Its Self-assembled Behavior of Nanocubes Formation in Relation to On-Off SERS: Understanding Morphology Control of Protein Aggregates. *Journal of Agricultural and Food Chemistry*, *64*(3), 596–607. Scopus. https://doi.org/10.1021/acs.jafc.5b05495

Pang, S., & He, L. (2016). Understanding the competitive interactions in aptamer–gold nanoparticle based colorimetric assays using surface enhanced Raman spectroscopy (SERS). *Analytical Methods*, *8*(7), 1602–1608. https://doi.org/10.1039/C5AY03158C

Papkov, D., Zou, Y., Andalib, M. N., Goponenko, A., Cheng, S. Z. D., & Dzenis, Y. A. (2013). Simultaneously Strong and Tough Ultrafine Continuous Nanofibers. ACS Nano, 7(4), 3324–3331. https://doi.org/10.1021/nn400028p

Selling, G. W. (2010). The effect of extrusion processing on Zein. *Polymer Degradation and Stability*, *95*(12), 2241–2249. https://doi.org/10.1016/j.polymdegradstab.2010.09.013

Shenoy, S. L., Bates, W. D., Frisch, H. L., & Wnek, G. E. (2005). Role of chain entanglements on fiber formation during electrospinning of polymer solutions: good solvent, non-specific polymer–polymer interaction limit. *Polymer*, *46*(10), 3372–3384. https://doi.org/10.1016/j.polymer.2005.03.011

Tatham, A., Field, J., Morris, V., Ianson, K., Cardle, L., Dufton, M., & Shewry, P. (1993). Solution Conformational-Analysis of the Alpha-Zein Proteins of Maize. *Journal of Biological Chemistry*, *268*(35), 26253–26259.

Thakur, M. S., & Ragavan, K. V. (2013). Biosensors in food processing. *Journal of Food Science and Technology*, *50*(4), 625–641. https://doi.org/10.1007/s13197-012-0783-z

Zhang, H., Xi, S., Han, Y., Liu, L., Dong, B., Zhang, Z., Chen, Q., Min, W., Huang, Q., Li, Y., & Liu, J. (2018). Determining electrospun morphology from the properties of protein–polymer solutions. *Soft Matter*, *14*(18), 3455–3462. https://doi.org/10.1039/C7SM02203D

Zhang, Y., Lim, C. T., Ramakrishna, S., & Huang, Z.-M. (2005). Recent development of polymer nanofibers for biomedical and biotechnological applications. *Journal of Materials Science: Materials in Medicine*, *16*(10), 933–946. https://doi.org/10.1007/s10856-005-4428-x

Zhao, W., Yalcin, B., & Cakmak, M. (2015). Dynamic assembly of electrically conductive PEDOT:PSS nanofibers in electrospinning process studied by high speed video. *Synthetic Metals*, *203*, 107–116. https://doi.org/10.1016/j.synthmet.2015.02.018

CHAPTER 2. MECHANICAL AND SPECTROSCOPIC CHARACTERIZATION OF CROSSLINKED ZEIN FILMS CAST FROM SOLUTIONS OF ACETIC ACID LEADING TO A NEW MECHANISM FOR THE CROSSLINKING OF OLEIC ACID PLASTICIZED ZEIN FILMS

Reprinted with permission. Full citation:
Turasan, H., Barber, E.A., Malm, M., Kokini, J.L., 2018. Mechanical and spectroscopic characterization of crosslinked zein films cast from solutions of acetic acid leading to a new mechanism for the crosslinking of oleic acid plasticized zein films. *Food Research International*. 108, 357-367. https://doi.org/10.1016/j.foodres.2018.03.063.

2.1 Abstract

This study discovered through FTIR, FT-Raman and rheological measurements that glutaraldehyde binds to zein through the amine groups of glutamine turns by replacing the already-bonded oleic acid molecules and forming imine structures. As a secondary crosslinking mechanism, glutaraldehyde unfolds some of the α-helices and turns them into β-sheets. While crosslinking resulted in stiffer and less ductile zein films, it made the surface of the films rougher, measured using AFM, and more hydrophilic, measured using WCA. In the crosslinking conditions in this study, the number of crosslinks estimated from rubber elasticity theory were not enough to change the water vapor permeability of the films significantly. Improving the understanding of crosslinking mechanism and its effects on physical and chemical properties of zein films can be useful to develop stiffer, stronger and more durable platforms for biodegradable biosensors, microfluidic devices or scaffolds.

2.2 Introduction

The massive use of petroleum based synthetic polymers in the applications of food packaging, clothing, electronic device engineering, agriculture, and their hazardous effects necessitates alternative, environmentally friendly ‘green’ polymers to replace these petroleum-based polymers in order to minimize their adverse effects on the environment (Rieger et al., 2012). The unique hydrophobic and film forming properties of zein, its low toxicity and compatibility in blends make zein a good candidate for ‘green’ polymer applications. In addition, its wide availability, because

it is a waste product of ethanol production from corn, makes zein an attractive green polymer for various applications.

Micro and nanoparticles produced from pristine zein or zein blends as well as electrospun zein fibers have been used as delivery systems from various drugs, nutrients and essential oils (Karthikeyan, Guhathakarta, Rajaram, & Korrapati, 2012; Lai & Guo, 2011; Li, Yin, Yang, Tang, & Wei, 2012; Luo & Wang, 2014; Parris, Cooke, & Hicks, 2005; Yang et al., 2017). Zein films have shown the potential to be used as microfluidic devices (Gezer et al., 2016a, Gezer et al., 2016b; Luecha, Hsiao, Brodsky, Logan Liu, & Kokini, 2011). There are also many studies using zein as platforms for inhibition of microbial growth (Kashiri et al., 2016; Li et al., 2012), in bone regeneration applications (Demir, Ramos-Rivera, Silva, Nazhat, & Boccaccini, 2017; Fereshteh, Nooeaid, Fathi, Bagri, & Boccaccini, 2015) and in wound recovery applications (Unnithan et al., 2014). Due to its film forming ability, zein is also one of the most commonly explored plant-based coating materials for antibacterial food packaging applications (Kashiri et al., 2017; Ozcalik & Tihminlioglu, 2013).

Pristine zein products lack sufficient mechanical barrier and surface properties to be competitive in many applications. Plasticization is a widely applied method to reduce the brittleness of zein films and increase their tensile strength and elongation (Budi Santosa & Padua, 1999; Shi, Yu, Lakshmana Rao, & Lee, 2012; Xu, Chai, & Zhang, 2012) as well as to reduce barrier properties; however, the effects of plasticization on physical properties is not clear (Shi et al., 2012; Xu et al., 2012). The mechanism of zein plasticization has been repeatedly studied with various plasticizers including water, glycerol, triethylene glycol, polyethylene glycol, palmitic acid, stearic acid, sugars, and oleic acid appears to be the best plasticizer for zein (Di Gioia & Guilbert, 1999; Ghanbarzadeh et al., 2007; Kokini, Cocero, Madeka, & de Graaf, 1994; Lai, Geil, & Padua, 1999; Lai, Padua, & Wei, 1997; Lawton, 2004).

Crosslinking with different crosslinkers, and with and without the addition of plasticizers to enhance mechanical and barrier properties has also been studied (Masamba et al., 2016; Parris & Coffin, 1997; Selling, Woods, & Biswas, 2011; Sessa, Mohamed, & Byars, 2008). Although the results are promising, these studies lack understanding the specific bonding interactions of zein

with the crosslinker and at the effects of the plasticizer on the chemistry of crosslinking. Prior studies mostly looked at the combined effects of crosslinking and plasticization through its impact on macroscopic property changes in zein, such as its mechanical and water vapor transmission properties. There are no studies that offer any specific mechanistic understanding of the chemistry of crosslinking either in the presence or in the absence of a plasticizer. The only study that offered an explanation to the chemistry between zein and glutaraldehyde (GA) crosslinking is only for unplasticized zein films and only focuses on the structure of glutaraldehyde and does not offer any specific mechanistic explanation for what happens to bonding interactions between zein and glutaraldehyde during crosslinking (Sessa et al., 2008). They referred to zein not through the specific parts of its protein chemistry, but as a vague entity. This project focuses on improving the understanding of the specific chemical bonding interactions involved in glutaraldehyde-crosslinking of zein films in the presence of oleic acid as plasticizer by focusing on what happens to the secondary and tertiary structure of zein during crosslinking. We used FTIR and FT-Raman spectroscopies to monitor the chemical changes occurring during crosslinking and conducted rheological measurements to monitor the gelation. Based on these results, we proposed a new crosslinking mechanism between zein and glutaraldehyde in the presence of oleic acid. This more specific understanding helped us improve the elegant but incomplete models proposed by Lai et al. (1999) and Sessa et al. (2008).

In addition, there is no clear understanding in the literature on how crosslinking affects the surface properties of zein-based products, which is especially important in applications where the surface of these products are used for cell growth, chemical or antibody binding in biosensors, fluid flow in microfluidic devices, food packaging and antimicrobial coatings or in wound recoveries. By conducting AFM and water contact angle measurements, we have offered specific new explanations building on the existing understanding related to the changes in surface topography and surface wettability. We also studied the effects of this specific crosslinking chemistry on the mechanical and barrier properties to have a complete understanding of the effects of crosslinking on plasticized zein films. We believe improving the understanding of the mechanism of zein crosslinking and its effects on the end-products would reveal new and better ways to optimize crosslinking conditions, to modify the zein products more effectively and eventually to produce zein products with superior properties.

2.3 Materials and Methods

2.3.1 Materials

Crude zein powder was obtained from the Sigma Aldrich Company. Glacial acetic acid and oleic acid (90%) were purchased from Fisher Scientific. Monoglyceride (Alphadim 90 MAK) was supplied by Corbion Caravan Company. PDMS kits (184 Silicone Elastomer Kits) were purchased from Sylgard, Dow Corning (Midland, MI).

2.3.2 Film Preparations

10 g of zein powder was dissolved in 50 mL 70% aqueous acetic acid solutions (1:5 (w/v) ratio) and the solutions were stirred with a magnetic stirrer at 60–65 °C for 1 h. Oleic acid as the plasticizer and monoglyceride as the emulsifier were added at the same time to the solutions in a ratio of 1 g:1 g:0.15 g (zein:oleic acid:monoglyceride) as previously optimized (Gezer, Brodsky, Hsiao, Liu, & Kokini, 2015; Luecha et al., 2011). The solutions were stirred at 60–65 °C for another hour. Then, the aqueous glutaraldehyde solution (25 wt%) was added to the mixtures at ratios of 0%, 4%, 8%, 10% and 12% of zein weight, 0% being the control ratio. The solutions were then stirred for 20 h without any heat treatment. To eliminate the air bubbles from the solutions, after 20 h, solutions were homogenized with an ultrasonic homogenizer (Fisher Scientific Model 505, operating frequency 20 kHz) for 2.5 min using 195 W. 10 mL from degassed solutions were then cast on petri dishes covered with cured “PDMS films” following the procedure developed previously (Gezer et al., 2015). The zein films were dried under the fume hood at 22°C until all the solvent has evaporated.

2.3.3 Gel Preparations

For gel preparation, zein solutions were prepared with the same method as explained above. After the sonication step, the solutions were left in room temperature in sealed containers without stirring for 115 days. In order to test the rheological properties of the gels, samples were taken periodically by carefully slicing thin layers and placing them between the parallel plates of the DHR-3 Rheometer.

2.3.4 Fourier transform infrared spectroscopy

Nitrogen cooled Attenuated Total Reflectance FTIR (ThermoScientific Nicolet Nexus) was used to observe the chemical changes occurring in the films. Zein films were analyzed in solid form. The resolution was 4 cm−1 and the spectra were obtained between 800 and 4500 cm−1. For the analysis of the secondary structures of zein proteins, amide I peak 1600–1700 cm−1 was analyzed. To prevent the effect of water on amide I peak, water spectra was subtracted from each sample spectra, based on the moisture content of the samples. Then, the amide I peaks were Fourier self-deconvoluted using the Omnic software. The deconvoluted spectra were then peak fitted using Gaussian curves and the percentages of specific secondary structures were calculated separately. The measurements were replicated 12 times and the averages were obtained through the software.

2.3.5 Fourier transform Raman analysis

Dried films were analyzed with FT-Raman in solid form. NXR FT-Raman Spectrometer from ThermoScientific with 1064 cm−1 laser was used. The spectra were obtained with Omnic software between 200 and 3500 cm−1 wavenumbers. 12 replications were averaged in the software to report the average spectra for each formulation.

2.3.6 Rheological properties of the gels

The rheological measurements of the solutions and gels were conducted with the Discovery HR-3 Rheometer (TA Instruments). Oscillatory measurements were conducted on each sample placed between a 40-mm crosshatched parallel plate geometry and a flat plate covered with adhesive sandpaper (3 M SandBlaster, 100 grit/meduim) to prevent sample slip from the surface of parallel plates. The gap between the parallel plates was zeroed after the sandpaper was placed on the lower plate. The thickness between the plates was set at 1000 μm. To determine the linear region, strain sweeps were obtained between 0.1 and 100% strain as a function of frequency (ranging from 1 rad/s to 100 rad/s). Based on the linear region at different frequencies, a strain value was determined for each sample, which differed between samples. The frequency sweeps were conducted between 1 and 100 rad/s applying the determined strain value for each sample. The storage (G'), loss (G") and complex (G*) moduli were plotted as a function of frequency. The

storage and loss moduli were periodically measured until full gelation was observed, where plateau moduli were obtained.

2.3.7 Water vapor permeability

Permeability measurements were conducted using Gardco permeability cups by following ASTM E96. The face opening of the cups was 25 cm^2 and 13 mL of distilled water was placed into the permeability cups before placing the films. Each film was cut into circular shapes larger than the opening of the permeability cups to ensure perfect coverage of the opening. The films were also tightened using circular gaskets around the opening. Initial weight and thickness of the samples and the weights of the whole apparatus were recorded before the experiment. The samples were stored at constant 38% relative humidity in desiccators containing $MgCl_2$ solution, and their weights were measured daily at the same time each day, until a stable weight loss was obtained for 6 subsequent days. During the entire experiment, humidity meters were placed in the desiccators for monitoring relative humidity and temperature. The weight changes versus time were plotted to calculate the water vapor transmission (WVT) ($g/(h * m^2)$) of the samples using Eqn. 1, in which G represents the total weight change (g), t represents the time during which G occurred (h) and A represents the cup mouth area (m^2).

$$WVT = G/tA \qquad \text{(Eqn. 1)}$$

The calculated WVT values were then used to calculate the permeance ($g/(h * m^2 * mm\ Hg)$) of the samples using Eqn. (2), in which S represents the saturation vapor pressure at test temperature (mmHg), R_1 represents the relative humidity in the cup and R_2 represents the relative humidity in the chamber that samples were stored in.

$$Permeance = WVT/S(R_1 - R_2) \qquad \text{(Eqn. 2)}$$

The water vapor permeability (WVP) ($(g * cm)/(Pa * s * m^2)$) values were calculated using Eqn. 3, in which averaged thickness values of the films were used.

$$Permeability = Permeance\ x\ Thickness \qquad \text{(Eqn. 3)}$$

2.3.8 Mechanical properties of films

Mechanical measurements were performed using TA.XT plus Texture Analyzer (Texture Technologies Corp, South Hamilton, MA), which has a load cell capacity of 30 kg. The uncrosslinked and crosslinked zein films were stored in 50±5% relative humidity at 22°C for 15 days prior to the experiment. The films were then cut in strips with gauge length 40 mm and width 25 mm. Four thickness measurements were taken across the gauge length of the films with a micrometer and averaged. The tensile grips were placed 40 mm apart from each other at the beginning of the experiment and the force was applied to the films until the grips were 100 mm apart to ensure rupture. Test speed was set at 0.5 mm/s. Stress versus strain graphs obtained from the experiments were used to calculate the tensile strength (MPa), elongation at break (%) and the Young's moduli (GPa) of the films. Each test was replicated 4 times and the results were compared statistically.

2.3.9 Measurement of water contact angle

Water contact angle measurements were taken from the PDMS contact sides of the films using Attension Theta Tensiometer (Biolin Scientific). The contact angles were recorded for 10 s with 12 frames per second. The droplet size of the water placed on each sample was 2 μL. Right and left contact angles were averaged by the software and the initial average contact angles were recorded. Standard deviations of the contact angles were calculated in the software.

2.3.10 Atomic force microscopy

Cypher ES Atomic Force Microscopy from Asylum Research was used to obtain the surface morphologies of the films. TAP300AL-G-10 type silicon probes coated with 30 nm Al for enhanced reflectivity and having tip radius < 10 nm, which have 300 kHz frequency and 40 N/m force constant, were purchased from Ted Pella Company. In the analysis of solid zein films, 0.5 × 0.5 in. pieces were cut and superglued on AFM/STM Metal Specimen Discs. During 3D imaging, 0.08 focusing factor was used for each sample. After superglue-drying, the samples were analyzed. The images were taken from 2 μm × 2 μm scanning areas. The average roughness values were calculated by MFP3D software.

2.3.11 Statistical analysis

For all the measurements, data was statistically analyzed and compared by Minitab 16. One-way ANOVA was used to see the differences and Tukey's comparison tests were applied to the data ($p < 0.05$). The letter system was used throughout the paper to show significant differences; such that, different letters indicate significant difference between the values. The error bars represent the standard error mean (SEM) values.

2.4 Results and Discussion

2.4.1 FTIR

Figure 2 shows the average FTIR spectra of uncrosslinked and glutaraldehyde (GA)-crosslinked zein films with different crosslinker ratios. All the films show typical characteristics of proteins at amide I (1600–1700 cm^{-1}, –C=O stretching), amide II (1480–1570 cm^{-1}, –C-N stretching and NH bending) and amide III (1200–1300 cm^{-1} –C-N stretching and NH bending) bands. Amide I along with amide III are sensitive to secondary structure changes. The peak at 3290 cm^{-1} is mainly from NH2 stretching in primary amines and partially from bound water (about 2–5% of the mass of the sample) (Lin-Vien, Colthup, Fateley, & Grasselli, 1991a). The peaks at 2800–3000 cm^{-1} and 1400–1483 cm^{-1} are due to CH_3 and CH_2 stretching of the side chains. These appear due to the high percentage of leucine (CH_2 and CH_3 on the side chains), proline (CH_2 on the side chain), alanine (CH_3 on the side chain), glutamine (CH_2 on the side chain), serine (CH_2 on the side chain) and isoleucine (with CH_2 and CH_3 on the side chains) of zein, and from the side chains of plasticizer, emulsifier and crosslinker. The low intensity peak around 1707 cm^{-1} is due to the C=O stretching of acetic acid trapped within the zein matrix which appears as a very strong and sharp peak in pure acetic acid spectra and due to C=O stretching of oleic acid in the matrix (data not shown).

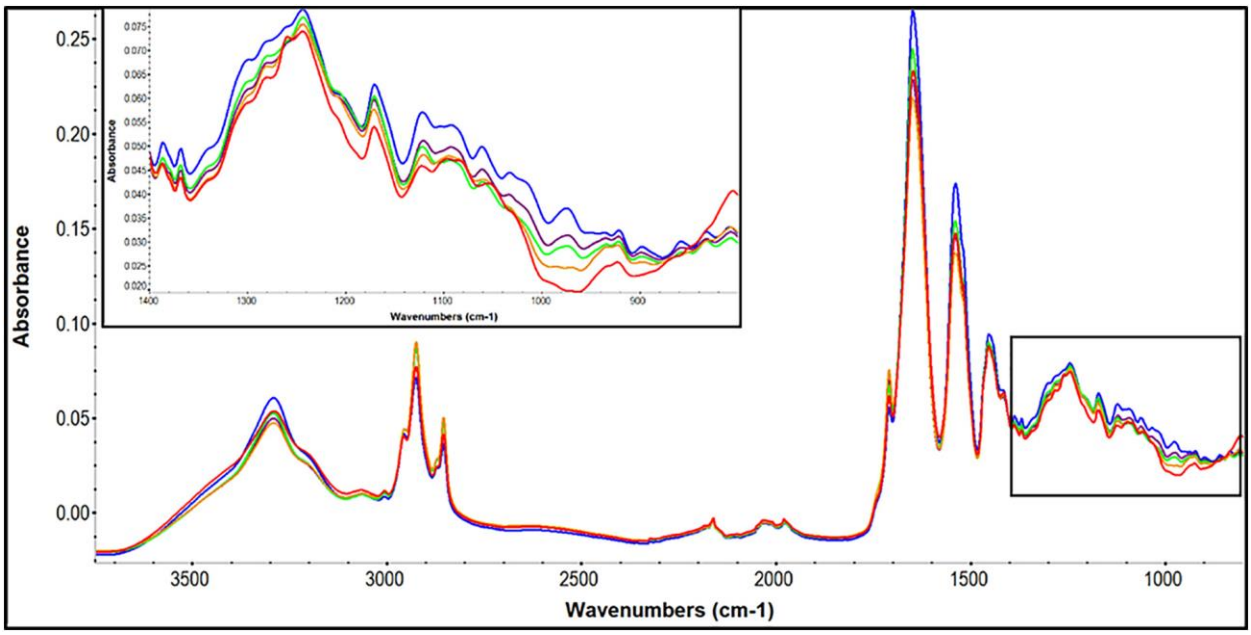

Figure 2. FTIR spectra of uncrosslinked and crosslinked zein films. Red line: 0% crosslinked, yellow line: 4% crosslinked, green line: 8% crosslinked, purple line: 10% crosslinked and blue line: 12% crosslinked zein films.

In the fingerprint region, the peak intensities at 1230–1240 cm^{-1} and at 1441 cm^{-1} increased significantly due to the sensitivity of amide III region to crosslinking and increasing CH_2 stretching with the addition of GA, respectively. Amide III region intensity increases are due to increasing number of free NH bond, consistent with the results on GA-crosslinked unplasticized zein films (Sessa et al., 2008). The intensities of these peaks in plasticized GA-crosslinked zein films in this study, however, did not increase as much due to the previously bound oleic acid. Increasing GA ratio also increased the intensity of 960–990 cm^{-1} peak (Fig. 1 inset). No such peak is seen in uncrosslinked films. Formation of this peak is due to C-O-C bond stretching in cyclic hemiacetal structure, indicating that some portion of GA remains in cyclic form in 25% aqueous solution (Whipple & Ruta, 1974).

The effects of crosslinking on the secondary structures of crosslinked and uncrosslinked zein were also analyzed by FTIR spectroscopy. The amide I band is influenced by the presence of water in the sample. Therefore, before analyzing the amide I peaks, pure water spectrum was subtracted from the sample spectra based on the moisture content of the films (Mejia, Mauer, & Hamaker, 2007).

In amide I band, α-helix structures give strong peaks around 1650–1660 cm^{-1}, β-sheets give strong peaks around 1610–1640 cm^{-1} and β-turn structures show peaks around 1639 cm^{-1}, 1655 cm^{-1}. 1670 cm^{-1} and 1680–1686 cm^{-1} (Forato, Bicudo, & Colnago, 2003; Georget, Barker, & Belton, 2008; Krimm & Bandekar, 1986; Mizutani, Matsumura, Imamura, Nakanishi, & Mori, 2003). In this study, the higher wavenumber peaks (1670 and 1685 cm^{-1}), caused by glutamine turns (1659–1696 cm^{-1}) (Barth, 2000), have been attributed to β-turns (Fig. 3).

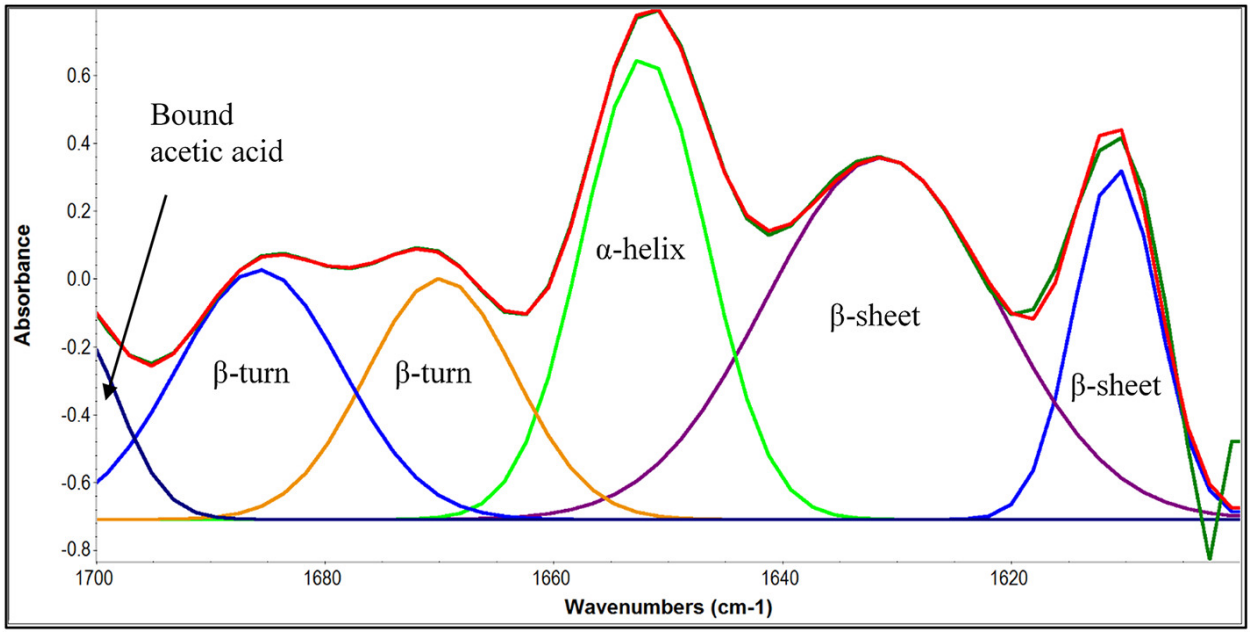

Figure 3. Peak fitted amide I band for secondary structure analysis.

The effect of crosslinking on the secondary structure distribution can be seen in Figure 4. The statistical analysis showed that the addition of GA decreased the α-helix content and increased the β-sheet content of the films. There were no significant differences between the β-turn content of the uncrosslinked and crosslinked films statistically. The overall results indicated that, with the addition of crosslinker, some of the α-helices, the most ordered and compact form of secondary structures, are turning into β-sheets, which are slightly less ordered secondary structure forms. Also, the peak intensity of the deconvoluted peak at 1670 cm^{-1}, which is affected by the CN stretching in RHCN-R structures, increased significantly with GA addition, implying a non-conjugated imine formation during crosslinking (Lin-Vien, Colthup, Fateley, & Grasselli, 1991b).

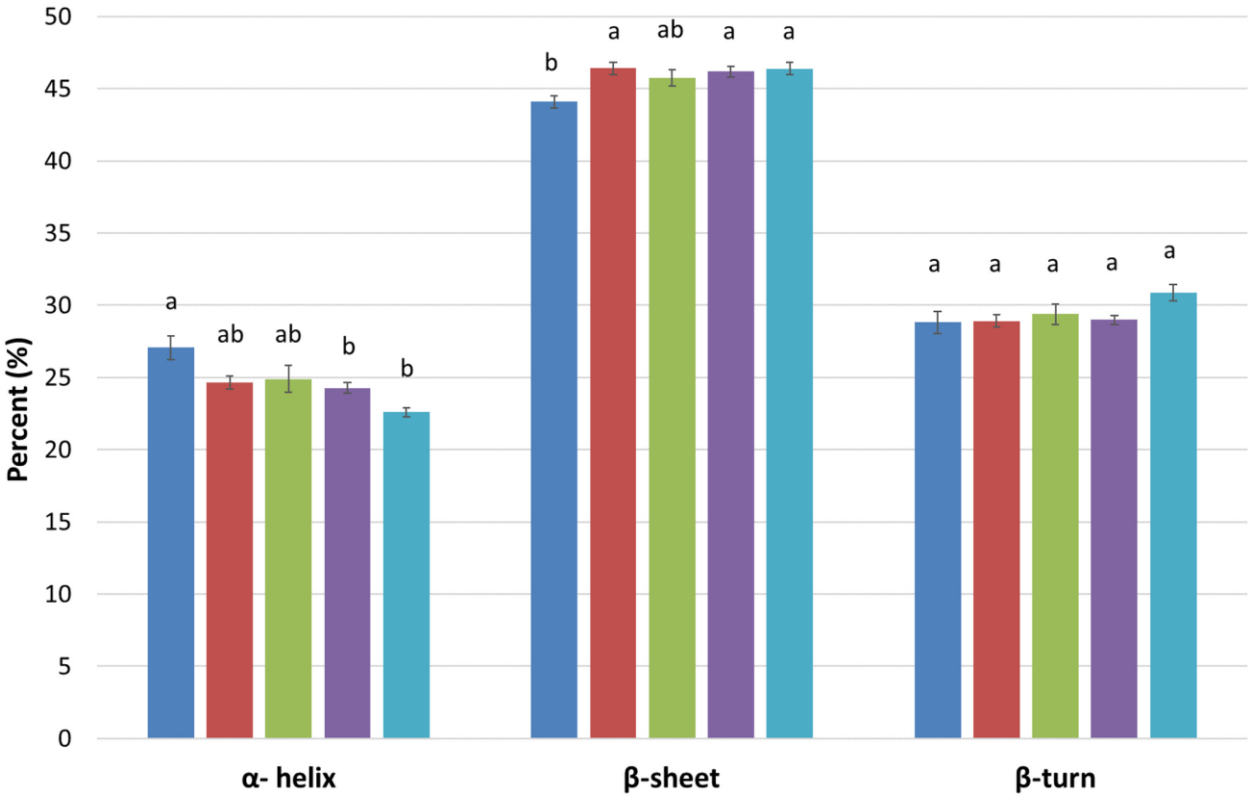

Figure 4. Secondary structure distribution of zein films with different GA concentrations (Data represents means±SEM). Blue bars: 0% crosslinked, red bars: 4% crosslinked, green bars: 8% crosslinked, purple bars: 10% crosslinked and cyan bars: 12% crosslinked zein films.

In this study, a new mechanism for GA-crosslinked plasticized zein films cast from acetic acid solutions is proposed (Fig. 5). It is well known that zein organizes itself in mostly compact helical structures which are bound to each other through glutamine residues residing at the bottom and the top of these helices (Argos, Pedersen, Marks, & Larkins, 1982; Matsushima, Danno, Takezawa, & Izumi, 1997; Turasan & Kokini, 2017). Our results showed that our films also have a high number of β-sheet structures, aligning themselves between these helix stacks. During plasticization, oleic acid binds to the most exposed glutamine ends of zein molecules, forming a bilayer between zein layers which creates free volume between the stacks of zein and contributes to mobility (Lai et al., 1999). Based on their findings, Sessa et al. (2008) proposed a model for glutaraldehyde crosslinking of unplasticized zein films from acetic acid solutions, where in the mechanism, only the details of glutaraldehyde part of the complex were focused on. Our preliminary results showed that the addition of plasticizer before the crosslinker retards the gelation process and therefore crosslinking is partially hindered by existing oleic acid. Therefore, it is logical to consider that

glutaraldehyde reacts with the exposed hydrophilic glutamine ends of zein, where oleic acid binds to zein. In the comprehensive review of Migneault, Dartiguenave, Bertrand, and Waldron (2004), the possible forms of GA in aqueous solutions and its possible reactions with proteins were discussed. The overall conclusion was that GA consists of a mixture of monomers in free aldehyde form, cyclic hemiacetals and polymers in acidic aqueous solutions. In another study that focused on the effects of temperature on the form of GA in aqueous solutions, heating GA aqueous solution at 60 °C was found to cause a breakdown of cyclic hemiacetals and the formation of more free monomeric GA (Ruijgrok, Boon, & Wijn, 1990). Therefore, in our experiments, heating the acidic (pH = 2–3) zein solutions to a temperature between 60 and 65 °C converts most of the cyclic hemiacetal glutaraldehydes to linear monomeric form (Fig. 5, step 1).

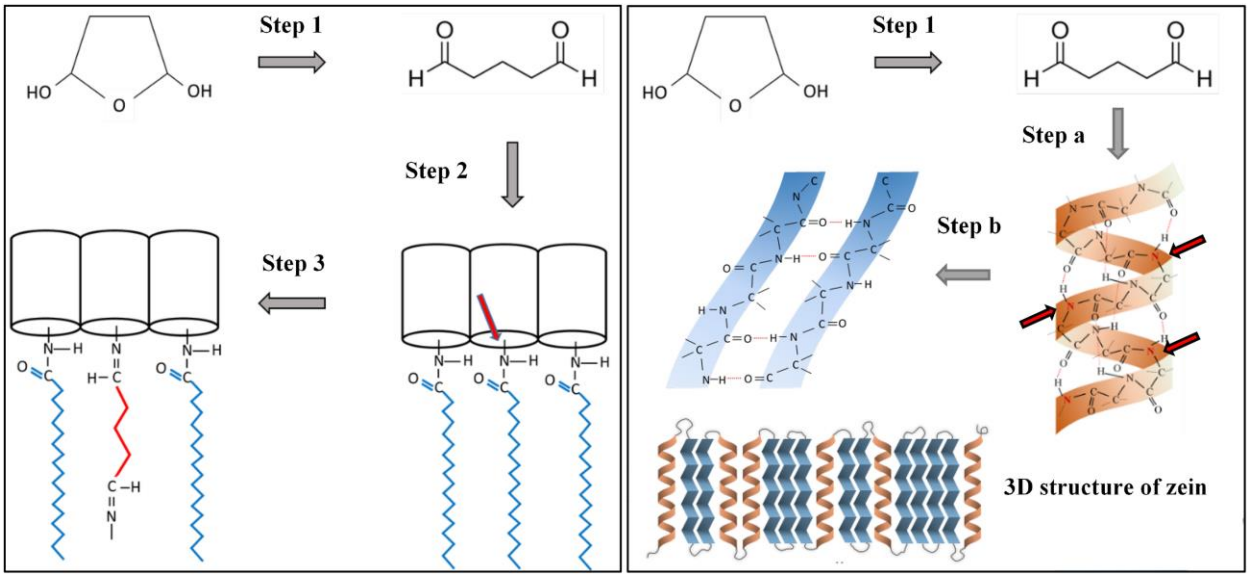

Figure 5. Glutaraldehyde crosslinking mechanism of plasticized zein films.

In the reported reactions of GA with proteins in acidic solutions, GA was found to attack to the amine groups of proteins, forming –C=N- bonds (Schiff base reaction) (Migneault et al., 2004). In our mechanism, GA undergoes the Schiff base reaction by attacking to the amine groups of glutamine ends of zein (step 2). This imine formation results in a replacement of some of the bound oleic acid molecules, leading to a tighter linkage formation between zein layers. The changes observed in the secondary structure content with crosslinking can be explained with a secondary mechanism, where some of the GA molecules target the N atoms in the hydrophobic sites of α-

helices, disrupting some of the hydrogen bonds that hold the helices together (step a) causing them to turn into β-sheet structures (step b), supported by the data on secondary structure changes. The effects of this secondary structure transformation can be observed in surface wettability of the films.

2.4.2 FT-Raman

Figure 6 shows the average FT-Raman spectra of zein films with 0% (uncrosslinked), 4%, 8%, 10% and 12% GA. Similar to FTIR, FT-Raman spectra also show amide I (1600–1700 cm^{-1}) and amide III peaks (1220–1300 cm^{-1}). However, amide II bands that appear at 1480–1570 cm^{-1} in FTIR do not appear in FT-Raman spectra (Matthäus et al., 2008). Unlike FTIR, amide III peaks have a higher intensity in FT-Raman spectra at 1220–1300 cm^{-1}. The peak observed between 1400 and 1483 cm^{-1} is responsible for aliphatic $–CH_2$ and $–CH_3$ vibrations. The peak at 1000 cm^{-1} appears in FT-Raman spectra but not in FTIR spectra, which is due to the in-phase radial vibration of mono-substituted benzene ring in phenylalanine structure. The high intensity of this peak is due to the high phenylalanine content of zein (Li, Xia, Shi, & Huang, 2011).

The intensities of the peaks do not show a clear trend with the change in GA concentration. The only major difference between the spectra of the films is the disappearance of the peak at 1400 cm^{-1} when GA is added as crosslinker (Fig. 6 inset). This peak represents –C-N- single bond vibration and partially in plane OH bending in carboxylic acids (Lambert, 1998; Larkin, 2011). Since this peak only appears in the uncrosslinked (0% GA) samples and disappears in all other samples with GA, it suggests that during the crosslinking, there is a reduction in the C-N single bond content of zein. This finding supports the proposed mechanism of crosslinking, where the amount of C-N single bonds decreases due to the decreasing interaction between zein and oleic acid, and the amount of C=N bonds increases during imine formation due to the interaction between GA and zein.

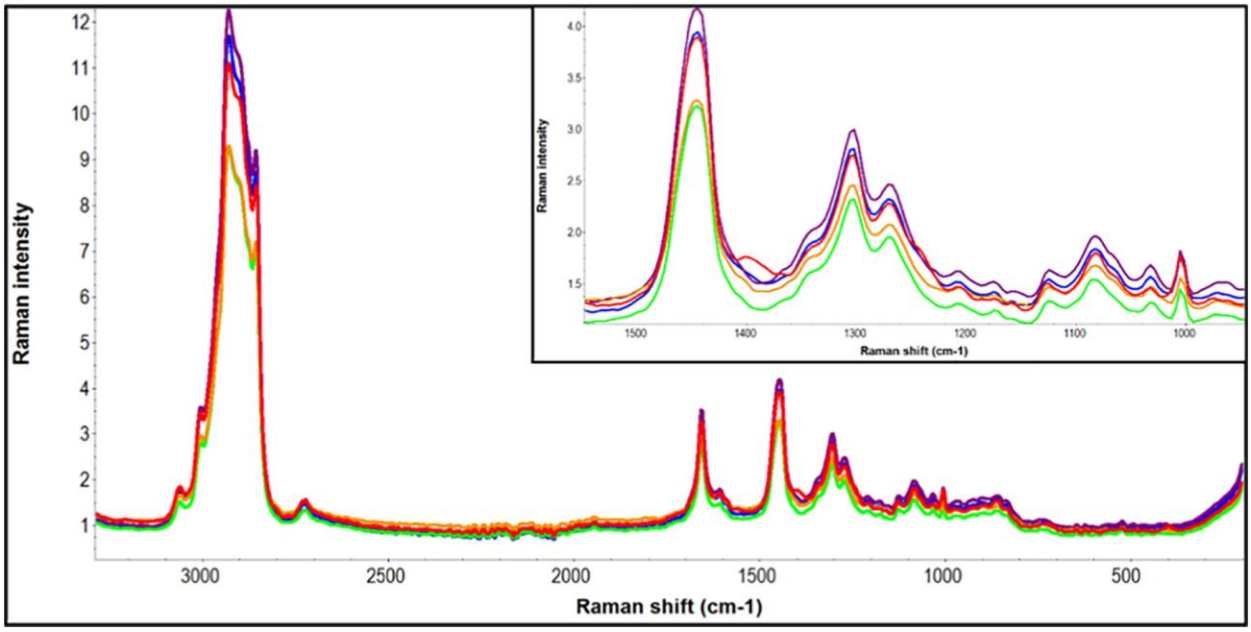

Figure 6. FT-Raman spectra of uncrosslinked and crosslinked zein films. Red line: 0% crosslinked, yellow line: 4% crosslinked, green line: 8% crosslinked, purple line: 10% crosslinked and blue line: 12% crosslinked zein films.

2.4.3 Rheological measurements

Figure 7 shows the G', G" and G* values of 0% (uncrosslinked), 4%, 8% and 12% crosslinked zein solutions at the indicated days. The results show that, in 0% (uncrosslinked) zein solutions, the G' values did not increase with time, remained below 0.1 Pa for 115 days, and G" values always remained greater than the G' values, indicating no sign of gelation. In the crosslinked formulations, G' values increased with time, proving gelling of the solutions. For 4% crosslinked zein solutions, a sharp increase in G' values started on day 20, and the crossover between G' and G" occurred on day 30. The sharp increase of G' values started earlier for 8% crosslinked (on day 8) and 12% crosslinked (before day 4) solutions, showing a faster gelation than 4% crosslinked solutions. The crossover between G' and G" values occurred between days 12 and 16 for 8% crosslinked zein solutions and between days 8 and 12 for 12% crosslinked zein solutions. An example of gelation profile can be seen in the frequency sweep of 12% crosslinked zein solution (Fig. 8). On each day of measurement, 12% crosslinked zein solutions had the highest G' values compared to the other solutions except for the first two testing days, where all the solutions were still in dilute liquid form and the G' values were too small to be compared. The rest of the formulations followed a decreasing order of G' values with decreasing crosslinker concentration. The highest G' value (the

plateau G' value) for each formulation was recorded at day 115 (Fig. 7). Based on the highest G' values obtained for each formulation, the average number of crosslinks between zein molecules (NC) were calculated using the method developed previously (Gluck-Hirsch & Kokini, 1997; Kokini et al., 1994; Lambert & Kokini, 2001; Madeka & Kokini, 1996) using Eqns. (4), (5). ρ represents the unswollen density of zein, 1.22 g/cm^3 (Beck, Tomka, & Waysek, 1996) and c is the weight fraction of zein, calculated from the solutions prepared with 50 mL aqueous acetic acid and 10 g of zein (1:5 (w/v)) (Table 1). R is the gas constant and T is the temperature. MC represents the average molecular weight between crosslinks and M^*_w represents the molecular weight of zein. The molecular weight of zein is taken as 22 kDa (Paulis & Wall, 1977; Shukla & Cheryan, 2001).

$$M_C = \frac{c^{1/3}\rho^{2/3}RT}{G'} \qquad \text{(Eqn. 4)}$$

$$N_C = \frac{M^*_w}{2M_c} \qquad \text{(Eqn. 5)}$$

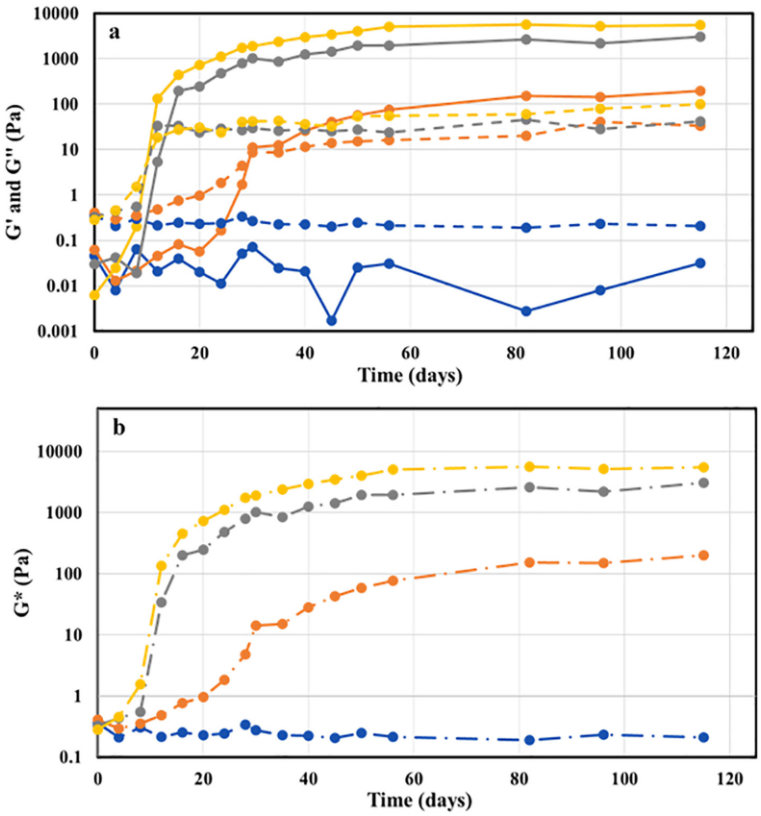

Figure 7. a) G' (solid lines), G" (dashed lines) and b) G* values of zein solutions over crosslinking time at 2.5 rad/s and 25°C. Blue line: 0% crosslinked, orange line: 4% crosslinked, grey line: 8% crosslinked, and yellow line: 12% crosslinked zein films.

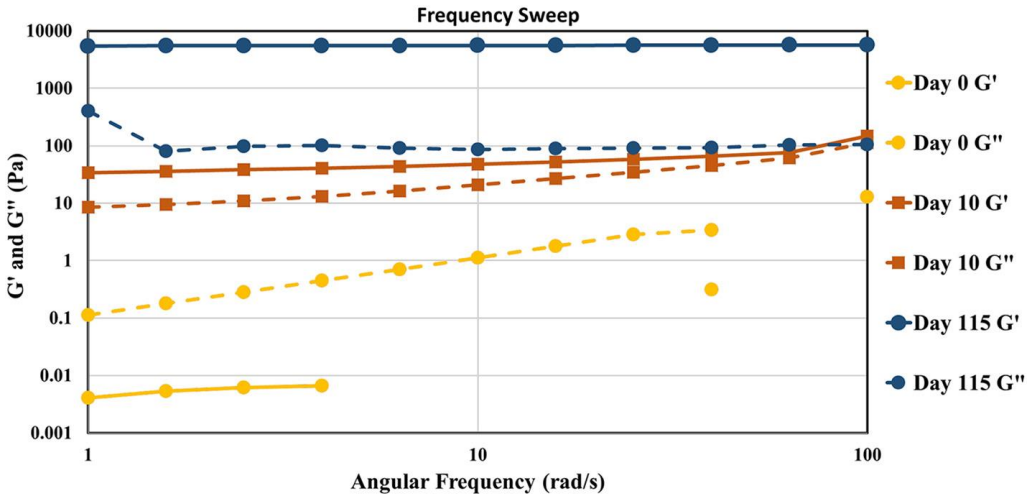

Figure 8. Frequency sweeps for 12% crosslinked zein gels. Solid lines represent G' values and dashed lines represent G" values for corresponding days.

In 4% crosslinked zein solutions, a crosslink between zein molecules occurred twice in a thousand zein molecules. For 8% crosslinked solution, this number was approximately 2 for every hundred zein molecules and for 12% crosslinked gels, the crosslink occurred approximately four times in every hundred zein molecules.

Based on the results of FTIR and FT-Raman, a new mechanism was previously developed in this paper to show the crosslinking between zein molecules and GA. With the addition of rheological measurements, we understand that, the proposed bond formation between zein molecules and GA molecules occurs very rarely, approximately once in 27 zein molecules at most and that is what makes these gels weak gels. This low number of crosslinks may be due to steric hindrance created by plasticization of zein molecules with oleic acid. Oleic acid is substantially larger than GA ($Mw_{oleic\ acid}$ = 282 g/mol, Mw_{GA} = 100 g/mol) and is added to the zein solutions one hour prior to the addition of GA. During this plasticization hour, oleic acid molecules already start binding to the glutamine ends of zein molecules, occupying these sites and disabling subsequently added GA molecules from forming crosslinks.

Table 1. Calculation of number of crosslinks between zein molecules.

Formulation	c (g/cm^3)	ρ (g/cm^3)	G' (Pa)	M_C (g/mol)	N_C (per zein molecule)*10^3
0% GA	0.225	1.22	0.031	5.55*10^{10}	0.0
4% GA	0.221	1.22	308.391	5.55*10^6	2.0
8% GA	0.217	1.22	3127.035	5.44*10^5	20.2
12% GA	0.215	1.22	5679.850	2.99*10^5	36.8

2.4.4 Water vapor permeability

The comparison of water vapor permeability values of zein films is shown in Table 2. The statistical analysis of the data showed that GA addition did not change the permeability data significantly at any ratio. The water vapor transmission values of the films were in the range of 2.74–3.05 g/(h·m^2), permeance values were in the range of 2.35*10^{-3}–2.62*10^{-3} g/(h·m^2·mm Hg), and water vapor permeabilities were in the range of 1.08*10^{-3}–1.20*10^{-3} g.mm/(h·m^2·mm Hg).

Table 2. Physical property results of uncrosslinked and crosslinked zein films.

	0% crosslinked	4% crosslinked	8% crosslinked	10% crosslinked	12% crosslinked
Water Vapor Permeability (g.mm/h.m^2.mmHg) x10^3	1.20±0.05 ^{a}	1.09±0.02 ^{a}	1.12±0.03 ^{a}	1.13±0.06 ^{a}	1.08±0.03 ^{a}
Tensile Strength (MPa)	2.03±0.08 ^{c}	3.23±0.44 ^{b}	4.08±0.17 ^{ab}	3.89±0.13 ^{ab}	4.72±0.16 ^{a}
Young's Modulus (GPa)	7.15±0.40 ^{c}	12.69±1.37 ^{b}	14.61±1.25 ^{ab}	12.76±1.97 ^{ab}	20.93±0.56 ^{a}
Elongation at break (%)	27.42±5.26 ^{a}	23.69±4.51 ^{a}	8.72±2.19 ^{ab}	8.30±1.69 ^{ab}	5.81±1.77 ^{b}
Water Contact Angle (°)	79.35±6.17 ^{a}	60.13±0.72 ^{b}	62.54±2.58 ^{b}	67.51±1.50 ^{b}	66.34±1.09 ^{b}
Average Roughness (nm)	0.78±0.13 ^{c}	1.22±0.25 ^{c}	2.56±0.20 ^{b}	1.35±0.04 ^{c}	3.65±0.15 ^{a}

Note: Data represents mean ± SEM. Statistical analyses were conducted separately for each property. Different letters represent significant difference ($p < .05$).

The calculated values for both uncrosslinked and crosslinked zein films are smaller than the value reported previously for unplasticized 8% GA-crosslinked zein films cast from acetic acid solutions (Sessa, Mohamed, Byars, Hamaker, & Selling, 2007). Also in the same study, crosslinking was claimed to increase the water vapor permeability values. In our study, however, crosslinking was not found to affect the permeability significantly. These results are expected since the rheology

results showed that the degree of crosslinking was very low, even for the highest crosslinker concentration (1 crosslink in every 27 zein molecules). These low number of crosslinks in any of the formulations are clearly not enough to create a dense network to prevent relatively small water molecules from passing through the films. Therefore, no significant difference between formulations could be observed.

2.4.5 Mechanical properties

Tensile strength results for crosslinked and uncrosslinked films are shown in Table 2, where the control films have the lowest tensile strength value of 2.03 MPa. As the crosslinker concentration increased, the tensile strength of the films increased, 12% having the highest tensile strength of 4.72 MPa, which is consistent with the previous observations (Sessa et al., 2007). The Young's moduli of the films also followed the same trend with the tensile strength of the films. As GA concentration increased, the Young's moduli of the films increased significantly (Table 2). These results, however, are different than Sessa et al.'s (2007) study, where the highest Young's modulus was found for 4% crosslinked unplasticized zein film and there was no trend found with the addition of more GA. Our rheological measurements prove that number of crosslinks increases with increasing crosslinker ratio. Therefore, it is logical to see an increasing trend for both tensile strength and Young's moduli for increasing GA ratio.

Elongation at break decreased as more GA was added to the films (Table 2) as would be expected from films which become stiffer as more crosslinking occurs. The uncrosslinked zein films had the highest elongation with 27.4%, while the 12% crosslinked films had the lowest elongation with 5.8%. In the study of Sessa et al. (2007), the elongation values for the unplasticized and uncrosslinked zein films had the lowest elongation values, while in our study, uncrosslinked plasticized zein films had the highest elongation. The authors explained this elongation increase with the linear chain formations occurring due to increasing intramolecular reactions of GA with zein. However, our mechanism of crosslinking suggests that shorter-chain GA molecules are replacing some of the longer-chain oleic acid molecules, which creates tighter junctions between zein molecules. Therefore, the flexibility of the films decreased with increasing number of crosslinks in this study.

The overall mechanical property measurements showed that with more crosslinking, films became stiffer, stronger, and less ductile, which is expected since with the increasing number of junction-points the molecules are more tied together which limit their mobility.

2.4.6 Water contact angle

The effect of crosslinking on the surface wettability was investigated for the first time for zein films in our study. WCA values were collected at time t = 0 on the PDMS contact sides of the films since water starts being absorbed by the zein films immediately. Table 2 shows the average WCA values for films with different glutaraldehyde ratios. All the films had hydrophilic surfaces with contact angles lower than 90°. Among all the ratios, uncrosslinked zein films had the highest average contact angle value, 79.4°. This value is consistent with the previously reported WCA values of zein films where the films were spin coated from uncrosslinked and unplasticized zein solutions in 70% aqueous acetic acid (Shi, Kokini, & Huang, 2009). Crosslinked zein films had lower contact angle values ranging between 60 and 67.5°. Statistical analysis showed that, uncrosslinked film surfaces are significantly less hydrophilic than crosslinked film surfaces. There was no significant difference between WCA values of 4%, 8%, 10% and 12% crosslinked films showing that increasing GA ratio did not influence surface hydrophilicity. In the literature, there are studies focused on the effect of plasticization (Ghanbarzadeh et al., 2007), the effect of solvent type (Ghanbarzadeh et al., 2007; Shi et al., 2009) and the effect of water vapor treatment (Wang, Fu, & Wang, 2009) on WCA values of zein films. However, there is no other study conducted on the effects of GA-crosslinking on zein film surface properties. Our surface topography analysis proves that this change in contact angles was not due to the changing surface roughness values of the films since there was no exact correlation between the contact angles and the surface roughness values, which will be explained in detail in section 2.4.7. Therefore, the changing contact angle values can only be explained with the changing chemistry of the zein films as GA ratio increases. FTIR results showed that a portion of α-helix structures are unfolding during crosslinking and turn into β-sheet structures. This transformation increased the exposure of hydrogen bonding sites of amino acids which resulted in increased water contact angle values. These results are consistent with the findings of Bugs et al. (2004) and Mejia et al. (2007), where increasing water amount increased the β-sheet content of zein in aqueous ethanol solutions and dough formations,

respectively. These studies also prove that β-sheet structures are more hydrophilic than α-helix structures.

2.4.7 Atomic force microscopy

The effects of GA-crosslinking on the surface morphology of plasticized zein films were also studied with AFM for the first time in this paper. The images were taken at 2 μm × 2 μm scanning areas. Figure 9 shows the images of zein films with different GA concentrations. The uncrosslinked zein films had the smoothest surfaces among all the formulations with some short and sharp structures on their surfaces. The structures observed on the surface of the crosslinked films, on the other hand, were slightly thicker and more dome-shaped than the structures on uncrosslinked films. Also, as the crosslinker ratio increased, the number of these structures increased significantly. Table 2 shows the average roughness values for the zein films. Although the lowest average roughness value was calculated for uncrosslinked zein films (0.78 nm), statistical analysis showed that there was no significant difference between uncrosslinked films, 4% crosslinked films and 10% crosslinked films. Statistically, films with 12% GA had the highest average roughness value of 3.65 nm. The overall roughness results showed that increasing crosslinker ratio increased the surface roughness of the films. Our roughness values are in correlation with the reported roughness values for spin coated uncrosslinked zein films from acetic acid solutions (Shi et al., 2009).

In a study conducted on the phosphorylation of zein films with POCl3, the surface roughness of the films was found to increase significantly (Wu, Wen, Yang, Xu, & Yin, 2011). The authors explained this phenomenon with increasing agglomeration of the zein molecules due to increasing self-attraction with phosphorylation. The same phenomenon is seen in our zein films, where stronger attractions between zein molecules are created by crosslinking. The tighter junction points, which are created between the glutamine ends of zein molecules, create denser regions in the zein matrix which is similar to agglomeration. Upon evaporation of the solvent, these denser regions form structures on the surface of the films and increase the surface roughness. Since the number of junction points increase with increasing crosslinker ratio, the number of the structures also increase consequently.

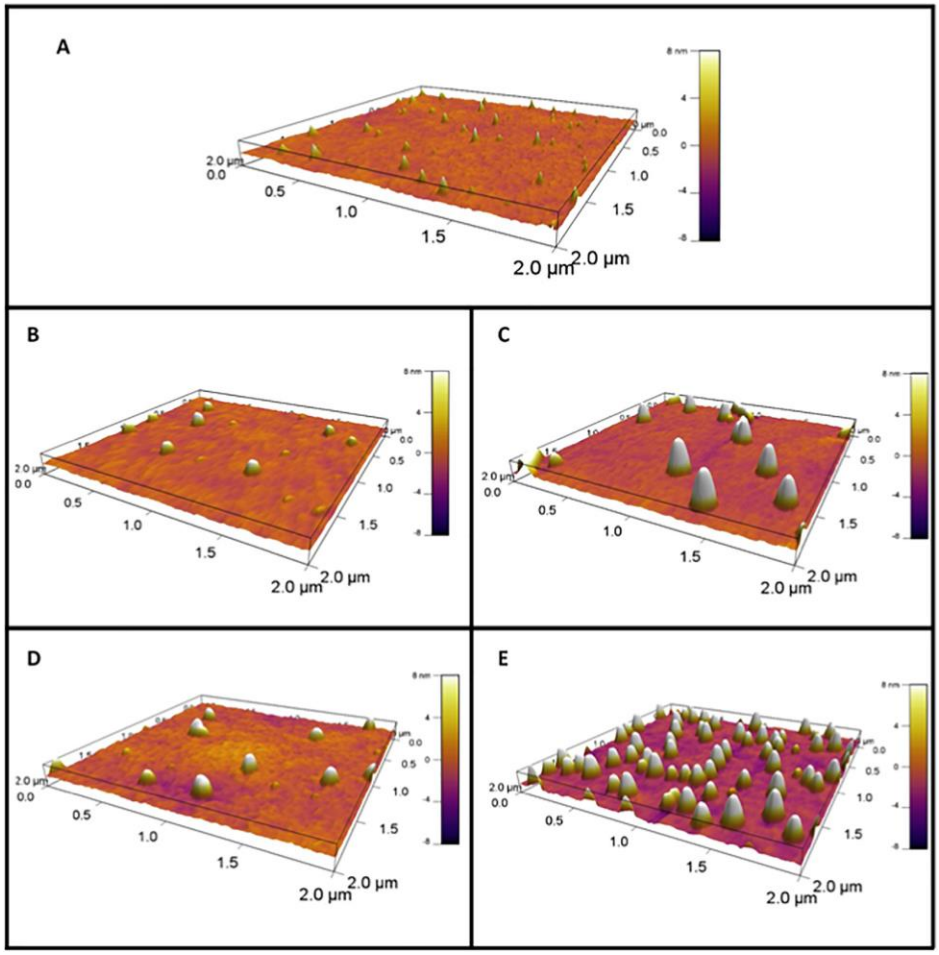

Figure 9. AFM images of zein films containing A) 0% GA, B) 4% GA, C) 8% GA, D) 10% GA and E) 12% GA.

2.5 Conclusions

In this study, a new mechanism is proposed for the first time for glutaraldehyde (GA) crosslinking of plasticized zein films cast from acetic acid solutions using FTIR, FT-Raman, mechanical and surface properties. As a primary mechanism, GA binds to the glutamine ends of zein molecules by replacing the already existing plasticizer molecules through imine structure formation. This mechanism creates tighter junction points in the zein matrix. Crosslinking enhanced the mechanical properties of zein films and increased their surface roughness significantly. As a secondary crosslinking mechanism, some of the GA molecules bind to the –NH sites of zein located on the lateral sides of α-helix structures and convert these α-helix structures into less ordered β-sheet structures, resulting in an increased hydrophilicity of zein films. Water vapor

permeability values of the films were not affected by crosslinking since even the highest number of crosslinks (1 in every 27 zein molecules) was not enough to create a significant barrier for water.

This study is an example of how the physical, mechanical and surface properties of zein films, cast from aqueous acetic acid solutions, can be modified with crosslinking. Such developments in the properties of zein films are crucially necessary since the industrial applications of zein are very limited due to the weaknesses of unmodified zein products. Therefore, improving the understanding of zein crosslinking is especially important for a proper application of crosslinkers and development of zein products with superior properties, such as much stiffer and durable platforms for biodegradable biosensors or scaffolds in tissue engineering, or more hydrophilic surfaces for better fluid flow in biodegradable microfluidic devices made from zein.

2.6 References

Argos, P., Pedersen, K., Marks, M., & Larkins, B. (1982). A Structural Model for Maize Zein Proteins. *Journal of Biological Chemistry*, *257*(17), 9984–9990.

Barth, A. (2000). The infrared absorption of amino acid side chains. *Progress in Biophysics and Molecular Biology*, *74*(3–5), 141–173. https://doi.org/10.1016/S0079-6107(00)00021-3

Beck, M. I., Tomka, I., & Waysek, E. (1996). Physico-chemical characterization of zein as a film coating polymer: A direct comparison with ethyl cellulose. *International Journal of Pharmaceutics*, *141*(1), 137–150. https://doi.org/10.1016/0378-5173(96)04630-3

Budi Santosa, F. X., & Padua, G. W. (1999). Tensile Properties and Water Absorption of Zein Sheets Plasticized with Oleic and Linoleic Acids. *Journal of Agricultural and Food Chemistry*, *47*(5), 2070–2074. https://doi.org/10.1021/jf981154p

Bugs, M. R., Forato, L. A., Bortoleto-Bugs, R. K., Fischer, H., Mascarenhas, Y. P., Ward, R. J., & Colnago, L. A. (2004). Spectroscopic characterization and structural modeling of prolamin from maize and pearl millet. *European Biophysics Journal with Biophysics Letters*, *33*(4), 335–343. https://doi.org/10.1007/s00249-003-0354-3

Demir, M., Ramos-Rivera, L., Silva, R., Nazhat, S. N., & Boccaccini, A. R. (2017). Zein-based composites in biomedical applications. *Journal of Biomedical Materials Research Part A*, *105*(6), 1656–1665. https://doi.org/10.1002/jbm.a.36040

Di Gioia, L., & Guilbert, S. (1999). Corn Protein-Based Thermoplastic Resins: Effect of Some Polar and Amphiphilic Plasticizers. *Journal of Agricultural and Food Chemistry*, *47*(3), 1254–1261. https://doi.org/10.1021/jf980976j

Fereshteh, Z., Nooeaid, P., Fathi, M., Bagri, A., & Boccaccini, A. R. (2015). Mechanical properties and drug release behavior of PCL/zein coated 45S5 bioactive glass scaffolds for bone tissue engineering application. *Data in Brief*, *4*, 524–528. https://doi.org/10.1016/j.dib.2015.07.013

Forato, L. A., Bicudo, T. C., & Colnago, L. A. (2003). Conformation of alpha Zeins in solid state by Fourier transform IR. *Biopolymers*, *72*(6), 421–426. https://doi.org/10.1002/bip.10481

Georget, D. M. R., Barker, S. A., & Belton, P. S. (2008). A study on maize proteins as a potential new tablet excipient. *European Journal of Pharmaceutics and Biopharmaceutics*, *69*(2), 718–726. https://doi.org/10.1016/j.ejpb.2008.01.006

Gezer, P. G., Brodsky, S., Hsiao, A., Liu, G. L., & Kokini, J. L. (2015). Modification of the hydrophilic/hydrophobic characteristic of zein film surfaces by contact with oxygen plasma treated PDMS and oleic acid content. *Colloids and Surfaces B: Biointerfaces*, *135*, 433–440.

Gezer, P. G., Liu, G. L., & Kokini, J. L. (2016a). Detection of acrylamide using a biodegradable zein-based sensor with surface enhanced Raman spectroscopy. *Food Control*, *68*, 7–13. https://doi.org/10.1016/j.foodcont.2016.03.002

Gezer, P. G., Liu, G. L., & Kokini, J. L. (2016b). Development of a biodegradable sensor platform from gold coated zein nanophotonic films to detect peanut allergen, Ara h1, using surface enhanced raman spectroscopy. *Talanta*, *150*, 224–232. https://doi.org/10.1016/j.talanta.2015.12.034

Ghanbarzadeh, B., Musavi, M., Oromiehie, A. R., Rezayi, K., Razmi Rad, E., & Milani, J. (2007). Effect of plasticizing sugars on water vapor permeability, surface energy and microstructure properties of zein films. *LWT - Food Science and Technology*, *40*(7), 1191–1197. https://doi.org/10.1016/j.lwt.2006.07.008

Gluck-Hirsch, J. B., & Kokini, J. L. (1997). Determination of the molecular weight between crosslinks of waxy maize starches using the theory of rubber elasticity. *Journal of Rheology*, *41*(1), 129–140. https://doi.org/10.1122/1.550804

Karthikeyan, K., Guhathakarta, S., Rajaram, R., & Korrapati, P. S. (2012). Electrospun zein/eudragit nanofibers based dual drug delivery system for the simultaneous delivery of aceclofenac and pantoprazole. *International Journal of Pharmaceutics*, *438*(1), 117–122. https://doi.org/10.1016/j.ijpharm.2012.07.075

Kashiri, M., Cerisuelo, J. P., Dominguez, I., Lopez-Carballo, G., Hernandez-Munoz, P., & Gavara, R. (2016). Novel antimicrobial zein film for controlled release of lauroyl arginate (LAE). *Food Hydrocolloids*, *61*, 547–554. https://doi.org/10.1016/j.foodhyd.2016.06.012

Kashiri, M., Cerisuelo, J. P., Domínguez, I., López-Carballo, G., Muriel-Gallet, V., Gavara, R., & Hernández-Muñoz, P. (2017). Zein films and coatings as carriers and release systems of Zataria multiflora Boiss. essential oil for antimicrobial food packaging. *Food Hydrocolloids*, *70*(Supplement C), 260–268. https://doi.org/10.1016/j.foodhyd.2017.02.021

Kokini, J. L., Cocero, A. M., Madeka, H., & de Graaf, E. (1994). The development of state diagrams for cereal proteins. *Trends in Food Science & Technology*, *5*(9), 281–288. https://doi.org/10.1016/0924-2244(94)90136-8

Krimm, S., & Bandekar, J. (1986). Vibrational Spectroscopy and Conformation of Peptides, Polypeptides, and Proteins. In J. T. E. and F. M. R. C.B. Anfinsen (Ed.), *Advances in Protein Chemistry* (Vol. 38, pp. 181–364). Academic Press. Retrieved from http://www.sciencedirect.com/science/article/pii/S0065323308605288

Lai, H. M., Geil, P. H., & Padua, G. W. (1999). X-ray diffraction characterization of the structure of zein-oleic acid films. *Journal of Applied Polymer Science*, *71*(8), 1267–1281. https://doi.org/10.1002/(SICI)1097-4628(19990222)71:8<1267::AID-APP7>3.0.CO;2-O

Lai, H.-M., Padua, G. W., & Wei, L. S. (1997). Properties and microstructure of zein sheets plasticized with palmitic and stearic acids. *Cereal Chemistry*, *74*(1), 83–90.

Lai, L. F., & Guo, H. X. (2011). Preparation of new 5-fluorouracil-loaded zein nanoparticles for liver targeting. *International Journal of Pharmaceutics*, *404*(1-2), 317–323. https://doi.org/10.1016/j.ijpharm.2010.11.025

Lambert, I. A., & Kokini, J. L. (2001). Effect of l-Cysteine on the Rheological Properties of Wheat Flour. *Cereal Chemistry Journal*, *78*(3), 226–230. https://doi.org/10.1094/CCHEM.2001.78.3.226

Lambert, J. B. (1998). *Organic structural spectroscopy*. Upper Saddle River, N.J.: Prentice Hall.

Lawton, J. W. (2004). Plasticizers for Zein: Their Effect on Tensile Properties and Water Absorption of Zein Films. *Cereal Chemistry Journal*, *81*(1), 1–5. https://doi.org/10.1094/CCHEM.2004.81.1.1

Li, K.-K., Yin, S.-W., Yang, X.-Q., Tang, C.-H., & Wei, Z.-H. (2012). Fabrication and Characterization of Novel Antimicrobial Films Derived from Thymol-Loaded Zein-Sodium Caseinate (SC) Nanoparticles. *Journal of Agricultural and Food Chemistry*, *60*(46), 11592–11600. https://doi.org/10.1021/jf302752v

Lin-Vien, D., Colthup, N. B., Fateley, W. G., & Grasselli, J. G. (1991a). CHAPTER 10 - Compounds Containing –NH2, –NHR, and –NR2 Groups. In *The Handbook of Infrared and Raman Characteristic Frequencies of Organic Molecules* (pp. 155–178). San Diego: Academic Press. Retrieved from http://www.sciencedirect.com/science/article/pii/B978008057116450016X

Lin-Vien, D., Colthup, N. B., Fateley, W. G., & Grasselli, J. G. (1991b). CHAPTER 12 - Double Bonds Containing Nitrogen Atoms. In *The Handbook of Infrared and Raman Characteristic Frequencies of Organic Molecules* (pp. 191–211). San Diego: Academic Press. Retrieved from https://www.sciencedirect.com/science/article/pii/B9780080571164500183

Li, Y., Xia, Q., Shi, K., & Huang, Q. (2011). Scaling Behaviors of alpha-Zein in Acetic Acid Solutions. *Journal of Physical Chemistry B*, *115*(32), 9695–9702. https://doi.org/10.1021/jp203476m

Luecha, J., Hsiao, A., Brodsky, S., Logan Liu, G., & L. Kokini, J. (2011). Green microfluidic devices made of corn proteins. *Lab on a Chip*, *11*(20), 3419–3425. https://doi.org/10.1039/C1LC20726A

Luo, Y., & Wang, Q. (2014). Zein-based micro- and nano-particles for drug and nutrient delivery: A review. *Journal of Applied Polymer Science*, *131*(16), 40696. https://doi.org/10.1002/app.40696

Madeka, H., & Kokini, J. L. (1996). Effect of glass transition and cross-linking on rheological properties of zein: Development of a preliminary state diagram. *Cereal Chemistry*, *73*(4), 433–438.

Masamba, K., Li, Y., Hategekimana, J., Zehadi, M., Ma, J., & Zhong, F. (2016). Evaluation of mechanical and water barrier properties of transglutaminase cross-linked zein films incorporated with oleic acid. *International Journal of Food Science & Technology*, *51*(5), 1159–1167. https://doi.org/10.1111/ijfs.13069

Matsushima, N., Danno, G., Takezawa, H., & Izumi, Y. (1997). Three-dimensional structure of maize alpha-zein proteins studied by small-angle X-ray scattering. *Biochimica Et Biophysica Acta-Protein Structure and Molecular Enzymology*, *1339*(1), 14–22. https://doi.org/10.1016/S0167-4838(96)00212-9

Matthäus, C., Bird, B., Miljković, M., Chernenko, T., Romeo, M., & Diem, M. (2008). Infrared and Raman Microscopy in Cell Biology. *Methods in Cell Biology*, *89*, 275–308. https://doi.org/10.1016/S0091-679X(08)00610-9

Mejia, C. D., Mauer, L. J., & Hamaker, B. R. (2007). Similarities and differences in secondary structure of viscoelastic polymers of maize α-zein and wheat gluten proteins. *Journal of Cereal Science*, *45*(3), 353–359. https://doi.org/10.1016/j.jcs.2006.09.009

Migneault, I., Dartiguenave, C., Bertrand, M. J., & Waldron, K. C. (2004). Glutaraldehyde: behavior in aqueous solution, reaction with proteins, and application to enzyme crosslinking. *BioTechniques*, *37*(5), 790–796, 798–802.

Mizutani, Y., Matsumura, Y., Imamura, K., Nakanishi, K., & Mori, T. (2003). Effects of Water Activity and Lipid Addition on Secondary Structure of Zein in Powder Systems. *Journal of Agricultural and Food Chemistry*, *51*(1), 229–235. https://doi.org/10.1021/jf0205007

Ozcalik, O., & Tihminlioglu, F. (2013). Barrier properties of corn zein nanocomposite coated polypropylene films for food packaging applications. *Journal of Food Engineering*, *114*(4), 505–513. https://doi.org/10.1016/j.jfoodeng.2012.09.005

Parris, N., & Coffin, D. R. (1997). Composition Factors Affecting the Water Vapor Permeability and Tensile Properties of Hydrophilic Zein Films. *Journal of Agricultural and Food Chemistry*, *45*(5), 1596–1599. https://doi.org/10.1021/jf960809o

Parris, N., Cooke, P. H., & Hicks, K. B. (2005). Encapsulation of Essential Oils in Zein Nanospherical Particles. *Journal of Agricultural and Food Chemistry*, *53*(12), 4788–4792. https://doi.org/10.1021/jf040492p

Paulis, J. W., & Wall, J. S. (1977). Fractionation and characterization of alcohol soluble reduced corn endosperm glutelin proteins. *Cereal Chemistry*, *54*, 1223–1228.

Peter. Larkin. (2011). *Infrared and Raman Spectroscopy Principles and Spectral Interpretation*. Burlington: Elsevier Science.

Rieger, B., Künkel, A., Coates, G. W., Reichardt, R., Dinjus, E., & Zevaco, T. A. (2012). *Synthetic Biodegradable Polymers*. Springer Science & Business Media.

Ruijgrok, J. M., Boon, M. E., & Wijn, J. R. D. (1990). The effect of heating by microwave irradiation and by conventional heating on the aldehyde concentration in aqueous glutaraldehyde solutions. *The Histochemical Journal*, *22*(6-7), 389–393. https://doi.org/10.1007/BF01003175

Selling, G. W., Woods, K. K., & Biswas, A. (2011). Electrospinning formaldehyde-crosslinked zein solutions. *Polymer International*, *60*(4), 537–542. https://doi.org/10.1002/pi.3009

Sessa, D. J., Mohamed, A., & Byars, J. A. (2008). Chemistry and Physical Properties of Melt-Processed and Solution-Cross-Linked Corn Zein. *Journal of Agricultural and Food Chemistry*, *56*(16), 7067–7075. https://doi.org/10.1021/jf800712k

Sessa, D. J., Mohamed, A., Byars, J. A., Hamaker, S. A. H., & Selling, G. W. (2007). Properties of films from corn zein reacted with glutaraldehyde. *Journal of Applied Polymer Science*, *105*(5), 2877–2883. https://doi.org/10.1002/app.26272

Shi, K., Kokini, J. L., & Huang, Q. (2009). Engineering Zein Films with Controlled Surface Morphology and Hydrophilicity. *Journal of Agricultural and Food Chemistry*, *57*(6), 2186–2192. https://doi.org/10.1021/jf803559v

Shi, K., Yu, H., Lakshmana Rao, S., & Lee, T.-C. (2012). Improved mechanical property and water resistance of zein films by plasticization with tributyl citrate. *Journal of Agricultural and Food Chemistry*, *60*(23), 5988–5993.

Shukla, R., & Cheryan, M. (2001). Zein: the industrial protein from corn. *Industrial Crops and Products*, *13*(3), 171–192. https://doi.org/10.1016/S0926-6690(00)00064-9

Turasan, H., & Kokini, J. L. (2016). Advances in Understanding the Molecular Structures and Functionalities of Biodegradable Zein-based Materials Using Spectroscopic Techniques: A Review. *Biomacromolecules*. https://doi.org/10.1021/acs.biomac.6b01455

Unnithan, A. R., Sasikala, A. R. K., Sathishkumar, Y., Lee, Y. S., Park, C. H., & Kim, C. S. (2014). Nanoceria doped electrospun antibacterial composite mats for potential biomedical applications. *Ceramics International*, *40*(8), 12003–12012. https://doi.org/10.1016/j.ceramint.2014.04.038

Wang, H.-J., Fu, J.-X., & Wang, J.-Y. (2009). Effect of water vapor on the surface characteristics and cell compatibility of zein films. *Colloids and Surfaces B: Biointerfaces*, *69*(1), 109–115. https://doi.org/10.1016/j.colsurfb.2008.11.015

Whipple, E. B., & Ruta, M. (1974). Structure of aqueous glutaraldehyde. *The Journal of Organic Chemistry*, *39*(12), 1666–1668. https://doi.org/10.1021/jo00925a015

Wu, L.-Y., Wen, Q.-B., Yang, X.-Q., Xu, M.-S., & Yin, S.-W. (2011). Wettability, surface microstructure and mechanical properties of films based on phosphorus oxychloride-treated zein. *Journal of the Science of Food and Agriculture*, *91*(7), 1222–1229.

Xu, H., Chai, Y., & Zhang, G. (2012). Synergistic Effect of Oleic Acid and Glycerol on Zein Film Plasticization. *Journal of Agricultural and Food Chemistry*, *60*(40), 10075–10081. https://doi.org/10.1021/jf302940j

Yang, H., Feng, K., Wen, P., Zong, M.-H., Lou, W.-Y., & Wu, H. (2017). Enhancing oxidative stability of encapsulated fish oil by incorporation of ferulic acid into electrospun zein mat. Lwt-Food Science and Technology, 84, 82–90. https://doi.org/10.1016/j.lwt.2017.05.045

CHAPTER 3. EFFECT OF PLASTICIZING AND CROSSLINKING AT ROOM TEMPERATURE ON MICROSTRUCTURE REPLICATION USING SOFT LITHOGRAPHY ON ZEIN FILMS

Reprinted with permission. Full citation:
Barber, E.A., Turasan, H., Gezer, P.G., Devina, D., Liu, G.L., & Kokini, J. 2019. Effect of plasticizing and crosslinking at room temperature on microstructure replication using soft lithography on zein films. Journal of Food Engineering. 250, 55-64 https://doi.org/10.1016/j.jfoodeng.2019.01.018

3.1 Abstract

This study examined various zein film formulations to improve the properties for a Surface Enhanced Raman Spectroscopy (SERS) sensor application. Both oleic acid (OA) plasticizer and glutaraldehyde (GDA) crosslinker were simultaneously incorporated in the films to heighten particular mechanical and surface properties and enhance fidelity of transfer of micro/nano structures. It was found that both GDA and OA concentrations played a significant role in the overall properties of the film to make an effective SERS substrate. The formulation with the best fidelity of transfer during micro/nano lithography was found to be the one containing 0.8 OA with 4% GDA. SERS measurements proved that better nanostructure fidelity enhances the intensity of the Raman signal.

3.2 Introduction

An abundant and inexpensive byproduct of ethanol manufacture, zein, is an amphiphilic storage protein from corn with applications as packaging material, edible coatings, and microfluidic devices. These functions are plausible uses for zein due to its biodegradable film forming capabilities with a depletion rate of 80% within 20 days (Romero-Bastida et al. 2004) as well as tunable surface, strength, and permeability properties. As an amphiphilic protein, zein has a large fraction of hydrophobic amino acids like proline, alanine, and leucine in addition to a considerable fraction of hydrophilic glutamine (Watson and Ramstad 1987). The structure of zein is currently under debate, but most structures build off of the two most cited models of Argos et al. (1982) and Matsushima et al. (1997) (Bugs et al. 2004; Forato et al. 2004; Momany et al. 2006; Li et al. 2011). Overall, most scientists agree that the zein structure consists of α-helices, β-pleated sheets, and

random coils wrapped around one another in a cylindrical dowel like structures with hydrophobic lateral sides. These dowels are then connected to one another by hydrophilic, glutamine β-turns (Matsushima et al. 1997). This amphiphilic nature allows for zein films plasticized by oleic acid, to flexibly arrange and mimic the hydrophilicity of the contact surface on which it was cast (Gezer et al. 2015).

One interesting application of ethanol solution cast plasticized zein films presented by Gezer et al. (2015) is as a biodegradable platform for a surface enhanced Raman spectroscopy (SERS) sensor. Gezer et al. (2016) fabricated zein substrates through the simultaneous transfer of gold and imprinted nano/microstructures from a polydimethylsiloxane (PDMS) platform into plasticized zein films using soft lithography. While these were relatively successful prototypes, they did not attain the sensitivity needed to meet FDA regulations. One setback was the insufficient replication, or fidelity of the nano/microstructures. This lack of fidelity causes a decrease in the number of hot spots through faulted structures as well as an inconsistency in the signal collected across the biosensor surface. To improve the fidelity of these zein substrates, this paper focuses on studying the network formation of oleic acid (OA) plasticized zein films through crosslinking with glutaraldehyde (GDA) for the optimization of zein films in this application. The previous work used OA plasticizer in a 1:1 w/w zein ratio to prevent the film from being excessively brittle (Gezer et al. 2016a; Gezer et al. 2016b), but possible contributions to the decrease in nanostructure fidelity include a film that may not have the optimal ductility.

Therefore, this study investigates the use of different concentrations of OA plasticizer and GDA chemical crosslinking agent to optimize the mechanical as well as surface properties of zein films for an optimal nano/microstructure transfer from the PDMS mold to zein-based SERS substrate during soft lithography to enhance the intensity of the SERS signal. The ratios of both additives were varied within the film matrix. SEM analysis helped determine the fidelity of the replicated nanostructures, while the indentation, rheology, and WCA were used to better understand the physical properties that could contribute to differences seen with the SEM. FTIR and FT-Raman data was tied in with the mechanical and surface analyses to understand the films' chemical natures and the process in these films affecting the fidelity of nanostructures on a molecular level.

3.3 Materials and Methods

3.3.1 Materials

Ethyl Alcohol (140 Proof) was purchased from Decon Laboratories Inc. (King of Prussia, PA); Zein (Z3625) and glutaraldehyde (GDA) (25% in water solution) were obtained from Sigma-Aldrich (St. Louis, MO); Oleic Acid (OA) (technical grade 90%) from Alfa Aesar (Ward Hill, MA); mono-diglyceride emulsifier (BFP 65K 1004200364) from Caravan Ingredients (Lenexa, KS), and Sylgard (184 Silicone Elastomer Kits) from Dow Corning (Midland, MI).

3.3.2 Zein Film Preparation Procedure

Zein film solutions were made by the dissolution of protein in 70% ethanol at a 1:5 w/v ratio heated to 62°C. After the zein was dispersed, the oleic acid (OA) plasticizer was added. The ratio of OA varied from 0.8:1 to 1:1 to 1.2:1 (w/w) with zein. A mono/diglyceride emulsifier was also added along with the plasticizer at a constant 0.05:1 (w/w) ratio with the plasticizer. The solutions were thoroughly mixed at 62°C for 10 minutes and the uncrosslinked (0% GDA) solutions were poured directly into 100 mm polystyrene petri dishes to fabricate films without any crosslinker. The crosslinked solutions were prepared by adding GDA at 4 or 8% w/w zein, after the solutions were cooled down to room temperature. The crosslinking reaction was carried out at room temperature under continuous stirring for 12, 15 or 18 h for solutions containing 0.8:1, 1:1 and 1.2:1 oleic acid (w/w zein) ratios respectively. Rheological measurements were used to determine the time to stop the reaction. These times corresponded to where the storage modulus (G') and the loss modulus (G") were equal for each formulation as discussed in section 2.4.2 and the data was given in Figure 4. At this point, gelation has progressed enough to begin the formation of an infinite molecular weight network and were poured into petri dishes. To keep the film thicknesses consistent, a constant solution mass of 17.6 ± 0.7 g was poured into each petri dish for both crosslinked and uncrosslinked films. This resulted in films with an average thickness of 0.95 ± 0.20 mm. The petri dishes used to form zein films were coated on the bottom with polydimethylsiloxane (PDMS). In prior work, it has been shown that the surface energy between zein and PDMS favors and facilitates the removal of zein films (Gezer et al. 2015). The PDMS was prepared by combining the base and curing solutions in a 10:1 volume ratio from the elastomer kit. After vigorous stirring of the elastomer mixture by hand, the solution was placed under vacuum (10 in Hg) to remove trapped

air bubbles. The liquid elastomer was then poured on the bottom of a 100 mm petri dish and was left at room temperature for 3 days to cure (Gezer et al 2016). After casting zein solutions on cured PDMS layers, all were placed in desiccators to remove free water and ethanol, creating protein films. The films were dried in the desiccators until their weights had equilibrated.

3.3.3 Microstructure Imprinting on Zein Films

Microstructures were imprinted onto zein films to evaluate the fidelity of their transfer. The transfer process was completed through soft lithography. This technique involves the transfer of microstructures from a master mold to the final product (zein films) through PDMS as the intermediate material. The master mold in this study was created on a photocured polyethylene plastic with an inverted micropyramidal structure. This particular microstructure was used because earlier studies have shown that this shape generated the highest SERS enhancement when compared to nanopillars and nanodomes (Gezer et al. 2016). The dimensions of the inverted micropyramids were 2μm x 2μm x 2.1μm. PDMS was first cured atop the PET master mold and was imprinted with the reverse of the original structures (aka positive micropyramids). Then the PDMS was removed from the PET mold and placed in a small petri dish (60mm in diameter) for casting zein solutions for film formation (as stated in section 2.2). This way a zein film with the same structures as the PET master mold (inverted pyramids) is fabricated.

3.3.4 Characterization of the Physical and Chemical Properties of Zein Films

Vicker's Hardness Indentation

The mechanical properties of the dried films were first tested using a Vicker's hardness indenter. The Vicker's hardness diamond indenter was used for these tests with a load size of 10 gf. The hardness values of the equilibrated films were analyzed to establish the overall hardness of the films. The indentation areas for each formulation were converted to Vicker's hardness values for evaluation

Rheological Measurements

Rheological measurements were conducted at 25 ℃ on the zein film formulations to determine the degree of gelation. The measurements were conducted using the parallel plate geometry with a 40 mm cross-hatched plate to avoid slip. After solutions were prepared, they were stored in 250 ml glass bottles with caps. The bottles were closed tightly to avoid loss of ethanol. The solutions were equilibrated to room temperature, prior to the addition of GDA. The point at which the crosslinker was added to the solutions was denoted as 0 h point for crosslinking purposes. The solutions were kept tightly sealed for the entirety of the experiment. All formulations were continuously stirred at 600 rpm through the duration of the experiment.

Strain sweeps were conducted from 0.1% to 100% strain to determine the linear viscoelastic region for all solutions and gels at 10 rad/s. A higher strain was selected for the low viscosity fluid at 0 hours in order to ensure that stress signal was high enough to be reliable and accurate. Since $\tau_0 = G"\gamma_0/sin\delta$ and the material is very dilute where the phase angle $\delta \approx 90°$ and ≈ 1 . The stress equation becomes $\tau_0 = G"\gamma_0$ where the higher γ_0 values result in higher τ_0. Both the storage and loss moduli (G' and G") were then measured as a function of frequency in the range of 1-100 rad/sec at a strain of 10% for the low viscosity fluid and 1% strain was used for the gels. Both of these strains were in the linear region for the respective fluid. All measurements were conducted with a TA Discovery HR-3 Hybrid Rheometer. At the beginning of each rheological measurement, parts of the sample to be measured were taken out of the sealed glass containers, and the rest of the sample was kept sealed until the next measurement. During the rheological measurements a solvent trap containing 70% ethanol was used to avoid loss of solvent. Both the amplitude and frequency sweeps were done in triplicate every 12 hours until the G' values reached an equilibrium.

Based on the rubber elasticity theory (Gluck-Hirsch and Kokini 1997), the final storage modulus values (G'_T) were then used to determine the total number of network junctions (N_T) in the various formulations. At 0% GDA, all junctions are due to aggregation, while the introduction of GDA yields the inclusion of chemical crosslinking. Using the rubber elasticity theory the molecular weight between all network junctions (M_T) is estimated using Eqn. 6, where ρ is the dry density of zein (1.22 g/cm^3) (Turasan et al. 2018), c is the concentration of zein within the sample (g/cm^3),

R is the gas constant (8314000 cm^3.Pa/mol.K), T is absolute temperature (298 K), and G'_T is the storage modulus of the sample.

$$M_T = \frac{\rho^{2/3} c^{1/3} RT}{G'_T} \qquad \text{(Eqn. 6)}$$

The total number of network junctions (N_T) is estimated using Eqn. 7, where M_w is the molecular weight of zein (22 kDa) (Turasan and Kokini 2017):

$$N_T = \frac{M_w}{2M_T} \qquad \text{(Eqn. 7)}$$

N_T for the 0% GDA formulations represents the number of network junctions due to aggregation. The N_T for the 4% and 8% GDA formulations gives the total number of network junctions from the protein aggregation as well as crosslinking with GDA.

Fourier Transform Infrared (FTIR) and Fourier Transform (FT) - Raman Spectroscopies

The FTIR and FT-Raman data were collected to determine chemical changes in the films due to plasticization, aggregation and crosslinking. The FTIR spectra were collected by a Thermo Nicolet Nexus FTIR with a mercury cadmium telluride (MCT) detector and a Potassium Bromide (KBr) beam splitter. The spectra were collected in the range of 800-4500 cm^{-1} from 500 line-scans. These spectra were compared between formulations through the determination of peak creation and depletion as well as peak shifts and changes in intensity.

FT-Raman spectra were collected with a coupled Thermo Nicolet 6700 FTIR/FT-Raman Spectrophotometer. A 1064 nm laser was used with an InGaAs detector, a KBr beam splitter, and a spectrum range of 400-3600 cm^{-1}. The low laser energy results in considerable variability in the FT-Raman spectra intensities when comparing spectra collected on different days. Therefore, only the appearance and disappearance of peaks along with peak shifts were investigated. Baseline corrections were automatically applied to the spectra during Fourier transformation by the OMNIC software, and further correction was made manually during the investigation of specific peaks.

Secondary structure changes were also investigated using FTIR. The analysis was performed through a comparison of the Amide I band (1600-1700 cm^{-1}). Using OMNIC software, the Amide I peaks were first Fourier self-deconvoluted and then peak fitted using a Gaussian distribution with a constant baseline and a full width half height of 3.857 cm^{-1}. The deconvoluted peaks were then assigned to a secondary structure based on their locations: β-sheet (1600-1640 cm^{-1}), α-helix (1640-1660 cm^{-1}), β-turn (1660-1700 cm^{-1}) (Byler and Sushi 1986; Kong and Yu 2007; Xie and Tsou 1993). The percent area of each peak was calculated and compared between all formulations for secondary structure content determination.

Water Contact Angle Measurements

The change in hydrophobicity/hydrophilicity of the films with different formulations was determined on the PDMS contact side through static water contact angle measurements using an Attension Theta Auto 1 Optical Tensiometer. A constant droplet size of 2 μl was used. All contact angle measurements were collected after 30s in triplicate and analyzed using a manual baseline.

Scanning Electron Microscopy (SEM)

Scanning electron microscopy (SEM) images were taken to determine the quality of the imprinted nanostructures on a Nova NanoSEM 200. Once the films were dried, they were cut from the PDMS molds, and attached to 1 in. SEM stubs with double sided carbon tape. The samples were then coated with a platinum/palladium mixture for 60 s with a Cressington 208 HR sputter coater. The films were imaged with a spot size setting of 3.0 nm, an accelerating voltage of 5.0 kV, and a working distance of 5.7 mm. The images were examined for differences in micro pattern fidelity.

Surface Enhanced Raman Spectroscopy (SERS)

A Thermo Fisher Scientific DXR2 Raman Microscope was used to collect Raman spectra of nanostructured zein films. Rhodamine 6G was used as the Raman active molecule to test the intensity of the Raman signal. In order to create hotspots to enhance the Raman signal, the surface of the zein films were decorated with 50 nm gold nanoparticles (Ted Pella, Inc.) where nanostructures were imprinted. First, Rhodamine 6G solution and the 50 nm gold nanoparticle solution were mixed and a 2 μl droplet from this mixture was placed on the nanostructured area

on the zein films. The Rhodamine 6G concentration was 100 μM (Gezer, et al., 2016) and the 50 nm gold nanoparticle solution concentration was $2.3*10^{10}$ particles/ml. After the samples were dried in the desiccators containing Drierite (W.A. Hammond Drierite Company), they were taken to Raman measurements. A 633 nm laser was used at a power of 0.8 mW using 25 μm pinhole aperture. A long working distance 50x objective lens was used to image the samples. Due to the high fluorescence of zein, before each measurement, the samples were photo-bleached for 2 minutes. For each Raman spectrum, 20 spectra were averaged and each measurement was replicated 4 times, making 80 spectra for each formulation. After each spectrum was manually baseline corrected, they were averaged using the OMNIC software.

3.3.5 Statistical ANOVA Analysis

All statistics were analyzed using the MiniTab 17. The data was compared with a one-way ANOVA at a 95% confidence level with a Tukey's pairwise comparison, where different letters represent significant difference ($p<0.05$). The statistical analyses were conducted within each group based on oleic acid concentration, and between formulations with 0% GDA- unless otherwise stated. Significant difference within 0.8 OA group was shown using letters a-c; within 1.0 OA group using letters g-i; and within 1.2 OA group using letters u-w. Letters x-z were used to show significant difference between the formulations with 0% GDA and varying plasticizer content.

3.4 Results and Discussion

3.4.1 Vicker's Hardness of Zein Films

The indents varied based upon formulation due to different levels of plasticizer and crosslinking agent. An increase in GDA concentration caused a decrease in the Vicker's hardness (VH) value (Fig. 10). An increase in glutaraldehyde concentration did not necessarily increase the hardness of the films, but instead increased the elasticity of the films. The statistics showed that there was no difference between the 4% and 8% GDA addition at any level of plasticizer. However, all of the crosslinked films were statistically different from their uncrosslinked counterparts- except for the 4% GDA, 1.0 OA film. For this formulation, the VH was equivalent to that of the 0% GDA film as opposed to the 8% GDA film. This change in measurements could be due to the low degree of

crosslinking. The 4% GDA could be forming aggregates of crosslinked zein that did not have enough time or crosslinker to from an infinite molecular weight network with 1.0 OA. This response would cause the larger deviation observed between indents as well as be the reason for the overall average showing a larger VH value than what is needed to complete the trend from 0 to 8% GDA. For 0% GDA samples, as the OA concentration increased the VH decreased. There was a clear inverse trend between VH and amount of OA for all these films (Fig. 10). When plotted, this relationship becomes perfectly linear giving a trend line with an R^2 of 0.999. Therefore, this linear equation will predict the VH of any uncrosslinked zein films with varying OA concentration.

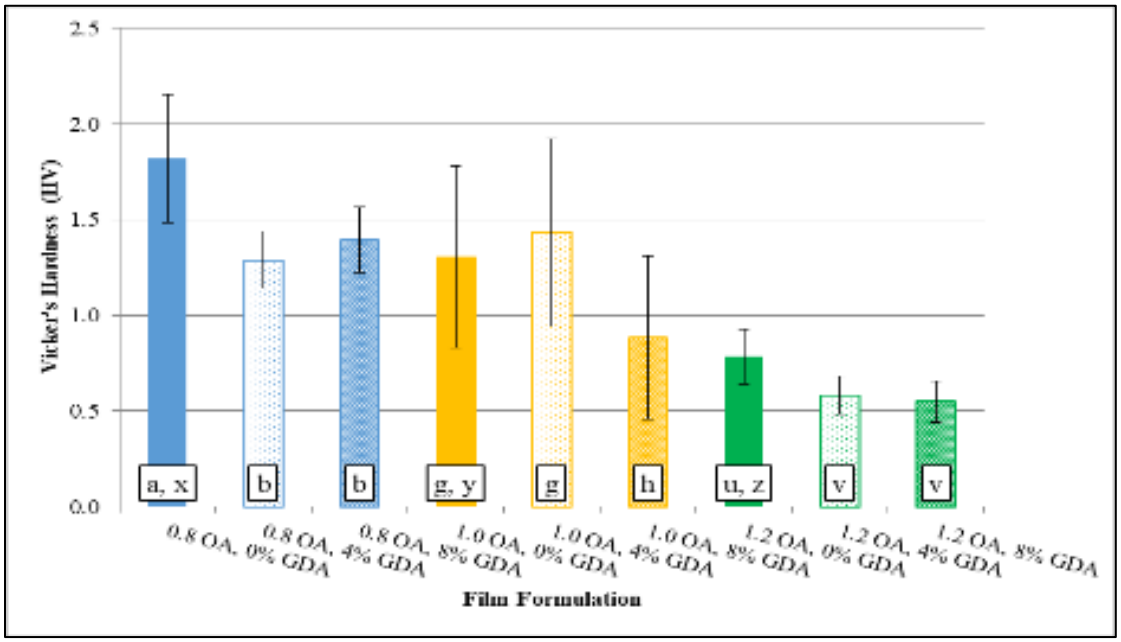

Figure 10. Vicker's hardness of zein film formulations: *different letter groupings represent different ANOVAs ($p<0.05$).*

3.4.2 Rheology of Zein Solution Gelation

An example of an amplitude sweep is given in Figure 11, where at 0 h the zein solution where crosslinking has not started shows a linear behavior up to 100% higher strain and at 72 h where the sample has appreciably crosslinked the linear region shifts to lower strain region and linearity is observed up to 4%. The strain amplitude sweeps showed a decrease in the linear region with gelation time (Fig. 11).

To understand structure development and gelation as well as crosslinking in the zein formulations frequency sweeps were conducted and G' and G" were plotted vs. frequency on log-log coordinates. The change in slope and magnitude in both G' and G" are indicative of gelation/crosslinking development. Initially G" was considerably larger than G', but as gelation time increased, G' crossed G" and became considerably larger- indicating structure development and gelation (Winter and Chambon, 1986). The frequency sweeps showed a decrease in the slope of G' vs. frequency (Fig. 12) a strong indication of gelation/crosslinking as well.

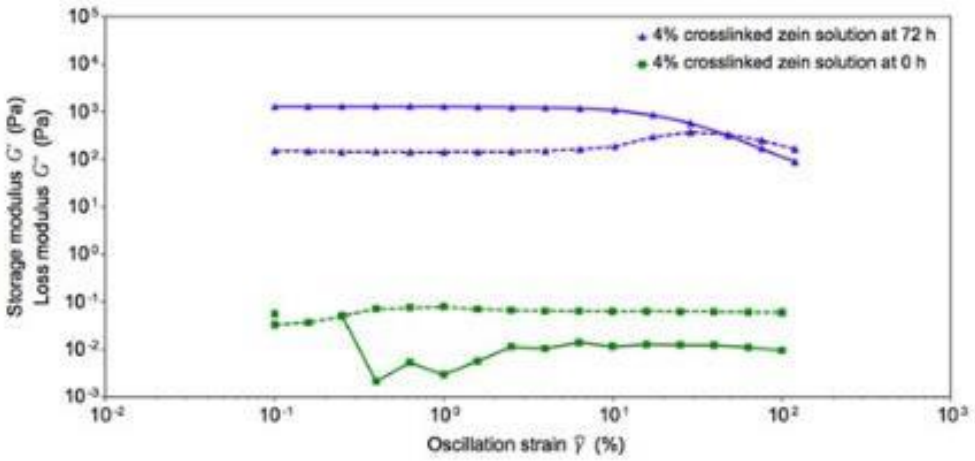

Figure 11. Amplitude sweeps of 4% crosslinked (1:1 OA) zein solution at 0 hour (green) and 72 hour (blue). The solid lines represent the storage moduli (G') and the dashed lines represent loss moduli (G").

To compare the formulations, the G' values at 10 rad/s from each frequency sweep were plotted as a function of time (Fig. 13). All the formulations show an increase in G' and reach an equilibrium plateau over time (Table 1). At 0% GDA, a large increase in G' is displayed with a decrease in OA concentration. The decrease in the amount of OA reduces the plasticization between zein molecules and facilitates network formation. The GDA, on the other hand, results in crosslinks that create a network that holds zein molecules together producing a firmer gel. For both the 1.0 and 1.2 OA concentrations the addition of GDA increased the storage modulus, due to network formation resulting in more solid-like behavior compared to the uncrosslinked formulations. The 0.8 OA gels did not show differences in G' with and without the crosslinker.

The decrease in OA content facilitated interaction between zein molecules, increasing the protein aggregation and resulting in considerable gelation.

This behavior is further confirmed by the estimated number of junctions (N_T) per zein molecule for each formulation (Table 3). The $N_T$is highest for the 0.8 OA gels, while the 1.0 and 1.2 OA gels showed slightly lower numbers of junctions. The N_T values for the 0% GDA films are very close to one another, as expected from the magnitude of the G' values and showing that aggregation plays a very large role in the gelation of these formulations. Overall, these numbers are very low and explain why very soft gels were obtained with these zein formulations.

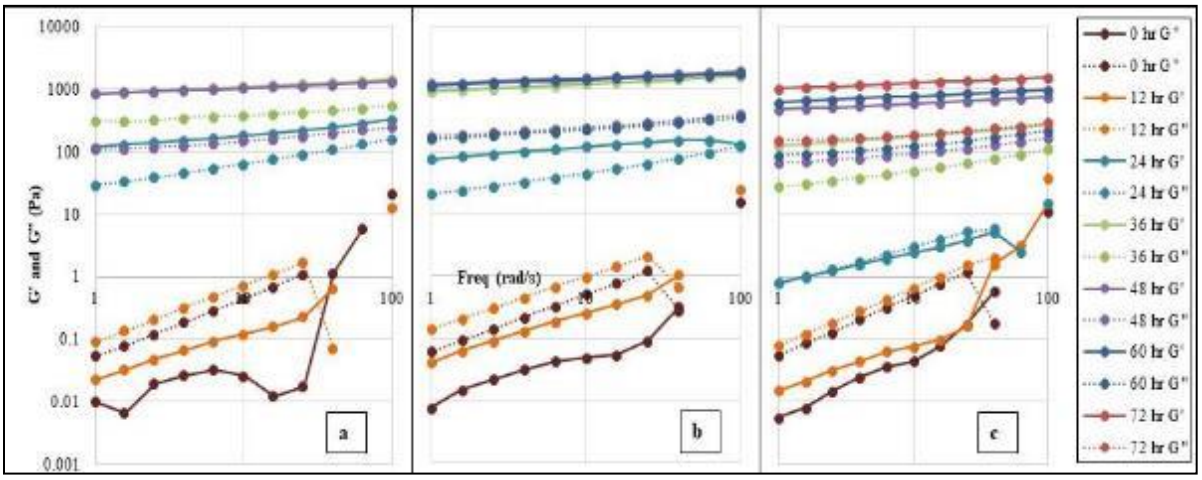

Figure 12. Frequency sweeps of 0.8 OA zein gels at: a) 0% GDA, b) 4% GDA, and c) 8% GDA.

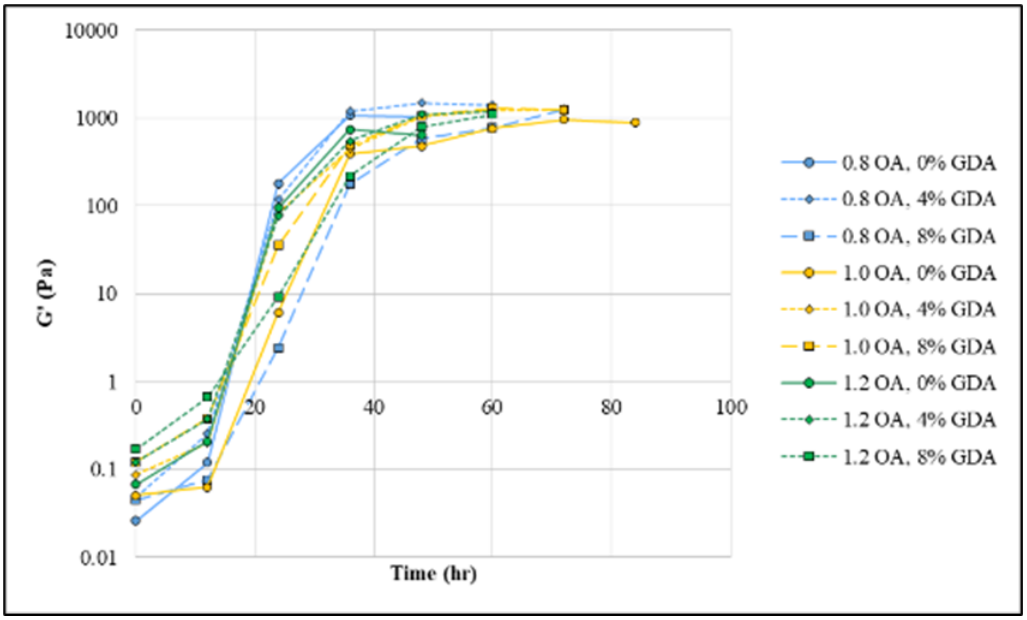

Figure 13. Storage moduli (G') for zein gel formulations over time at 10 rad/s.

Table 3. Water contact angles of crosslinked and uncrosslinked zein nanofibers with and without heat treatment (each time period was statistically compared within itself, and different letters show significant difference, $p<0.05$)

OA (w/w zein)	GDA (w/w zein)	Final G' (Pa)	M_T (Da)	N_T (per zein molecule)
0.8	0%	1040 ± 147*ax*	1.59E+06	0.007
	4%	1413 ± 222*a*	4.46E+06	0.009
	8%	1245 ± 182*a*	8.15E+06	0.008
1.0	0%	889 ± 120*gxy*	2.04E+06	0.006
	4%	1266 ± 168*h*	4.85E+06	0.008
	8%	1250 ± 180*h*	5.07E+06	0.008
1.2	0%	639 ± 105*uy*	3.07E+06	0.004
	4%	1180 ± 169*v*	3.65E+06	0.008
	8%	1101 ± 161*v*	4.23E+06	0.007

3.4.3 Mechanism of Zein Networking

Spectroscopic Analyses

The FTIR and FT-Raman spectra were analyzed to help determine the zein networking mechanism. For FT-Raman, the major difference was the presence of the 880 cm^{-1} peak (Fig. 14). This peak is an indication of the hydrogen bonding present on the indole group of the tryptophan amino acid (Miura, Takeuchi, and Harada 1988; Takeuchi 2003; Rygula et al. 2013). The peak at 880 cm^{-1} is present in the FT-Raman spectra for some formulations and absent in others. This peak is strong in all formulations with a 0.8 OA concentration, as well as the 4 and 8% GDA films at 1.0 OA. In the uncrosslinked 1.0 OA film, this peak is not as prominent as the previous formulations. The 1.2 OA films at all GDA concentrations do not have this peak. This kind of trend demonstrates that the indole ring could be involved in zein-zein networking through aggregation. However, tryptophan only accounts for one or two building blocks within the entire zein structure (Matthews et al. 2011; Hynd et al. 2014). Therefore the primary mechanism for aggregation is probably hydrophobic bonding between the aliphatic side chains of amino acids and OA.

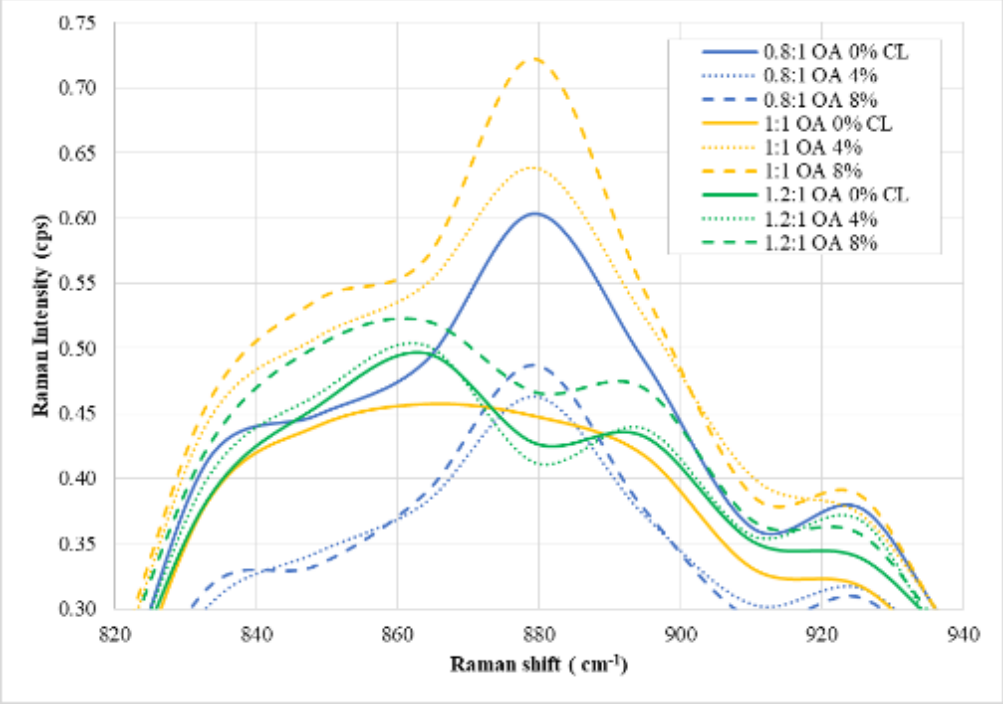

Figure 14. FT-Raman peak at 880 cm^{-1}.

The FTIR peak at 1540 cm^{-1} is the Amide II peak, representing the N-H bending of amine molecules in an amide bond (Lin-Vien et al. 1991). The 1540 cm^{-1} peak height significantly decreases with the addition of GDA across all OA ratios (Fig. 15). Although no difference was found between the 4% and 8% GDA concentrations, there is a slight decrease in the height of the 1540 cm^{-1} peak with an increase in OA ratio without GDA. This change could be due to the decrease in zein concentration with an increase in plasticizer content. The consistency in the peak height from 1.0 to 1.2 OA concentrations would then be due to the phase separation of OA at the film-air interface of the 1.2 OA films. There is a consistent drop of 0.03 abs in the 1540 cm^{-1} peak height from 0% to 4% GDA or 8% GDA for both the 0.8 and 1.0 OA films. The 1.2 OA films show a smaller difference, having a peak height drop of only 0.015 abs. The larger decrease in the lower OA ratios is because the lower amount of OA allows for zein molecules to be closer together than for the 1.2 OA films, creating a better environment for zein crosslinking. Overall, the decrease in 1540 cm^{-1} peak height shows that the crosslinking is causing a decrease in the number of free amine groups on amide molecules.

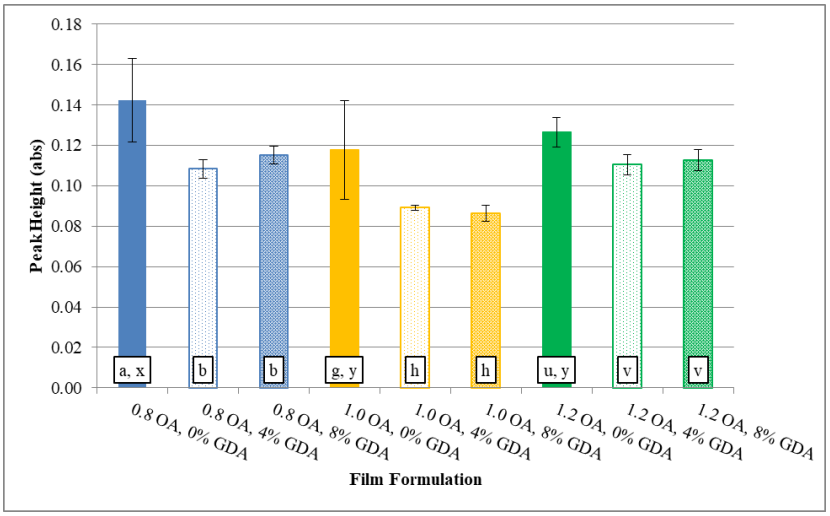

Figure 15. Height of FTIR peak at 1540 cm^{-1}: *different letter groupings represent different ANOVAs ($p<0.05$).*

The area of the 1080 cm^{-1} peak (Fig. 16), indicative of the N-H stretches on primary amines (Larkin, 2011), shows a similar trend to that of the 1540 cm^{-1} peak. For both the 0.8 OA and the 1.2 OA formulations, the addition of GDA causes a decrease in the peak area. There was again no difference found between the 4% and 8% GDA ratios for these 2 OA concentrations. However,

the 1.0 OA films showed a significantly steady decrease from 0 to 4 to 8% GDA. The 0% GDA films showed no difference between OA ratios.

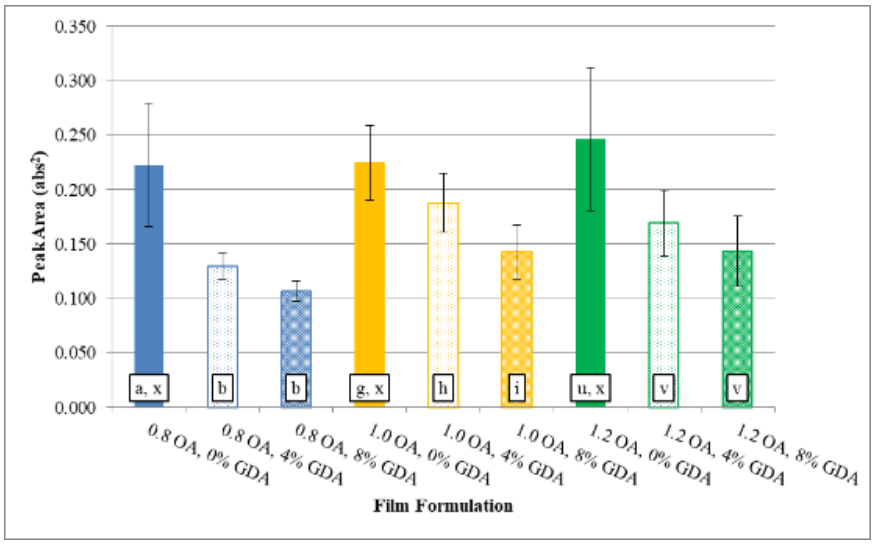

Figure 16. Area of FTIR peak at 1080 cm^{-1}: *different letter groupings represent different ANOVAs ($p<0.05$).*

Together these trends suggest that the crosslinking reaction involves all amine groups and not just those in an amide bond, shown by the 1540 cm^{-1} peak. At an OA concentration of 0.8, the GDA reacts with all possible amines. Therefore, there is no change in the 1080 cm^{-1} peak with the increase to 8% GDA. This may be due to the fact that the concentration in the vicinity of 4% GDA is the maximum amount needed to affect crosslinking sites and anything above that is in excess and does not participate in the chemical crosslinking reaction. At 1.2 OA, there is no difference between the 4% and 8% GDA films either, but the overall areas for the 1080 cm^{-1} are higher because of the large amount of plasticizer that creates a barrier for crosslinking. For the 1.0 OA films there is a steady decline in the 1080 cm^{-1} peak area suggesting that there is a better balance between OA and GDA compared to the 0.8 and 1.2 OA films. At 1.0 OA and 4% GDA, the plasticizer interferes with crosslinking, while adding 8% GDA allows for the crosslinker to work well- causing a further decrease in the 1080 cm^{-1} peak area.

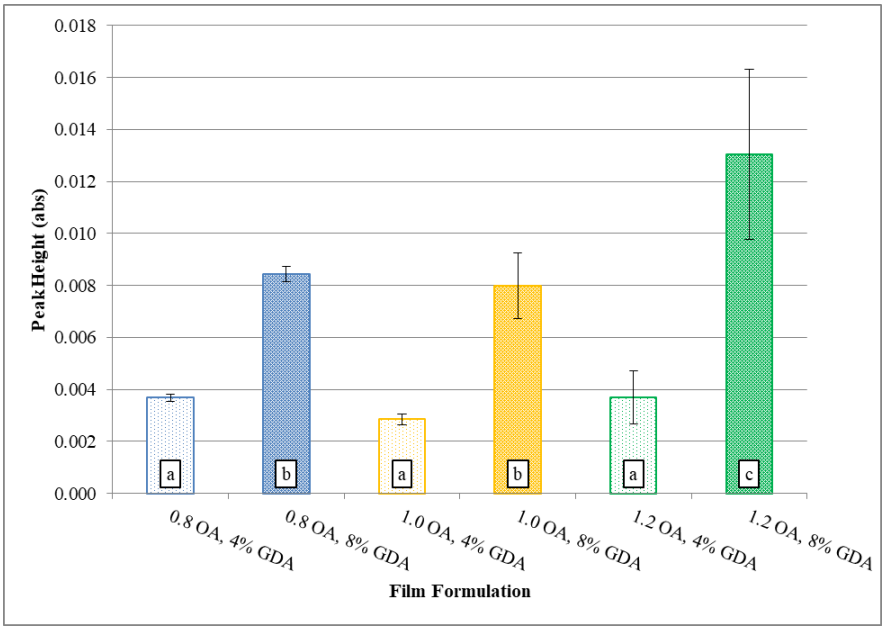

Figure 17. Height of FTIR peak at 970 cm^{-1}: *different letter groupings represent different ANOVAs ($p<0.05$).*

FTIR also exhibits the emergence of a peak at 970 cm^{-1} with GDA addition. This peak represents the C-O-C out of phase ring vibrations (Larkin 2011). It is not present within the uncrosslinked formulations but appears and increases in size with increasing concentration of crosslinker (Fig. 17). The reason for this may be that GDA is kept in a diluted water solution. In this state, the molecule can form many different isomers as well as crosslink with itself forming an oligomer. The hemiacetal structure was reported to form these oligomers within zein solutions by Sessa, Mohamed, and Byars (2008). The 970 cm^{-1} peak height also increases with plasticizer content. The peak height is the same for all 4% GDA films, but at 8% GDA the 1.2 OA film is much higher than the 1.0 and 0.8 OA. Together these trends show that this particular peak is a marker of GDA crosslinking with itself as well as an indicator of the amount of GDA participating in zein crosslinking.

Description of Zein Gelation and Film Formation Mechanism

The FTIR and FT-Raman data together with rheology show that the gelation and network formation of zein protein in ethanol with glutaraldehyde involves both protein aggregation and crosslinking. The FTIR and FT-Raman data provide useful chemical markers for the crosslinking

of protein molecules in the different formulas while the rheological measurements better describe the cohesion between the zein aggregation and GDA crosslinking. Altogether, these analyses explain the mechanism of network formation in plasticized zein gels at room temperature.

In the context of chemical crosslinking, the crosslinker aldehydes are reacting with the protein amine groups consistent with other studies focusing on crosslinking of protein using GDA (Migneault et al. 2004). The simultaneous decrease of the 1540 and the 1080 cm^{-1} FTIR peaks show that the glutaraldehyde reaction reduces the number of amines within the gel/film structure. When reacted with aldehydes, amines transform into imines through the -C=N- bond between amino acids and produce water as a byproduct. This reaction is a common mechanism for protein polymerization with aldehyde crosslinkers (Das and Pal 2015). This study focuses on gelation in ethanol, but Sessa et al. (2008) also showed this kind of a reaction with zein and GDA in acetic acid.

The polymerization through the imine bonding mechanism is responsible for the increase in the G' values for the crosslinked gel formulations. Consistent with the behavior of the 1540 and 1080 cm^{-1} peak trends, the 4% and 8% GDA formulations for 1.0 and 1.2 OA showed a significant difference in the development and increase in G' vs. time compared to the 0% GDA formulations (Table 3). However, the 4% and 8% GDA formulations showed no difference in G' vs. time when compared to the 0% GDA for 0.8 OA formulations. At this OA concentration, protein aggregation played a much larger role than at 1.0 and 1.2 OA. The protein aggregation gelation is achieved mainly through hydrophobic interactions with some hydrogen bonding. The hydrophobic interactions are possibly through the hydrophobic amino acids whose aliphatic or aromatic R-groups are sticking out of the cylindrical capsules proposed by Argos et al (1982), while the hydrogen bonding could also be achieved by amino acid side groups- like the indole ring of tryptophan (shown by the 880 cm^{-1} peak). The hydrophobic interactions go undetected by FTIR and FT-Raman because it is caused by secondary bonding interactions. The increase in both the G' with time and the N_T values (Table 3) in 0% GDA formulations offer the proof for this aggregation, trending inversely with the plasticizer content.

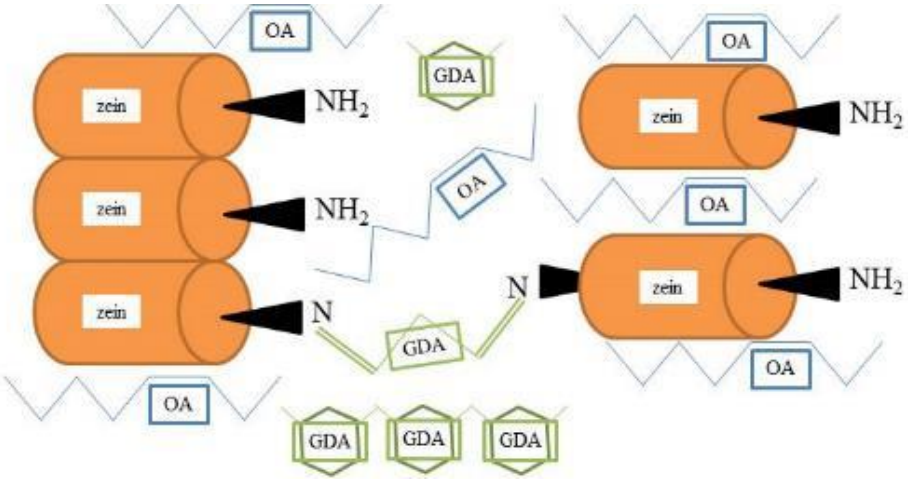

Figure 18. Zein film and gel molecular interactions: *zein aggregation (LHS); zein-OA interactions through hydrophobic interactions (RHS); zein-GDA crosslinking (middle); GDA-GDA oligomerization (bottom).*

Based on the zein structure, the GDA bonding sites and the OA hydrophobic aggregation interactions are occurring in different places on the zein molecule. The plasticizer is more than likely layering between the hydrophobic helices since the aliphatic tail of the plasticizer is highly hydrophobic and would be attracted to the hydrophobic groups in the zein molecule (Wang, Geil, and Padua 2004). This protein aggregation was also observed in the rheological data, as the OA content decreased the N_T aggregation values at 0% GDA (Table 3). However, the protein aggregation may also be driven by hydrogen bonding, as demonstrated by the tryptophan peak at 880 cm^{-1}. If the protein and OA interactions do occur along the hydrophobic helices, this arrangement would leave the polar glutamine turns open for reacting with GDA. Glutamine has both a primary amine and an amide group that would be involved in the crosslinking reaction. In conclusion the contribution of aggregation to the networking formation process at room temperature has been shown to consist of both hydrogen bonding and hydrophobic interactions mediated by the amount of plasticizer and the crosslinking contribution has been shown to be driven by covalent crosslinking generated by the GDA molecules as proposed in detail in Fig. 18.

3.4.4 Determination of Zein Secondary Protein Structure

The Amide I band of each formulation was analyzed to determine changes in the zein protein's secondary structure. The deconvolution of this peak yielded between 5 and 6 peaks for each

formulation with average central wavenumbers at: 1610 (1), 1626 (2), 1634 (3), 1654 (4), 1674 (5) and 1687 (6) cm^{-1} (Fig. 19). Based on the central wavenumber of each peak, the band was assigned to one of 3 secondary structures: β-sheet (peaks 1-3), α-helix (peak 4), or β-turn (peaks 5 & 6). Peak 2, which arose due to a splitting of peak 3, was only present in some spectra.

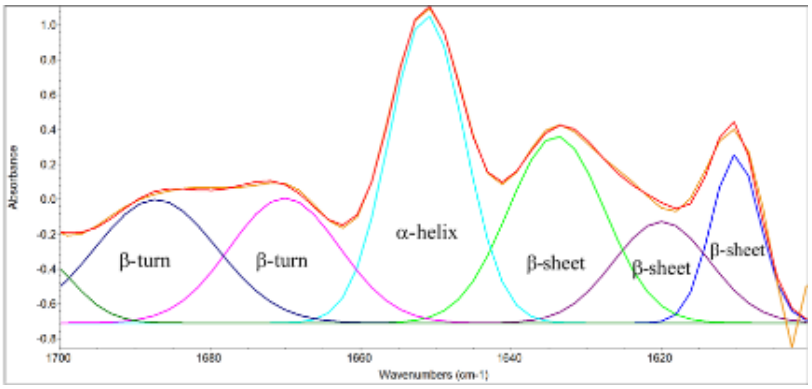

Figure 19. Fourier self-deconvoluted and peak fitted Amide I band in FTIR spectra with secondary structure assignments.

The β-sheet structure appears to have a direct relationship with plasticizer content (Table 4). Although no statistical difference was found between GDA concentrations for the 0.8 and 1.2 OA films, the 1.0 OA films showed a significant increase in β-sheet content with 8% GDA. Since no change was seen with the 0.8 OA films with the addition of GDA, this change at 1.0 OA with 8% GDA is more than likely due to the additional water added along with the GDA than the actual crosslinker. Water better interacts with the zein β-sheet secondary structure and further plasticizes the film (Xiao et al. 2015). The GDA was a 25% solution, and no water was added to the 0 and 4% GDA formulations to counteract any possible effects observed with 8% GDA solution, as in order to add more glutaraldehyde it is necessary to add more water which accompanies the glutaraldehyde in the 25% glutaraldehyde solution. Although not soluble in water, zein is well known to be plasticized by water (Kokini et al. 1994). Therefore, the 1.0 OA formulation along with the GDA at 8% increased the plasticization to mimic the 1.2 OA films rather than the 1.0 OA films. The ANOVA further supports this explanation, showing that the 0.8 and 1.0 OA films with 0% GDA were significantly different than their 1.2 OA counterpart.

Table 4. Secondary structure content of zein films: *different letter groupings represent different ANOVAs ($p<0.05$)*

Formulation	% β-sheets	ANV	% α-helix	ANV	% β-turn	ANV
0.8 OA, 0% GDA	38±2	*a, x*	33±4	*a, x*	28±6	*a, xy*
0.8 OA, 4% GDA	37±0	*a*	36±1	*ab*	27±2	*A*
0.8 OA, 8% GDA	38±1	*a*	37±4	*b*	25±5	*A*
1.0 OA, 0% GDA	38±1	*g, x*	29±1	*g, y*	33±1	*g, x*
1.0 OA, 4% GDA	39±0	*g*	33±1	*h*	28±1	*H*
1.0 OA, 8% GDA	40±2	*h*	33±3	*h*	26±1	*I*
1.2 OA, 0% GDA	43±5	*u, y*	30±4	*u, y*	27±6	*u, y*
1.2 OA, 4% GDA	46±4	*u*	28±10	*u*	25±6	*u*
1.2 OA, 8% GDA	43±3	*u*	32±5	*u*	25±8	*u*

The α-helix structure showed a very different trend (Table 4). A significant increase was observed in the crosslinked films compared to the uncrosslinked films for both 0.8 and 1.0 OA films. The 0.8 OA films showed a progressive increase in α-helix content with GDA, while the 1.0 OA films showed a significant increase when 0% is compared with both the 4% and 8% GDA films. On the other hand, the 1.2 OA films showed no statistical difference with GDA content, presumably due to the large amount of plasticizer present and resulting ineffective crosslinking. For the 0% GDA films, the α-helical content displayed an inverse relationship with plasticizer content. The 1.2 and 1.0 OA films showed about the same fraction of α-helix content, while the 0.8 OA films showed a significant increase. These indirect trends in alpha α-helical content with OA content as well as the direct relationship with GDA are due to changes in the hydrophobic environment caused by changes in OA and GDA content. The α-helical secondary structure is known to be very ordered and to drive hydrophobicity in proteins (Xiao et al. 2015). The crosslinker promotes interactions leading to networking between the protein molecules, while the plasticizer counteracts these interactions giving varying trends (Table 4).

The β-turn structure is a relatively open structure compared to the highly compact α-helical structure. There was a significant decrease in β-turn content with an increase in GDA concentration for the 1.0 OA films, but no difference was seen between the crosslinked and uncrosslinked films

for both 0.8 and 1.2 OA presumably because the β-turns are not involved in the crosslinking process (Table 4). There was also a random trend observed for the 0% GDA films with varying plasticizer content. The 1.0 OA films showed the highest β-turn content, while the 1.2 OA showed the lowest- leaving the 0.8 OA formulations in the middle. These results may be due to the interference of the carboxylic acid C=O bond vibrations of oleic acid peak near 1700 cm^{-1} (Lin-Vien et al. 1991). Although this peak was not considered in the determination of secondary structures, its low-end tail may have affected the overall shape of the Amide I band and caused some changes in the higher wavenumber peaks.

On average, the film formulations showed a zein structure of approximately 40% β- sheet, 32% α-helix, and 28% β-turn (Table 4). In comparison Chen, Ye, and Liu (2014) reported the secondary structure distribution to be 21% α-helix, 54% β- sheet, 25% β-turn. The results in this study are pretty consistent with the estimates of Chen, Ye, and Liu (2014) considering that the films discussed here contain both OA and GDA while this study did not. The increase in β-sheet structure with an increase in plasticizer content is a response to the interference caused by the plasticizer, while the increase in α-helical content with crosslinking is due to the increase in order from crosslinking. The β-turn structure showed a decrease with GDA due to an increase in order, but also gave varying trends due to the counteracting action of OA detected through the 1700 cm^{-1} peak near the Amide I band.

The crosslinking mechanism of zein in 70% ethanol is also consistent with zein crosslinking mechanism in 70% acetic acid, with minor differences (Turasan et al., 2018). In acetic acid, GDA is crosslinking zein molecules mainly through the glutamine turns (β-turns) of zein molecules, similar to the mechanism in 70% ethanol. In the acetic acid gelation study, FTIR results showed that a secondary mechanism exists where some of the GDA is forcing some of the α-helices to turn into beta sheets, by breaking the hydrogen bonds. This mechanism is occurring in acetic acid's case, since acetic acid is a primary solvent for zein and dissolves zein better than ethanol, eliminating almost all the possible aggregation. The more freely floating zein molecules in acetic acid, therefore, have bigger spaces in between them, making the lateral sides more accessible for GDA interactions. However, in ethanol's case aggregation is responsible for a larger portion of the gelation (section 3.2), which leaves little room between the neighboring zein molecules. Therefore,

the increase in GDA within the same OA concentration does not result in a decrease in helical content, since the GDA molecules are not able to interact with the sides of the helices and to break down the helical structures.

3.4.5 Surface Hydrophilic/Hydrophobic Balance

At 0% GDA there is no difference in WCA between the zein film surfaces with different plasticizer contents (Table 5). The same is observed across GDA concentrations for the 0.8 and 1.2 OA films. The 1.0 OA films have no significant difference between the 0% and 4% GDA films, but the 8% GDA films are somewhat more hydrophilic- indicated by the smaller WCA. It is important to remember that all of the films were cast on PDMS surfaces. A likely explanation could be that the stacking of the protein and oleic acid caused a larger exposure of the more polar β-turns towards the PDMS than with the 0% and 4% GDA, 1.0 OA films. However, it is more likely that this is an anomaly, as the corners of the experiment showed no differences. This consistency across all formulations is primarily due to the way in which the experiment was conducted. The PDMS was already cured within the petri dish, when the formulation was poured on top of it. The free-flowing film solution then oriented itself to try and match the hydrophobicity of the cured PDMS. This caused all of the film formulations to reach a similar contact angle on the PDMS contact side of the film, as shown by this data.

Table 5. Water contact angle of zein films cured on PDMS:
different letter groupings represent different ANOVAs ($p<0.05$)

Formulation	Contact Angle
0.8 OA, 0% GDA	69.22 ±3.69 *a, x*
0.8 OA, 4% GDA	68.46 ±4.64 *a*
0.8 OA, 8% GDA	70.59 ±4.44 *a*
1.0 OA, 0% GDA	66.82 ±2.06 *g, x*
1.0 OA, 4% GDA	65.57 ±0.64 *g*
1.0 OA, 8% GDA	62.45 ±2.32 *h*
1.2 OA, 0% GDA	68.85 ±4.13 *u, x*
1.2 OA, 4% GDA	67.04 ±5.26 *u*
1.2 OA, 8% GDA	67.99 ±1.99 *u*

3.4.6 Summation of Analyses for Understanding of Hydrophobic Aggregation

The formulations in this study show the variability achieved from the utilization of two main parameters playing a competing role in the organization of zein molecules: plasticizer and crosslinker. The synergistic effect of these parameters must be analyzed, as these effects can be different than the ones achieved with these parameters separately. To see the bigger picture, all the analyses done in this study were further averaged based on OA content regardless of GDA concentration (Table 6). This approach was taken since the effect of chemical crosslinking through GDA was shown to be hindered by protein aggregation- partly achieved through hydrophobic interactions with OA. As seen in Table 4, the α-helix contents, plateau G' values and Vicker's hardness values share a direct relationship- all increasing with a decrease in OA content. Due to the high amount of self-hydrogen bonding, α-helical structures are the most compact secondary structures. These interactions result in less exposed hydrophilic sites and altogether higher hydrophobicity. Therefore, the forced helical structure separation brought on by the breaking of zein molecular aggregates through hydrophobic interactions of helices lateral sides, lowered the consistency of the gel formations and caused a simultaneous decrease in plateau G' values and α-helical content with increasing OA, resulting in stiffer films. During this aggregation breakage process, the OA molecules that are separating the helices from each other could be causing some of the helices to turn into other secondary structures on top of affecting the tertiary structure of the proteins. This conversion between secondary structures can also be seen when the averages of each OA formulations are compared, such that the average β-sheet content increases with increasing OA concentrations.

Table 6. Summation of analytical testing for understanding of OA content only: *different letter groupings represent different ANOVAs (p<0.05)*

Formulation	% α-helix	% β-sheet	Final G' (Pa)	Vicker's Hardness
0.8 OA, 0% GDA	33±4 *a,x*	38±2 *a,x*	1040 ± 147 *a,x*	1.82 ± 0.34 *a,x*
0.8 OA, 4% GDA	36±1 *ab*	37±0 *a*	1413 ± 222 *a*	1.29 ± 0.15 *b*
0.8 OA, 8% GDA	37±4 *b*	38±1 *a*	1245 ± 182 *a*	1.39 ± 0.17 *b*
0.8 average	**35±4**	**38±2**	**1233 ± 187**	**1.50 ± 0.10**
1.0 OA, 0% GDA	29±1 *g,y*	38±1 *g,x*	889 ± 120 *g,xy*	1.30 ± 0.48 *g,y*
1.0 OA, 4% GDA	33±1 *h*	39±0 *g*	1266 ± 168 *h*	1.43 ± 0.49 *g*
1.0 OA, 8% GDA	33±3 *h*	40±2 *h*	1250 ± 180 *h*	0.88 ± 0.43 *h*
1.0 average	**32±3**	**39±2**	**1135 ± 215**	**1.21 ± 0.03**
1.2 OA, 0% GDA	30±4 *u,y*	43±5 *u,y*	639 ± 105 *u,y*	0.78 ± 0.14 *u,z*
1.2 OA, 4% GDA	28±10 *u*	46±4 *u*	1180 ± 169 *v*	0.58 ± 0.10 *v*
1.2 OA, 8% GDA	32±5 *u*	43±3 *u*	1101 ± 161*v*	0.55 ± 0.11*v*
1.2 average	**32±6**	**44±4**	**973 ± 292**	**0.64 ± 0.02**

3.4.7 Comparison of differences in fidelity of the films fabricated using different formulations through scanning electron microscopy

The SEM images showed that the plasticizer and the crosslinker play a competing role in the fabrication of zein films (Fig. 20). The films without crosslinking (Fig. 20 a, d, g) show a decrease in the number of defects. Both the 0.8:1 OA and the 1.2:1 OA films without crosslinker have a higher number of defects, but the characteristics of the defects are different. The low concentration of plasticizer appears to result in a film with greater adhesion to the PDMS (causing a kind of pulling fault). This defect causes a distortion in the inverse pyramidal structures that may decrease the number of hot spots due to irregularity of the inverted pyramidal tips and a large flaw in uniformity. On the other hand, the high ratio of plasticizer caused a convergence of structures due to the larger mobility with increasing plasticizer content. These defects in the inverted structures disrupt the Raman signal intensity enhancement that would be gained with the utilization of the gold nanoparticle decoration.

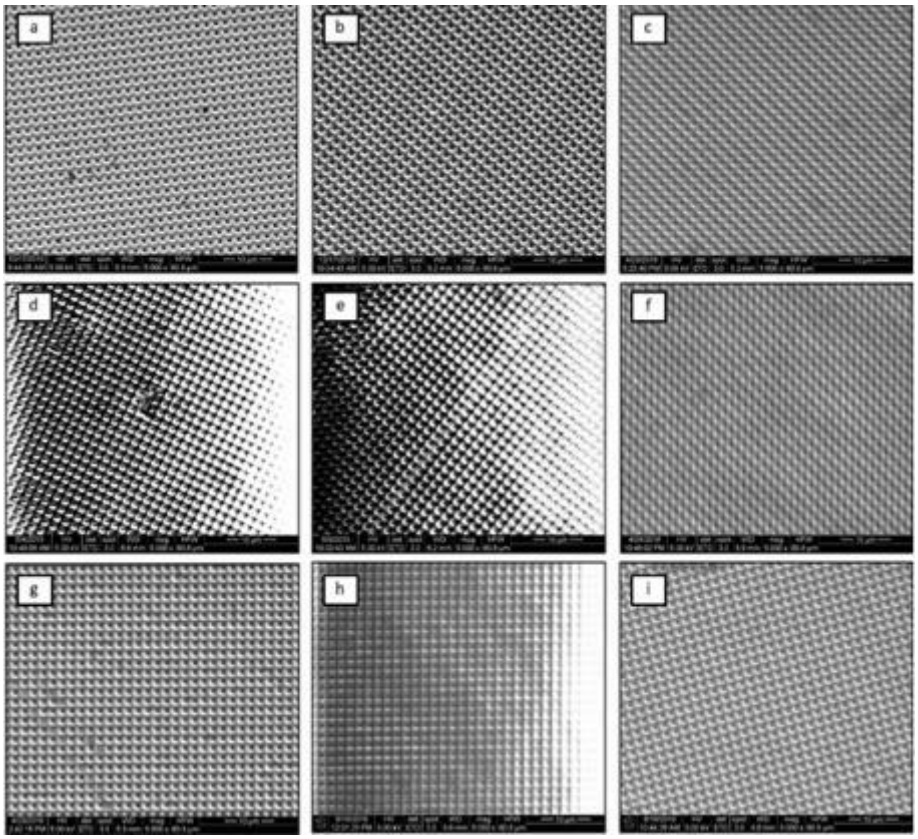

Figure 20. SEM images of inverted pyramidal nanostructures with various film formulations: *a) 0.8:1 OA, 0% CL; b)0.8:1 OA, 4%; CL; c) 0.8:1 OA, 8% CL; d) 1:1 OA, 0% CL; e) 1:1 OA, 4% CL; f) 1:1 OA, 8% CL; g) 1.2:1 OA, 0% CL; h) 1.2:1 OA, 4% CL; i) 1.2:1 OA, 8% CL.*

The crosslinking concentration also had an effect on the fidelity of the nanostructures. At 4% GDA concentrations (Fig. 20 b, e, h), the number of faults drastically decreased for the 0.8 and 1.0 OA films, while the 1.2 OA film showed no difference from the 0% GDA. On the other hand, a similar disconnect was observed between OA concentrations with the 8% GDA as well. A large number of faults were again visible for the 0.8 and 1.0 OA films, while the 1.2 OA with 8% GDA was the best film at the 1.2 plasticizer concentration. Both of the crosslinked 1.2 OA films showed a large amount of oil on the surface of the SEM samples due to phase separation. This change in surface chemistry made the samples very hard to coat with platinum and palladium and should prove to be a further complication with the adhesion of gold.

3.4.8 Surface Enhanced Raman Spectroscopy (SERS)

For SERS experiments the 0.8:1 OA, 4% CL sample was chosen as the best formulation and the 1:1 OA, 0% CL was chosen as the worst due to its nanostructure defects. Figure 21 shows the Raman spectra of 100 μM Rhodamine 6G measured with these two nanostructured zein films which are decorated with 50 nm Au nanoparticles. Both spectra show the signature Rhodamine 6G peaks located at 1654 cm^{-1}, 1514 cm^{-1}, 1365 cm^{-1}, 1186 cm^{-1}, 776 cm^{-1}, and 614 cm^{-1} (Gezer et al., 2016), but the 0.8:1 OA, 4% CL sample had almost twice as higher Raman signal intensity than the 1:1 OA, 0% CL sample. The insets in Figure 21 show the Raman microscopy images of the corresponding samples taken with a 50x objective lens. In both of the sample surfaces, inverted nanopyramid structures are visible. However, while the surface of the 0.8:1 OA, 4% CL sample is free of defects and the gold nanoparticle distribution is homogenous, on the 1:1 OA, 0% CL sample there are multiple defects and inhomogeneity seen on the sample surface. The lower Raman enhancement obtained with the defective zein film (1:1 OA, 0%) is due to the insufficient transfer of nanopyramid structures which lowers the number of hotspots created and reduces the Raman signal. It is also possible that the excessive amount of OA plasticizer is migrating to the surface, and interfering with the plasmonic activity of gold nanoparticles, which reduces Raman signal. The SERS results prove that the mechanical properties of zein films have a significant effect on the resulting Raman signal enhancement.

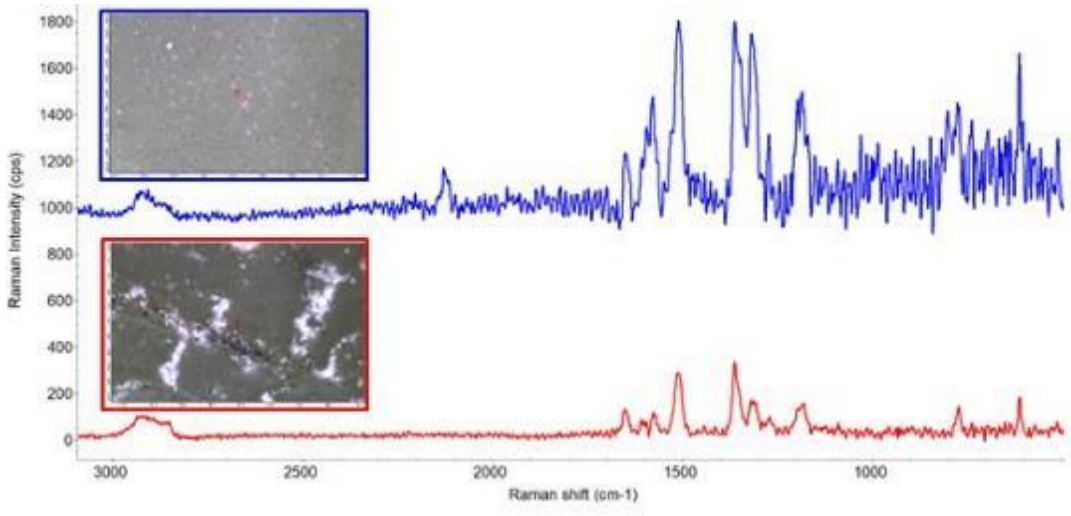

Figure 21. SERS spectra of Rhodamine 6G (100 μM) using 0.8:1 OA, 4% CL (blue) and 1:1 OA, 0% CL (red) as the zein-based platform. The insets show Raman microscopy images of corresponding samples (50x objective).

3.5 Conclusions

Zein's film forming capabilities make it a good candidate for a SERS substrate. In this study, various film formulations were investigated to determine their ability to improve zein films for this application. Both plasticizer and crosslinker content play a major role in the properties of the films, where plasticizer content appeared to have a larger effect on the storage modulus of the gels than the GDA content. This trend was mainly due to protein aggregation through both hydrophobic interactions and hydrogen bonding. The FTIR peaks showed a clear mechanism of crosslinking between the GDA aldehydes and amine groups on the zein protein- most likely with the glutamine amino acid β-turns. Only very slight changes were observed in secondary structure and WCA. Using SEM, it was found that the highest fidelity of nanostructures can be achieved with the 0.8 OA content with 4% GDA. SERS experiments showed that increasing nanostructure fidelity is significantly effective in enhancing the Raman signal.

3.6 Author Contributions

Barber, E.A.: Conceptualization, methodology, investigation, writing-original draft. **Turasan, H.:** Methodology, formal analysis, investigation, writing – review and editing. **Gezer, P.G.:** Methodology and validation. **Devina, D.:** Investigation. **Liu, G.L.:** Conceptualization and Resources. **Kokini, J.L.:** Conceptualization, methodology, resources, writing – review and editing, visualization, supervision, project administration, funding acquisition.

3.7 References

Argos, Patrick, Karl Pedersen, M. David Marks, and Brian A. Larkins. 1982. "A Structural Model for Maize Zein Proteins." *The Journal of Biological Chemistry* 257 (17): 9984–90.

Bugs, Milton Roque, Lucimara Aparecida Forato, Raquel Kely Bortoleto-Bugs, Hannes Fischer, Yvonne Primerano Mascarenhas, Richard John Ward, and Luiz Alberto Colnago. 2004. "Spectroscopic Characterization and Structural Modeling of Prolamin from Maize and Pearl Millet." *European Biophysics Journal* 33 (4): 335–43.

Byler, D. Michael, and Heino Susi. 1986. "Examination of the Secondary Structure of Proteins by Deconvolved FTIR Spectra." *Biopolymers* 25 (3): 469–87. https://doi.org/10.1002/bip.360250307.

Chen, Ye, Ran Ye, and Jun Liu. 2014. "Effects of Different Concentrations of Ethanol and Isopropanol on Physicochemical Properties of Zein-Based Films." *Industrial Crops and Products* 53 (February): 140–47. https://doi.org/10.1016/j.indcrop.2013.12.034.

Das, Dipankar, and Sagar Pal. 2015. “Modified Biopolymer-Dextrin Based Crosslinked Hydrogels: Application in Controlled Drug Delivery.” *RSC Adv.* 5 (32): 25014–50. https://doi.org/10.1039/C4RA16103C.

Forato, Lucimara A., Antonio C. Doriguetto, Hannes Fischer, Yvonne P. Mascarenhas, Aldo F. Craievich, and Luiz A. Colnago. 2004. “Conformation of the Z19 Prolamin by FTIR, NMR, and SAXS.” *Journal of Agricultural and Food Chemistry* 52 (8): 2382–85. https://doi.org/10.1021/jf035020+.

Gezer, P. Gizem, Serena Brodsky, Austin Hsiao, G. Logan Liu, and Jozef L. Kokini. 2015. “Modification of the Hydrophilic/hydrophobic Characteristic of Zein Film Surfaces by Contact with Oxygen Plasma Treated PDMS and Oleic Acid Content.” *Colloids and Surfaces B: Biointerfaces* 135 (November): 433–40. https://doi.org/10.1016/j.colsurfb.2015.07.006.

Gezer, P. Gizem, Austin Hsiao, Jozef L. Kokini, and G. Logan Liu. 2016. “Simultaneous Transfer of Noble Metals and Three-Dimensional Micro- and Nanopatterns onto Zein for Fabrication of Nanophotonic Platforms.” *Journal of Materials Science* 51 (8): 3806–16. https://doi.org/10.1007/s10853-015-9699-0.

Gezer, P. Gizem, G. Logan Liu, and Jozef L. Kokini. 2016a. “Development of a Biodegradable Sensor Platform from Gold Coated Zein Nanophotonic Films to Detect Peanut Allergen, Ara h1, Using Surface Enhanced Raman Spectroscopy.” *Talanta* 150: 224–32. https://doi.org/http://dx.doi.org/10.1016/j.talanta.2015.12.034.

Gezer, P. Gizem, G. Logan Liu, and Jozef L. Kokini. 2016b. “Detection of Acrylamide Using a Biodegradable Zein-Based Sensor with Surface Enhanced Raman Spectroscopy.” *Food Control* 68 (October): 7–13. https://doi.org/10.1016/j.foodcont.2016.03.002.

Gluck-Hirsch, J. B., and J. L. Kokini. 1997. “Determination of the Molecular Weight between Crosslinks of Waxy Maize Starches Using the Theory of Rubber Elasticity.” *Journal of Rheology* 41 (1): 129–40. https://doi.org/http://dx.doi.org/10.1122/1.550804.

Hynd, P. I, N. M Edwards, S Weaver, K Chenoweth, R Stobart, and N Heberle. 2014. “Biological Defleecing: Intravenous Infusion of Amino Acid Mixtures Lacking Lysine and Methionine Creates a Weakened Zone in the Wool Staple, Which Is Amenable to Mechanical Wool Harvesting” 55 (10): 1264–71. https://doi.org/10.1071/AN14137.

Kokini, J.L., A.M. Cocero, H. Madeka, and E. de Graaf. 1994. “The Development of State Diagrams for Cereal Proteins.” *Trends in Food Science & Technology* 5 (9): 281–88.

Kong, Jilie, and Shaoning YU. 2007. “Fourier Transform Infrared Spectroscopic Analysis of Protein Secondary Structures.” *Acta Biochimica et Biophysica Sinica* 39 (8): 549–59.

Larkin, Peter. 2011. *Infrared and Raman Spectroscopy*. Oxford: Elsevier. http://www.sciencedirect.com/science/article/pii/B978012386984510014X.

Lin-Vien, Daimay, Norman B. Colthup, William G. Fateley, and Janette G. Grasselli. 1991. *The Handbook of Infrared and Raman Characteristic Frequencies of Organic Molecules*. Boston: Academic Press.

Matsushima, Norio, Gen-ichi Danno, Hikaru Takezawa, and Yoshinobu Izumi. 1997. “Three-Dimensional Structure of Maize α-Zein Proteins Studied by Small-Angle X-Ray Scattering.” *Biochimica et Biophysica Acta (BBA) - Protein Structure and Molecular Enzymology* 1339 (1): 14–22. https://doi.org/10.1016/S0167-4838(96)00212-9.

Matthews, Laura B., M. Elizabeth Kunkel, James C. Acton, Amod A. Ogale, and Paul L. Dawson. 2011. “Bioavailability of Soy Protein and Corn Zein Films.” *Food and Nutrition Sciences* 02 (10): 1105–13. https://doi.org/10.4236/fns.2011.210148.

Miura, T, H Takeuchi, and I Harada. 1988. “Characterization of Individual Tryptophan Side Chains in Proteins Using Raman Spectroscopy and Hydrogen-Deuterium Exchange Kinetics.” Biochemistry 27 (1): 88. https://doi.org/10.1021/bi00401a015.

Momany, Frank A., David J. Sessa, John W. Lawton, Gordon W. Selling, Sharon A. H. Hamaker, and Julious L. Willett. 2006. “Structural Characterization of α-Zein.” *Journal of Agricultural and Food Chemistry* 54 (2): 543–47. https://doi.org/10.1021/jf058135h.

Romero-Bastida, Claudia A., Eduardo Flores-Huicochea, Martha O. Martin-Polo, Gonzalo Velazquez, and J. Antonio Torres. 2004. “Compositional and Moisture Content Effects on the Biodegradability of Zein/Ethylcellulose Films.” *Journal of Agricultural and Food Chemistry* 52 (8): 2230–35.

Rygula, A., K. Majzner, K. M. Marzec, A. Kaczor, M. Pilarczyk, and M. Baranska. 2013. “Raman Spectroscopy of Proteins: A Review.” Journal of Raman Spectroscopy 44 (8): 1061–76. https://doi.org/10.1002/jrs.4335.

Sessa, David J., Abdellatif Mohamed, and Jeffrey A. Byars. 2008. “Chemistry and Physical Properties of Melt-Processed and Solution-Cross-Linked Corn Zein.” *Journal of Agricultural and Food Chemistry* 56 (16): 7067–75. https://doi.org/10.1021/jf800712k.

Takeuchi, Hideo. 2003. “Raman Structural Markers of Tryptophan and Histidine Side Chains in Proteins.” Biopolymers 72 (5): 305–17. https://doi.org/10.1002/bip.10440.

Turasan, Hazal, Emma A. Barber, Morgan Malm, and Jozef L. Kokini. 2018. “Mechanical and Spectroscopic Characterization of Crosslinked Zein Films Cast from Solutions of Acetic Acid Leading to a New Mechanism for the Crosslinking of Oleic Acid Plasticized Zein Films.” Food Research International 108: 357–67. https://doi.org/10.1016/j.foodres.2018.03.063.

Turasan, Hazal, and Jozef L. Kokini. 2017. “Advances in Understanding the Molecular Structures and Functionalities of Biodegradable Zein-Based Materials Using Spectroscopic Techniques: A Review.” Biomacromolecules 18 (2): 331–354.

Wang, Qin, Phillip Geil, and Graciela Padua. 2004. “Role of Hydrophilic and Hydrophobic Interactions in Structure Development of Zein Films.” *Journal of Polymers and the Environment* 12 (3): 197–202. https://doi.org/10.1023/B:JOOE.0000038552.88467.fc.

Watson, Stanley A, and Paul E Ramstad. 1987. Corn : Chemistry and Technology. St. Paul, Minn., USA: St. Paul, Minn., USA : American Association of Cereal Chemists.

Winter, H. Henning, and Francois Chambon. 1986. “Analysis of Linear Viscoelasticity of a Crosslinking Polymer at the Gel Point.” *Journal of Rheology* 30 (2): 367–82. https://doi.org/10.1122/1.549853.

Xiao, Jie, Yunqi Li, Ji Li, Alejandro Perez Gonzalez, Qiuyang Xia, and Qingrong Huang. 2015. “Structure, Morphology, and Assembly Behavior of Kafirin.” Journal of Agricultural and Food Chemistry 63 (1): 216. https://doi.org/10.1021/jf504674z.

Xie, Ling, and Chen-Lu Tsou. 1993. “Comparison of Secondary Structures of Insulin and Proinsulin by FTIR.” *Journal of Protein Chemistry* 12 (4): 483–87. https://doi.org/10.1007/BF01025049.

CHAPTER 4. DETECTION OF PYOCYANIN USING A NEW BIODEGRADABLE SURFACE ENHANCED RAMAN SPECTROSCOPY (SERS) BIOSENSOR FABRICATED USING GOLD COATED ZEIN NANOSTRUCTURES FURTHER DECORATED WITH GOLD NANOPARTICLES

Reprinted with permission. Full citation:
Jia, F., Barber, E.A., Turasan, H., Seo S., Dai, R., Liu, G.L., Li, X., Bhunia, A.K. & Kokini, J. Detection of pyocyanin using a new biodegradable surface enhanced Raman spectroscopy (SERS) biosensor fabricated using gold coated zein nanostructures further decorated with gold nanoparticles. J. Agric. Food Chem. 2019, 67, 16, 4603-4610
https://doi.org/10.1021/acs.jafc.8b07317

4.1 Abstract

In this paper, a biodegradable gold coated zein film Surface Enhanced Raman Spectroscopy (SERS) platform, with gold nanoparticles (AuNPs) deposited on the surface to further enhance the Raman signal was used to detect pyocyanin (PYO), the toxin secreted by *Pseudomonas aeruginosa*. An inverted pyramid structure imprinted on a zein film and gold coated during the transfer process was further improved with the deposition and fixing of gold nanoparticles which resulted in enhancement of the SERS signal by approximately a decade. This new platform served as a lab-on-a-chip sensor to enable the sensitive and rapid detection of PYO in drinking water. The size, distribution and morphology of the zein film nanostructures including the presence and distribution of gold nanoparticles were characterized by scanning electron microscopy (SEM). The new zein-based platform has the advantage of being largely biodegradable compared with commercial silicon or glass-based platforms. The limit of detection for PYO using the newly developed zein-based SERS sensor platform was calculated as 25 μM, considerably lower than the concentration of PYO in the blood of people with cystic fibrosis which has been reported to be 70 μM.

4.2 Introduction

Pseudomonas aeruginosa is an opportunistic water-borne pathogen of major public health concern that can cause nosocomial infection leading to pneumonia, endocarditis, enterocolitis and other types of infections yielding substantial medical costs and high mortality (Buzid et al., 2016). Due to the great therapeutic challenges *P. aeruginosa* brings, it is very important to develop rapid

detection methods aiming at early detection and diagnosis (Baig et al., 2016). Pyocyanin (PYO, 1-methoxy-5-methylphenazine) is the most important and lethal toxin that is released by *P. aeruginosa*. This makes PYO an excellent and unique candidate biomarker for the indirect detection of *P. aeruginosa* (Pastells et al., 2016).

Currently, high performance liquid chromatography (HPLC) and high performance liquid chromatography-mass spectrometry (HPLC-MS) based methods are the most frequently used analytical methods to detect PYO in clinical specimens (Yong et al., 2015). Unfortunately, the high cost of the equipment and the time-consuming purification procedures needed, restrict timely detection of the toxin. Due to the redox active nature of PYO, electrochemical based biosensors are emerging as a rapid and sensitive way to detect PYO at the point of care (POC) (Yang et al., 2017). Some voltammetry methods, such as cyclic voltammetry (CV) (Alatraktchi et al., 2018, 2016), differential pulse voltammetry (DPV) (Webster and Goluch, 2012) and square wave voltammetry (SWV) (Webster et al., 2014), have been used to detect PYO exclusively at a negative potential around -250 mV to -300 mV. The disadvantage of this method is that false negative results inevitably occur, even if the redox peaks of PYO can be separated from other phenazines with similar electrochemical behavior (Li et al., 2018; Yong et al., 2011).

Surface Enhanced Raman Spectroscopy (SERS) has become a rapid and promising analytical approach with the ability to enhance Raman scattering patterns characteristic of the molecule by decorating the surface of the substrate with metal nanoparticles (usually gold or silver colloids) (Liao and Lu, 2016; Yoon et al., 2013). As a reliable and sensitive detection method, SERS has been widely used in different fields, such as biological diagnosis, environmental monitoring and food quality, to determine various analytes including chemical and biological hazards (Boardman et al., 2016; Driver et al., 2014; Sadeghi et al., 2017). By increasing the density of "hot spots" on the SERS substrate, the SERS enhancement factor can be increased, which would also increase the sensitivity of the detection (Zheng et al., 2014; Zheng and He, 2014). It is possible to create more "hot spots" either by decorating the substrate with micro/nano structures, or employing nanoparticles of different size and morphology (nanocage, nanorod, nanocube and nanosphere etc.) (Yang et al., 2010). In our previous study, we found that SERS substrate with inverted pyramid structure has the best enhancement of Raman signal compared with other structures that included

positive-pyramid, nanopillar and nanopore (Gezer et al., 2016c, 2016a). Biodegradable gold coated zein SERS substrate, have been rarely studied and offer a path to protect the environment from the burden created by non-biodegradable materials. So far, the most common SERS substrates that are commercially available are still made of non-biodegradable materials, such as silicon or glass.

Zein is a corn protein that can be easily obtained as a byproduct of ethanol production (Luecha et al., 2010). Due to the special physical and chemical characteristics, zein proteins are mainly used as biodegradable packaging material and a protein feed supplement for animals in the traditional animal industry (Navdeep et al., 2016). However, its favorable surface properties can 1) ensure the preferential adhesion of zein films with gold and 2) ability to modify its surface with nanostructure such as positive pyramids, inverted pyramids, nanopillars and nanopores (Gezer et al., 2016a; Turasan and Kokini, 2017) using soft lithography. These special properties make zein films a promising candidate as a biodegradable SERS platform in biosensor fabrication, instead of traditional non-biodegradable inorganic materials. It is also pretty inexpensive and easy to capture with an ethanol extraction of DDGS (dried distillers' grains with solubles) after ethanol production.

In this paper, we aim to demonstrate the feasibility of manufacturing a new biodegradable SERS biosensor consisting of our existing inverted pyramid gold coated nanostructure imprinted on zein film further improved by the deposition and fixing of gold nanoparticles on the surface of the gold film. This enabled fabrication of a novel platform for the rapid and sensitive, label-free point-of-care (POC) detection of PYO. We fabricated zein films with inverted nanopyramids coated with a 200 nm gold layer further decorated with 50 nm AuNPs fixed on the gold layer using cysteamine. It is anticipated that the number of "hot spots" will increase considerably by the contact of gold and AuNPs, especially at the bottom of inverted pyramids and the edge areas of the inverted pyramid structures. We therefore offer an alternative biodegradable new SERS platform, which is inexpensive and eco-friendly that may possibly offer an alternative to non-biodegradable substrates used in industry. We will show how PYO in optimized conditions can be rapidly detected by using the spectral signature of PYO at 676 $cm^{-1}$and 1353 cm^{-1} using SERS with a largely biodegradable platform.

4.3 Materials and Methods

4.3.1 Reagents and apparatus

Pyocyanin (PYO) from *P. aeruginosa*, ≥98% (HPLC), in dimethyl sulfoxide (DMSO) was obtained from Sigma Aldrich (St. Louis, MO, USA). Before use, a solution with a 1 mM concentration of PYO was prepared by adding appropriate amounts of ethanol and water, to get a 10% ethanol solution. Then dilutions between 1 mM to 1 nM were made by subsequent 10-fold dilutions. Gold nanoparticle dispersions with a diameter of 50 nm were purchased from Ted Pella (Redding, CA, USA) and stored at 4 °C when not in use. Zein powder and cysteamine were obtained from Sigma Aldrich (St. Louis, MO, USA). Oleic Acid was purchased from Alfa Aesar (Ward Hill, MA, U.S.A.). Monoglyceride was obtained from Caravan Ingredients (Lenexa, KS, USA).

The morphology of the zein film nanostructures was determined using a FEI Nova NanoSEM scanning electron microscope (Hillsboro, Oregon, USA) with an acceleration voltage of 10kV. Everhart-Thornley detector (ETD) and Through Lens detector (TLD) were used to obtain images with different magnifications. The gold layer was coated on polydimethylsiloxane (PDMS) by using Airco Temescal VES 2550 e-beam evaporator (Livermore, CA, USA). All the ultrapure water used in the experiments was obtained from a Barnstead™ GenPure™ ultrapure water purification system (Grand Island, NY, USA) and had a resistivity of 18.2 $M\Omega \cdot cm^{-1}$. Raman tests were conducted on a Thermo Scientific DXR2 Raman microscope (Grand Island, NY, USA). A Fisher brand Isotemp Advanced Stirring Hotplate was used to dissolve the zein powder (Chicago, IL, USA).

4.3.2 Zein/Au SERS substrate preparation

In order to fabricate zein/Au SERS substrate with inverted pyramid structure coated with gold a previously established procedure was used (Gezer et al., 2016a). Briefly, the original master molds with inverted pyramid structure made of polyethylene terephthalate (PET) with a base of 2 μm by 2 μm with a periodicity of 2 μm (from center to center), and height of 2.1 μm and were obtained from Dr. Liu`s laboratory at the University of Illinois. Then PDMS was used to transfer the microphotonic patterns and gold from PET to zein film. Zein films were cast on the PDMS molds

following the procedure below: Zein solution was prepared by dissolving zein powder in 70% ethanol, oleic acid (plasticizer) and monoglyceride (emulsifier) together. First, 100 mL of ethanol (70%) was heated to 65°C and 20 g of zein powder was added to the heated ethanolic solution. After dissolving zein for 5 minutes under stirring, 20 g of oleic acid and 0.1 g of monoglyceride were added to the solution. Air bubbles were removed by 2 min of sonication immediately after the mixing of zein, plasticizer and emulsifier to make bubble free zein films. Afterwards, 15 mL of the zein solution was poured into a petri dish containing the PDMS-Au mold in the middle. Then the solution was dried in a desiccator for 3 weeks at room temperature. Finally, zein films were cut carefully by using a razor blade after complete solidification. The surface energy of gold on PDMS is lower than the surface energy of gold on zein and therefore the gold spontaneously and flawlessly transfers onto the zein film. The zein/Au film with three-dimensional inverted pyramid structure was peeled from PDMS and the final gold coated zein nanophotonic SERS substrate was obtained.

4.3.3 AuNP decoration of the surface of the Zein/Au substrate

Once the gold coated zein sensors were fabricated, the effect of using gold nanoparticles to further increase the SERS intensity was investigated. Cysteamine was used as a crosslinker to bind the gold nanoparticles that decorate the surface of the SERS sensors. First, a 1M cysteamine solution was prepared using milli-Q water. The 1 M solution was then diluted to both 10 mM and 100 mM cysteamine. Concentrations a decade apart were selected to have a large enough difference so that the impact of cysteamine on gold density could easily be established. These cysteamine concentrations were explored for their ability to create a uniform monolayer of gold nanoparticles and for the effect of cysteamine concentration on the density of gold nanoparticles.

A 25 μL droplet of 10 mM or 100 mM cysteamine was placed on the surface of the gold coated zein sensor. This droplet size was enough to cover the portion of the sensor containing the inverted micropyramids in its entirety for both 10 mM and 100 mM cysteamine concentrations. The sensor was covered and left at room temperature for 2 h to allow for the cysteamine to form its own monolayer. The sensors were then washed using milli-Q water and dried with a stream of nitrogen gas.

A 25 μL droplet of a 4.5 * 10^{10} particle/mL solution of 50 nm gold nanoparticles (NP) solution was then placed on the zein sensor-again over the inverted nanoparticles. The sensor was placed in a petri dish, covered, and sealed with parafilm before being placed in the refrigerator at a temperature of 4°C for 20 h. The sensors were then washed again with milli-Q water and dried with nitrogen gas. The subsequent sensors emerged from this process decorated with gold nanoparticles, and the different concentrations of cysteamine were investigated for their ability to enhance the zein SERS signal.

4.3.4 Enhancement factor of the SERS substrate

Raman tests were conducted by measuring the Raman spectra on the substrate in different positions (with the inverted pyramid structure and without the structure) and different conditions (coated with AuNPs and without AuNPs) of the SERS substrate. In these experiments zein peaks were used as the basis for understanding the enhancement factor.

Additional experiments were also performed using Rhodamine 6G (R6G) as the analyte to test the Raman signal intensity. The zein SERS sensors compared were; 1) with no Au coating layer on zein, 2) with no Au nanoparticles deposited on the gold layer, 3) with Au nanoparticles deposited and bound on the gold layer using 10 mM cysteamine, and 4) with Au nanoparticles deposited and bound on the gold layer using 100 mM cysteamine.

Raman spectra were collected using a Thermo Scientific DXR2 Raman Microscope. The 633 nm laser was used at a power of 2 mW with a long working distance 50× objective lens. The laser power was optimized to get the highest intensity signal from the sample without saturating the detector. In conjunction with a 25 μm pinhole aperture, this lens created a total laser spot size was 1.3 μm. This aperture was chosen from 4 available apertures (25 μm pinhole, 25 μm slit, 50 μm pinhole and 50 μm slit) to give the highest possible intensity from the sample without having truncated peaks due to saturation of the detector. In this particular case 25 μm pinhole aperture gave the highest intensity without peak truncation. Atlμs software was used to perform xy-mapping of the sensor. Each map was a 6x6 μm square with a 2 μm step size in each direction, creating a total of 9 points captured for each map. This distance ensured that the laser focus was at the center of an inverted pyramid for each collection.

Every sample was photo bleached for 20 s before collecting a spectrum to decrease the fluorescence caused by the zein protein. The spectra were collected from 200 to 3600 cm^{-1}. All 9 spectra collected from each map were averaged together and then manually baseline corrected to remove any interference from zein fluorescence. Five maps were collected for each of the sensors tested, totaling 45 spectra collected for each sensor and 135 spectra for each formulation.

4.3.5 Determination of PYO concentration on the new zein/Au-AuNPs SERS platform

20 ml of different concentrations of PYO in a DMSO buffer with 10% ethanol (ranging from 50 μM to 1 mM) and the blank buffer solution without PYO were dropped at the center of the zein/Au-AuNPs substrate (prepared using 100 mM cysteamine). A 633 nm laser was used as the laser source. The slit selected was 50 μm and the grating used was 600 lines/mm. In contrast to the experiments above, of the 4 aperture choices that were available on this Raman instrument, the 50 μm slit aperture was used and gave the best peak without peak truncation and maximum intensity. The wavenumber range between 600 and 2000 cm^{-1} were recorded. Spectra were collected for 10 times for a period of 1 second. X-Y Mapping was used to collect data on a 30 μm by 30 μm square.

4.3.6 Test in drinking water

The effectiveness of the zein sensor platform was investigated with tap water spiked with PYO. In order to eliminate possible big particles such as plankton and suspended dust, the water was allowed to rest for thirty minutes in order to detect possible precipitated particles. These possible microparticles were removed by centrifugation for 30 min at 14,000 rpm. The supernatant was then further filtered (0.2 μm filter pore size) to remove any possible smaller microaggregates.

Three different concentration of PYO solution (500 μM, 1 mM and 2 mM) were prepared for addition to the treated water sample by mixing 0.9 mL of water with 0.1 mL standard PYO solution. A drop of the PYO solution in water was deposited on the surface of the zein/Au-AuNPs SERS sensor. Raman spectroscopy measurements were conducted in triplicate.

4.3.7 Biodegradability and gold recovery from the biosensor

To test the biodegradability of the zein/Au-AuNPs SERS substrate, recovery experiments were conducted by using 20 mL of 70% ethanol extraction to separate zein from gold. The biodegradable sensors were put into the ethanol solution on a magnetic stirrer with 700 rpm at room temperature and 65°C, respectively. Afterwards, gold material was filtered from the solution. The remaining gold free zein ethanol solution was disposed of by Purdue University Radiological and Environmental Management (REM).

4.4 Results and Discussion

4.4.1 Detection mechanism

As seen Figure 22, PYO is made of heterocyclic nitrogen with a methyl group at the N position. The Raman spectrum of 100 μM of PYO using commercially available 20 nm silver nanoparticles (AgNPs) as a SERS substrate gives characteristic peaks between 650 and 1600 cm^{-1} compared with pristine Ag. Three prominent peaks, at 676, 1353 and 1610 cm^{-1}, are observed originating from PYO. The peaks at around 850 and 1080 cm^{-1} are attributed to the molecular vibrations of ethanol. The Raman peak of 1353 cm^{-1} was assigned to C-C stretching, C-N stretching and C-H in-plane bending modes of the aromatic ring (Wu et al., 2014). The spectral peak at 1447 cm^{-1}, is the result of the CH_2 and CH_3 bending. In this study, we are using the 676 cm^{-1} and 1353 cm^{-1} peaks as markers of PYO to detect and determine the concentration of PYO in the sample.

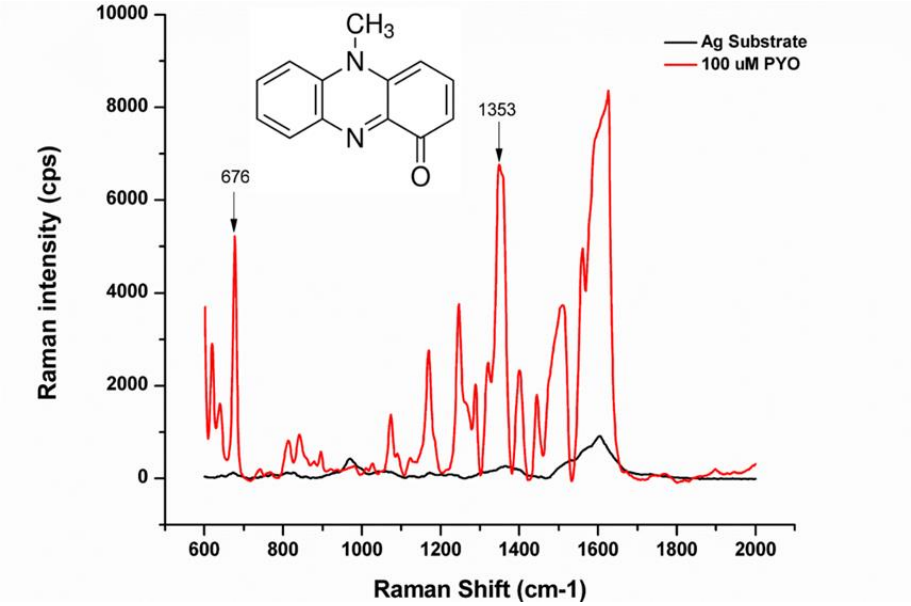

Figure 22. The chemistry of PYO and the standard Raman spectrum of PYO measured using Ag as a SERS substrate (red line).

4.4.2 Fabrication principle and sensing strategy

The basic fabrication principle and detection mechanism of the SERS nanosensor can be seen in Figure 23. The three steps needed to develop the nanosensor include fabricating the PDMS intermediate followed by zein substrate fabrication and PYO detection. The gold coated zein nanophotonic film was developed as in earlier studies (Gezer et al., 2016a). AuNPs to enhance the SERS signal were attached to the surface of the gold coated zein film. A 100 mM of the crosslinker, cysteamine, was used to ensure bonding between the AuNPs and the gold film on the surface of zein.

Raman measurements are then conducted by depositing a drop of PYO solution on the SERS substrate consisting of the gold coated zein film with AuNPs (Part III in Fig. 23). There is then an enhancement of the Raman spectrum intensity of the PYO solution as a function of the concentration of PYO deposited by the drop. The change in the intensity of the SERS signal as a function of concentration was used to quantitatively detect PYO.

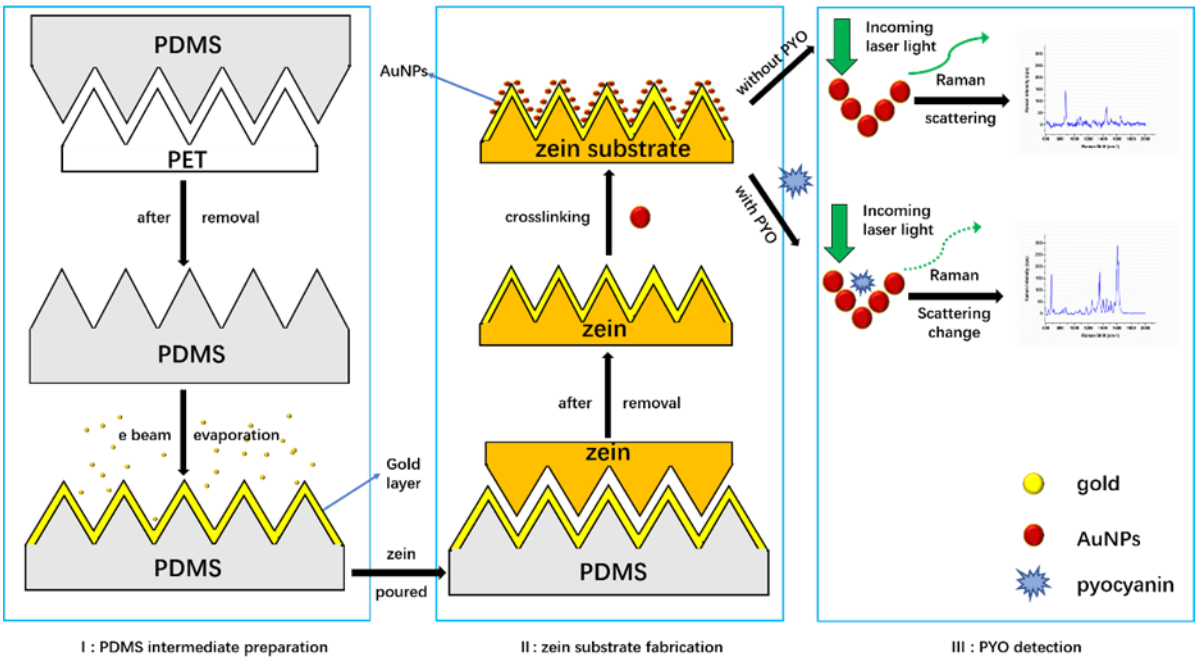

Figure 23. The fabrication of the zein substrate and sensing strategy using the SERS biosensor.

4.4.3 Characterization of the zein/Au substrate

The SEM images of the zein substrates with no Au layer and no NPs (Fig. 24a) show that a successful transfer of the inverted micropyramids was achieved through soft lithography using PDMS as the intermediate mold. Fig. 24b shows the zein film coated with 200 nm Au layer. It is clear that the inverted pyramid structure and the non-structure sections are distinctly seen. The upper area in Fig. 24b is the zein film without inverted pyramid structure showing a smooth and clean zein surface without pyramids. The lower area in Fig. 24b shows the well-organized inverted pyramid structure distributed uniformly on the surface.

The inverted pyramid structures can be observed clearly by the ultra-sensitive immersion mode and in detail in Fig. 24c. Each inverted pyramid has lateral base dimensions of 2 μm by 2 μm with a periodicity of 2.1 μm, which matched perfectly the positioning of the pyramids on the PET mold. The SEM comparison of the AuNP bound to the surface of the gold coated nanostructured zein film using 100 mM and the 10 mM cysteamine solutions showed that a much denser dispersion of nanoparticles was achieved with the 100 mM cysteamine solution compared to the 10 mM solution (Fig. 24d, 24e). The 10 mM concentration of cysteamine succeeded in attaching a considerable

number of gold nanoparticles to the sensor surface, but they were not evenly distributed. The nanoparticles mostly congregated in a few areas throughout the sensor surface. The large aggregates of gold NPs on the 10 mM cysteamine samples appeared to be mainly located at the top of the inverted micropyramids. This placement is not ideal, as the signal could be more enhanced if a considerable fraction of the particles were stacked up at the bottom of the inverted pyramid wells.

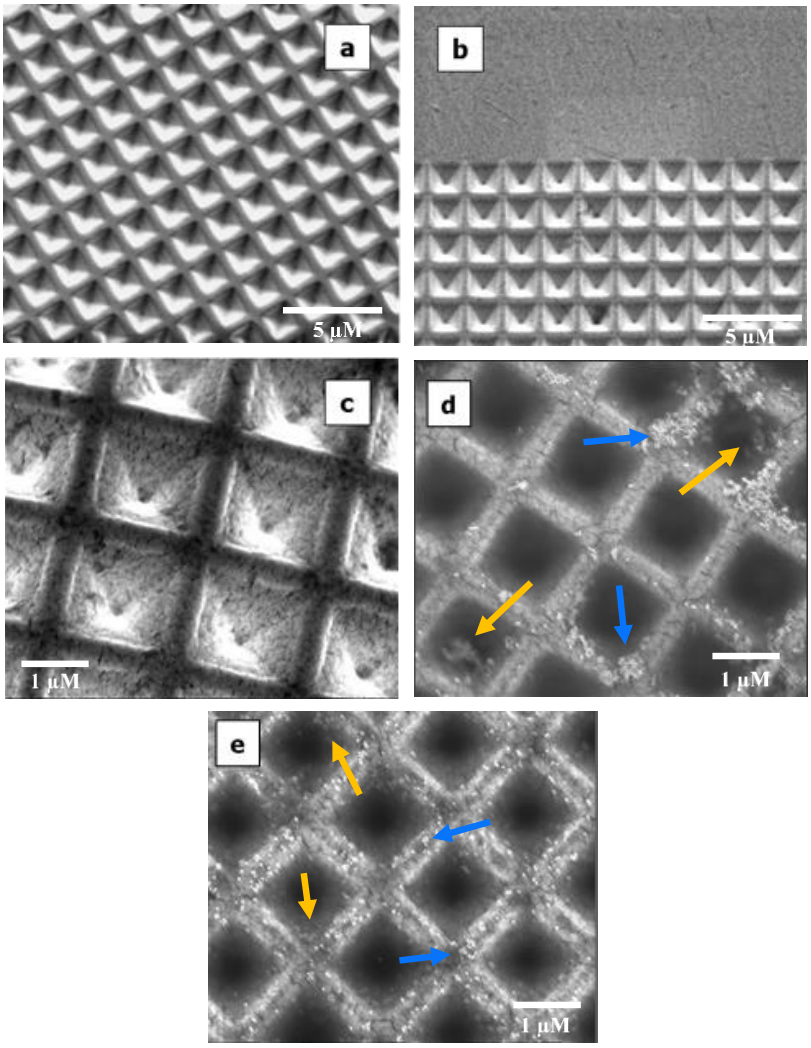

Figure 24. The characterization of the inverted pyramid structure in each step of the zein film fabrication (a) no Au and no AuNPs on the zein film, (b) gold coated zein film captured by an Everhart-Thornley detector (ETD), (c) gold coated zein film captured by the Through Lens detector (TLD), (d) gold coated and AuNPs functionalized zein film using 10 mM cysteamine, and (e) gold coated and AuNPs functionalized zein film using 100 mM cysteamine. Yellow arrows show AuNPs in the inverted pyramid wells and blue arrows show AuNPs on top of the wells.

The 100 mM solution of cysteamine was able to achieve a good dispersion of gold nanoparticles across the whole sensor surface. Particles were present both within the wells of the inverted pyramids as well as towards the top between the wells. Therefore the distribution of the nanoparticles with the 100 mM cysteamine sample provided a SERS signal of much greater intensity.

4.4.4 Relative SERS enhancement with the newly fabricated gold coated AuNPs decorated sensor platform

Figure 25 shows the results of Raman measurements at different locations of the zein SERS platforms (with and without inverted pyramid structure) and the same area with different gold decoration conditions (with and without AuNPs) under the same Raman setting parameters. The blue line is the Raman spectrum of the 200 nm gold coated zein platform with the inverted pyramid microstructure and the black line is the Raman spectrum of the same platform measured in the area without the inverted pyramid microstructure. The Raman signal of the two lines at the wavelength of 731 cm^{-1} generated by the zein protein, which is not particularly Raman active, gave a signal with an intensity around 200 cps (counts per second) for the blue line and 100 cps for the black line showing that the gold coated inverted pyramid structure improves the Raman signal considerably. The red line shows the Raman spectrum of the gold coated zein substrate decorated with AuNPs which gives a Raman signal is around 1200 cps for the 731 cm^{-1} zein peak which is 5 times higher compared to the blue spectrum. The enhancement of the Raman signal showed that the introduction of AuNPs to the substrate significantly increases the Raman response. The contact of AuNPs and the gold layer creates a large number of “hot spots”, which contribute to the enhancement of the Raman signal (Seo et al., 2018). To achieve the best sensitivity of the nanosensor, we use the 100 mM cysteamine zein/Au-AuNPs which maximize the enhancement of the SERS platform to detect PYO.

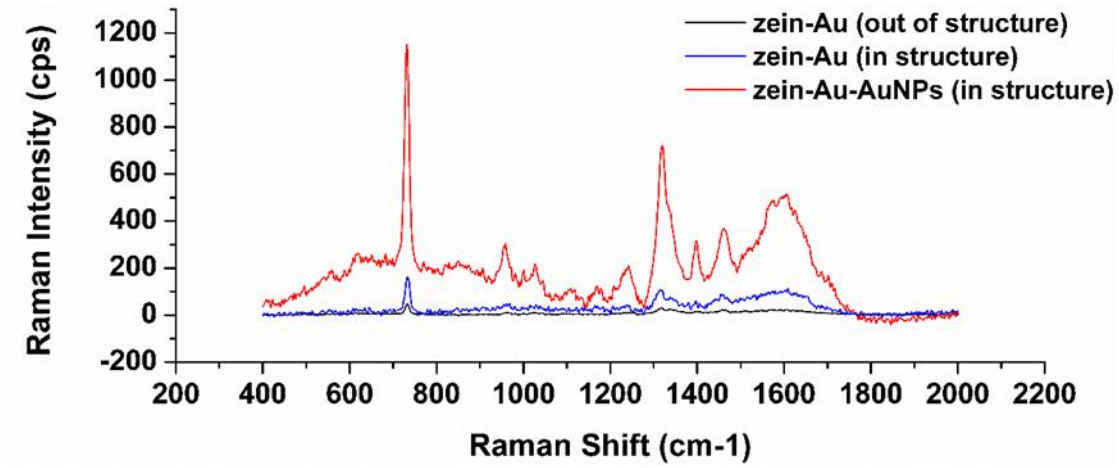

Figure 25. The Raman spectra of zein-Au substrate (without inverted pyramid structure), zein-Au (measured in the inverted pyramid structure) zein-Au-AuNPs (measured in the area with the inverted pyramid structure).

The enhancement of the SERS signal with different surface preparations was then tested using the Raman active molecule Rhodamine-6G (R6G) as the target analyte. The R6G peak intensity at 1360 cm^{-1} was measured as a reference of each sensor's enhancement. This peak is indicative of the aromatic ring vibrations that are highly present in the R6G molecule, but not present in the zein molecular structure. As shown in Figure 26, the AuNPs decorated sensor had the strongest Raman signal overall, and the Raman Intensity of the R6G peak at 1360 cm^{-1} is around 2016 cps. The intensity of the zein spectrum without any gold (No Au), however, was very small (176 cps) compared to the gold coated zein substrate (1089 cps). The SERS enhancement factor calculation is then given in Eqn. 8 for the gold decorated gold coated zein substrate (Gezer et al., 2016a):

$$\text{Enhancement Factor} = \frac{I_{SERS}}{I_{Raman}} \times \frac{C_{Raman}}{C_{SERS}} \times \frac{A_{SERS}}{A_{Raman}} \qquad \text{(Eqn. 8)}$$

where I_{SERS}, C_{SERS}, and A_{SERS} represent the SERS intensity, the concentration of Rhodamine 6G and the surface area covered by Rhodamine 6G molecules, respectively. Similarly, I_{Raman}, C_{Raman}, and A_{Raman} represent the Raman intensity, concentration of Rhodamine 6G, and the surface area covered by Rhodamine 6G molecules, respectively. The SERS enhancement of the gold coated (200 nm thickness) nanostructured zein platform without any gold nanoparticles have been previously calculated as 1.3×10^4 (Gezer et al., 2016a). To calculate the additional SERS enhancement achieved by the gold nanoparticle decoration, the surface area generated by the gold

nanoparticles from the gold nanoparticle colloid concentration and the volume of gold nanoparticles used was calculated. The Raman intensity improvement generated through the use of gold nanoparticles is also calculated. Multiplication of these two factors with the previously obtained SERS enhancement gave an improved SERS enhancement factor of 2.8×10^4.

Some of the inverted nanoparticle wells had no particles while others had a considerable number, creating a similar spectrum to the No NPs platform in the former case and a largely enhanced signal in the latter. Clearly, the Raman spectra showed that the zein sensor platform coated with gold and decorated with gold nanoparticles was the better platform. This sensor setup was further tested for detection of the PYO.

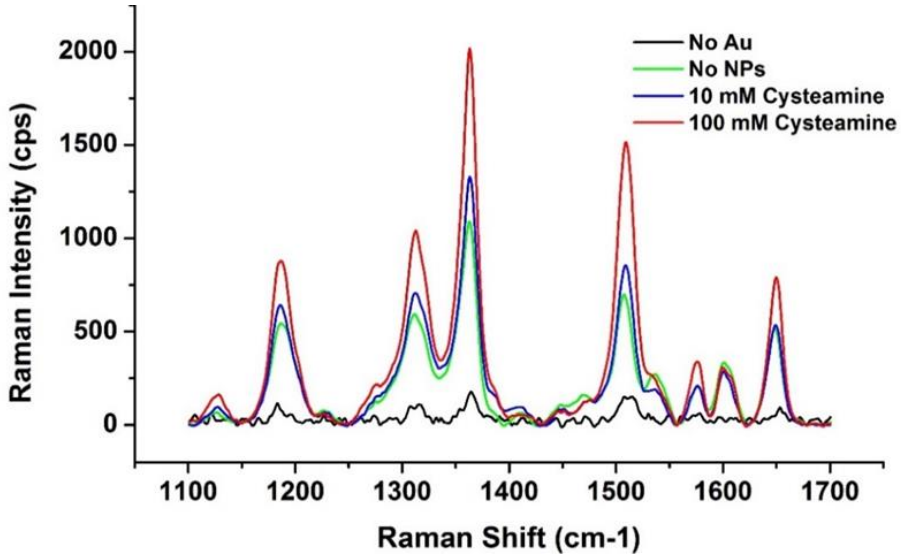

Figure 26. Raman spectra of zein SERS platforms with Rhodamine 6G analyte: No Au (black); No NPs (green); 10 mM Cysteamine (blue); 100 mM Cysteamine (red).

4.4.5 The detection ability of the SERS nanosensor for PYO

The results of the Raman tests to detect PYO at different concentrations from 0 to 1000 μM are in Figure 27a, where we can see the characteristic peaks of 676 cm^{-1} and 1353 cm^{-1} of PYO. At the concentration of 1000 μM, there are large PYO Raman peaks appearing while at 10 μM and below, there is no peak at the two characteristic wavenumbers. We deduced that the critical concentration of PYO for adequate detection should be between 10 and 100 μM. Figure 27b shows the Raman intensity changes of the characteristic peaks as a function of PYO concentration from 50 μM to

1000 μM. A 10% ethanol/water which was used to dilute PYO concentration and serves as a control shows no Raman peaks at the wavelength of 676 cm^{-1} and 1353 cm^{-1} in Figure 27a as expected. However, peaks began to appear when the PYO concentration reached 50 μM and showed an increasing Raman intensity when the concentration of PYO increased to 100 μM.

In order to further quantify the analysis, two calibration curves were developed for PYO at the characteristic peaks of 676 cm^{-1} and 1353 cm^{-1} at different concentrations of PYO ranging from 50 μM to 1000 μM. More detailed peak intensity information of the Raman spectra can be obtained by enlarging the spectra (Fig. 27b). Figure 28a shows the Raman 676 cm^{-1}peak of PYO. A Raman peak with an intensity of 20 is observed when the concentration of PYO is 50 μM and the area underneath the peak appears to increase linearly from 75 μM to 1000 μM giving a standard curve, with an equation of y=2.087x+381.7, using the change in peak areas as a function of concentration as shown in Figure 28c. The coefficient of determination R^2 for this calibration curve is 0.9879. A similar linear equation of y=2.447x+439.5 with an R^2 0.9629 was obtained at the wavelength of 1353 cm^{-1} (Figures 28b and 28d). The limit of detection (LOD) of 25 μM was calculated at this wavenumber according to the formula LOD=3N/S.

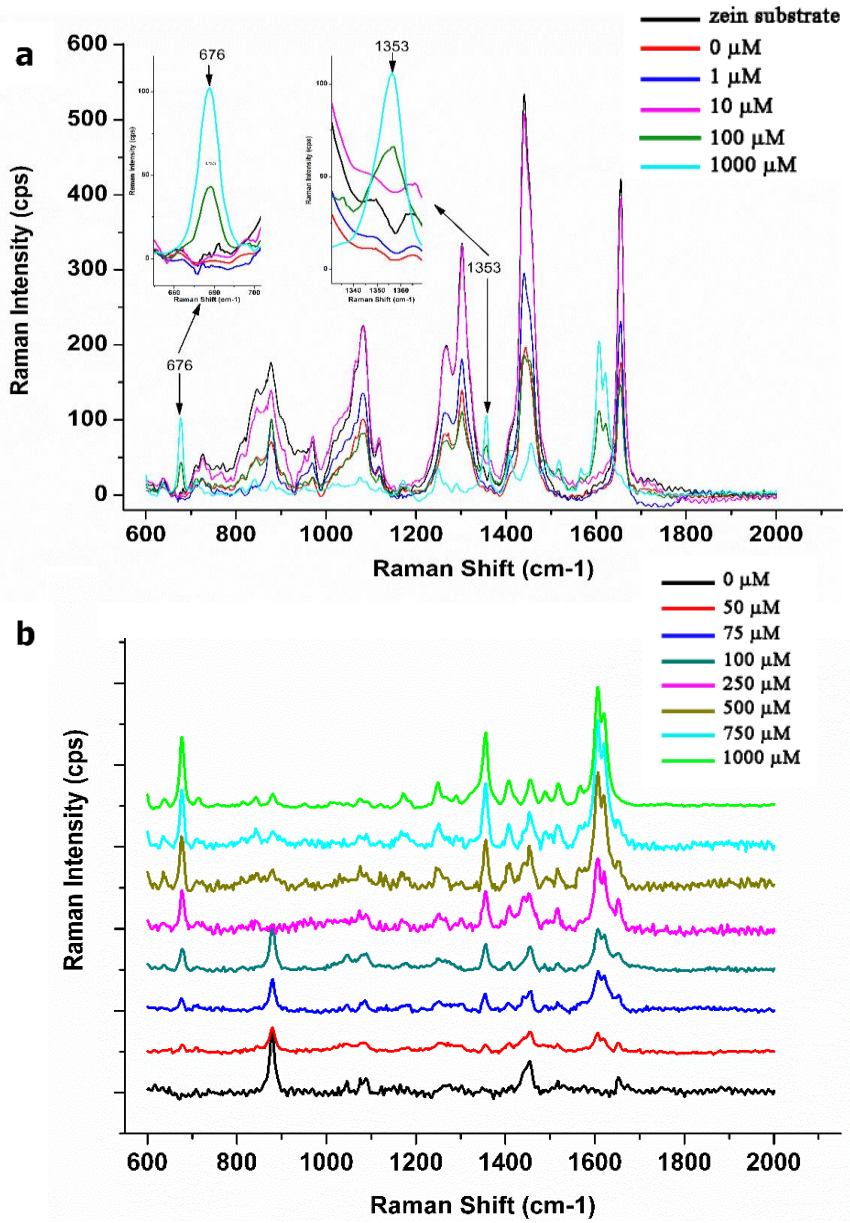

Figure 27. The Raman spectra of zein/Au-AuNPs substrate in detecting different concentration of PYO range from 1 to 1000 µM (a) The Raman intensity change along with the increase of PYO concentration from 50 µM to 1000 µM (b).

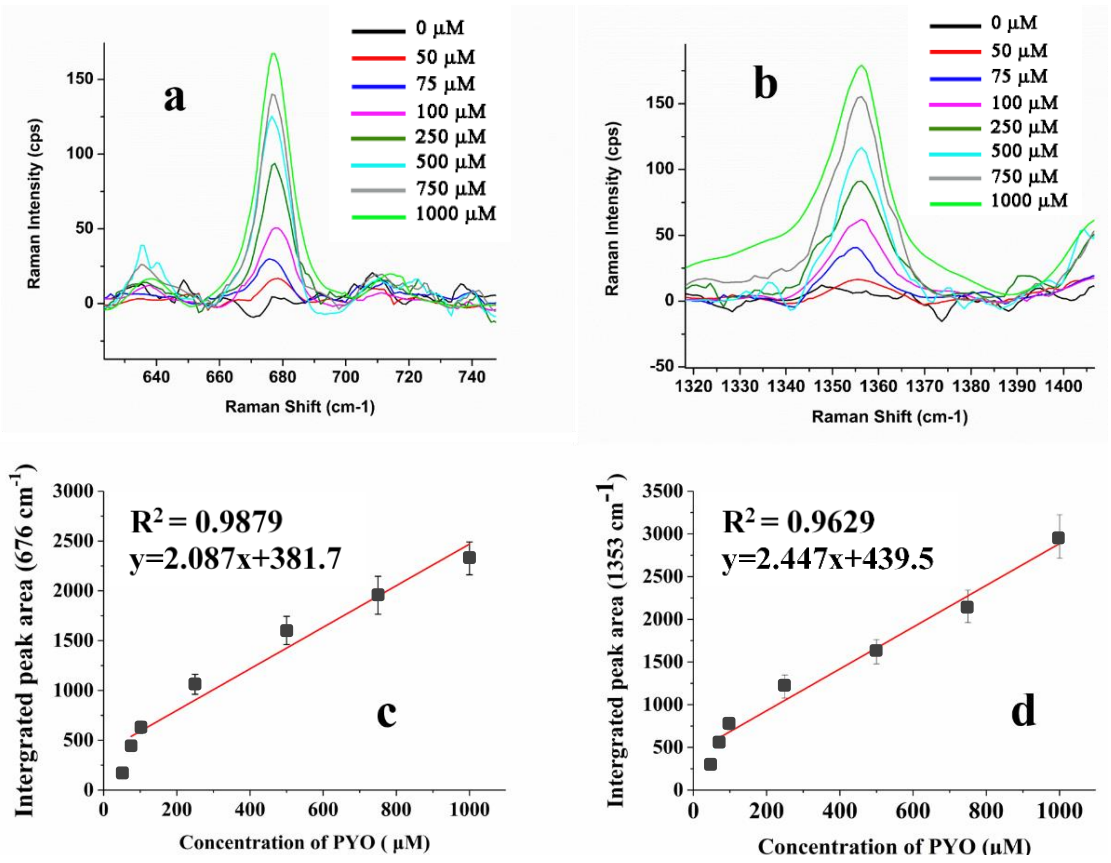

Figure 28. The Raman spectra of zein/Au-AuNPs substrate in detecting different concentration of PYO range from 50 to 1000 µM (a and b) and the standard curve of the SERS sensor in detecting different concentration of PYO range from 50 to 1000 µM (c and d) at 676 cm^{-1} and 1353 cm^{-1}

Pyocyanin is found in the sputum of patients with cystic fibrosis in concentrations as high as 16 µg/ml corresponding to 0.07 µmol/ml and has many toxic effects on eukaryotic cells, including the respiratory epithelium (Noto et al., 2017). In our current biosensor, the LOD was found to be 25 µmol/L corresponding to 0.025 µmol/ml. While there may be sensors with much higher sensitivity, the biodegradable nature of our sensor offers a different benefit coupled with a sensitivity which is in the range where damaging impact is observed on the part of pyocyanin. When other SERS-based nanosensors and the sensor in this paper for PYO detection are considered, we can see that the LOD of each nanosensor varies a lot with different nanomaterials used in the construction of the sensor and different characteristics peaks used (Bodelón et al., 2016; Nguyen et al., 2018; Wu et al., 2014; Žukovskaja et al., 2017). The ultra-high Raman enhancement factor on $Au@SiO_2$ supercrystal arrays for PYO gives the best limit of detection of 10^{-14} M in PYO

detection (Bodelón et al., 2016). Some silver nanoparticle based fabricated SERS nanosensors can also test PYO to a very low level successfully (Wu et al., 2014; Žukovskaja et al., 2017) (for detailed comparison between LODs of SERS PYO studies see *supplementary Table S-1*). However in this research we have shown that a reliable and biodegradable, sensor can be fabricated. The measurements were taken from three independently fabricated sensors and the outcome is a marker of the reproducibility of the method used with the standard deviation showing the variability from sensor to sensor. The sensor platform is also very stable. Our research on sequentially improvement platforms has been going for more than 8 years at this time. The early sensors manufactured in our lab still give good reproducibility showing the stability of our platforms. The zein based sensor is the only platform that is biodegradable among all the platforms studied so far, and exhibits great advantages over the conventional inorganic material based chips in terms of protecting the environment in an age of exponential growth in the development and commercialization of point of care sensors.

4.4.6 SERS detection of PYO in drinking water

In order to validate our methodology a relevant water safety application is considered in this study. A PYO recovery experiment from drinking water was used to evaluate the feasibility and reliability of the PYO bionanosensor. The peak area at 676 cm^{-1} was used to calculate the concentration of PYO detected in drinking water. As shown in Table 7, the recovery rates between 92.62% and 98.09% showed good capabilities of the nanosensor in this study for accurate PYO detection in drinking water.

Table 7. Recovery of PYO in Drinking Water Samples Using Developed SERS Nanosensor (n = 3)

Water Sample number	**Spiked concentration (µM)**	**Measured concentration by SERS (µM)**	**Recovery (%)**
Water 1	50.00	46.31 ± 0.66	92.62
Water 2	100.00	98.09 ± 0.48	98.09
Water 3	200.00	190.8 ± 1.57	95.40

4.4.7 Biodegradability test

It is known that zein is an alcohol soluble protein and one of the best solvents for it is 70% ethanol solution. We immersed our sensors in 70% ethanol and extracted the zein and the gold separately. In the extraction experiments, we can see clearly that the zein/Au-AuNPs substrate can be completely dissolved in the 70% ethanol solution. It takes 4.5 hours for the substrate to reach 100% dissolution at room temperature. Heat can accelerate the dissolution of zein in 70% ethanol. The SERS substrate was totally dissolved at 65°C within less than 1 hour. The gold material can be harvested easily by filtering.

4.5 Conclusions

In short, a new promising biodegradable SERS platform made of gold coated nanostructured zein decorated with 50 nm gold nanoparticles was fabricated and successfully detected PYO secreted by *P. aeruginosa*. The new platform gave a SERS enhancement factor of 2.8×10^4 and successfully enhanced the Raman intensity of PYO. PYO can be quantified in 30 mins directly without complex pretreatment and was used to detect PYO in PYO spiked drinking water. This point-of-care detection method for PYO can be further used for on-site detection of PYO in drinking water or beverages that are suspected to be contaminated with *P. aeruginosa*. The zein-based substrate, which was very easy to reclaim using ethanol extraction, is biodegradable and eco-friendly. Gold can be harvested and further used once the sensor has been used and discarded. Recycling silicone involves depolymerization to recover silicone monomers, which is a time and energy consuming process (HARMONY INDUSTRIES INC.). Glass is inert but it does not biodegrade in the environment (Center for Microbial Oceanography, Mote Marine Laboratory, 1993). Consequently the use of zein is a far superior platform from an environmental point of view.

4.6 Author Contributions

Jia, F.: Conceptualization, methodology, investigation, writing-original draft. **Barber, E.A.:** Conceptualization, methodology, investigation, writing-original draft. **Turasan, H.:** Methodology, formal analysis, writing – review and editing. **Seo, S.:** Methodology. **Dai, R.:** Supervision. **Liu, G.L.:** Conceptualization and Resources. **Li, X:** Supervision. **Bhunia, A.K.:** Resources and

supervision. **Kokini, J.L.:** Conceptualization, methodology, resources, writing – review and editing, visualization, supervision, project administration, funding acquisition

4.7 References

Alatraktchi, F. A., Breum Andersen, S., Krogh Johansen, H., Molin, S., & Svendsen, W. E. (2016). Fast Selective Detection of Pyocyanin Using Cyclic Voltammetry. *Sensors*, *16*(3), 408. https://doi.org/10.3390/s16030408

Alatraktchi, F. A., Noori, J. S., Tanev, G. P., Mortensen, J., Dimaki, M., Johansen, H. K., Madsen, J., Molin, S., & Svendsen, W. E. (2018). Paper-based sensors for rapid detection of virulence factor produced by Pseudomonas aeruginosa. *PLOS ONE*, *13*(3), e0194157. https://doi.org/10.1371/journal.pone.0194157

Baig, N., Polisetti, S., Morales-Soto, N., Dunham, S. J. B., Sweedler, J. V., Shrout, J. D., & Bohn, P. W. (2016). Label-free molecular imaging of bacterial communities of the opportunistic pathogen Pseudomonas aeruginosa. *Biosensing and Nanomedicine IX*, *9930*, 993004. https://doi.org/10.1117/12.2236695

Boardman, A. K., Wong, W. S., Premasiri, W. R., Ziegler, L. D., Lee, J. C., Miljkovic, M., Klapperich, C. M., Sharon, A., & Sauer-Budge, A. F. (2016). Rapid Detection of Bacteria from Blood with Surface-Enhanced Raman Spectroscopy. *Analytical Chemistry*, *88*(16), 8026–8035. https://doi.org/10.1021/acs.analchem.6b01273

Bodelón, G., Montes-García, V., López-Puente, V., Hill, E. H., Hamon, C., Sanz-Ortiz, M. N., Rodal-Cedeira, S., Costas, C., Celiksoy, S., Pérez-Juste, I., Scarabelli, L., La Porta, A., Pérez-Juste, J., Pastoriza-Santos, I., & Liz-Marzán, L. M. (2016). Detection and imaging of quorum sensing in Pseudomonas aeruginosa biofilm communities by surface-enhanced resonance Raman scattering. *Nature Materials*, *15*(11), 1203–1211. https://doi.org/10.1038/nmat4720

Buzid, A., Muimhneacháin, E. Ó., Reen, F. J., Hayes, P. E., Pardo, L. M., Shang, F., O'Gara, F., Sperry, J., Luong, J. H. T., Glennon, J. D., & McGlacken, G. P. (2016). Synthesis and electrochemical detection of a thiazolyl-indole natural product isolated from the nosocomial pathogen Pseudomonas aeruginosa. *Analytical and Bioanalytical Chemistry*, *408*(23), 6361–6367. https://doi.org/10.1007/s00216-016-9749-8

Center for Microbial Oceanography, Mote Marine Laboratory. (1993). *Survey of Underwater Plastic and Ecosystem Response Cruise: Marine Debris Biodegration Time Line*. http://cmore.soest.hawaii.edu/cruises/super/biodegradation.htm

Driver, M., Li, Y., Zheng, J., Decker, E., Julian McClements, D., & He, L. (2014). Fabrication of lipophilic gold nanoparticles for studying lipids by surface enhanced Raman spectroscopy (SERS). *The Analyst*, *139*(13), 3352–3355. https://doi.org/10.1039/c4an00502c

Gezer, P. G., Hsiao, A., Kokini, J. L., & Liu, G. L. (2016). Simultaneous transfer of noble metals and three-dimensional micro- and nanopatterns onto zein for fabrication of nanophotonic platforms. *Journal of Materials Science*, *51*(8), 3806–3816. https://doi.org/10.1007/s10853-015-9699-0

Gezer, P. G., Liu, G. L., & Kokini, J. L. (2016). Development of a biodegradable sensor platform from gold coated zein nanophotonic films to detect peanut allergen, Ara h1, using surface enhanced raman spectroscopy. *Talanta*, *150*, 224–232. https://doi.org/10.1016/j.talanta.2015.12.034

HARMONY INDUSTRIES INC. | HOME. (n.d.). Retrieved March 6, 2019, from http://www.harmonyrecycling.com/silicone_rubber_recycling.html

Li, S. H., Mou, Q. Q., Feng, N. Z., & Leung, P. H. M. (2018). A selective medium for pyocyanin-dependent fast electrochemical detection of pseudomonas aeruginosa in environmental microbial samples. *International Journal of Electrochemical Science*, *13*(4), 3789–3798. https://doi.org/10.20964/2018.04.20

Liao, W., & Lu, X. (2016). Determination of chemical hazards in foods using surface-enhanced Raman spectroscopy coupled with advanced separation techniques. *Trends in Food Science & Technology*, *54*, 103–113. https://doi.org/10.1016/j.tifs.2016.05.020

Luecha, J., Sozer, N., & Kokini, J. L. (2010). Synthesis and properties of corn zein/montmorillonite nanocomposite films. *Journal of Materials Science*, *45*(13), 3529–3537. https://doi.org/10.1007/s10853-010-4395-6

Navdeep, Banipal, T. S., Kaur, G., & Bakshi, M. S. (2016). Nanoparticle Surface Specific Adsorption of Zein and Its Self-assembled Behavior of Nanocubes Formation in Relation to On-Off SERS: Understanding Morphology Control of Protein Aggregates. *Journal of Agricultural and Food Chemistry*, *64*(3), 596–607. Scopus. https://doi.org/10.1021/acs.jafc.5b05495

Nguyen, C. Q., Thrift, W. J., Bhattacharjee, A., Ranjbar, S., Gallagher, T., Darvishzadeh-Varcheie, M., Sanderson, R. N., Capolino, F., Whiteson, K., Baldi, P., Hochbaum, A. I., & Ragan, R. (2018). Longitudinal Monitoring of Biofilm Formation via Robust Surface-Enhanced Raman Scattering Quantification of Pseudomonas aeruginosa-Produced Metabolites. *ACS Applied Materials & Interfaces*, *10*(15), 12364–12373. https://doi.org/10.1021/acsami.7b18592

Noto, M. J., Burns, W. J., Beavers, W. N., & Skaar, E. P. (2017). Mechanisms of Pyocyanin Toxicity and Genetic Determinants of Resistance in Staphylococcus aureus. *Journal of Bacteriology*, *199*(17), e00221-17. https://doi.org/10.1128/JB.00221-17

Pastells, C., Pascual, N., Sanchez-Baeza, F., & Marco, M.-P. (2016). Immunochemical Determination of Pyocyanin and 1-Hydroxyphenazine as Potential Biomarkers of Pseudomonas aeruginosa Infections. *Analytical Chemistry*, *88*(3), 1631–1638. https://doi.org/10.1021/acs.analchem.5b03490

Sadeghi, R., Rodriguez, R. J., Yao, Y., & Kokini, J. L. (2017). Advances in Nanotechnology as They Pertain to Food and Agriculture: Benefits and Risks. *Annual Review of Food Science and Technology*, *8*(1), 467–492. https://doi.org/10.1146/annurev-food-041715-033338

Seo, S., Chang, T.-W., & Liu, G. L. (2018). 3D Plasmon Coupling Assisted Sers on Nanoparticle-Nanocup Array Hybrids. *Scientific Reports*, *8*(1), 3002. https://doi.org/10.1038/s41598-018-19256-7

Turasan, H., & Kokini, J. L. (2017). Advances in Understanding the Molecular Structures and Functionalities of Biodegradable Zein-Based Materials Using Spectroscopic Techniques: A Review. *Biomacromolecules*, *18*(2), 331–354. https://doi.org/10.1021/acs.biomac.6b01455

Webster, T. A., & Goluch, E. D. (2012). Electrochemical detection of pyocyanin in nanochannels with integrated palladium hydride reference electrodes. *Lab on a Chip*, *12*(24), 5195–5201. https://doi.org/10.1039/c2lc40650k

Webster, Thaddaeus A., Sismaet, H. J., Conte, J. L., Chan, I. J., & Goluch, E. D. (2014). Electrochemical detection of Pseudomonas aeruginosa in human fluid samples via pyocyanin. *Biosensors and Bioelectronics*, *60*, 265–270. https://doi.org/10.1016/j.bios.2014.04.028

Wu, X., Chen, J., Li, X., Zhao, Y., & Zughaier, S. M. (2014). Culture-free diagnostics of Pseudomonas aeruginosa infection by silver nanorod array based SERS from clinical sputum samples. *Nanomedicine: Nanotechnology, Biology and Medicine*, *10*(8), 1863–1870. https://doi.org/10.1016/j.nano.2014.04.010

Yang, Yong, Tanemura, M., Huang, Z., Jiang, D., Li, Z.-Y., Huang, Y., Kawamura, G., Yamaguchi, K., & Nogami, M. (2010). Aligned gold nanoneedle arrays for surface-enhanced Raman scattering. *Nanotechnology*, *21*(32), 325701. https://doi.org/10.1088/0957-4484/21/32/325701

Yang, Yuan, Yu, Y.-Y., Wang, Y.-Z., Zhang, C.-L., Wang, J.-X., Fang, Z., Lv, H., Zhong, J.-J., & Yong, Y.-C. (2017). Amplification of electrochemical signal by a whole-cell redox reactivation module for ultrasensitive detection of pyocyanin. *Biosensors and Bioelectronics*, *98*, 338–344. https://doi.org/10.1016/j.bios.2017.07.008

Yong, Y.-C., Wu, X.-Y., Sun, J.-Z., Cao, Y.-X., & Song, H. (2015). Engineering quorum sensing signaling of Pseudomonas for enhanced wastewater treatment and electricity harvest: A review. *Chemosphere*, *140*, 18–25. https://doi.org/10.1016/j.chemosphere.2014.10.020

Yong, Y.-C., Yu, Y.-Y., Li, C.-M., Zhong, J.-J., & Song, H. (2011). Bioelectricity enhancement via overexpression of quorum sensing system in Pseudomonas aeruginosa-inoculated microbial fuel cells. *Biosensors and Bioelectronics*, *30*(1), 87–92. https://doi.org/10.1016/j.bios.2011.08.032

Yoon, J., Choi, N., Ko, J., Kim, K., Lee, S., & Choo, J. (2013). Highly sensitive detection of thrombin using SERS-based magnetic aptasensors. *Biosensors and Bioelectronics*, *47*, 62–67. https://doi.org/10.1016/j.bios.2013.03.003

Zheng, J., & He, L. (2014). Surface-Enhanced Raman Spectroscopy for the Chemical Analysis of Food. *Comprehensive Reviews in Food Science and Food Safety*, *13*(3), 317–328. https://doi.org/10.1111/1541-4337.12062

Zheng, J., Pang, S., Labuza, T. P., & He, L. (2014). Evaluation of surface-enhanced Raman scattering detection using a handheld and a bench-top Raman spectrometer: A comparative study. *Talanta*, *129*, 79–85. https://doi.org/10.1016/j.talanta.2014.05.015

Žukovskaja, O., Jahn, I. J., Weber, K., Cialla-May, D., & Popp, J. (2017). Detection of Pseudomonas aeruginosa Metabolite Pyocyanin in Water and Saliva by Employing the SERS Technique. *Sensors*, *17*(8), 1704. https://doi.org/10.3390/s17081704

CHAPTER 5. FABRICATION OF ZEIN-BASED ELECTROSPUN NANOFIBER DECORATED WITH GOLD NANOPARTICLES AS A SERS PLATFORM

Reprinted with permission. Full citation:
Turasan, H., Cakmak, M. & Kokini, J. Fabrication of zein-based electrospun nanofiber decorated with gold nanoparticles as a SERS platform. J Mater Sci 54, 8872–8891 (2019). https://doi.org/10.1007/s10853-019-03504-w.

5.1 Abstract

In this study, a new technique was developed to create an eco-friendly and biodegradable SERS sensor platform using electrospun corn zein fibers. First, electrospinning was used in conjunction with glutaraldehyde, a crosslinker for proteins, to create crosslinked zein nanofibers. The surface of the nanofibers was then decorated with 20 nm-diameter-gold nanoparticles and the biosensor platform was tested with the Raman active Rhodamine 6G. The high surface area and the high surface roughness enabled a SERS signal enhancement of $1.06 * 10^6$, which only required $2.8*10^{-7}$ g of gold nanoparticle deposition on the fibers. This electrospun zein-based gold nanoparticle decorated sensor platform is not only made with a quicker, simpler and an inexpensive method compared to the other techniques requiring etching procedures and has a very good shelf life stability, but also serves as a green alternative to the plastic-based SERS sensor platforms with an equivalent and sometimes lesser SERS signal enhancement.

5.2 Introduction

The advantages of biosensors, such as their rapid detection, specificity, ease of mass fabrication, economics and point-of-care applicability, make them useful and preferred diagnostic techniques for medicine, environmental monitoring, food safety/quality and agricultural applications (Thakur & Ragavan, 2013). Extensive studies have been carried out focusing on fabricating sensors in the literature (Lawal, 2016; Maduraiveeran et al., 2018; Tiwari et al., 2016). Surface enhanced Raman spectroscopy (SERS) is a sensor technique aiming to enhance the intensity of scattering obtained from the Raman active molecules by using noble metal nanoparticles and nanostructures which facilitate the formation of hotspots. SERS is a rapid technique, and it only takes minutes and

sometimes just seconds to make the measurements. The availability of portable, hand-held Raman devices makes point of care (on-site) measurements possible and practical (Ding et al., 2006).

The exponentially increasing number of sensors, being used to detect various molecules, brings up the concern for the amount of plastics and synthetic materials used for the production of these biosensors. Therefore, there is a need for more eco-friendly 'green' biosensors. Some of the examples where sensors are fabricated using eco-friendly materials include a chitosan-based biosensor and a zein-based biosensor (Gezer et al., 2016; C. Shan et al., 2010). Despite their advantages, using these food-grade polymers in the fabrication of biosensors has considerable challenges, such as there may be a need for the addition of a non-biodegradable filler or polymer to have the similar properties as a synthetic material (plastic) based sensor leading to fabrication methods that are very time and resource consuming. For example, for the fabrication of chitosan-based biosensors, the addition of nanocomposites (laponite (D. Shan et al., 2010) or graphene (C. Shan et al., 2010)) was necessary to increase the electro-catalytical activity of the chitosan films. The fabrication of SERS biosensors necessitates the incorporation of small amounts of highly dispersed noble metal components like gold or silver. For example, in the fabrication of zein (corn protein)-based SERS biosensor, the process includes master mold preparation, PDMS curing and solvent evaporation. Also a 200nm layer of gold coating was necessary to get a SERS enhancement of ~104 (Gezer et al., 2016). In applications like these, producing the biodegradable sensor defeats its purpose.

Electrospinning is a technique which enables the fabrication of nanoscale fibers using different polymeric substrates (Yan et al., 2014; Zhao et al., 2015). It may be possible that the large surface area created during the fabrication of these fibers may lead to an alternative design for SERS sensors. Therefore, in this study, we benefit from the high surface area created by electrospinning and from the biodegradability of a waste corn protein, zein, by producing electrospun zein nanofibers. The design parameters for the fabrication of zein nanofibers have been explored in depth (Brahatheeswaran et al., 2012; Li et al., 2012; Neo et al., 2012; Selling et al., 2007; Zhang et al., 2018). In a detailed study, the dependence of fiber morphology on the viscosity and the concentration of zein solutions were carefully analyzed (Neo et al., 2012). The critical entanglement concentration (Ce) of zein in 80% aqueous ethanol solution was found as 12 wt%

and for the fabrication of beadless fibers, the minimum zein concentration was calculated as 2-2.5*Ce (25 wt%). At viscosities lower than 100 mPa.s, the entanglement of zein molecules were not enough to create bead-free fibers, but at higher viscosities increasing chain entanglements were high enough to facilitate beadless fibers.(Neo et al., 2012) A more recent study, where pristine and blend (with PEO) zein fibers were fabricated from 80% ethanol solution, confirmed these findings (Zhang et al., 2018). The Ce of zein was found as 11.2 wt% and the minimum zein concentration for the fabrication of bead-free fibers was similarly twice as much as Ce (22 wt%). The specific concentration of zein, where the surface tension of the solution changed from the solvent's surface tension to zein monolayer surface tension, was found as 22wt%, further confirming the minimum necessary zein concentration for bead-free fiber formation (Li et al., 2012). Studies of bead-free zein fiber formation using other solvents showed slightly different concentration windows (>27 wt% for acetic acid, >35 wt% for DMF) possibly due to different behavior of zein in these solvents (Selling et al., 2007). For the fabrication of zein fibers in our study, we have studied concentrations above the reported critical concentrations.

In this study, electrospinning is used to create a new zein-based SERS biosensor platform. We aim to benefit from the increasing surface area of zein when fibers are fabricated. We hypothesize that increased surface area would enable a more effective gold deposition on the surface of zein, which would help to obtain SERS intensity enhancement higher than the previously developed zein film-based SERS platform (Gezer et al., 2016). We also aim to significantly reduce the amount of noble metal used in the fabrication of the zein based biosensor platform to preserve the biodegradability of the biosensor.

5.3 Materials and Methods

5.3.1 Materials

Zein powder was obtained from Sigma Aldrich. Ethanol, glacial acetic acid, glutaraldehyde (GLA) aqueous solution (25%) and Rhodamine 6G were purchased from Fisher Scientific. Gold (Au) nanoparticles (20 nm) were purchased from Ted Pella Inc. (Redding, CA) at a concentration of 7.0 * 10^{11} particles.ml^{-1}.

5.3.2 Solution Preparation

Zein solutions were prepared by dissolving zein powder in glacial acetic acid at ratios of 26 wt%, 28 wt% and 30 wt%. To prepare the solutions for the electrospinning process they were stirred for 2 hours at 50°C and cooled down to room temperature.

For crosslinked zein fibers, zein solutions were crosslinked with glutaraldehyde (GLA). Prior studies have shown that zein films crosslinked with GLA at a concentration of 12 wt% of the amount of zein were the strongest films and gave highest number of crosslinks (Turasan et al., 2018). Therefore, in this study, the relative amount of GLA was also set at 12 wt% of the amount of zein used to prepare the solutions. For instance, to prepare a solution with 6.5 g zein, 3.12 g aqueous GLA solution, which contained 0.78 g GLA, was measured in a beaker and was left under the fume hood overnight for the water to evaporate prior to zein solution preparation. After water evaporation, zein and acetic acid were added to the same beaker to reach a final zein concentration of 26 wt%. for the 26% zein sample. Similar calculations were made for the 28% and 30% solutions. The solutions with all the necessary ingredients were stirred similar to the uncrosslinked solutions.

5.3.3 Electrospinning

The zein solutions were electrospun at 20 kV using a high voltage power supply (Lambda Electronics). The distance between the needle and the collecting plate was fixed at 10 cm, and the collecting plate was covered with aluminum foil for high conductance and ease of handling. The two dispensing tip types (inner diameters 0.635 mm (JG20-0.5X) and 0.381 mm (JG24-0.5X)) were purchased from Jensen Global Inc.. A syringe pump (Pump Systems Inc.) was used to supply 5 in.H_2O pressure and a flow rate of 0.86 ml/h. Electrospinning was performed at 20% relative humidity (room relative humidity) and at 22°C. During the collection of the zein fibers glass slides were placed underneath the spinneret for collection of the fibers for optical microscopy imaging and Raman measurements. Due to the fast evaporation of the solvent at the nozzle caused by the very high surface area generated by electrospinning, occasional blockage of the zein solution stream occurred. In those cases, the power supply was turned off and the tip of the needle was

cleaned, and the system was started again. After the electrospun fibers were collected on the aluminum sheets or glass slides, the samples were kept in desiccators for further drying.

To manufacture fibers using crosslinked zein with glutaraldehyde, the fibers exiting the spinneret were collected as before but additionally were subjected to heat to accelerate the crosslinking process in a conventional oven at 140 °C for 10 minutes following a previously developed method (Selling et al., 2008). After they were taken out of the oven, these fibers were also stored at the desiccators containing Drierite (W.A. Hammond Drierite Co., LTD).

To compare the effect of heat on uncrosslinked zein fiber properties, a batch of uncrosslinked zein fibers was also similarly heated 140 °C. These samples were then used to compare the water contact angles (WCA) of the zein mats without crosslinking with those with crosslinking following the WCA methodology described in 2.7.

This is important in the SERS platform design of the fibers because when water droplets containing gold nanoparticles are deposited on the surface, it is highly desirable for the droplet not to spread so that gold nanoparticles are concentrated in one small spot. Therefore, the more hydrophobic the surface can be made, the less spreading of the droplet will occur. The samples prepared here enable the comparison of this relevant and important surface property.

5.3.4 Optical microscopy imaging

An optical microscope (Olympus BX51) was used to image the zein nanofibers collected on the glass slides during electrospinning at 10x magnification.

5.3.5 EDX to detect gold nanoparticles and scanning electron microscopy to study micro and nanostructure and confirm and augment data obtained with EDX

Nova NanoSEM 200 Scanning Electron Microscopy was used for SEM imaging of the samples collected on the aluminum foil (used to ensure conductance). 1 cm x 1 cm squares were cut from aluminum foils covered with fibers and coated with a platinum/palladium mixture for 60 seconds (Cressington 208 HR sputter coater). The images were collected with an accelerating voltage of

5.0 kV and at a working distance ranging between 3.8-5.6 mm. The images were collected at varying magnifications.

To see the distribution of the gold nanoparticles on zein nanofibers, first, energy dispersive X-ray analysis (EDX) was done. However, for some of the zein nanofiber mats, the gold nanoparticles are distributed on the nanofibers as individual particles (away from each other) instead of aggregating. This separate distribution of gold nanoparticles on the surface is mostly seen on the uncrosslinked zein nanofiber mats, where spreading of the drop of gold nanoparticle solution to a wider area separated the gold nanoparticles from each other and prevented aggregation. Because the size of the nanoparticles (20 nm diameter) is lower than the pixel size of EDX mapping, especially in low magnification (wider area) images, EDX maps did not show significant peaks of individual gold nanoparticles, and most of the information was lost during EDX mapping for uncrosslinked fibers.

Instead of EDX mapping, SEM images of the samples taken with a backscattered electron detector (vCD) displayed the distribution of gold nanoparticles on the nanofibers more accurately. Because in backscattered electron detection, gold nanoparticles can be easily spotted and differentiated from platinum/palladium (used to cover the surface of the sample for conductivity) due to their higher atomic number. This higher atomic number makes the gold nanoparticles shine more brightly than platinum during backscattered electron imaging.

5.3.6 Gold nanoparticle decoration of the electrospun zein fibers

The zein nanofibers were decorated with 20 nm gold nanoparticles using two different methods. No crosslinker was used in either of the decoration methods. In the first method, the nanoparticle colloids were added into the zein solutions before the electrospinning step. After the solutions were cooled down to room temperature, 60 μl of the gold colloid solution ($7.0 * 10^{11}$ particles.ml^{-1}) was added to 10 ml of zein solution and stirred for another 15 minutes to ensure homogenous distribution. Then, the solutions were electrospun as described before.

In the second way of nanoparticle decoration, 2 μl droplets of nanoparticle colloids ($7.0 * 10^{11}$ particles.ml^{-1}) were deposited on the dried electrospun zein fiber mats. The fiber mats were then

placed in desiccators containing desiccant (W.A. Hammond Drierite Co., LTD) to ensure the complete drying of the colloids. To further enhance the concentration of gold nanoparticles multiple droplet deposition was used. Multiples of 2 μl droplets (3 consecutive droplets) were placed on the same spot on the fibers with drying periods in between, such that the new droplets were placed on the same spot after the previous droplet has dried.

5.3.7 Water contact angle measurements

Water contact angle measurements were conducted on zein fiber mats electrospun directly onto glass slides using Attension Theta Tensiometer (Biolin Scientific). The contact angles were recorded for 50 seconds with 12 frames per second. The droplet size of the water placed on each sample was 2 μl. Right and left contact angles were averaged by the software. The initial average contact angles (t=0 s) and contact angles at 5 s, 10 s, and 50 s were reported.

5.3.8 Degradation in aqueous environment

To test the stability of both uncrosslinked and crosslinked electrospun zein nanofibers in aqueous environment, water immersion test was conducted. 1 cm × 1 cm pieces of zein nanofiber mats, which were directly electrospun on aluminum foil, were immersed in 15 ml deionized water in 60 mm ×15 mm petri dishes for 30 minutes. To ensure complete immersion in water, the samples were taped to the bottom of the petri dishes. After 30 minutes of immersion, the samples were dried in an oven at 120 ℃ for 1 hour to evaporate the water for SEM imaging. SEM images were taken with the parameters explained before.

5.3.9 Atomic Force Microscopy

Cypher ES Atomic Force Microscopy from Asylum Research was used to characterize the surface roughness of the electrospun fiber mats. TAP300AL-G-10 type silicon probes coated with 30nm Al for enhanced reflectivity (tip radius <10 nm) with 300 kHz frequency and 40 $N.m^{-1}$ force constant were purchased from Ted Pella Company. AFM analysis was conducted on the zein fibers electrospun directly on aluminum sheets. 0.5 cm x 0.5 cm pieces were cut from the fiber coated aluminum sheets and superglued on AFM/STM Metal Specimen Discs. The images were taken

from 10μm x 10μm and 300 nm x 300 nm scanning areas. The average roughness values were calculated by MFP3D software.

5.3.10 Raman spectroscopy measurements

Raman spectroscopy was conducted on zein nanofibers with a dispersive Raman spectrometer (DXR 2 Raman Microscope ThermoFisher Scientific). The spectra were collected between wavenumbers of 200 and 3600 cm^{-1} using a 633 nm laser at 6 mW laser power, 10x objective lens with a 50 μm slit aperture. 10 replications were taken for each spectrum and averaged using OMNIC software. Due to the fluorescence of zein protein, the baseline of all the spectra was initially corrected for fluorescence using 5^{th} order polynomial. Then, all the spectra were manually fine-tuned for baseline correction. The Raman active Rhodamine 6G (R6G) was used as a Raman marker. First, electrospun zein nanofiber mats were decorated with Au nanoparticles using two consecutive droplets of 2 μl ($7.0 * 10^{11}$ particles.ml^{-1}). Then a third droplet of 2 μl, containing 1 μl Rhodamine 6G (200 μM) mixed with 1 μl Au nanoparticles ($7.0 * 10^{11}$ particles.ml^{-1}), was deposited on the zein nanofibers prior to Raman measurements, giving a final Rhodamine 6G concentration of 100 μM. The electrospun zein fiber mats were then put into desiccators for complete evaporation of the solvent. The measurements were taken after the Rhodamine 6G solvent evaporated.

5.3.11 Statistical Analysis

Minitab 18 (One-way ANOVA) was used for statistical analyses with 95% confidence level. Tukey's comparison tests were applied ($p<0.05$) to compare the zein fiber diameters and the water contact angle data. Lettering system was used to show significant difference, such that different letters represent significant difference.

5.4 Results and Discussion

In this paper, we report the design and optimization of zein fiber mat fabrication for the best possible Au nanoparticle decoration to obtain a higher SERS enhancement than what has previously been reported (Gezer et al., 2016a). Effects of solvent, zein concentration, crosslinking, and nanoparticle decoration methods have been studied to obtain fibers with smaller diameters and

highest resistance to swelling. Smaller diameters are important to get highest possible surface area to enable more particle decoration and resistance to swelling is important for Au colloid and sample depositions. The optimized fibers were then tested for SERS measurements to calculate the enhancement factor.

5.4.1 Effect of solvent on fiber morphology

In this study 70% ethanol and glacial acetic acid were tested as the solvents for the fabrication of zein fiber mats in terms of their suitability for SERS sensors because they are known as the two best solvents for zein (Turasan and Kokini, 2017). Figure 29 shows the optical microscopy images of zein fibers prepared from these two solvents at 26 wt%. When 70% ethanol was used as the solvent, there were a lot of inhomogeneity and discontinuities in the fibers in the form of beads, which led to frequent fiber rupture and discontinuous fiber formation (Fig. 29a). The fibers fabricated using glacial acetic acid were largely bead-free and there were almost no fiber breakages (Fig. 29b), consistent with the previous studies (Selling et al., 2008, 2007).

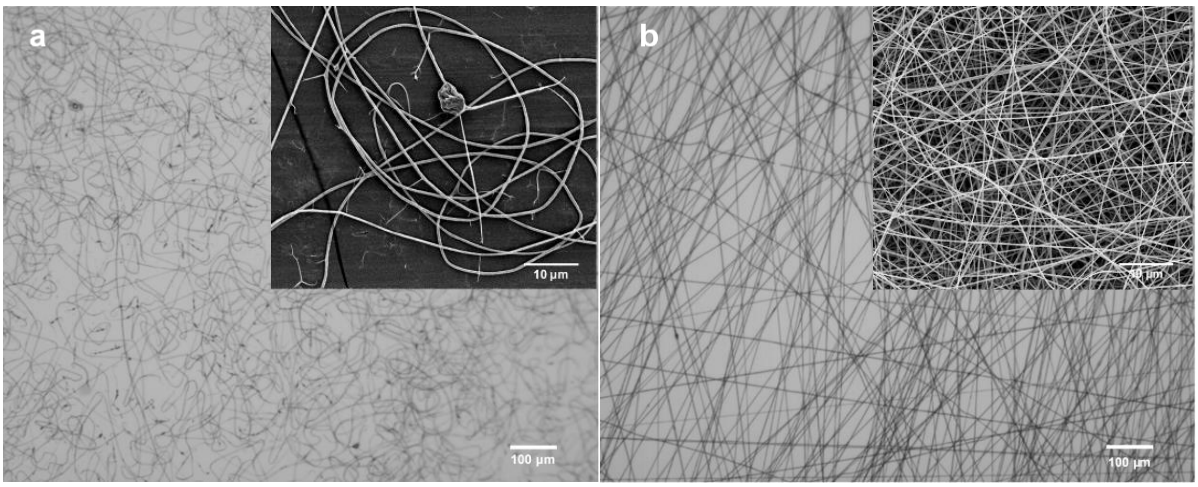

Figure 29. Optical microscopy images (at 10x magnification) of zein electrospun fibers prepared using 70% ethanol solution (a) and glacial acetic acid (b) as solvents. Corresponding SEM images are given as insets.

The different morphologies of zein fibers in 70% ethanol and glacial acetic acid is due to different chain entanglement behavior of zein molecules in these solvents as explained in introduction. The incomplete unfolding of zein molecules in ethanol solutions leads to multimer formation of zein

molecules through hydrophobic interactions (Li et al., 2012). Clearly, at this concentration of zein in 70% ethanol, the lack of interaction between zein multimers does not allow enough chain entanglement between zein molecules to provide the continuity of the macromolecular phase in solution during electrospinning, which leads to bead formation and fiber rupture (Shenoy et al., 2005). Even though the zein concentration used in this study for 70% ethanol (26 wt%) was above the reported critical entanglement concentrations (22-25 wt%) (Neo et al., 2012; Zhang et al., 2018), beaded fibers were still observed, which is probably due to different sources of zein used and the small variations in the solubility of zein at this ethanol concentration in the solvent. In the case of acetic acid, zein molecules have been shown to better and fully dissolve and unfold, leading to only monomer formation in the solvent (Li et al., 2012). This complete unfolding of zein molecules at the same concentration allows more chain entanglement of zein molecules in acetic acid solution, which leads to a continuous fiber formation during solvent evaporation. A schematic representation of zein fiber formations in aqueous ethanol and in acetic acid are shown in Figure 30.

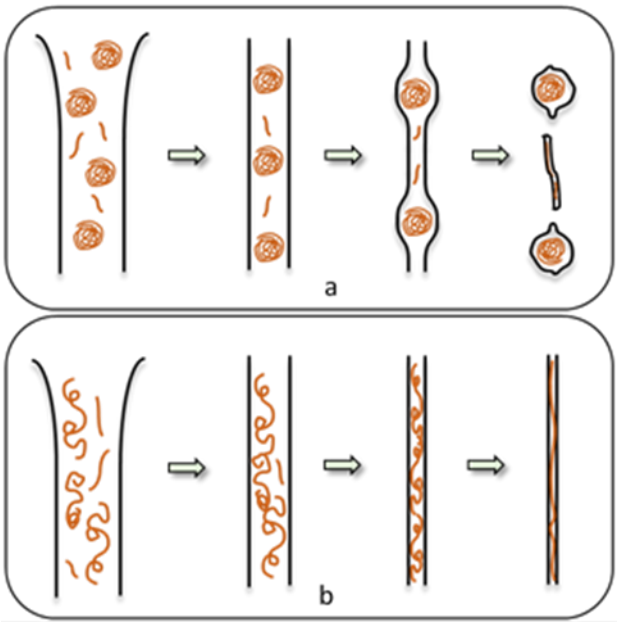

Figure 30. Schematic representation of electrospun zein fiber formation using 70% aqueous ethanol (a) and glacial acetic acid (b) as solvent.

Because fabricating zein fibers using acetic acid as the solvent resulted in continuous fiber formation with significantly less defects and preparing fibers from 70% aqueous ethanol solution

caused frequent bead formation and fiber breakages, for the rest of the experiments, only acetic acid was used as the solvent.

5.4.2 Effect of zein concentration on fiber morphology

Three different zein concentrations (26 wt%, 28 wt%, and 30 wt%) were tested to fabricate fibers and their behaviors under aqueous media deposition were studied. In the fabrication of zein fiber-based SERS biosensor platforms, decreasing fiber diameter would result in increased surface area, which would also increase the number of gold nanoparticles that can be deposited/decorated on the surface of zein, leading to an increase in hotspot formation and therefore an increased SERS signal. The fibers need to have resistance to swelling leading to limited swelling when aqueous samples are applied on them to keep their 3D structures. Initially all three zein solutions were electrospun using a dispensing tip having an inner diameter of 0.381 mm. However, the solution prepared with 30 wt% zein could not be drawn out due to its higher viscosity (2.0 Pa.s) and dispensing tips with an inner diameter of 0.635 mm were used. The viscosity of the solutions that have 26 wt% and 28 wt% zein concentrations were low enough to use dispensing tips with 0.381 inner diameter (0.8 Pa.s and 1.3 Pa.s, respectively) and at the same time high enough to be above the critical concentration (2Ce) for entanglement to successfully manufacture fibers.

Zein fibers were successfully fabricated from all three concentrations as shown in SEM images in Figure 31. All the fibers had smooth surfaces without cracks. In almost all of the fibers the cores of the fibers are darker compared to the walls possibly because of the shrinking during drying that may result in a somewhat higher concentration in the middle compared to the walls. However, this shrinkage did not prevent the fibers from having round shapes. Almost no fusion of the fibers was observed at the junction points, which shows that zein fibers are drying efficiently before being collected on the collecting plate without causing any fusion. The fibers with highest zein concentration (30 wt%) had the highest average diameter (830±156 nm) as expected based on prior studies of the electrospinning of zein, followed by 28 wt% zein fibers with an average diameter of 312 ± 66 nm and 26 wt% zein with an average diameter of 289 ± 63 nm (Yao et al., 2007). Statistical analysis (ANOVA) showed that while fibers with 30 wt% zein had significantly larger diameters, fibers with 26 and 28 wt% were not significantly different from each other.

Our results are consistent with previous studies where round and beadless zein fibers were fabricated using zein in the concentration range (27-30 wt%) in glacial acetic acid as the solvent (Selling et al., 2007; Vogt et al., 2018). Lower concentrations of zein caused electrospraying instead of electrospinning. In this study, zein fibers were successfully fabricated with a good geometry with 26 wt% zein. This difference may be due to using dispensing tips with different inner diameters.

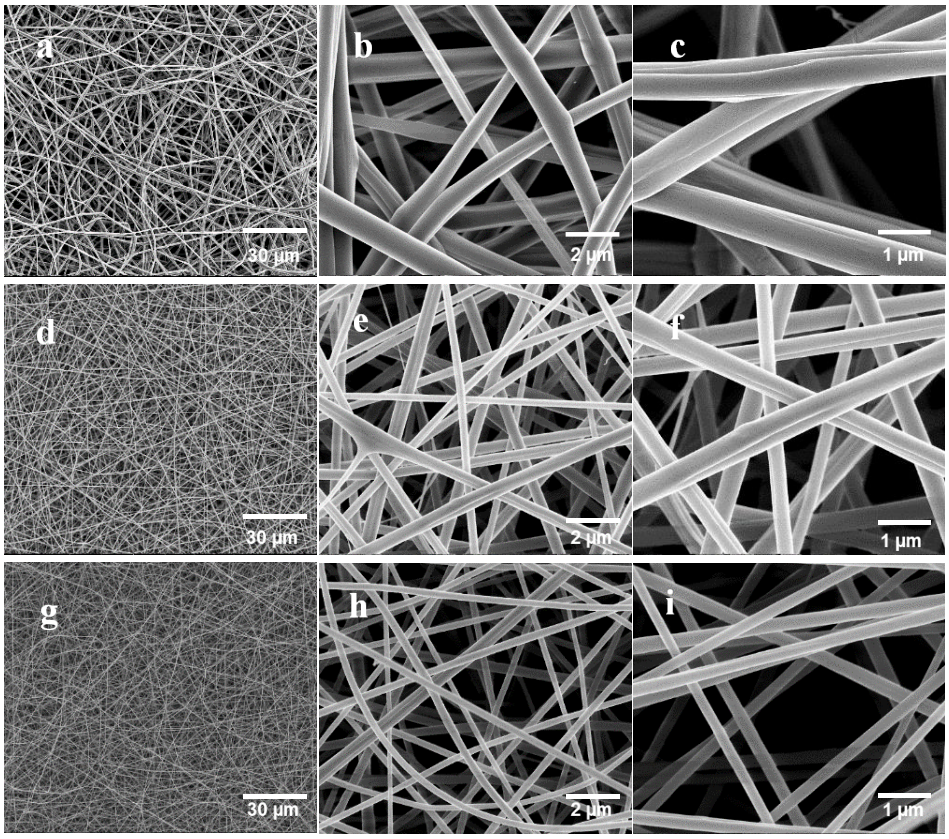

Figure 31. SEM images of zein nanofibers with (a-c) 30 wt%, (d-f) 28 wt% and (g-i) 26 wt% zein concentration at different magnifications (a/d/g at 2000x, b/e/h at 25000x and c/f/i at 50000x).

5.4.3 Decoration of zein fibers with gold nanoparticles

EDX analysis vs. backscattered electron (BSE) imaging

To display the distribution of gold nanoparticles EDX and BSE imaging techniques were compared. An example of poor mapping of gold nanoparticles with EDX analysis is shown below. Figure 32a

is the SEM image of an uncrosslinked zein nanofiber mat decorated with 3 consecutive droplets (2 µl each) of Au nanoparticles taken using a backscattered electron detector (vCD) at high magnification (gold nanoparticles are highlighted artificially with red dots). Figures 32b and 32c are the Au EDX map and EDX map spectrum of the same sample, respectively. The EDX map (Fig. 32b) does not show the accurate distribution of the nanoparticles on the fiber structure, but instead it shows a background signal distribution. For comparison, an EDX map of a crosslinked zein nanofiber mat showing a more accurate distribution gold nanoparticles is shown in the inset of Figure 32b. However, this accurate nanoparticle distribution could not be captured for uncrosslinked samples. Also in Figure 32c, the Au peaks have low intensities in the spectra and are mostly hidden in the background signal. This also shows that correct information could not be obtained from all of our samples using EDX mapping.

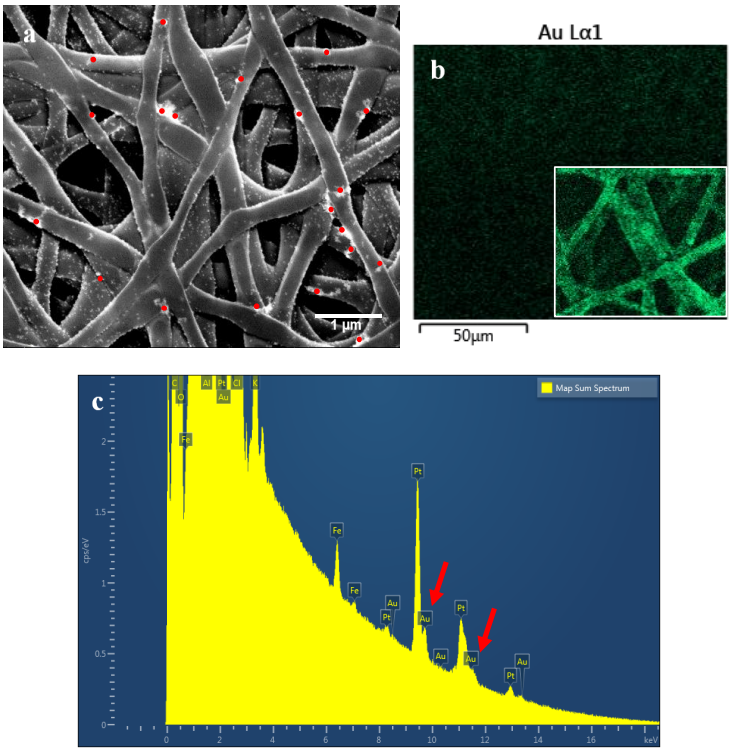

Figure 32. BSE image (a), Au EDX map (b), and EDX map spectrum (c) of uncrosslinked zein nanofiber decorated with Au nanoparticles. Inset in b shows Au EDX map of crosslinked zein nanofiber decorated with Au nanoparticles.

Instead of EDX mapping, SEM images of the samples taken with a backscattered electron detector (vCD) displayed the distribution of gold nanoparticles on the nanofibers more accurately. In

backscattered electron detection, gold nanoparticles can be easily spotted and differentiated from platinum due to their higher atomic number. This higher atomic number providing more electrons makes the gold nanoparticles shine more brightly than platinum during backscattered electron imaging. Figure 33a shows the difference between two areas on the fiber mats decorated and non-decorated with Au nanoparticles imaged with backscattered electron detector. Both of these areas were covered with platinum before imaging. It is clear that brightness comes only from gold and not from platinum. EDX analysis of the crosslinked fiber mats with no platinum cover but only with gold nanoparticle decoration (Fig 33b) also proves that the brightness is due to the distribution of gold nanoparticles and not platinum (Fig 33c). Therefore to better show the distribution of the gold nanoparticles on zein nanofibers, backscattered electron imaging was conducted instead of EDX mapping.

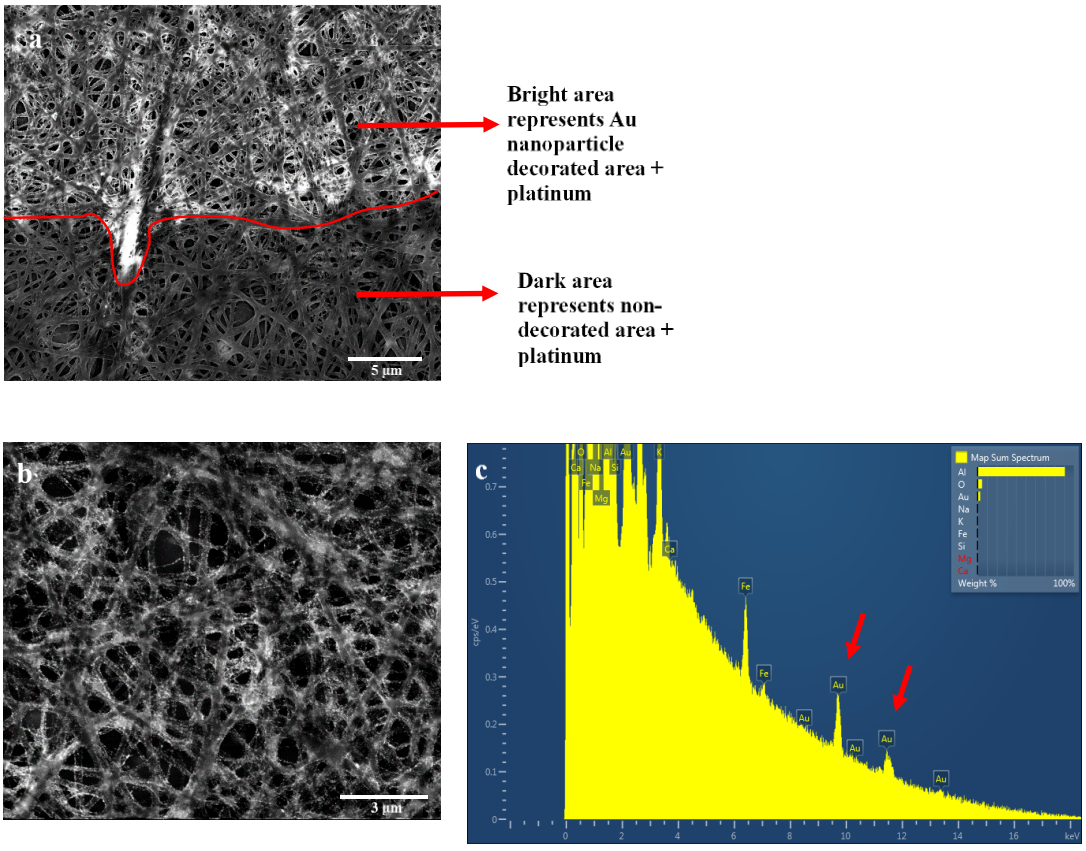

Figure 33. BSE image of crosslinked zein nanofibers decorated with Au nanoparticles coated with platinum/palladium for imaging (a). BSE image (b) and EDX map spectrum (c) of uncoated crosslinked zein nanofibers decorated with Au nanoparticles.

In-solution method

In this technique 20 nm Au nanoparticles were used. The SEM images of the zein nanofibers decorated with 'in solution' method are shown in Figure 34. All the fibers have similar morphologies to those of control nanofibers. All the samples had quite smooth surfaces. Occasionally some cracks formed caused by the high energy of SEM imaging. In almost none of the fibers, nanoparticles were seen on the surface of the fibers. This is possibly due to fast drying of nanofibers, which ended up encapsulating the gold nanoparticles in the interior region of the fibers. Au nanoparticles were very rarely seen during SEM imaging (data not shown) especially around broken fibers, which probably surfaced by diffusing to the surface through the cracks. SEM image of 26 wt% zein nanofibers taken with a backscattered electron (BSE) detector also proves that there are no gold nanoparticles on the surface of the nanofibers decorated with 'in-solution' decoration method, since there are no distinctive brighter spots in the image (Fig. 34d). It was concluded that as far as SERS application was concerned this was not successful method and as a result was not pursued any further.

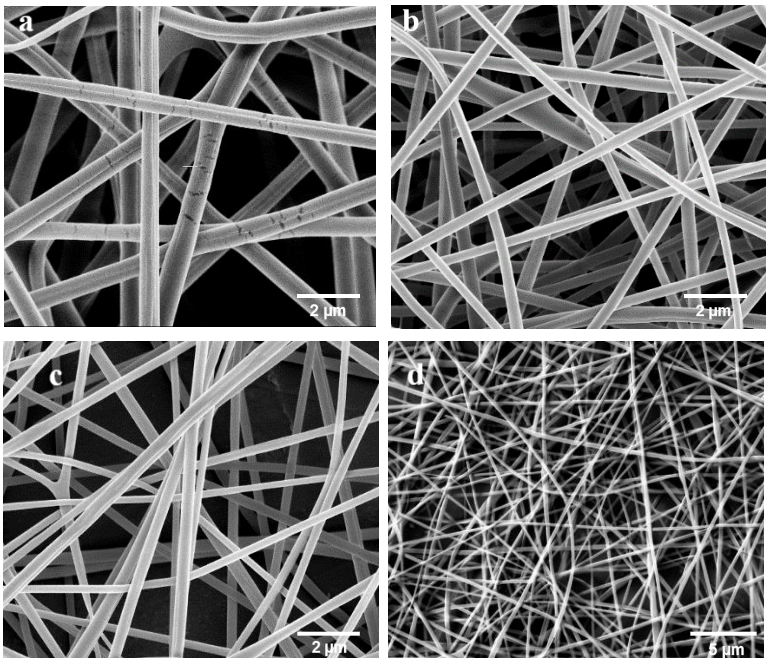

Figure 34. SEM images of zein nanofibers decorated with gold nanoparticles using 'in solution' method having 30 wt% (a), 28 wt% (b), and 26 wt% (c) zein concentrations. SEM image of 26 wt% zein nanofibers taken with a BSE detector (d).

Drop deposition method

Zein nanofibers decorated with the drop deposition technique show some similarities and some differences in morphology to those decorated with the 'in solution' method as shown in Figure 35a-c. At the junction points where the fibers cross after electrospinning, there are some distortions and some fibers merge, possibly due to localized absorption of water and swelling coming from the liquid drop. The general structure of the fibers is nevertheless well preserved (Fig. 35a-c). The gold colloid filled droplet deposition does not seem to change the surface smoothness of the fibers compared to the control fibers. Fibers fabricated from a solution of 30 wt% zein, seem to be less distorted compared to 28 wt% or 26 wt% zein fibers at single drop deposition. During solvent evaporation of the drop, the water may not be able to diffuse deep into the 30 wt% fibers compared to the fibers with lower zein concentrations because the diameter of the fibers fabricated from 30% zein solution is considerable larger than the fibers from 26 and 28% zein solutions.

The nanoparticle concentration is kept constant for all the fibers ($7*10^{11}$ particles.ml^{-1}). However, for all the nanofibers, at some places the nanoparticles are aggregating while at other places they are better dispersed on the surface (Fig. 35a-c). Aggregation of nanoparticles is seen more around the intersection of nanofibers. It would be expected that as the liquid from the droplet is being absorbed into the fiber mat through capillary action the gold nanoparticles would be attracted toward regions where there is an abundance of zein (intersections of fibers) given the proven affinity of gold to zein (Gezer et al., 2016a).

To test if increasing the number of gold nanoparticle droplets increase the nanoparticle density on the surface of the nanofibers, 2 and/or 3 consecutive droplets (each droplet having a 2 µl volume) were deposited on the same spot of the nanofiber mats. Between the depositions of two consecutive drops the earlier gold colloid droplet was dried in the desiccator. This way, the liquid volume on that spot was not doubled or tripled at once, since it would cause further swelling and the gold nanoparticles would spread themselves to a larger surface adversely affecting the Raman enhancement, but instead, the concentration of gold nanoparticles on the same spot of the mats was increased by applying 2 or 3 droplets consecutively once the spot dried. The number of Au nanoparticles was increased on the same spot with the goal of increasing the intensity of the Raman signal during SERS because the decrease in gold interparticle distance would enhance hotspot

formation. Fig. 35d-i show the zein nanofiber mats with Au gold nanoparticles deposited on the surface with 1, 2, and 3 consecutive droplets.

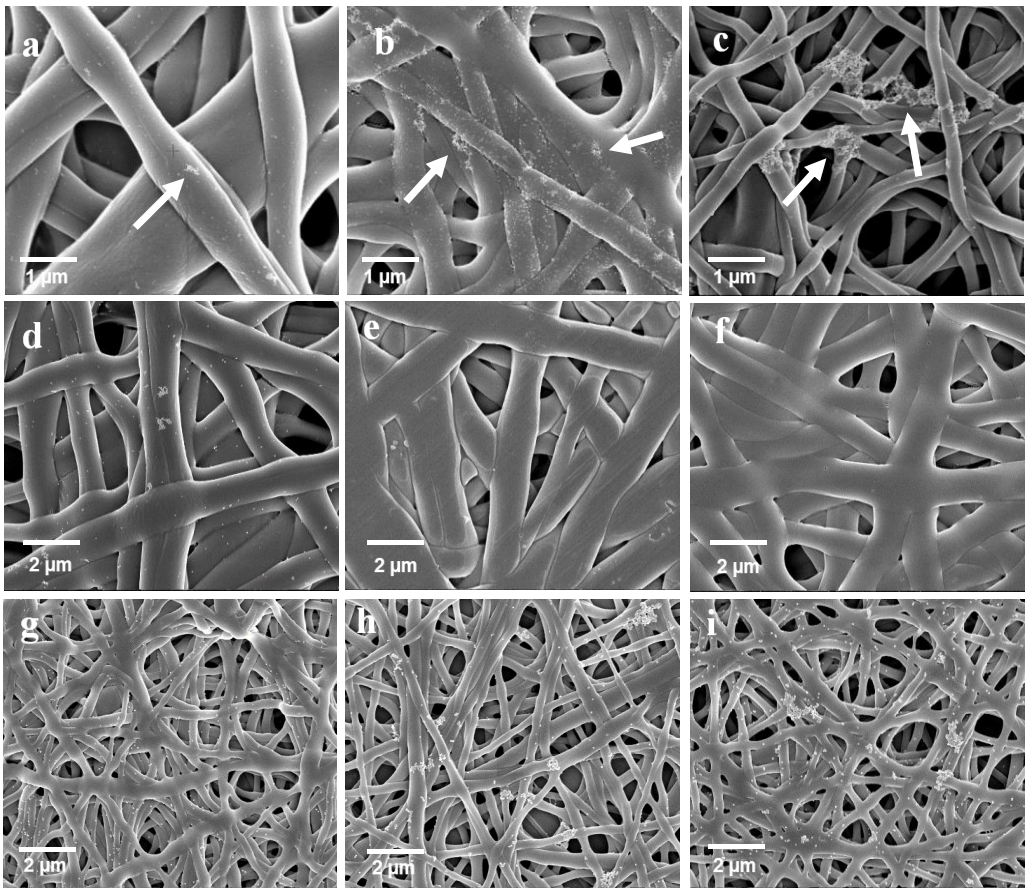

Figure 35. SEM images of zein nanofibers decorated with single drop deposition having 30 wt% (a), 28 wt% (b), and 26 wt% (c) zein concentrations. The arrows are showing the Au nanoparticle clusters on the surface of the nanofibers. Effect of multiple Au colloid droplet deposition on 30 wt% (d-f) and 26 wt% (g-i) zein nanofibers (d, g: single droplet; e, h: two consecutive droplets; f, i: three consecutive droplets).

To display the increasing concentration of gold nanoparticles decorated on the surface of the zein nanofibers with increasing number of gold colloid droplets, BSE images of 26 wt% zein nanofibers decorated with 1 droplet and 3 droplets of gold nanoparticle colloid are shown in Figure 36a and 36b, respectively. It is clear from the higher number of brighter spots seen on the fibers decorated with 3 droplets, the concentration of gold nanoparticles increases significantly with multiple droplet deposition, which is favorable to increase the number of hot spots for enhancing the Raman signal.

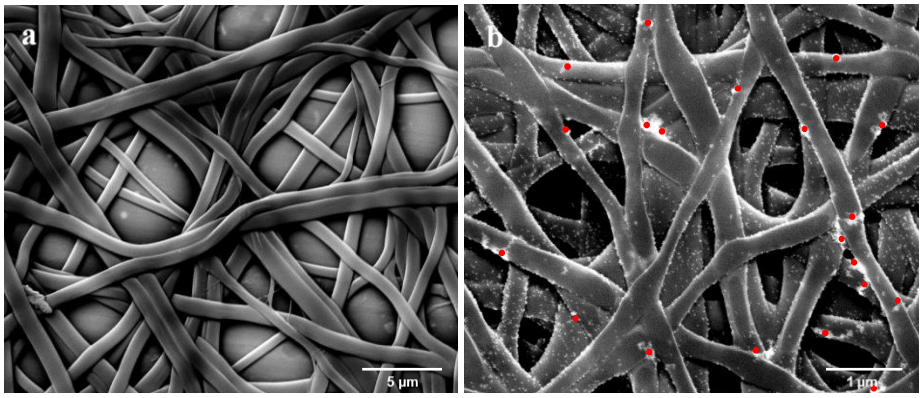

Figure 36. Backscattered electron images of 26 wt% zein nanofibers decorated with 1 droplet (a), and 3 droplets (b) of gold nanoparticle colloid solution. Some of the gold nanoparticle dense spots are highlighted with red dots.

The addition of 2 or 3 droplets sequentially further increased the swelling for the largest diameter fibers (30 wt% zein), but no significant increase in the surface density of gold nanoparticles was observed. The additional swelling also caused partial loss of 3D structure and formation of a more planar structure (Fig. 35d-f).

The 26 wt% fibers on the other hand, representing the smallest diameter fibers, did not further swell with more droplet deposition. The morphology of the fiber mats decorated with 2 droplets were very similar to those decorated with 3 droplets (Fig. 35g-i). Multiple droplet deposition was also helpful in increasing the number of Au nanoparticles on the surface of the fibers. For this reason, 26 wt% zein concentration was used further in this study to understand the effect of gold decorated fibers on SERS enhancement.

5.4.4 Effect of crosslinking on surface wettability of zein nanofibers

In this study, the effect of crosslinking of zein with glutaraldehyde on surface properties of the fiber mat was tested to determine if the surface would become progressively more hydrophobic in order to prevent the spreading of gold nanoparticle containing droplets so that the gold nanoparticles are assembled in a relatively small surface area to maximize the intensity of the SERS signal. The number of crosslinks in zein films increase with increasing glutaraldehyde concentration in the range of 0-12% glutaraldehyde with 12% giving the highest crosslink density (Turasan et al., 2018). Therefore, the nanofibers were crosslinked with glutaraldehyde at 12 wt%

and heated at 140 ºC for 10 minutes (Selling et al., 2008). There were no visual differences between the crosslinked and uncrosslinked or heated and non-heated fiber mats. Also, there was no visible changes occurring in the sample morphology with heat treatment (Fig. 37). No visible contraction or collapse of the fibers were observed after heating the samples.

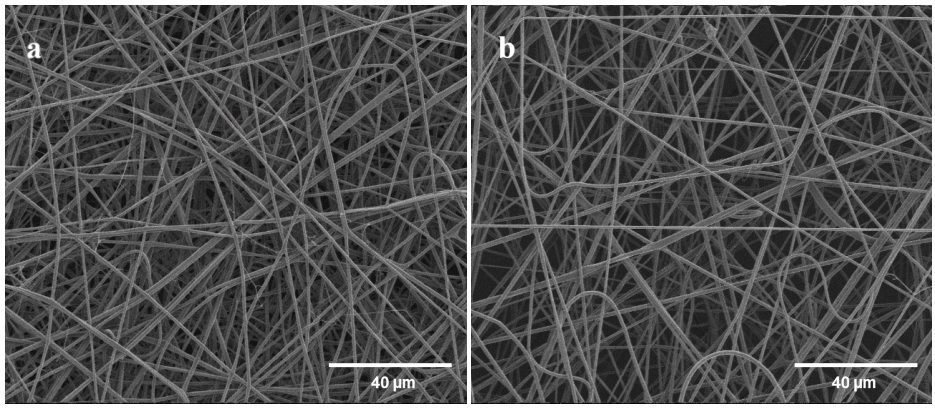

Figure 37. SEM images of 12% crosslinked zein fiber mats without (a) and with (b) 140 ºC heat treatment for 10 mins.

The surface wettability properties of the nanofiber mats, measured using the WCA, changed significantly with both crosslinking and heat treatment. Table 8 shows the water contact angles of crosslinked and uncrosslinked zein nanofiber mats with and without heat treatment at different times.

Table 8. Water contact angles of crosslinked and uncrosslinked zein nanofibers with and without heat treatment (each time period was statistically compared within itself, and different letters show significant difference, $p<0.05$)

WCA	**0% GLA non-heated (º)**	**12% GLA non-heated (º)**	**0% GLA heated at 140ºC (º)**	**12% GLA heated at 140ºC (º)**
t= 0 s	57.34±12.07 ^{d}	86.25±4.76 ^{c}	123.19±4.68 ^{b}	134.40±3.25 ^{a}
t= 5 s	12.39±3.30 ^{c}	16.81±1.61 ^{c}	71.77±6.64 ^{b}	115.20±4.09 ^{a}
t= 10 s	0	0	17.78±6.55 ^{b}	87.60±18.20 ^{a}
t= 50 s	0	0	0	59.99±18.59

As expected, the lowest initial contact angles were recorded for the uncrosslinked samples that were not subjected to any heat treatment. The absorption of the water droplet by the nanofiber mat was the fastest for this sample; 10 seconds after the droplet was placed on the nanofiber mat, the droplet was fully absorbed. 12% crosslinking increased the initial (t=0) contact angle of the nanofiber mats, however without extensive crosslinking, after 10 seconds the water droplet was again fully absorbed. The initial contact angle of the uncrosslinked fiber mats increased to 123º and the absorption rate of the water droplet into the fiber matrix significantly decreased because of heat treatment at 140 ºC. The slowest water droplet absorption and the highest initial contact angle were seen in the 12% crosslinked nanofiber mat subjected to heat treatment at 140 ºC. The initial WCA rose to 134° and even after 50 seconds, the water droplet was not fully absorbed caused by the combined effects of crosslinking and heat treatment. Consistent with our observations, previous studies have shown that forming electrospun fibers from a material increases its surface hydrophobicity, due to the increase in surface roughness both at the micro and nano levels, which is also known as the lotus effect (Cheng et al., 2006; Ma et al., 2005; Ma and Hill, 2006; Singh et al., 2005). In addition crosslinking zein films with 12% glutaraldehyde also increases their surface roughness (Turasan et al., 2018). Additionally, heat treatment enhances chemical crosslinking, contributing to the surface roughness, and may help the evaporation of the bound hydrophilic solvent trapped inside the nanofibers, further increasing the surface hydrophobicity.

The changing surface wettability, caused by the combined effects of crosslinking and heat treatment, had a significant effect on gold nanoparticle decoration of the nanofibers (Fig. 38a-b). For the uncrosslinked and non-heated nanofibers (Fig. 38a), the nanoparticles deposited on the surface of the fibers were located far apart from each other with the exception of a few clusters. This is due to the fast spreading of water through the gaps between fibers, which widened the area that Au nanoparticles were deposited on. Also, a part of the gold nanoparticles is possibly dragged by water to the bottom of the nanofiber mats and lose their effectiveness in Raman signal amplification. The nanoparticles on the surface of the 12% crosslinked and heated nanofibers (Fig. 38b) are more densely populated. The increasing surface hydrophobicity prevented the spreading of the water carrying the gold nanoparticles, which resulted in a higher concentration of nanoparticles. Backscattered electron images of these nanofibers at lower magnifications show the

increasing concentration of gold nanoparticles with crosslinking and heat treatment more clearly and effectively (Fig. 36c-d). Since higher concentrations and more clustering of the gold nanoparticles are expected to enhance hotspot formation during the SERS measurements, samples that are 12% crosslinked and heat treated were used in SERS experiments.

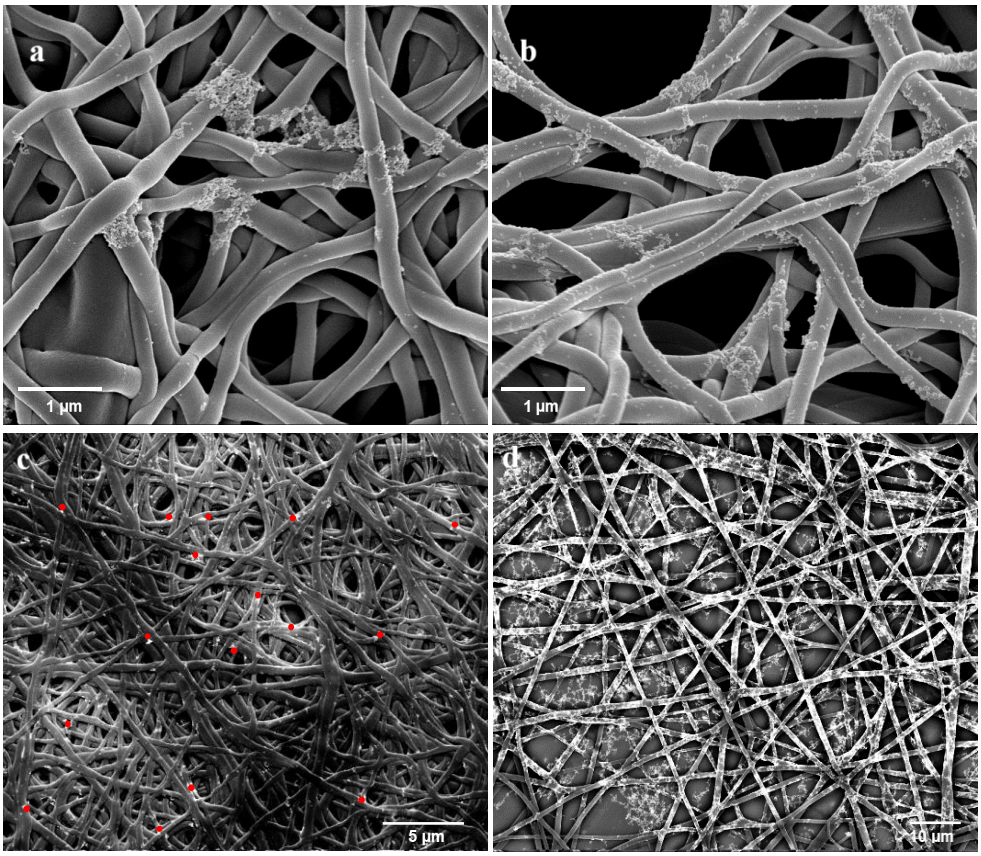

Figure 38. Combined effects of crosslinking and heat treatment on nanoparticle decoration. SEM images of uncrosslinked non-heated (a) and 12% crosslinked and heated (b) zein nanofibers decorated with 20 nm Au nanoparticles. BSE images of uncrosslinked non-heated (c) and 12% crosslinked and heated (d) zein nanofibers decorated with 20 nm Au nanoparticles. Some of the gold nanoparticle dense spots are highlighted with red dots.

5.4.5 Degradation in aqueous environment and during storage in an average relative humidity environment

SEM images of uncrosslinked and crosslinked zein nanofibers before and after immersion in deionized water are shown in Figure 39. For uncrosslinked zein nanofibers, even though there were a few fibrous structures seen after the water immersion test, most of the fiber morphology was lost.

The swelling of zein nanofibers with water caused merging and flattening of the fibers, forming a film structure (Fig. 39c).

The crosslinked zein nanofibers maintained their fibrous structures against swelling much better than the uncrosslinked zein nanofibers. However, partial film formation due to swelling and merging was also seen in crosslinked zein nanofibers (Fig. 39d). This higher stability of crosslinked zein nanofibers in an aqueous environment is due to the stronger structure of zein created by tighter junctions during chemical crosslinking with glutaraldehyde (Turasan et al., 2018).

However, the most relevant storage experiment are those that are conducted in an average relative humidity environment. We have stored crosslinked zein nanofibers in the relative humidity environment of our laboratory for 8 months. The results are shown in Figure 39e. As can be seen from the figure, we fibers maintained their integrity and have almost unappreciable distortion and degradation. This is a good indicator of how these laboratory results when translated to a real manufacturing and storage environment would behave and the results are encouraging.

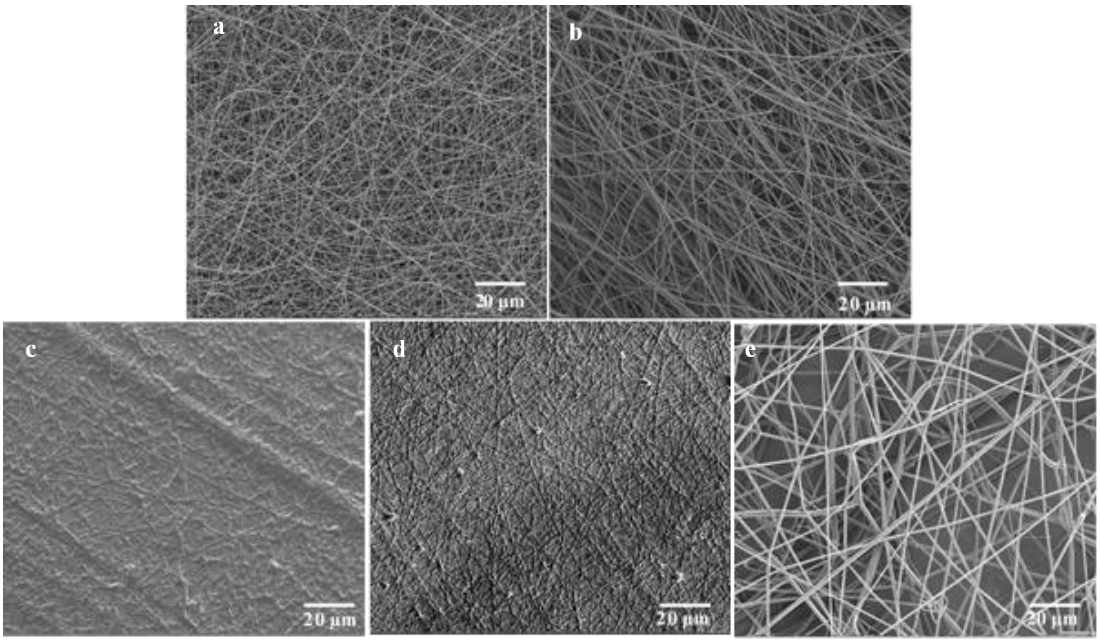

Figure 39. SEM images of uncrosslinked (a, c) and 12 % crosslinked (b, d) zein nanofibers before (a, b) and after (c, d) water immersion for 30 mins. Morphology of 12 % crosslinked zein nanofibers after 8 months of storage in an uncontrolled relative humidity (e).

5.4.6 Atomic Force Microscopy

Nanofiber morphology can be clearly seen on the topography (uppermost layer) of fiber mats of both uncrosslinked and crosslinked fibers (Fig. 40a-b). The individual fiber contours are very visible and discernable on each AFM micrograph. In order to make them clear and observable contours have been drawn around individual fibers. In the uncrosslinked fiber mats it is possible to visually observe that the fibers are more rounded and less densely packed; for the crosslinked zein fiber mats the individual fibers stand taller and are more densely packed which may be the outcome of the crosslinking of zein. At a surface area of 10 μm x 10 μm, the average surface roughness of the uncrosslinked nanofiber mats were calculated as 316.5 nm. The surface roughness is clearly linked to the contours of the fibers. At the same surface area, crosslinked zein nanofiber mats had a significantly higher surface roughness of 449.1 nm ($p<0.05$) consistent with the observation that the fibers stand taller and are more densely packed.

When single fiber surfaces are studied the roughness values were much lower. Uncrosslinked nanofibers had an average roughness value of 333.9 picometers (pm) and 12% crosslinked nanofibers had a roughness of 233.3 pm (Fig. 40c-d). The higher picometer scale roughness on the uncrosslinked fibers may be a reflection of the higher porosity which results in rapid water absorption. The decrease of surface roughness with crosslinking on fiber surfaces, may be the outcome of loss of porosity generated by the chemical crosslinking process. This results in a fiber unable to absorb water as rapidly as uncrosslinked zein fibers. The net relevant outcome is a higher degree of hydrophobicity to prevent the spreading of the water droplet, therefore concentrating gold nanoparticles to a much smaller area (Table 8). In addition it is apparent from the micrographs that the micron-size roughness values increased with crosslinking, consistent with the changing surface wettability of the nanofiber mats. The micron size roughness is larger for crosslinked zein fiber mats compared to the uncrosslinked fiber mats increasing the hydrophobicity of the surface by generating an effect similar to the lotus leaf effect. With gold nanoparticle decorated crosslinked fibers, gold nanoparticles can also be clearly seen on the decorated nanofiber surface either as single nanoparticles or clustered nanoparticles (Fig. 40e). Gold nanoparticle decoration increased the average surface roughness of the crosslinked nanofibers to 712.7 pm

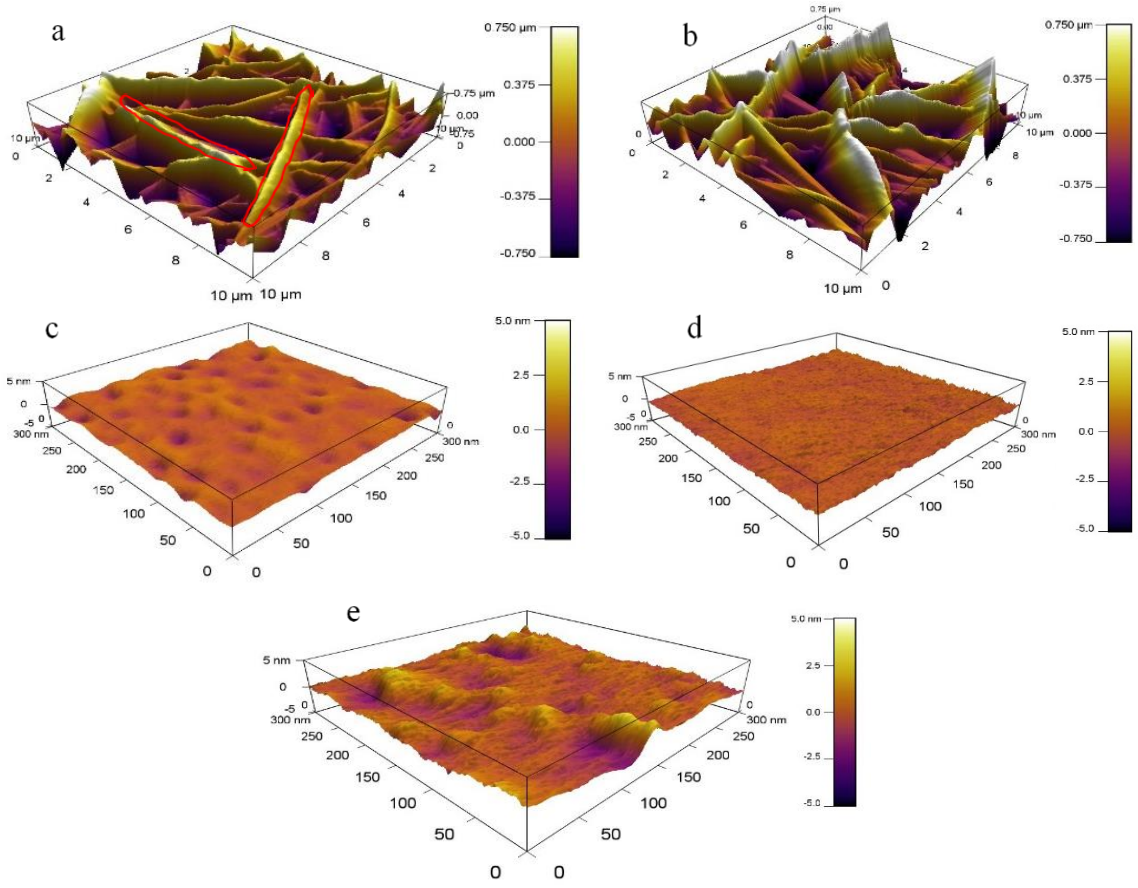

Figure 40. 3D AFM images of zein nanofiber mats; a: uncrosslinked zein nanofibers (10 µm x 10 µm), b: crosslinked zein nanofibers (10 µm x 10 µm), c: surface of single uncrosslinked zein nanofiber (300 nm x 300 nm), d: surface of single crosslinked zein nanofiber (300 nm x 300 nm), e: surface of Au nanoparticle decorated crosslinked zein nanofiber (300 nm x 300 nm). Red contours show single fibers in the mat.

5.4.7 Testing the zein nanofiber SERS platform

To test the effectiveness of the zein nanofiber platform SERS experiments were conducted using Rhodamine 6G (R6G) as the Raman active molecule. Initially different concentrations of R6G were tested on the zein nanofiber platforms, to determine the lowest concentration of R6G that can be used in the SERS experiments without any loss of peak information. All the operating parameters were kept constant while the effect of R6G concentration was studied. The concentrations tested were 1mM, 100 µM, 10 µM, and 1 µM (Fig. 41). The R6G signature peaks at 616 cm^{-1} (C-C-C ring in plane bending), 776 cm^{-1} (C-C-C ring, out-of-plane bending), 1186 cm^{-1} (C-C stretching vibrations), 1365 cm^{-1}, 1513 cm^{-1} and 1654 cm^{-1} (aromatic) bands were compared

(Pristinski et al., 2006). The spectra with 1 mM R6G had the most prominent peaks among all concentrations, as expected. These peaks are also present at 100 µM concentration but as expected they have lower intensities than 1 mM peaks. 10 µM concentration spectra barely shows any peaks, and almost no peaks were seen at 1 µM R6G concentration. Based on these results 100 µM was chosen as the R6G concentration to be used in testing for the Raman enhancement.

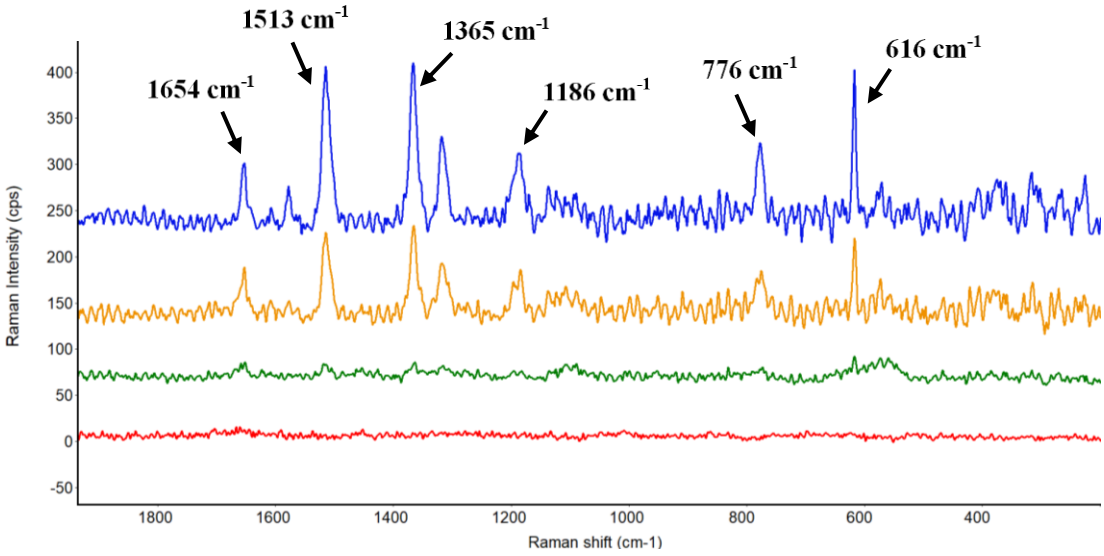

Figure 41. Raman spectra of Rhodamine 6G on zein nanofiber mats at different R6G concentrations; 1 µM (red), 10 µM (green), 100 µM (yellow), and 1 mM (blue).

To study the total SERS enhancement obtained with the crosslinked and uncrosslinked zein elctrospun nanofiber platforms (with combined effects of Au nanoparticles and surface structure), the spectra of R6G on glass slide, on Au NP decorated glass slide and on zein nanofiber sensor platform were compared (Fig. 42). For the measurement of R6G on glass slide, 100 mM R6G concentration was used, since lower concentrations of R6G did not show measurable peaks compared to the peaks obtained from the sensor platform. For R6G on Au NP decorated glass slide and the zein-based sensor platforms, 100 µM R6G was used. To increase the surface density of Au nanoparticle decoration on the surface of the fibers, crosslinked and uncrosslinked zein fiber mats were decorated with 3 Au colloid droplets. To clearly illustrate the SERS enhancement the glass slide was also decorated with 3 droplets of Au NPs.

0.1 M R6G on plain glass slide had the lowest Raman intensity, despite its much higher concentration, as expected based on prior studies since there is no gold nanoparticles present to enhance the signal (Gezer et al., 2016a). When the glass slide was decorated with 3 consecutive Au nanoparticle droplets, a higher Raman signal was obtained from a lower R6G concentration (100 μM). The Raman signal of R6G on uncrosslinked zein nanofiber platforms was slightly lower than R6G on Au nanoparticle decorated glass slide. This is the result of the outward diffusion of gold nanoparticles to a wider area on the nanofiber mat due to its high hydrophilicity (Table 8). R6G on crosslinked zein nanofiber mats gave significantly higher Raman signals compared to uncrosslinked zein nanofiber mats because, the increasing surface hydrophobicity resulting from crosslinking prevented spreading of Au nanoparticles to a wider area and increased the surface density AuNP and of hotspots.

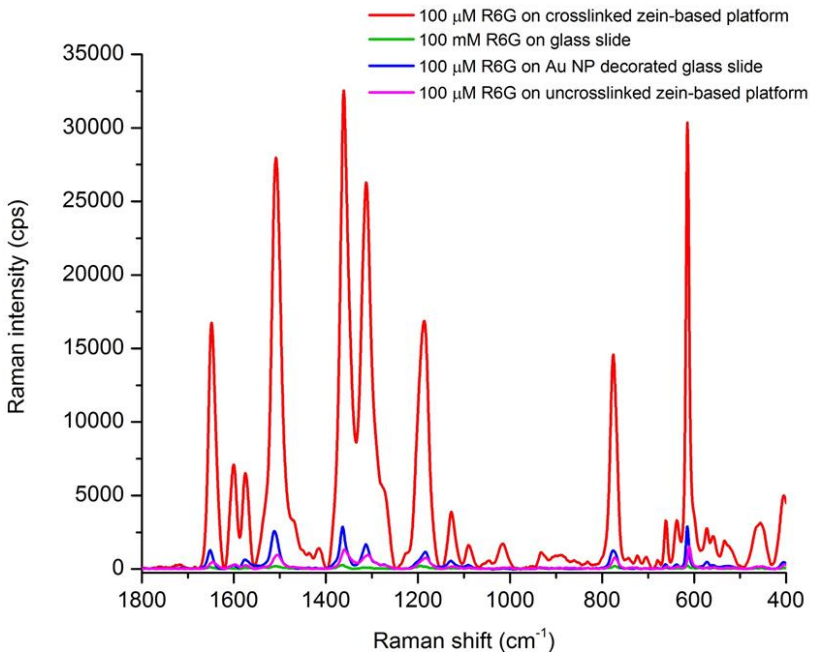

Figure 42. SERS enhancement of fabricated zein nanofiber platform. Red: spectrum of R6G on crosslinked zein nanofiber sensor platform (100 μM R6G), magenta: spectrum of R6G on uncrosslinked zein nanofiber sensor platform (100 μM R6G), blue: spectrum of R6G on Au nanoparticle decorated glass slide (100 μM R6G), green: spectrum of R6G on glass slide (100 mM R6G).

For the calculatation of total SERS enhancement, Eqn. 9 was used and the intensities of R6G were compared based on the 1365 cm^{-1} peak (Gezer et al., 2016a).

$$\text{Enhancement Factor} = \frac{I_{SERS} \times N_{Normal}}{I_{Normal} \times N_{SERS}} \qquad \text{(Eqn. 9)}$$

where I_{SERS} and I_{Normal} are the intensities obtained from SERS and non-SERS (normal) Raman experiments, while N_{SERS} and N_{Normal} are the number of R6G molecules contributing to these signals (Chang et al., 2014; Liu et al., 2011). To calculate the surface area covered with R6G on the glass slide was considered a flat circle (d=2.28±0.13 mm), while for the surface area created by the zein nanofibers, the result of a prior study on electrospun zein nanofibers was adopted (8.17 m^2g^{-1}) (Brahatheeswaran et al., 2012).

The total enhancement obtained from crosslinked AuNP decorated zein nanofiber sensor platform is calculated to be $1.06 * 10^6$. The enhancement factor of uncrosslinked zein nanofiber mats, on the other hand, is $4.3 * 10^4$. These enhancements are obtained by depositing $2.8 * 10^{-7}$ g of Au nanoparticles on the surface on zein nanofiber platform. This new strategy appears to be an improvement over our previous strategies using soft lithography where the surface of the zein platform with nanophotinic structures was covered by a gold layer with a thickness of 200 nm and the reported enhancement factor was $1.3 * 10^4$ (Gezer et al., 2016a). The enhancement obtained with crosslinked electrospun zein nanofiber platform in this study is almost 100 times higher than zein film-based substrate while the amount of gold used is approximately 803 times less (the calculations are done on weight basis). In addition, the SERS enhancement factor obtained in this study is comparable to some of the non-biodegradable disposable SERS sensor platforms in the literature (Qu et al., 2012; Zhai et al., 2012). There are also higher SERS enhancement factors achieved with different SERS sensor platform designs, such as Au nanoparticle monolayer with ultrasmall nanogaps (Si et al., 2016) or g-C_3N_4-intercalated graphene oxide membranes (Qu et al., 2017) in the literature, however, the biodegradable protein sensor platform fabricated in this study offers better sustainability.

The sensor platform fabricated in this study uses a significantly less amount of gold while increasing the SERS enhancement due to its higher the surface area. Less use of gold is also more advantageous from the biodegradability point of view. In addition, the electrospinning technique is easy to operate and is more rapid compared to soft lithography, which includes curing of PDMS and drying of zein films for days (Gezer et al., 2016a). Also in the technique developed in this

study, there is no requirement for a master mold preparation through etching, which requires a considerable amount of time is challenging and can be expensive. Therefore the zein nanofiber-based SERS sensor platform serves an excellent green alternative from the production and the biodegradability point of view.

5.5 Conclusion

This paper summarizes the development and optimization of a novel biodegradable zein (corn protein)-based SERS sensor platform. To obtain a good SERS intensity and enhancement factor, the zein-based sensor platform was formed from zein nanofibers using electrospinning, which provides a very high surface area and surface roughness, the two key elements in increasing SERS intensity. Acetic acid was chosen as the better solvent relative to 70% ethanol for forming zein nanofibers, and the optimum zein concentration was found as 26 wt%, which yielded an average nanofiber diameter of 289 nm. Among the two gold nanoparticle decoration techniques, drop deposition technique gave a better surface coverage, with the limitation that it caused a slight fiber swelling (305 nm). 12% glutaraldehyde crosslinking prevented the swelling of zein nanofibers, and increased the surface wettability, which also prevented the spreading diffusion of the gold nanoparticles through the fiber mat and increased hotspot formation. SERS measurements of Rhodamine 6G, a marker molecule, gave an enhancement factor of $1.06 * 10^6$, which is 100 times higher than the reported enhancement factor of a previously developed zein-based SERS sensor, by using 803 times less gold (by weight) (Gezer et al., 2016a). The enhancement factor obtained is comparable if not somewhat superior to the plastic-based SERS sensor platforms while offering a largely eco-friendly, green alternative.

5.6 References

Brahatheeswaran, D., Mathew, A., Aswathy, R. G., Nagaoka, Y., K Venugopal, Yoshida, Y., Maekawa, T., & Sakthikumar, D. (2012). Hybrid fluorescent curcumin loaded zein electrospun nanofibrous scaffold for biomedical applications. *Biomedical Materials*, *7*(4), 045001. https://doi.org/10.1088/1748-6041/7/4/045001

Chang, T.-W., Gartia, M. R., Seo, S., Hsiao, A., & Liu, G. L. (2014). A wafer-scale backplane-assisted resonating nanoantenna array SERS device created by tunable thermal dewetting nanofabrication. *Nanotechnology*, *25*(14), 145304. https://doi.org/10.1088/0957-4484/25/14/145304

Cheng, Y. T., Rodak, D. E., Wong, C. A., & Hayden, C. A. (2006). Effects of micro- and nano-structures on the self-cleaning behaviour of lotus leaves. *Nanotechnology*, *17*(5), 1359. https://doi.org/10.1088/0957-4484/17/5/032

Ding, S.-Y., Zhang, X.-M., Ren, B., & Tian, Z.-Q. (2006). Surface-Enhanced Raman Spectroscopy (SERS): General Introduction. In *Encyclopedia of Analytical Chemistry*. John Wiley & Sons, Ltd. https://doi.org/10.1002/9780470027318.a9276

Gezer, P. G., Hsiao, A., Kokini, J. L., & Liu, G. L. (2016). Simultaneous transfer of noble metals and three-dimensional micro- and nanopatterns onto zein for fabrication of nanophotonic platforms. *Journal of Materials Science*, *51*(8), 3806–3816. https://doi.org/10.1007/s10853-015-9699-0

Lawal, A. T. (2016). Synthesis and utilization of carbon nanotubes for fabrication of electrochemical biosensors. *Materials Research Bulletin*, *73*, 308–350. https://doi.org/10.1016/j.materresbull.2015.08.037

Li, Y., Li, J., Xia, Q., Zhang, B., Wang, Q., & Huang, Q. (2012). Understanding the Dissolution of alpha-Zein in Aqueous Ethanol and Acetic Acid Solutions. *Journal of Physical Chemistry B*, *116*(39), 12057–12064. https://doi.org/10.1021/jp305709y

Liu, Y., Xu, S., Li, H., Jian, X., & Xu, W. (2011). Localized and propagating surface plasmon co-enhanced Raman spectroscopy based on evanescent field excitation. *Chemical Communications*, *47*(13), 3784–3786. https://doi.org/10.1039/C0CC04988C

Ma, M., & Hill, R. M. (2006). Superhydrophobic surfaces. *Current Opinion in Colloid & Interface Science*, *11*(4), 193–202. https://doi.org/10.1016/j.cocis.2006.06.002

Ma, M., Mao, Y., Gupta, M., Gleason, K. K., & Rutledge, G. C. (2005). Superhydrophobic Fabrics Produced by Electrospinning and Chemical Vapor Deposition. *Macromolecules*, *38*(23), 9742–9748. https://doi.org/10.1021/ma0511189

Maduraiveeran, G., Sasidharan, M., & Ganesan, V. (2018). Electrochemical sensor and biosensor platforms based on advanced nanomaterials for biological and biomedical applications. *Biosensors and Bioelectronics*, *103*, 113–129. https://doi.org/10.1016/j.bios.2017.12.031

Neo, Y. P., Ray, S., Easteal, A. J., Nikolaidis, M. G., & Quek, S. Y. (2012). Influence of solution and processing parameters towards the fabrication of electrospun zein fibers with sub-micron diameter. *Journal of Food Engineering*, *109*(4), 645–651. https://doi.org/10.1016/j.jfoodeng.2011.11.032

Pristinski, D., Tan, S., Erol, M., Du, H., & Sukhishvili, S. (2006). In situ SERS study of Rhodamine 6G adsorbed on individually immobilized Ag nanoparticles. *Journal of Raman Spectroscopy*, *37*(7), 762–770. https://doi.org/10.1002/jrs.1496

Qu, L., Wang, N., Xu, H., Wang, W., Liu, Y., Kuo, L., Yadav, T. P., Wu, J., Joyner, J., Song, Y., Li, H., Lou, J., Vajtai, R., & Ajayan, P. M. (2017). Gold Nanoparticles and g-C3N4-Intercalated Graphene Oxide Membrane for Recyclable Surface Enhanced Raman Scattering. *Advanced Functional Materials*, *27*(31), 1701714. https://doi.org/10.1002/adfm.201701714

Qu, L.-L., Li, D.-W., Xue, J.-Q., Zhai, W.-L., S. Fossey, J., & Long, Y.-T. (2012). Batch fabrication of disposable screen printed SERS arrays. *Lab on a Chip*, *12*(5), 876–881. https://doi.org/10.1039/C2LC20926H

Selling, G. W., Biswas, A., Patel, A., Walls, D. J., Dunlap, C., & Wei, Y. (2007). Impact of solvent on electrospinning of zein and analysis of resulting fibers. *Macromolecular Chemistry and Physics*, *208*(9), 1002–1010. https://doi.org/10.1002/macp.200700056

Selling, G. W., Woods, K. K., Sessa, D., & Biswas, A. (2008). Electrospun zein fibers using glutaraldehyde as the crosslinking reagent: Effect of time and temperature. *Macromolecular Chemistry and Physics*, *209*(10), 1003–1011. https://doi.org/10.1002/macp.200700606

Shan, C., Yang, H., Han, D., Zhang, Q., Ivaska, A., & Niu, L. (2010). Graphene/AuNPs/chitosan nanocomposites film for glucose biosensing. *Biosensors and Bioelectronics*, *25*(5), 1070–1074. https://doi.org/10.1016/j.bios.2009.09.024

Shan, D., Li, Q.-B., Ding, S.-N., Xu, J.-Q., Cosnier, S., & Xue, H.-G. (2010). Reagentless biosensor for hydrogen peroxide based on self-assembled films of horseradish peroxidase/laponite/chitosan and the primary investigation on the inhibitory effect by sulfide. *Biosensors and Bioelectronics*, *26*(2), 536–541. https://doi.org/10.1016/j.bios.2010.07.051

Shenoy, S. L., Bates, W. D., Frisch, H. L., & Wnek, G. E. (2005). Role of chain entanglements on fiber formation during electrospinning of polymer solutions: good solvent, non-specific polymer–polymer interaction limit. *Polymer*, *46*(10), 3372–3384. https://doi.org/10.1016/j.polymer.2005.03.011

Si, S., Liang, W., Sun, Y., Huang, J., Ma, W., Liang, Z., Bao, Q., & Jiang, L. (2016). Facile Fabrication of High-Density Sub-1-nm Gaps from Au Nanoparticle Monolayers as Reproducible SERS Substrates. *Advanced Functional Materials*, *26*(44), 8137–8145. https://doi.org/10.1002/adfm.201602337

Singh, A., Steely, L., & Allcock, H. R. (2005). Poly[bis(2,2,2-trifluoroethoxy)phosphazene] Superhydrophobic Nanofibers. *Langmuir*, *21*(25), 11604–11607. https://doi.org/10.1021/la052110v

Thakur, M. S., & Ragavan, K. V. (2013). Biosensors in food processing. *Journal of Food Science and Technology*, *50*(4), 625–641. https://doi.org/10.1007/s13197-012-0783-z

Tiwari, J. N., Vij, V., Kemp, K. C., & Kim, K. S. (2016). Engineered Carbon-Nanomaterial-Based Electrochemical Sensors for Biomolecules. *ACS Nano*, *10*(1), 46–80. https://doi.org/10.1021/acsnano.5b05690

Turasan, H., Barber, E. A., Malm, M., & Kokini, J. L. (2018). Mechanical and spectroscopic characterization of crosslinked zein films cast from solutions of acetic acid leading to a new mechanism for the crosslinking of oleic acid plasticized zein films. *Food Research International*, *108*, 357–367. https://doi.org/10.1016/j.foodres.2018.03.063

Turasan, H., & Kokini, J. L. (2017). Advances in Understanding the Molecular Structures and Functionalities of Biodegradable Zein-Based Materials Using Spectroscopic Techniques: A Review. *Biomacromolecules*, *18*(2), 331–354. https://doi.org/10.1021/acs.biomac.6b01455

Vogt, L., Liverani, L., Roether, J. A., & Boccaccini, A. R. (2018). Electrospun Zein Fibers Incorporating Poly(glycerol sebacate) for Soft Tissue Engineering. *Nanomaterials*, *8*(3), 150. https://doi.org/10.3390/nano8030150

Yan, H., Mahanta, N. K., Wang, B., Wang, S., Abramson, A. R., & Cakmak, M. (2014). Structural evolution in graphitization of nanofibers and mats from electrospun polyimide–mesophase pitch blends. *Carbon*, *71*, 303–318. https://doi.org/10.1016/j.carbon.2014.01.057

Yao, C., Li, X., & Song, T. (2007). Electrospinning and crosslinking of Zein nanofiber mats. *Journal of Applied Polymer Science*, *103*(1), 380–385. https://doi.org/10.1002/app.24619

Zhai, W.-L., Li, D.-W., Qu, L.-L., S. Fossey, J., & Long, Y.-T. (2012). Multiple depositions of Ag nanoparticles on chemically modified agarose films for surface-enhanced Raman spectroscopy. *Nanoscale*, *4*(1), 137–142. https://doi.org/10.1039/C1NR10956A

Zhang, H., Xi, S., Han, Y., Liu, L., Dong, B., Zhang, Z., Chen, Q., Min, W., Huang, Q., Li, Y., & Liu, J. (2018). Determining electrospun morphology from the properties of protein–polymer solutions. *Soft Matter*, *14*(18), 3455–3462. https://doi.org/10.1039/C7SM02203D

Zhao, W., Yalcin, B., & Cakmak, M. (2015). Dynamic assembly of electrically conductive PEDOT:PSS nanofibers in electrospinning process studied by high speed video. *Synthetic Metals*, *203*, 107–116. https://doi.org/10.1016/j.synthmet.2015.02.018

CHAPTER 6. A NOVEL BIODEGRADABLE ESERS (ENHANCED SERS) PLATFORM WITH DEPOSITION OF AU, AG AND AU/AG NANOPARTICLES ON GOLD COATED ZEIN NANOPHOTONIC STRUCTURES FOR THE DETECTION OF FOOD ANALYTES

Reprinted with permission. Full citation:
Ma, X., Turasan, H., Jia, F., Seo, S., Wang, Z., Liu, G. L., & Kokini, J. L. (2020). A novel biodegradable ESERS (enhanced SERS) platform with deposition of Au, Ag and Au/Ag nanoparticles on gold coated zein nanophotonic structures for the detection of food analytes. *Vibrational Spectroscopy*, *106*, 103013. https://doi.org/10.1016/j.vibspec.2019.103013. Copyright 2020 Elsevier.

6.1 Abstract

In this paper we studied the fabrication of a family of new biodegradable SERS sensors using a gold coated zein film with inverted pyramid structures that we had fabricated previously and coupled it with deposition of gold, silver and silver-shelled-gold nanoparticles. The proximity and contact between the gold surface and the new added nanoparticles help create new hot spots, which enhance the SERS intensity. Rhodamine 6G was used as the Raman active molecule to evaluate the SERS enhancement effect. Results revealed that different nanoparticles exhibit different SERS effects. Silver-shelled-gold nanoparticles gave the highest enhancement factor of 3 x10^5 followed by silver and gold nanoparticles relative to a glass surface. The enhancement factor of the new silver-shelled-gold nanoparticle decorated platform with the best performance relative to the gold coated zein nanophotonic structures is 10^2, a remarkable improvement. This sensitivity improvement takes the newly developed zein based biodegradable SERS biosensor platform one step closer to non-biodegradable sensors.

6.2 Introduction

Since Fleischman first used the roughened silver electrode to obtain the Raman spectra of pyridine molecules in 1974 (McQuillan, 2009), SERS has been widely used in mapping technology and single molecule detection (Chang et al., 2017; Chen et al., 2015; Gong et al., 2016; Kneipp et al., 2002; Prinz et al., 2016). The traditional SERS substrates include roughened metal electrodes, metal nanoparticles, roughened metal films, etc. In recent years, the three-dimensional

nanostructure complexes including bimetallic nanoparticles such as gold coated silver nanoparticles or hollow nanoparticles have emerged and widespread attention has been given to them due to their unique optical characteristics which contribute to the enhancement of the Raman signal (Li et al., 2016; Olea-Mejía et al., 2015; Zhang et al., 2016).

SERS is an excellent method for the detection of toxic and allergic food contaminants, due to its ability to detect very low concentrations of analytes, even single molecules (Lim et al., 2010). For example, with SERS, restricted antibiotics were detected with a limit of detection of 20 ppb (He et al., 2010), real-time monitoring of pesticides can be conducted directly on plant tissues (Yang et al., 2019) (Yang et al., 2016). In-situ SERS detection of three gram-positive bacteria, *Staphylococcus xylosus*, *Listeria monocytogenes*, and *Enterococcus faecium* was successfully conducted with limits of detections of 50, 100, and 100 CFU/mL, respectively (Qiu et al., 2016). Food adulterants, such as melamine, have been detected with very low limits of detection using SERS (Li et al., 2014). Pharmaceutical compounds can also be detected with limit of detection levels reaching ng/ml using nanostructured SERS platforms (Wu and T. Cunningham, 2014).

Despite these successful measurements, the use of synthetic polymers and plastics for the fabrication of SERS platforms is gradually becoming an issue from the sustainability point of view, as the used/disposed sensor platforms take many years to fully degrade in the environment. For this reason, in our group we are focusing on fabricating environmentally friendly, biodegradable green alternatives to the plastic-based biosensors (Gezer et al., 2016a; Jia et al., 2019a; Turasan et al., 2019). Our team has developed an innovative biodegradable protein-based SERS sensor platform using corn zein with replicating nanophotonic structures using soft lithography (Barber et al., 2019; Gezer et al., 2016b, 2016c, 2016a; Jia et al., 2019a). Briefly, the nanophotonic structures were first transferred to polydimethylsiloxane (PDMS) films from a PET master molds and coated with gold. Zein solutions were then cured on top of the gold coated PDMS films and peeled off, with excellent and unanticipated fidelity leading to a complete transfer of nanostructures and the gold layers. Out of inverted nanopyramid, nanopore and nanodome structures, inverted nanopyramids gave the highest enhancement factor of 10^4 relative to a flat glass surface. These zein based SERS sensors were then successfully used in the detection of acrylamide, a food toxin, and Ara h1 the main peanut allergen protein (Gezer et al., 2016b, 2016c).

In our recent study, we were able increase the SERS enhancement factor of zein-based SERS platforms twice, with the decoration of gold nanoparticles on the surface of gold coated nanostructured zein platforms (Jia et al., 2019a). This enhancement enabled detection of pyocyanin, the lethal toxin of water-borne pathogen *Pseudomonas aeruginosa*, from water with a detection level of 25 μM. Even though SERS enhancement factor of zein-based platforms was increased with the decoration of Au nanoparticles, there is still room for improving the sensitivity to match the sensitivity of plastic-based SERS platforms.

Another recent study confirms that SERS enhancement increases significantly when gold coated nanocup array SERS substrates were additionally decorated with metallic nanoparticles (Seo et al., 2018). Decoration of a gold layer coated flat surface with Au nanoparticles increased SERS signal 6 times relative to the gold layer coated flat surface while Au nanoparticle decoration onto a gold coated nanocup array instead of gold coated flat surface increased the SERS signal 25 times. This study shows, a more sensitive SERS biosensor platform can be achieved, due to a higher number of hotspot formation, by incorporating nanoparticles on the surface of nanostructured arrays.

The use of bimetallic nanostructures for SERS detections have been shown to have advantages over monometallic structures. Bimetallic nano-mushroom structures were created by orienting the growth of silver on the surface of DNA-modified gold nanoparticles, and the enhancement factor of 10^9 was achieved (Shen et al., 2015). When bimetallic core-shell nanoparticles of gold and silver were compared to monometallic gold or silver nanoparticles, the SERS enhancement factor was found to be the highest for gold core-silver shell nanoparticles (Pande et al., 2007, p. 200). Gold/silver core-shell nanorods were compared with gold nanorods for the SERS detection of human immunoglobulin G with a detection limit of 70 fM was achieved with gold/silver core-shell nanorods, which was 10^4 times lower than the limit of detection of gold nanorods (L. Wu et al., 2012).

The goal of the study is to further increase the sensitivity of nanostructured zein-based SERS platforms by decorating the surface with gold, silver and bimetallic silver-shelled-gold nanoparticles. The effects of surface decoration with silver, gold and silver-shelled-gold nanoparticles separately on the enhancement of the SERS intensity was investigated using

Rhodamine 6G as the Raman active molecule. In addition, the enhancement created by the same concentration of nanoparticles deposited on a glass surface was also studied to offer a comparison between the SERS performance of a non-biodegradable surface with a biodegradable sensor platform.

6.3 Materials and Methods

6.3.1 Materials

Ethyl Alcohol (140 Proof) was purchased from Decon Laboratories Inc. (King of Prussia, PA); Zein (Z3625), cysteamine (98%), glutaraldehyde (GDA) (25% in water solution) and Rhodamine-6G (R6G) were obtained from Sigma-Aldrich (St. Louis, MO); Oleic Acid (OA) (technical grade 90%) from Alfa Aesar (Ward Hill, MA); mono-diglyceride emulsifier (BFP 65K 1004200364) from Caravan Ingredients (Lenexa, KS); Acrylamide (98.5%) was purchased from Fisher Scientific (Pittsburgh, PA). Au and Ag nanoparticles with 20 nm diameters were purchased from Ted Pella Inc. (Redding, CS) at $7.0 * 10^{11}$ and $7* 10^{10}$ particles/ml concentrations, respectively. Silver shelled gold nanoparticles with a total diameter of 20 nm and a shell thickness of 6.4 nm were purchased from nanoComposix (San Diego, CA) at a concentration of $2.6 * 10^{13}$ particles/ml. To show the suspension stability of the nanoparticles, zeta potentials of the nanoparticles in deionized water were measured. The average zeta potentials were -30.0 mV, -47.17 mV, and -31.03 mV for silver-shelled-gold, silver and gold nanoparticles, respectively. These zeta potentials which are larger than -30 mV show that all nanoparticles repulse one another and the nanosized organization of the nanoparticles remains stable.

6.3.2 Preparation of zein films with inverted pyramid structures

Zein solutions were prepared following our methodology reported before (Barber, 2018). Briefly, the zein protein was dissolved in 70% ethanol at a 1:5 w/v ratio and heated to 62°C and oleic acid (OA) plasticizer and mono/diglyceride emulsifier were added. Then glutaraldehyde was added for crosslinking in the ratio of 4% glutaraldehyde to zein (w/w) stirred for 1 h, after heating to cool the solution to room temperature.

For the preparation of zein films with inverted pyramid structures, the gold coated PDMS films with positive pyramids with dimensions of $2 \times 2 \times 2.1$ μm were obtained from Dr. Logan Liu's laboratory at the University of Illinois and used as template (Gezer et al., 2016a, 2016b). Other aspects of this fabrication procedure were also discussed before. The zein solution mixture was then poured onto petri dishes with a 60 mm diameter with the PDMS template already in it. Then, zein films were peeled off from the PDMS template and complete transfer of nanostructures covered with gold onto zein was achieved. The final product consisted of zein films fabricated with inverted pyramid structures.

6.3.3 Decoration of different nanoparticles on the surface of zein films

The SERS effect of the deposition of different nanoparticles (gold, silver and silver-shelled-gold nanoparticles) chemically bound onto the surface of zein films with inverted pyramid structures was investigated. Cysteamine was used to fix the nanoparticles on the gold surface of zein films through its thiol group and an amine group at each end forming an Au-S bond. The amine group is positively charged while the three (Au, Ag and Au/Ag) nanoparticles are all negatively charged with the use of a citrate-capping layer and the amine group electrostatically attracts the nanoparticles (Barber, 2018). First, a 25 μL droplet of 100 mM cysteamine was placed on the surface of the gold coated zein films. The film was then left at room temperature for 2 h to allow cysteamine to bind to the gold layer. The film was then washed using milli-Q water to remove the excess unbonded and free cysteamine and dried with a stream of nitrogen gas for a firm linkage. Five consecutive drops of 20 nm gold nanoparticles solution (10 μL/drop, 7×10^{10} particles/mL) were then placed on the zein film to fabricate the gold coated nanoparticle added zein sensor. The sensor was placed in a petri dish, covered and placed in the refrigerator at a temperature of 4°C for 24 h (Barber, 2018) to enable bonding of gold nanoparticles to cysteamine. The zein sensors were then washed with milli-Q water and dried with nitrogen gas so that only the bonded nanoparticles remain on the sensor surface. The zein sensors decorated with 20 nm silver nanoparticles and 20 nm silver-shelled-gold nanoparticles followed the same procedure as gold nanoparticles.

6.3.4 SERS Detection of Rhodamine 6G

For the deposition of Rhodamine 6G (R6G) molecules on various platforms tested in this study, the drop deposition technique was used, following our previously developed method (Gezer et al., 2016a; Jia et al., 2019b; Turasan et al., 2019). To show the good distribution obtained with drop deposition technique, Raman spectra of R6G molecules were taken from multiple spots on a flat glass surface. The replications showed that drop deposition technique is a technique that gives reproducible results when measurements are conducted at many points along the dried R6G molecules.

First, Raman spectra of 10 mM Rhodamine 6G (R6G) was obtained directly on the glass slide, zein film with only nanophotonic structures and no gold, and zein film with nanophotonic structures and a 200 nm layer of gold, following our previously developed method (Gezer et al., 2016a). Then, in order to compare the effect of the deposition of nanoparticles on enhancement of SERS intensity, 0.1 mM R6G was placed on the surface of nanoparticle decorated zein sensors. Their SERS spectra with R6G were obtained and used for SERS enhancement factor calculation.

Raman and SERS spectra were collected using a Thermo Scientific DXR2 Raman Microscope. The laser used had a wavelength of 633 nm and a power of 2 mW. An objective lens with 50x magnification was used in Raman microscope. A 25 μm pinhole aperture was used to collect Raman scattering, which gave a total laser spot size of 1.3 μm. The Raman measurements were repeated 3 times and the averages were obtained using the OMNIC software.

6.3.5 Scanning Electron Microscopy

Scanning electron microscopy images of the samples were taken with a Nova NanoSEM 200, using ETD and TLD detectors to visualize the deposition of nanoparticles on the gold coated surface. 1 cm x 1 cm pieces were cut from samples and fixed on SEM discs with double sided tape. During imaging, working distance was kept in the range of 4.3 mm - 5.0 mm, with an accelerating voltage range of 5.00 kV- 10.00 kV and a spot size of 3.0 nm. No additional metal coating was applied to the samples, since all the imaged samples were already coated with a 200 nm thick gold layer.

6.4 Results and Discussion

6.4.1 Preparation of gold coated inverted pyramid zein films and their decoration with gold, silver and silver-shelled-gold nanoparticles

The fabrication process of the nanoparticle decorated nanostructured zein film sensor platforms and the detection of R6G using this platform is schematically illustrated in Figure 43. The fabrication of gold coated nanostructured zein films follows our earlier studies (Gezer et al., 2016a), where gold coated PDMS films with positive pyramid structures were used as the template to transfer the nanopyramid structures and the gold layer onto the zein film surface using soft lithography (Fig. 43a). After the 200 nm gold layer and the nanopyramid structures were transferred to cast zein films, as a new strategy 20 nm nanoparticles of gold, silver and silver-shelled-gold were used to decorate the surface of nanostructured zein films using cysteamine as a binding agent (Fig. 43b). The SERS enhancement as a result of the addition of different nanoparticles using R6G spectra were then used for SERS enhancement factor calculations (Fig. 43c).

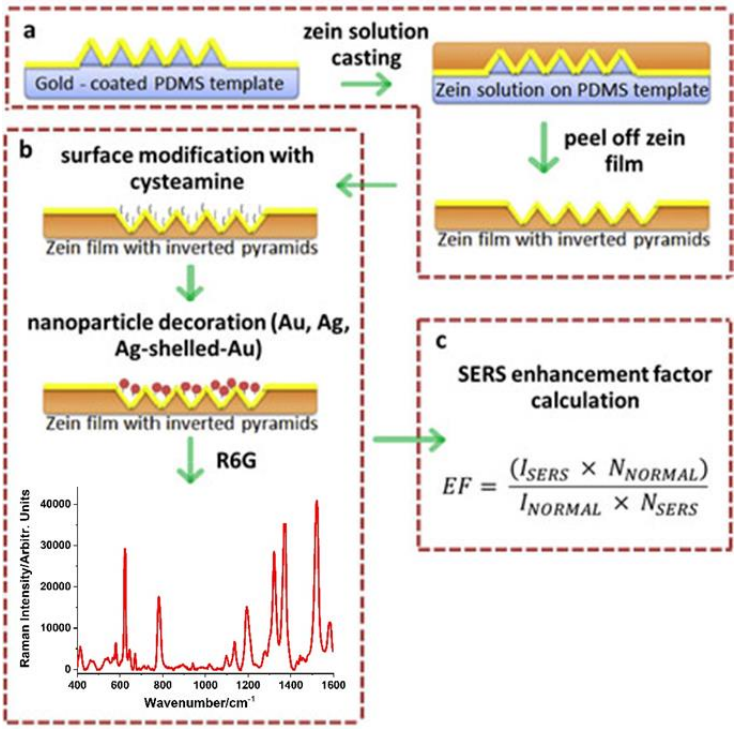

Figure 43. The diagram for fabrication of zein film sensor and its detection of R6G.

6.4.2 Characterization of the zein based SERS platforms with SEM imaging

The effectiveness of gold coated nanophotonic zein film preparation can be clearly seen (Fig. 44c), where the peeled off zein film contains the intact gold layer. Even though there are some regions around the edges of the zein film pieces where gold layer is scratched off during cutting and peeling, the inverted nanostructure region (red square in Fig. 44c) is coated with gold perfectly without any defects as was shown before (Barber, 2018; Gezer et al., 2016a). The fidelity of the transfer of the nanophotonic structures is further characterized with SEM imaging (Fig. 45). This gold coated zein surface was used for further decoration with gold, silver and silver-shelled-gold nanoparticles.

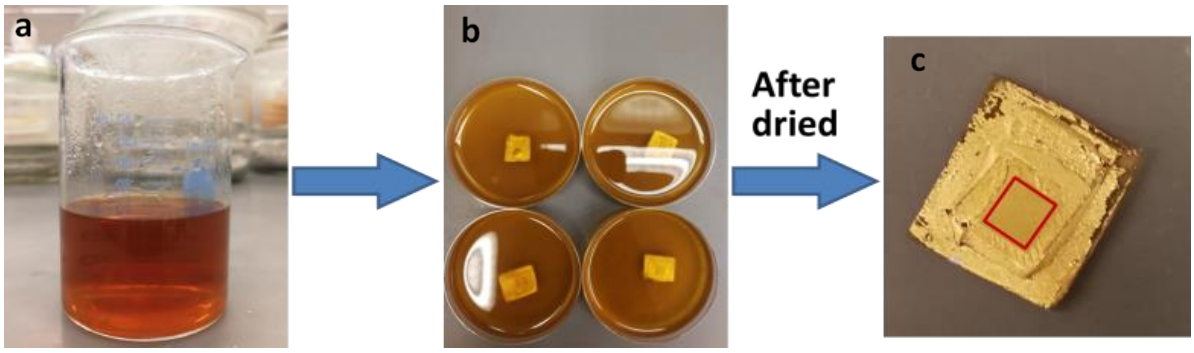

Figure 44. Photographs of the zein film preparation; a) zein solution before casting, b) zein solutions cast on gold coated PDMS films, c) peeled off zein films from PDMS layers with complete gold layer transfer. Red square shows the nanophotonic region on zein film surface.

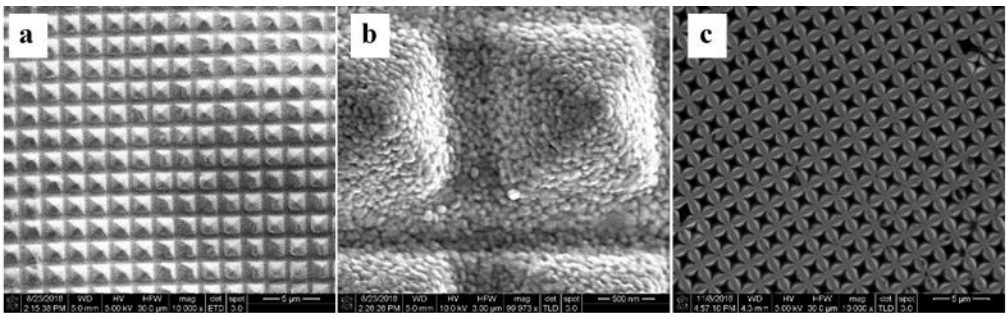

Figure 45. SEM images of PDMS based films with positive pyramid structures (a and b) and zein based films with inverted pyramid structures (c).

Figure 45 shows the SEM images of the gold coated PDMS template with positive pyramid structures (a and b) and a zein based film with inverted pyramid structures that is peeled off from that PDMS template (c). The nanostructures are transferred with great fidelity and are all arranged

in an orderly fashion consistent with our earlier work with this platform. Figure 45b shows the surface deposition of gold with a nano granular structure which should facilitate the formation of hot spots. The inverted pyramid structures along with the gold layer were also successfully transferred on the zein film from PDMS as before (Gezer et al., 2016a).

The three different 20 nm nanoparticles (gold nanoparticles, silver nanoparticles and silver-shelled-gold nanoparticles) were diluted to the same concentration of 7×10^{10} particles/mL and were used for decoration of the surface of gold coated zein based inverted pyramid structures to study the relative enhancement of the Raman signal. The effectiveness of the binding of nanoparticles was also studied using SEM images. Figure 46 shows the distribution of silver-shelled-gold nanoparticles on the surface of inverted pyramid structures. The SEM images show clustering of particles at different locations which brings them closer together in individual clusters rather than a uniform distribution of particles throughout the surface. The closeness of the particles facilitates the formation of hotspots and enhances the intensity of the Raman signal.

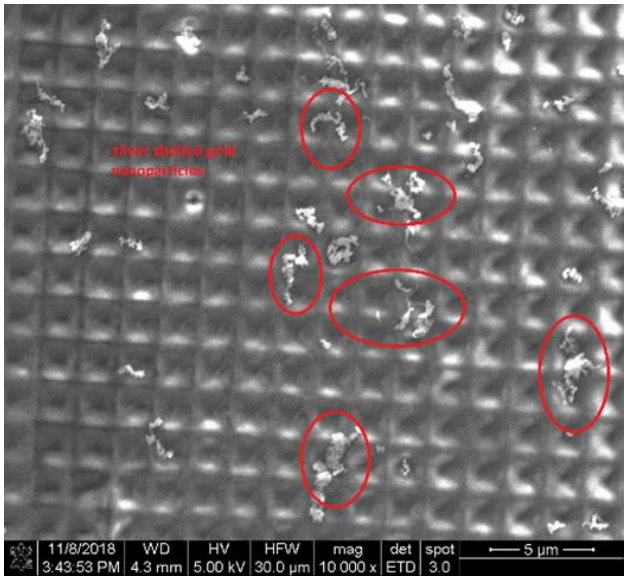

Figure 46. SEM images of silver-shelled-gold nanoparticles decorated on the surface of gold coated zein films with inverted pyramid structures.

6.4.3 SERS measurement of Rhodamine 6G on nanostructured, gold coated, nanoparticle decorated zein film sensor

First, Raman spectra of the nanoparticle decorated zein-based sensors were measured without Rhodamine 6G (R6G) to show the base signals of the sensors (Fig. 47). All the sensors show some of the characteristic peaks of cysteamine in the Raman spectra in low intensities located at 732 cm^{-1} (C-S stretching), 940 cm^{-1} (C-C-N stretching), 1030 cm^{-1} (C-C-N stretching), 2853 cm^{-1} (CH_2 stretching) and 2908 cm^{-1} (CH_2 stretching) due to the presence of cysteamine in the design of the sensors (Kudelski and Hill, 1999). Since cysteamine gives a peak of negligible intensity compared to Rhodamine 6G, it is of no consequence in the detection of R6G in this study.

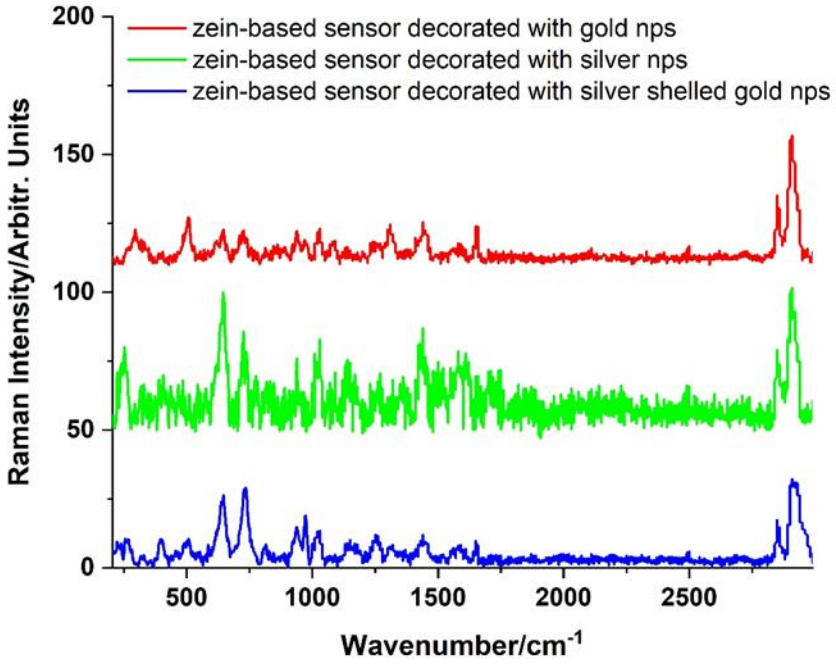

Figure 47. Raman spectra of 200 nm gold layer coated nanostructured zein-based sensors decorated with gold (red), silver (green), and silver shelled gold (blue) nanoparticles using cysteamine as the linker molecule.

Raman spectra of 10 mM Rhodamine 6G (R6G) on 1) a glass surface, 2) zein sensor surface with inverted nanophotonic structures and without any gold layer coating, and 3) zein sensor surface with 200-nm-thick gold layer coated inverted nanopyramid structures were measured to observe and compare the effects of nanostructures and the gold layer coated nanostructures (Fig. 48). R6G was used at a concentration of 10 mM since lower concentrations did not provide enough intensity

on samples without any gold addition. All three samples showed the characteristic peaks of R6G which are approximately located at 1513 cm^{-1}, 1364 cm^{-1}, 1314 cm^{-1}, 1183 cm^{-1}, 776 cm^{-1}, and 616 cm^{-1} but with different intensities when compared to each other. 10 mM R6G gave the lowest intensity peaks on the flat glass surface due to the absence of gold deposition and therefore no hotspot formation (Fig. 48A). Zein film with inverted nanostructures but without gold layer showed slightly higher intensities than flat glass surface due to the roughened surface with the nanostructure (Fig. 48B). The 200-nm-thick gold layer coated zein sensor surface with inverted nanostructures gave the highest intensities among these three samples, due to hotspot formation caused by the gold coated pyramid structures (Fig. 48C).

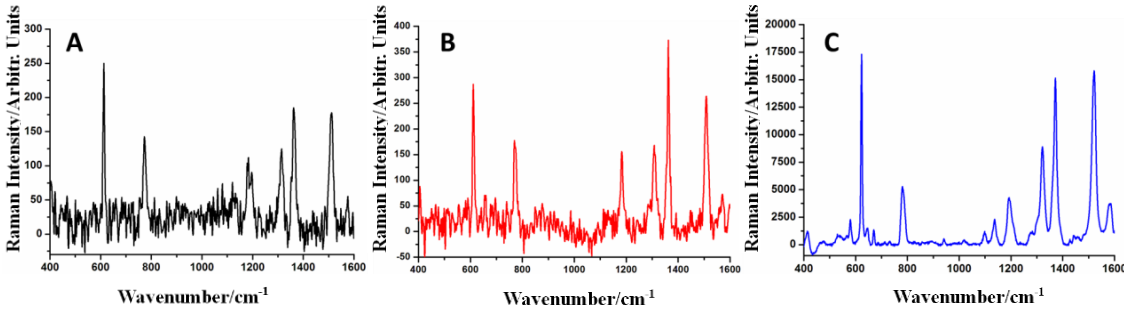

Figure 48. (A) Raman spectra of 10 mM R6G on a glass slide (B) SERS spectra of 10 mM R6G on zein film with only inverted pyramid structures but no layer of gold (C) SERS spectra of 10 mM R6G on zein film with both inverted pyramid structures and a 200 nm layer of gold.

To calculate the SERS enhancement factor (EF) obtained with gold coated zein sensor compared to the flat glass surface, Eqn. 10 was used using the intensities of the 1364 cm^{-1} peak as the basis for comparison.

$$EF = \left(I_{SERS} \times N_{NORMAL}\right) \Big/ \left(I_{NORMAL} \times N_{SERS}\right) \qquad \text{(Eqn. 10)}$$

I_{SERS} is the intensity of 1364 cm^{-1} peak of SERS measurement with 200-nm-thick gold layer coated zein sensor, and N_{SERS} is the number of R6G molecules on this area. I_{Normal} is the intensity of 1364 cm^{-1} peak on the flat glass surface without any gold deposition, and N_{Normal} is the number of R6G molecules on this area. For calculating N_{Normal} and N_{SERS}, the number of R6G molecules per unit

sensor area with and without nanoparticles was calculated and multiplied with the Raman laser area. The relative EF in was calculated to be 1.2×10^3.

SERS enhancement effects using 100 mM R6G for gold, silver and silver shelled gold nanoparticles on the gold coated nanostructured zein films are shown in (Fig. 49). Zein sensor decorated with silver-shelled-gold nanoparticles had the highest Raman enhancement, followed by the sensor decorated with silver nanoparticles. Zein sensor decorated with gold nanoparticles had the lowest enhancement effect among the three types of nanoparticles used.

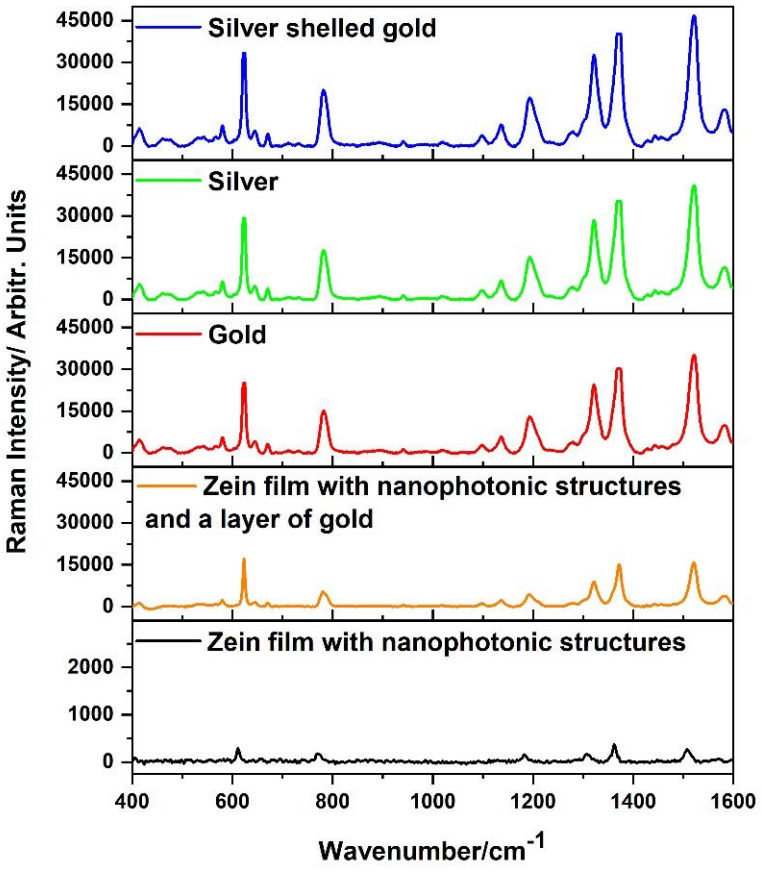

Figure 49. SERS measurement of 0.1 mM R6G using different nanoparticles decorated zein film sensor compared with zein film with inverted pyramid structures and a 200 nm layer of gold using 10mM of R6G (orange) and with the zein film with inverted pyramid structures (black).

To compare the SERS enhancements obtained with nanoparticle decorations only, enhancement factors for each type of nanoparticle decorated gold coated zein sensors were calculated in contrast

to gold coated zein sensors using Eqn. 10. The enhancement factor relative to the gold coated nanostructured zein surface was 3. 29×10^2 for silver-shelled-gold nanoparticles, 2.88×10^2 for silver nanoparticles and 2.46×10^2 for gold nanoparticles.

Figure 49 also shows the different nanoparticle enhancement factors compared with zein film with nanophotonic structures only and without gold coating. The enhancement factor for silver-shelled-gold nanoparticles was 1.26×10^4. It was 1.10×10^4 for silver nanoparticles and 0.95×10^4 for gold nanoparticles. The enhancement factor substantially increased with the addition of the three sets of nanoparticles compared with zein with inverted pyramids coated with a layer of 200 nm of gold. In order to compare the total zein film sensor ability as SERS substrate, we dropped three different nanoparticles directly on a glass slide and used it as the SERS substrate to detect R6G (Fig. 50). The enhancement factor calculated between the silver-shelled-gold nanoparticle decorated zein sensor and silver-shelled-gold nanoparticle decorated glass slide was 2.78×10^3 and was the highest among three types of nanoparticles. The enhancement was 2.69×10^3 and 2.12×10^3 for silver and gold nanoparticles respectively. The comparison of the enhancement factors shows the improvement of the Raman signal with the nanoparticle decorated nanophotonic structures on zein sensors.

In order to measure only the effect of nanophotonic structures, enhancement factors between the nanoparticle decorated 200 nm-gold layer-coated zein sensors were compared to those of nanoparticle decorated and 200 nm-gold layer coated flat glass slides (Fig. 50). The effect of nanophotonic structures were similar for all nanoparticle types. For the sensors decorated with silver and silver-shelled-gold nanoparticles the SERS signal was enhanced 2.02×10^3 and 1.99×10^3 times, respectively. For sensors decorated with gold nanoparticles, the nanophotonic structures enhanced the signal 1.50×10^3 times. These enhancement factors show the importance of nanophotonic structures imprinted on zein film surface in creating hotspots to increase the sensitivity of the sensors.

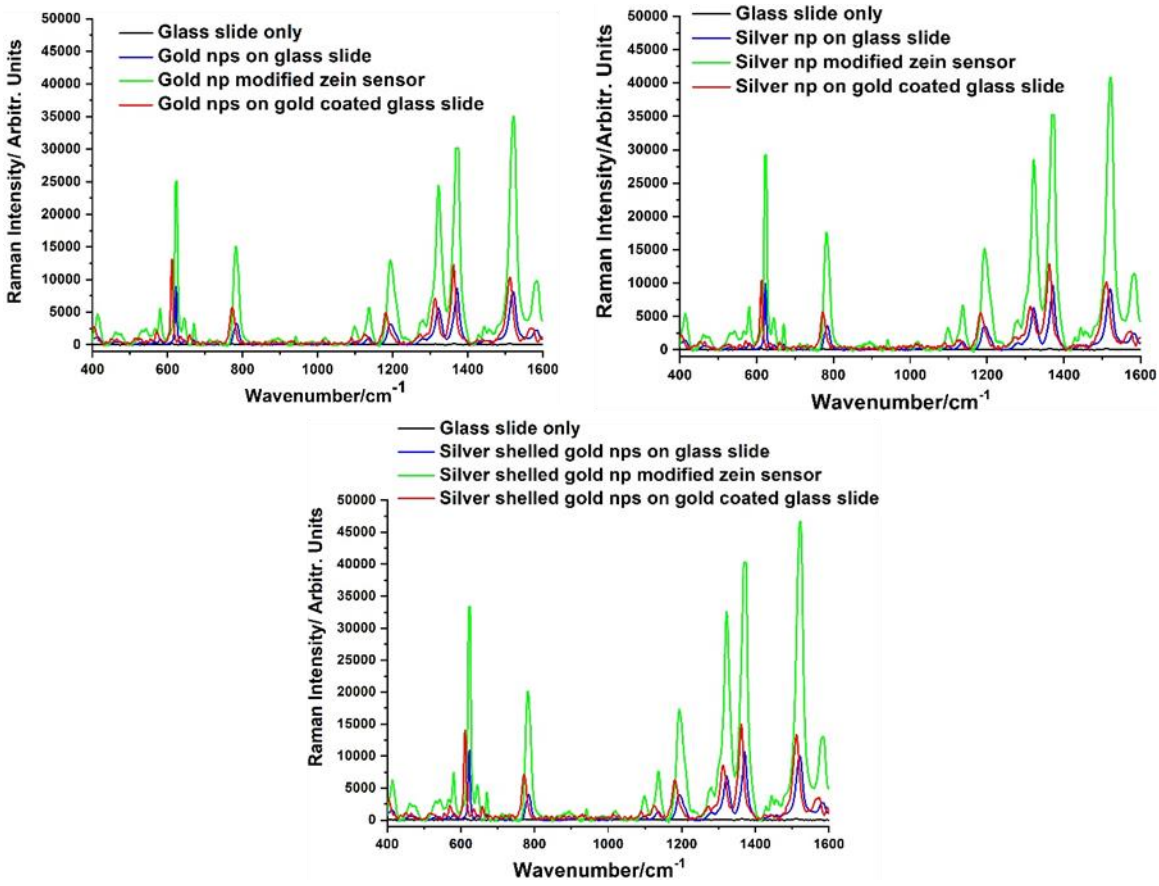

Figure 50. SERS intensity of Rhodamine 6G measured with nanoparticle decorated zein film sensors, nanoparticle decorated gold coated glass slides, nanoparticle decorated glass slides, and directly on glass slide.

The total enhancement factors of nanoparticle decorated zein sensor platforms were calculated using R6G spectra on a flat glass slide without any gold nanoparticles. The highest enhancement factor of 3.36×10^5 was obtained from silver-shelled-gold nanoparticle decorated zein sensor. Silver nanoparticle decorated zein sensor had a total enhancement factor of 2.94×10^5, and gold nanoparticle decorated zein sensor had a total enhancement of 2.51×10^5. All these total enhancements obtained with nanoparticle decorated zein sensor platforms are at least a decade higher than the previously obtained enhancement factor with gold coated nanostructured zein sensor (Gezer et al., 2016a).

The SERS enhancement factor obtained with the zein-based SERS biosensor platform in this paper is comparable to some of the other non-biodegradable SERS biosensor platforms. For example,

the SERS enhancement factor of Au nanorod-covered Fe_3O_4 microspheres used for the detection of a pesticide, thiram, was 2×10^5, which is very similar to the SERS enhancement of the zein-based SERS platform. In another study, Ag-Au bimetallic nanostructures were fabricated using a seeding technique and the highest SERS enhancement factor of 10^4 was obtained with gold ion to silver atom ratio of 4 (Zou et al., 2007), which is an order of magnitude lower than the zein based SERS platform enhancement factor in this paper. Bimetallic Ag-Au nanowires fabricated for the detection of a Raman active molecule, 4-MBA, in colloid solutions yielded SERS enhancement factors in the range of 10^6-10^7, slightly higher but still comparable to the SERS enhancement factor in this study (E. Hunyadi and J. Murphy, 2006). There are of course, studies achieving higher SERS enhancement factors with the use of bimetallic nanoparticles with unique structures, such as a SERS enhancement factor of 10^7 was obtained with bimetallic concave gold and palladium nanostar structures (Zhang et al., 2013). Au or Ag deposited GaN nanoflowers gave enhancement factors of 10^7 (Zhang et al., 2017). In the detection of *p*-aminothiophenol, Ag-Au bimetallic hollow nanostructures reached an enhancement factor of 10^8 (Wang et al., 2006), and the use of bimetallic Ag-Au nano-mushroom structures gave an enhancement factor of 10^9 (Shen et al., 2015). Despite their higher SERS enhancement factors, fabrication of these SERS platforms usually necessitates the use of non-biodegradable metal, plastic or glass. The major advantage and uniqueness of the platform in this study is that it is largely (>98%) biodegradable. The biodegradable zein-based SERS platform fabricated in this paper offers a more sustainable alternative for non-biodegradable SERS platforms.

6.4.4 Conclusions

This study aims to further increase the sensitivity of nanostructured zein-based SERS platforms by decorating the surface with gold, silver and bimetallic silver-shelled-gold nanoparticles to match the sensitivity of non-biodegradable, plastic-based SERS sensor platforms. The effects of silver, gold and silver-shelled-gold nanoparticles on the enhancement of the SERS intensity was investigated separately. Silver-shelled-gold nanoparticle decoration on the gold layer coated nanostructured zein platform gave the highest enhancement factor of 10^5 among all the nanoparticle types and made the SERS biosensor platform 100 times higher more sensitive than the previously developed zein based SERS platform (Gezer et al., 2016a). This sensitivity

improvement takes the newly developed zein based biodegradable SERS biosensor platform one step closer to non-biodegradable sensors and creates a new greener alternative.

6.5 Author Contributions

Ma, X.: Conceptualization, methodology, investigation, writing-original draft. **Turasan, H.:** Conceptualization, methodology, investigation, formal analysis, writing – original draft and review and editing. **Jia, F.:** Methodology. **Seo, S.:** Methodology. **Wang, Z:** Supervision. **Liu, G.L.:** Conceptualization and Resources. **Kokini, J.L.:** Conceptualization, methodology, resources, writing – review and editing, visualization, supervision, project administration, funding acquisition

6.6 References

Barber, E. A., Turasan, H., Gezer, P. G., Devina, D., Liu, G. L., & Kokini, J. (2019). Effect of plasticizing and crosslinking at room temperature on microstructure replication using soft lithography on zein films. *Journal of Food Engineering*, *250*, 55–64. https://doi.org/10.1016/j.jfoodeng.2019.01.018

Barber, Emma A. (2018). *Optimization of Zein Based Surface Enhanced Raman Spectroscopy Biosensor for the Detection of Gliadin as a Marker for Celiac Disease* [Purdue University]. https://docs.lib.purdue.edu/dissertations/AAI10844563

Chang, T.-W., Wang, X., Mahigir, A., Veronis, G., Liu, G. L., & Gartia, M. R. (2017). Marangoni Convection Assisted Single Molecule Detection with Nanojet Surface Enhanced Raman Spectroscopy. *Acs Sensors*, *2*(8), 1133–1138. https://doi.org/10.1021/acssensors.7b00427

Chen, H.-Y., Lin, M.-H., Wang, C.-Y., Chang, Y.-M., & Gwo, S. (2015). Large-Scale Hot Spot Engineering for Quantitative SERS at the Single-Molecule Scale. *Journal of the American Chemical Society*, *137*(42), 13698–13705. https://doi.org/10.1021/jacs.5b09111

E. Hunyadi, S., & J. Murphy, C. (2006). Bimetallic silver–gold nanowires: fabrication and use in surface-enhanced Raman scattering. *Journal of Materials Chemistry*, *16*(40), 3929–3935. https://doi.org/10.1039/B607116C

Gezer, P. G., Hsiao, A., Kokini, J. L., & Liu, G. L. (2016). Simultaneous transfer of noble metals and three-dimensional micro- and nanopatterns onto zein for fabrication of nanophotonic platforms. *Journal of Materials Science*, *51*(8), 3806–3816. https://doi.org/10.1007/s10853-015-9699-0

Gezer, P. G., Liu, G. L., & Kokini, J. L. (2016a). Development of a biodegradable sensor platform from gold coated zein nanophotonic films to detect peanut allergen, Ara h1, using surface enhanced raman spectroscopy. *Talanta*, *150*, 224–232. https://doi.org/10.1016/j.talanta.2015.12.034

Gezer, P. G., Liu, G. L., & Kokini, J. L. (2016b). Detection of acrylamide using a biodegradable zein-based sensor with surface enhanced Raman spectroscopy. *Food Control*, *68*, 7–13. https://doi.org/10.1016/j.foodcont.2016.03.002

Gong, T., Zhang, N., Kong, K. V., Goh, D., Ying, C., Auguste, J.-L., Shum, P. P., Wei, L., Humbert, G., Yong, K.-T., & Olivo, M. (2016). Rapid SERS monitoring of lipid-peroxidation-derived protein modifications in cells using photonic crystal fiber sensor. *Journal of Biophotonics*, *9*(1–2), 32–37. https://doi.org/10.1002/jbio.201500168

He, L., Lin, M., Li, H., & Kim, N.-J. (2010). Surface-enhanced Raman spectroscopy coupled with dendritic silver nanosubstrate for detection of restricted antibiotics. *Journal of Raman Spectroscopy*, *41*(7), 739–744. https://doi.org/10.1002/jrs.2505

Jia, F., Barber, E., Turasan, H., Seo, S., Dai, R., Liu, L., Li, X., Bhunia, A. K., & Kokini, J. L. (2019a). Detection of Pyocyanin Using a New Biodegradable SERS Biosensor Fabricated Using Gold Coated Zein Nanostructures Further Decorated with Gold Nanoparticles. *Journal of Agricultural and Food Chemistry*. https://doi.org/10.1021/acs.jafc.8b07317

Jia, F., Barber, E., Turasan, H., Seo, S., Dai, R., Liu, L., Li, X., Bhunia, A. K., & Kokini, J. L. (2019b). Detection of Pyocyanin Using a New Biodegradable SERS Biosensor Fabricated Using Gold Coated Zein Nanostructures Further Decorated with Gold Nanoparticles. *Journal of Agricultural and Food Chemistry*, *67*(16), 4603–4610. https://doi.org/10.1021/acs.jafc.8b07317

Kneipp, K., Kneipp, H., Itzkan, I., Dasari, R. R., Feld, M. S., & Dresselhaus, M. S. (2002). Nonlinear Raman Probe of Single Molecules Attached to Colloidal Silver and Gold Clusters. In V. M. Shalaev (Ed.), *Optical Properties of Nanostructured Random Media* (pp. 227–249). Springer Berlin Heidelberg. https://doi.org/10.1007/3-540-44948-5_11

Kudelski, A., & Hill, W. (1999). Raman Study on the Structure of Cysteamine Monolayers on Silver. *Langmuir*, *15*(9), 3162–3168. https://doi.org/10.1021/la9811463

Li, J.-M., Yang, Y., & Qin, D. (2014). Hollow nanocubes made of Ag–Au alloys for SERS detection with sensitivity of 10 −8 M for melamine. *Journal of Materials Chemistry C*, *2*(46), 9934–9940. https://doi.org/10.1039/C4TC02004A

Li, T., Vongehr, S., Tang, S., Dai, Y., Huang, X., & Meng, X. (2016). Scalable Synthesis of Ag Networks with Optimized Sub-monolayer Au-Pd Nanoparticle Covering for Highly Enhanced SERS Detection and Catalysis. *Scientific Reports*, *6*, 37092. https://doi.org/10.1038/srep37092

Lim, D.-K., Jeon, K.-S., Kim, H. M., Nam, J.-M., & Suh, Y. D. (2010). Nanogap-engineerable Raman-active nanodumbbells for single-molecule detection. *Nature Materials*, *9*(1), 60–67. https://doi.org/10.1038/nmat2596

McQuillan, A. J. (2009). The discovery of surface-enhanced Raman scattering. *Notes and Records of the Royal Society of London*, *63*(1), 105–109.

Olea-Mejía, O., Fernández-Mondragón, M., Rodríguez-de la Concha, G., & Camacho-López, M. (2015). SERS-active Ag, Au and Ag–Au alloy nanoparticles obtained by laser ablation in liquids for sensing methylene blue. *Applied Surface Science*, *348*, 66–70. https://doi.org/10.1016/j.apsusc.2015.01.075

Pande, S., Ghosh, S. K., Praharaj, S., Panigrahi, S., Basu, †, Jana, S., Pal, A., Tsukuda, T., & Pal, T. (2007). *Synthesis of Normal and Inverted Gold−Silver Core−Shell Architectures in β-Cyclodextrin and Their Applications in SERS*. https://doi.org/10.1021/jp0702393

Prinz, J., Heck, C., Ellerik, L., Merk, V., & Bald, I. (2016). DNA origami based Au–Ag-core–shell nanoparticle dimers with single-molecule SERS sensitivity. *Nanoscale*, *8*(10), 5612–5620. https://doi.org/10.1039/C5NR08674D

Qiu, L., Wang, W., Zhang, A., Zhang, N., Lemma, T., Ge, H., Toppari, J. J., Hytönen, V. P., & Wang, J. (2016). Core–Shell Nanorod Columnar Array Combined with Gold Nanoplate–Nanosphere Assemblies Enable Powerful In Situ SERS Detection of Bacteria. *ACS Applied Materials & Interfaces*, *8*(37), 24394–24403. https://doi.org/10.1021/acsami.6b06674

Seo, S., Chang, T.-W., & Liu, G. L. (2018). 3D Plasmon Coupling Assisted Sers on Nanoparticle-Nanocup Array Hybrids. *Scientific Reports*, *8*(1), 3002. https://doi.org/10.1038/s41598-018-19256-7

Shen, J., Su, J., Yan, J., Zhao, B., Wang, D., Wang, S., Li, K., Liu, M., He, Y., Mathur, S., Fan, C., & Song, S. (2015). Bimetallic nano-mushrooms with DNA-mediated interior nanogaps for high-efficiency SERS signal amplification. *Nano Research*, *8*(3), 731–742. https://doi.org/10.1007/s12274-014-0556-2

Turasan, H., Cakmak, M., & Kokini, J. (2019). Fabrication of zein-based electrospun nanofiber decorated with gold nanoparticles as a SERS platform. *Journal of Materials Science*, *54*(12), 8872–8891. https://doi.org/10.1007/s10853-019-03504-w

Wang, Y., Chen, H., Dong, S., & Wang, E. (2006). Surface-enhanced Raman scattering of silver-gold bimetallic nanostructures with hollow interiors. *The Journal of Chemical Physics*, *125*(4), 044710. https://doi.org/10.1063/1.2216694

Wu, H.-Y., & T. Cunningham, B. (2014). Point-of-care detection and real-time monitoring of intravenously delivered drugs via tubing with an integrated SERS sensor. *Nanoscale*, *6*(10), 5162–5171. https://doi.org/10.1039/C4NR00027G

Wu, L., Wang, Z., Zong, S., Huang, Z., Zhang, P., & Cui, Y. (2012). A SERS-based immunoassay with highly increased sensitivity using gold/silver core-shell nanorods. *Biosensors and Bioelectronics*, *38*(1), 94–99. https://doi.org/10.1016/j.bios.2012.05.005

Yang, T., Doherty, J., Guo, H., Zhao, B., Clark, J. M., Xing, B., Hou, R., & He, L. (2019). Real-Time Monitoring of Pesticide Translocation in Tomato Plants by Surface-Enhanced Raman Spectroscopy. *Analytical Chemistry*, *91*(3), 2093–2099. https://doi.org/10.1021/acs.analchem.8b04522

Yang, T., Zhang, Z., Zhao, B., Hou, R., Kinchla, A., Clark, J. M., & He, L. (2016). Real-Time and in Situ Monitoring of Pesticide Penetration in Edible Leaves by Surface-Enhanced Raman Scattering Mapping. *Analytical Chemistry*, *88*(10), 5243–5250. https://doi.org/10.1021/acs.analchem.6b00320

Zhang, C., Jiang, S. Z., Yang, C., Li, C. H., Huo, Y. Y., Liu, X. Y., Liu, A. H., Wei, Q., Gao, S. S., Gao, X. G., & Man, B. Y. (2016). Gold@silver bimetal nanoparticles/pyramidal silicon 3D substrate with high reproducibility for high-performance SERS. *Scientific Reports*, *6*, 25243. https://doi.org/10.1038/srep25243

Zhang, L.-F., Zhong, S.-L., & Xu, A.-W. (2013). Highly Branched Concave Au/Pd Bimetallic Nanocrystals with Superior Electrocatalytic Activity and Highly Efficient SERS Enhancement. *Angewandte Chemie International Edition*, *52*(2), 645–649. https://doi.org/10.1002/anie.201205279

Zhang, M.-R., Jiang, Q.-M., Wang, Z.-G., Zhang, S.-H., Hou, F., & Pan, G.-B. (2017). Three-dimensional gallium nitride nanoflowers supports decorated by gold or silver nanoparticles to fabricate surface-enhanced Raman scattering substrates. *Sensors and Actuators B: Chemical*, *253*, 652–659. https://doi.org/10.1016/j.snb.2017.07.002

Zou, X., Ying, E., & Dong, S. (2007). Preparation of novel silver–gold bimetallic nanostructures by seeding with silver nanoplates and application in surface-enhanced Raman scattering. *Journal of Colloid and Interface Science*, *306*(2), 307–315. https://doi.org/10.1016/j.jcis.2006.10.084

CHAPTER 7. FABRICATION AND VALIDATION OF ULTRASENSITIVE BIODEGRADABLE ELECTROSPUN ZEIN NANOFIBER-BASED SERS SENSOR FOR ACRYLAMIDE DETECTION

7.1 Abstract

In this paper, a biodegradable, environmentally friendly, ultrasensitive new electrospun zein nanofiber-based surface enhanced Raman spectroscopy (SERS) biosensor platform was fabricated, tested and validated using acrylamide. The effects of gold, silver, and silver shelled gold nanoparticles, as well as the physical mixture of gold and silver nanoparticles, on the SERS signal enhancement of rhodamine 6G was first studied. Silver shelled gold nanoparticles gave the highest SERS enhancement factor of 2.49×10^6, the highest enhancement factor ever reported for a zein based biodegradable platform. Detection of a carcinogenic food contaminant with this platform showed that the limit of detection was 1.2 ng/mL, a concentration much lower than the threshold for toxicity of acrylamide. This sensitivity is much lower than any other previous attempts to detect acrylamide with biodegradable sensors.

7.2 Introduction

Pathogen and/or toxin detection methods must be reliable highly sensitive, rapid and inexpensive in order to be useful. Surface enhanced Raman spectroscopy (SERS) enables highly sensitive detection of various analytes that are important to the food chain (Jia et al., 2019b; Lin and He, 2019; Liu et al., 2017; Neng et al., 2018; Tu et al., 2019; Wijaya et al., 2014) . Target molecules in the vicinity of nanostructured noble metals used in SERS greatly enhance Raman scattering as high as 10 to 11 orders of magnitude (Eustis and A. El-Sayed, 2006; Gezer et al., 2016a; Maruoka et al., 2017; Seo et al., 2018; Xu et al., 2011). Noble metals, such as gold, silver, copper and platinum, in different geometries, such as nanoparticles, nanorods, nanostars, nanopyramids, or nano-mushrooms have been used in SERS measurements for the sensitive detection of biological analytes (Baruah et al., 2018; Dowgiallo and Guenther, 2019; Gezer et al., 2016a; Lin and Stanciu, 2018; Orendorff et al., 2006; Sankar et al., 2018; Shen et al., 2015). For example, among gold and silver nanorods with varying aspect ratios between 1 and 16, silver nanorods with an aspect ratio of 10 and gold nanorods with an aspect ratio of 1.7 were shown to have the highest SERS

enhancement factors of 10^7 and 10^5, respectively (Orendorff et al., 2006). Nano-mushroom structures fabricated using gold stipes and silver caps gave an enhancement factor of 10^9 (Shen et al., 2015). When bimetallic core-shell spherical nanoparticles of gold and silver were compared to monometallic spherical gold or silver nanoparticles the SERS enhancement factor was found the be the highest for Au core-Ag shell nanoparticles (Pande et al., 2007). A synthetic dye, rhodamine B, in hot sauce samples were detected with SERS using Au core-Ag shell nanoparticles with a limit of detection of 2.4 ng/mL (Wang et al., 2015). Au-Ag nanoparticles with worm-like chain structures were used for the SERS detection of thiram, a pesticide, on apples and the limit of detection was found to be 24.04 ng/mL (Jiao et al., 2019).

In our earlier work, we tested the detection of acrylamide in solution, deposited on an inverse pyramid gold coated ordered nanostructures cast on zein. When this platform was used to conduct SERS measurements, a limit of detection of 10 μg/ml was obtained. Similarly, these renewable zein film-based SERS platforms were also successfully used to detect a peanut allergen, Ara h1, and pyocyanin, the toxin secreted by the microorganism *Pseudomonas aeruginosa* (Gezer et al., 2016c; Jia et al., 2019b).

The aim of this research is to fabricate and test a new, highly sensitive, zein electrospun nanofiber-based flexible SERS platform by decorating with 1) gold, 2) silver, 3) mixture of gold and silver or 4) bimetallic silver shelled gold (Au-in-Ag) spherical nanoparticles. This approach leads to facile and versatile fabrication of SERS platforms which are renewable and mostly biodegradable. In addition, the noble metal concentration is greatly reduced compared to our earlier attempts with gold coated inverted pyramid zein SERS platforms. Because zein is soluble in 70% ethanol the noble metal part of the sensor can be easily recoverable and can be used again (Jia et al., 2019b). The electrospun nanofiber form factor is ideal for sensitivity enhancement as the fibers offer the highest surface to volume ratio. Hence the nanomat form factor substantially enhances the surface area to capture contaminants and help enhance their detection sensitivity with various metal nanoparticles, which in this research include gold, silver, mixture of gold and silver, and bimetallic silver shelled gold spherical nanoparticles to decorate the surface of zein nanofibers. Acrylamide is chosen as the model food carcinogen to test the limit of detection of the new zein nanofiber-

based SERS platform and compared with our previous study (Gezer et al., 2016b). This approach is new and has never been taken before with electrospun renewable protein platforms.

7.3 Materials and Methods

7.3.1 Materials

Zein was purchased from Sigma Aldrich. Glacial acetic acid used as the solvent for zein, aqueous glutaraldehyde solution (25%) used for crosslinking, Rhodamine 6G, and acrylamide were purchased from Fisher Scientific. Gold (Au) and silver (Ag) nanoparticles (20 nm) were purchased from Ted Pella Inc. (Redding, CS) at a concentration of 7.0×10^{11} and 7×10^{10} particles/ml, respectively. Silver shelled gold nanoparticles (Au-in-Ag) were purchased from nanoComposix (San Diego, CA) at a concentration of 2.6×10^{13} particles/ml. The average zeta potentials of nanoparticle colloids (Au nanoparticles: -31 mV, Ag nanoparticles: -47 mV, Au-in-Ag nanoparticles: -30 mV) show that these nanoparticles exhibit excellent suspension stability and electrical repulsion with no aggregation, since all the zeta potentials are equal to or larger than -30 mV.

7.3.2 Nanofiber mat preparation from crosslinked zein

To fabricate nanofibers, first, glutaraldehyde solutions (25%) were used to crosslink zein for better electrospinning performance and higher hydrophobicity to enable concentrating nanoparticles (Turasan et al., 2019). Glutaraldehyde solutions were kept in the fume hood for the evaporation of the water overnight. Then zein solution was prepared in the same beaker containing glutaraldehyde by mixing zein with glacial acetic acid at a concentration of 26 wt%. Then the solution was electrospun at 20 kV using a needle with an inner diameter of 0.381 mm with a needle to collector distance of 10 cm. 5 in Hg pressure was used during electrospinning and the fibers were collected either on aluminum sheets for SEM imaging and on glass slides for SERS measurements. After the collection of the electrospun fibers, they were heated in the oven for 10 minutes at 140 ℃ to further enhance the crosslinking and to evaporate the remaining solvent in the nanofibers. The heated nanofibers were then kept in desiccators containing Drierite until they were completely dry.

7.3.3 Zein nanofiber mat decoration with nanoparticles

Three consecutive droplets (2 μl) of nanoparticle colloids were placed on the nanofiber mats, with drying steps in between (Turasan et al., 2019). For the decoration of nanofibers, 4 different nanoparticle solutions consisting of 20 nm Au nanoparticles, 20 nm Ag nanoparticles, a mixture of 20 nm Ag and Au (Au+Ag) nanoparticles with a ratio of (1:1), and 20 nm Au-in-Ag nanoparticles were used. The nanoparticle concentrations were kept constant (7×10^{10} particles/mL) for uniformity and comparison. Four (4) concentrations of Au-in-Ag nanoparticles were used (2.6×10^{10}, 2.6×10^{11}, 2.6×10^{12}, 2.6×10^{13} particles/mL) for the concentration optimization tests. When comparing SERS enhancement of nanoparticle types the nanoparticle concentrations were kept constant at 7×10^{10} particle/mL. Nanoparticle decorations were done similarly using the 3-droplet method.

7.3.4 Scanning electron microscopy

Mats were imaged using a Nova NanoSEM 200 Scanning Electron Microscope. To provide electrical conductance, zein nanofibers were collected on aluminum foil during electrospinning. The samples having a dimension of 1cm x 1cm were first coated with a platinum/palladium mixture for 60 seconds using a sputter coater (Cressington 208 HR), and then imaged at a voltage of 5 kV with a working distance of 3-6 mm.

7.3.5 SERS measurements

Raman spectra of all the samples were obtained using a DXR2 Raman Microscope (ThermoFisher). Rhodamine 6G (R6G) (100 μM) was used as the Raman active molecule, and the SERS enhancement factors were calculated from each nanoparticle colloid type (Turasan et al., 2019). The R6G deposition on the zein nanofiber mats were carried out using the drop deposition technique. This technique was shown to provide a good distribution of R6G molecules on SERS biosensor platforms and to obtain reproducible spectra (Ma et al., 2020). First, two consecutive droplets (2 μl) of nanoparticle colloids were deposited onto the same spot on the nanofiber mats, with a drying step in between droplet depositions (section 5.3.3). For the third droplet, nanoparticle colloid and R6G solution were mixed and a droplet (2 μl) from this mixture was deposited onto the same spot of nanofiber mats. The concentration of R6G in the third droplet is kept constant

(100 μM). The Raman spectra were collected for a range of 200-3600 cm^{-1} using a 633 nm laser at 6 mW laser power, a 50-slit aperture, and a 10x objective lens. Fluorescence correction was used to eliminate protein fluorescence. Minimum of 5 spectra were collected from different locations and averaged using OMNIC software. Each individual spectrum was collected 15 times with an exposure time of 1s, adding up to a total of 5×15 replications for each formulation.

For the optimization of nanoparticle concentration, four concentrations of Au-in-Ag nanoparticles were used (2.6×10^{10}, 2.6×10^{11}, 2.6×10^{12}, 2.6×10^{13} particles/mL). The decoration of these nanoparticles was done similarly (3 consecutive 2 μl droplets, with last droplet containing 100 μM R6G). For Raman measurements, same operational parameters were used, except for the laser power and the aperture. Since, 6 mW of laser power combined with a 50-slit aperture caused a CCD overflow, these parameters were changed to 3 mW and 25 μm pinhole aperture.

7.3.6 Detection of acrylamide with zein nanofiber-based SERS platforms

First, to determine the characteristic peaks of acrylamide, a high concentration of 0.5 g/mL acrylamide solution was dried on a glass slide and Raman spectra of it was taken. After preparation of crosslinked zein nanofibers (as explained in section 2.2), first a 2 μl of colloidal nanoparticles (2.6×10^{12} particles/mL) was placed on the nanofiber mat and dried for 1 h. After the first droplet of nanoparticle droplet dried, a second droplet of 2 μL of nanoparticles was placed on the same spot on the nanofibers mats and dried for another hour. Lastly, acrylamide solutions prepared at varying concentrations, including 100 μg/mL, 10 μg/mL, 1 μg/mL, and 100 ng/mL, 10 ng/mL were placed on the same spot on decorated zein nanofiber mats and dried for another hour. For Raman measurements, same operating parameters were used but the laser power and the aperture were optimized to 2.5 mW and 25 μm pinhole.

7.4 Results and Discussion

7.4.1 Organization and morphology of different nanoparticles used for surface decoration of zein nanofiber mats

SEM images of nanoparticle decorated zein nanofibers mats are shown in Figure 51. Each type of nanoparticles (Ag, Au, Au+Ag, Au-in-Ag) exhibit some differences in distribution on the surface

of the nanofibers: The nanofibers decorated with gold (Au) exhibit uniform distribution of nanoparticles (Figure 51a). Silver (Ag) nanoparticles were also distributed uniformly on the nanofiber surfaces however, the number of nanoparticles seems significantly less than the Au nanoparticles (Figure 51b). When Au+Ag nanoparticles were used for decoration, a similar qualitative distribution with Ag nanoparticles was observed. This distribution was qualitatively closer to the distribution of Ag nanoparticles rather than Au nanoparticle distribution, with slightly more nanoparticles on the surface of nanofibers when compared to Ag nanoparticles alone possibly due to the existing Au nanoparticles in the mixture (Figure 51c). In the presence of silver nanoparticles, gold nanoparticles image very differently and are not as clearly visible as they were in Figure 51a. This difference between the decoration of Au and Ag nanoparticles might be due to the interaction between these metals and zein. It would be expected that the higher surface energy of Au (~1500 mJ/m^2) allows for a stronger adhesion of Au nanoparticles than Ag nanoparticles, which have lower surface energy (~1250 mJ/m^2) (Gezer et al., 2016a; Vitos et al., 1998). During the drying of colloid droplets on the surface of the mats, the less strongly bound Ag nanoparticles are possibly moving through the gaps between nanofibers, leaving fewer particles on the uppermost layer.

Another reason why the visibility of gold nanoparticles is better than silver nanoparticles could be the better secondary electron yield of gold. Secondary electron emission yield (number of secondary electrons emitted per incident electron) of gold (0.70) is higher than silver (0.40) at an acceleration voltage of 5 kV, used in SEM imaging (Walker et al., 2008). The higher secondary electron emission yield of gold leads to a much brighter appearance of gold nanoparticles compared to silver nanoparticles.

In the case of Au-in-Ag nanoparticles (Figure 51d), the distribution was similar to the Au nanoparticle distribution. The distribution of Au-in-Ag nanoparticles showed a slightly larger aggregates distribution than the rest of the nanoparticle aggregate distributions. This clustering of nanoparticles is mostly seen where the nanofibers merge, which creates a bigger surface area for nanoparticles to attach themselves. The larger the aggregates after drying the greater the number of particles that are close enough to one another for SERS enhancement the more intense the hotspots would be which would result in greater enhancement.

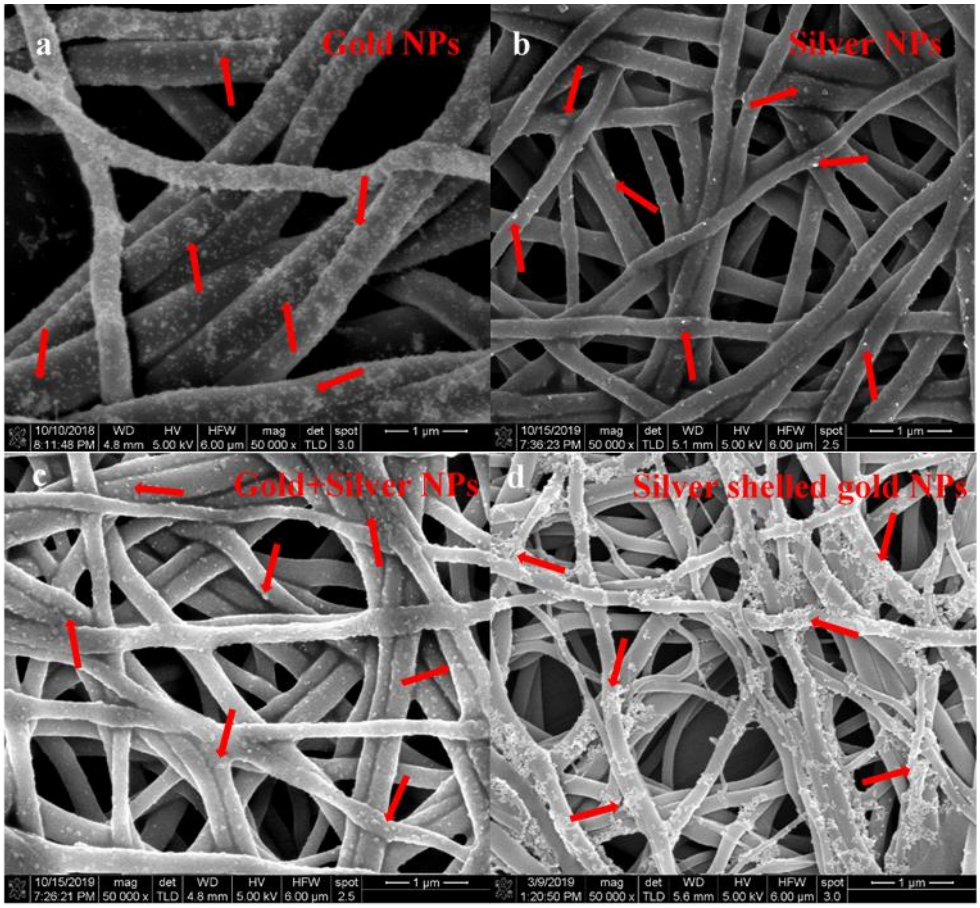

Figure 51. SEM image of electrospun zein nanofibers decorated with (a) Au nanoparticles, (b) Ag nanoparticles, (c) Au+Ag nanoparticles, (d)Au-in-Ag nanoparticles.

7.4.2 Effect of different nanoparticles on SERS enhancement of zein nanofiber mats

Figure 52 shows the Raman spectra of Rhodamine 6G (R6G) measured with zein nanofiber-based platforms decorated with Au, Ag, Au+Ag or Au-in-Ag nanoparticles at a fixed concentration of 7 $\times$ 10^{10} particle/mL. To calculate the total enhancement of nanoparticle decorated zein nanofiber mats, the SERS signals were compared to Rhodamine 6G (R6G) signal measured on a flat glass surface at a concentration of 0.1 M, following our previous method (Turasan et al., 2019). The drying of R6G droplets on the glass slide left a somewhat nonuniform pattern where the ring appeared to be more concentrated (Gezer et al., 2016b). In a previous study we showed that SERS spectra obtained from these locations still provide consistent replications and reproducible data (Ma et al., 2020). The SERS enhancement was calculated using, Eqn. 11 below (Gezer et al., 2016a; Turasan et al., 2019).

$$\text{Enhancement Factor} = \frac{I_{SERS} \times N_{Normal}}{I_{Normal} \times N_{SERS}} \qquad \text{(Eqn. 11)}$$

where I_{SERS} and I_{Normal} are the intensities obtained from SERS and non-SERS (glass surface) Raman experiments, while N_{SERS} and N_{Normal} are the number of R6G molecules contributing to these signals, respectively (Chang et al., 2014; Liu et al., 2011). R6G signature peaks were observed at 1652 cm^{-1}, 1511 cm^{-1}, 1362 cm^{-1}, 1313 cm^{-1}, 1185 cm^{-1}, 776 cm^{-1}, and 614 cm^{-1}. For the enhancement factor calculations the distinct and most intense Raman signal at 614 cm^{-1} as well as the peak at 1362 cm^{-1} was used as was done before (Turasan et al., 2019). The enhancement factors obtained from these two peaks are compared and shown in Table 9.

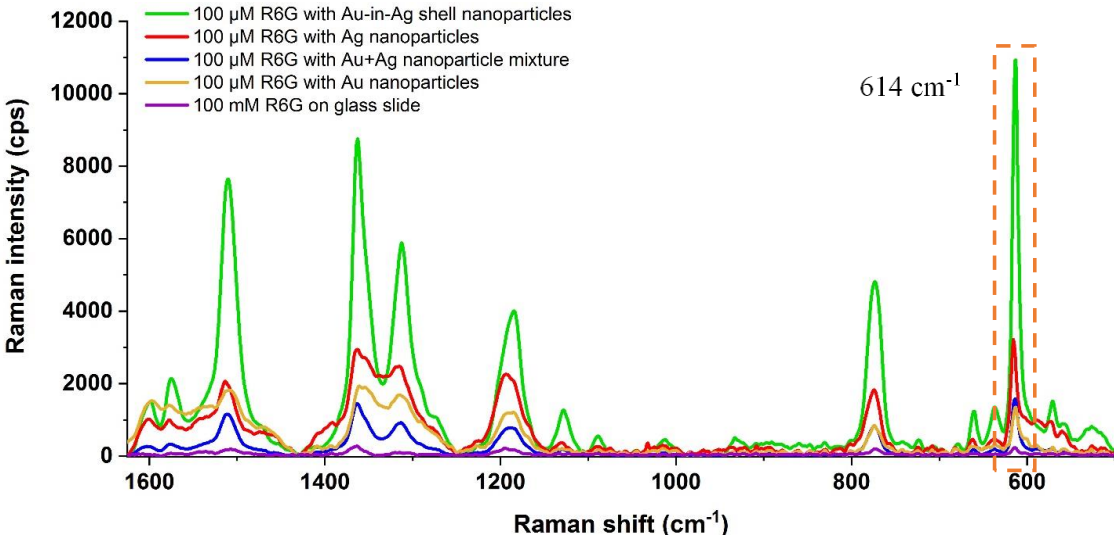

Figure 52. SERS enhancements obtained with Rhodamine 6G using different types of nanoparticles for decorating the surface of zein nanofiber platform.

Table 9 shows that the SERS signals obtained at both 614 cm^{-1} peak and at 1362 cm^{-1} peak with Au-in-Ag nanoparticles were significantly higher than the rest of the nanoparticles, with the highest enhancement factor of 4.16×10^5 obtained at 614 cm^{-1} peak and 2.87×10^5 obtained at 1362 cm^{-1} peak. The second highest SERS signal was obtained with Ag nanoparticles with an enhancement factor of 1.22×10^5 calculated from the 614 cm^{-1} peak and 0.96×10^5 from the 1362 cm^{-1}. Au nanoparticles and the mixture of Ag and Au nanoparticles (Au+Ag) gave similar SERS intensities throughout the spectra as shown in Table 9.

Table 9. SERS enhancement factors of different types of nanoparticles calculated based on 614 cm^{-1} and 1362 cm^{-1} peaks separately.

	SERS Enhancement Factor based on 614 cm^{-1} peak	**SERS Enhancement Factor based on 1362 cm^{-1} peak**
Au-in-Ag nanoparticles	4.16×10^5	2.87×10^5
Ag nanoparticles	1.22×10^5	0.96×10^5
Au+Ag nanoparticles	6.04×10^4	4.75×10^4
Au nanoparticles	5.14×10^4	6.34×10^4

The higher SERS signal enhancing capacity of Ag nanoparticles over Au nanoparticles is due to the higher surface plasmon strength of Ag compared to Au (Rycenga et al., 2011). Ag has the highest plasmonic activity (quality factor, Q) among various metals including Au, Al, Cu, Li, Pd and Pt, across a wider excitation wavelength spectrum, and a higher capability of enhancing the Raman signals. The findings in this study are consistent with the earlier results, such that Raman enhancement of R6G was significantly higher with Ag nanoparticles. Consistent with results in this study, it has been shown that bimetallic nanoparticles exhibit higher SERS enhancement than monometallic nanoparticles (Pande et al., 2007; Wang et al., 2015). This enhanced ability of bimetallic nanoparticles is considered to be due to the synergistic effects of Ag and Au in one structure (Bai et al., 2017; Farrokhpour and Ghandehari, 2019; Hong et al., 2011). When an Ag layer is surrounding Au layer the plasmonic activity of Au can be augmented with the Ag layer, leading to higher signals (Rycenga et al., 2011). Since Au-in-Ag nanoparticles gave the highest enhancement in this study, they were tested for acrylamide detection.

7.4.3 Effect of nanoparticle concentration on surface decoration of zein nanofiber mats

The concentration of nanoparticles on the surface of the nanofibers is very important, since hotspots form between the nanoparticles to enhance the SERS signal and their closeness up a distance of 10 nm defines the intensity of the hotpots (H.-Y. Wu et al., 2012). The effect of nanoparticle concentration in the colloid solution on the distribution of nanoparticles is shown in Figure 53 using Au-in-Ag nanoparticles at four different concentration one order of magnitude apart; 2.6×10^{13}, 2.6×10^{12}, 2.6×10^{11}, and 2.6×10^{10} particles/mL. Decreasing the concentration

of nanoparticles decreased the number of nanoparticles on the surface of the nanofibers. At the highest concentration of nanoparticles (2.6×10^{13} particles/mL), the very high number of nanoparticles created extremely dense clustering (Figure 53a), bringing the particles too close together. Decoration at a concentration of 2.6×10^{12} particles/mL gave the second highest number nanoparticles on the surface of the fibers (Figure 53b). The clustering of nanoparticles appears somewhat less than 2.6×10^{13} particles/mL concentration. The presence of distinct individual particles close to one another favors the formation of hotspots to enhance the SERS signal of analytes (Turasan et al., 2019).

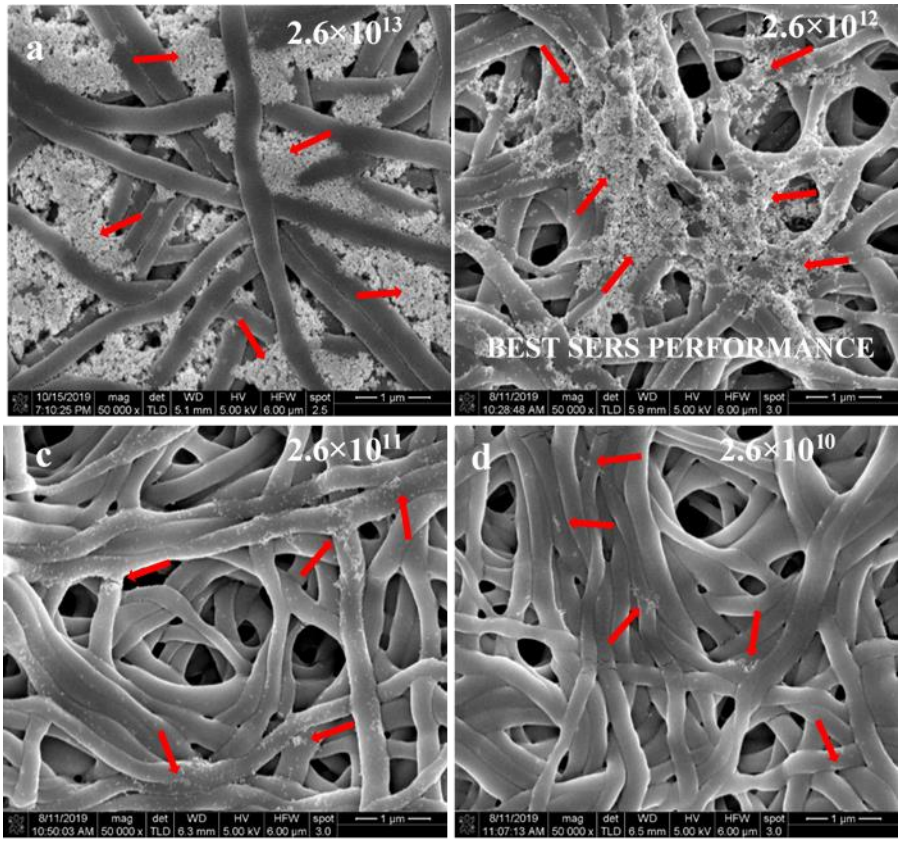

Figure 53. SEM images of zein nanofibers decorated with Au-in-Ag nanoparticles at a concentration of 2.6×10^{13} particle/mL (a), 2.6×10^{12} particle/mL (b), 2.6×10^{11} particle/mL (c), and 2.6×10^{10} particle/mL (d). Arrows are used to highlight the locations of nanoparticles.

To show the reproducibility of this changing nanoparticle aggregation behavior with the two highest concentrations, same concentration of Au-in-Ag nanoparticles were drop deposited on aluminum sheets and SEM images were taken and are shown in Figure 54. Very similar

nanoparticle behaviors were observed, where a concentration of 2.6×10^{13} particles/mL created highly compact nanoparticle clusters where there is complete contact between the nanoparticles, and 2.6×10^{12} particles/mL created fewer compact aggregates with some individual nanoparticles, favoring the hotspot formation.

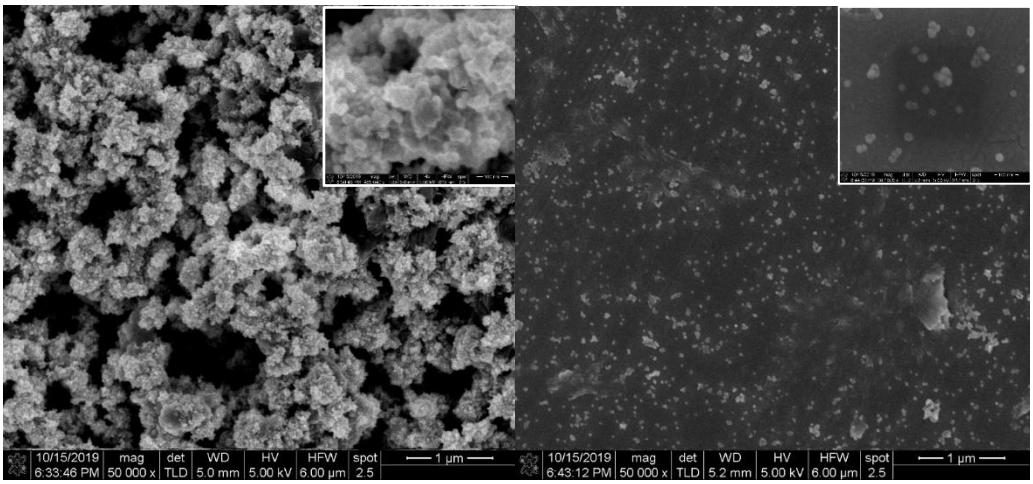

Figure 54. SEM images of aluminum sheets decorated with Au-in-Ag shell nanoparticles at a concentration of 2.6×10^{13} particle/mL (top) and 2.6×10^{12} particle/mL (bottom). Insets show magnified SEM images.

At a dilution of 2.6×10^{11} particles/mL, the distance between the nanoparticles also significantly increased (Figure 53c), but a more uniform distribution was seen across the surface with a few clusters. At the lowest concentration tested (2.6×10^{10} particles/mL), the nanoparticle number on the uppermost layer of the fibers significantly decreased (Figure 53d). There were only a few nanoparticle clusters visible, which would also significantly decrease the number of hotspots forming during SERS analysis. The SERS enhancement at each nanoparticle concentration using, RG6 spectra are shown in Figure 55.

7.4.4 Effect of nanoparticle concentration on SERS enhancement of zein nanofiber mats using R6G

SERS spectra of Rhodamine 6G measured with zein nanofiber mats decorated with different Au-in-Ag nanoparticle concentrations are shown in Figure 55, and the enhancement factors are calculated using the 614 cm^{-1} peak intensity. The highest peak intensities across the entire spectrum were observed at the concentration 2.6×10^{12} particles/mL, with the highest enhancement factor

of 2.5×10^6. The second highest peak intensities were obtained for 2.6×10^{13} particles/mL, with an enhancement factor of 1.85×10^6. Even though there is a significant difference between the peak intensities between these two nanoparticle concentrations, their enhancement factors are close. This is due to additional surface area covered by the one order of magnitude greater number of nanoparticles during calculation of the enhancement factors. The enhancement factors obtained with 2.6×10^{11} and 2.6×10^{10} particles/mL were 1.40×10^5 and 3.37×10^3 respectively, much lower than the first two concentrations. This comparison showed that, optimizing the nanoparticle concentration is important to obtain hotspot intensity to maximize Raman signal enhancement. Interestingly, the highest nanoparticle concentration (2.6×10^{13}) did not give the highest enhancement factor, caused by the highly compact clustering of nanoparticles and the complete coverage of the 3D nanofiber network structure. The decreasing surface area of the fibers allows only a limited number of hotspot formations and less Raman intensity.

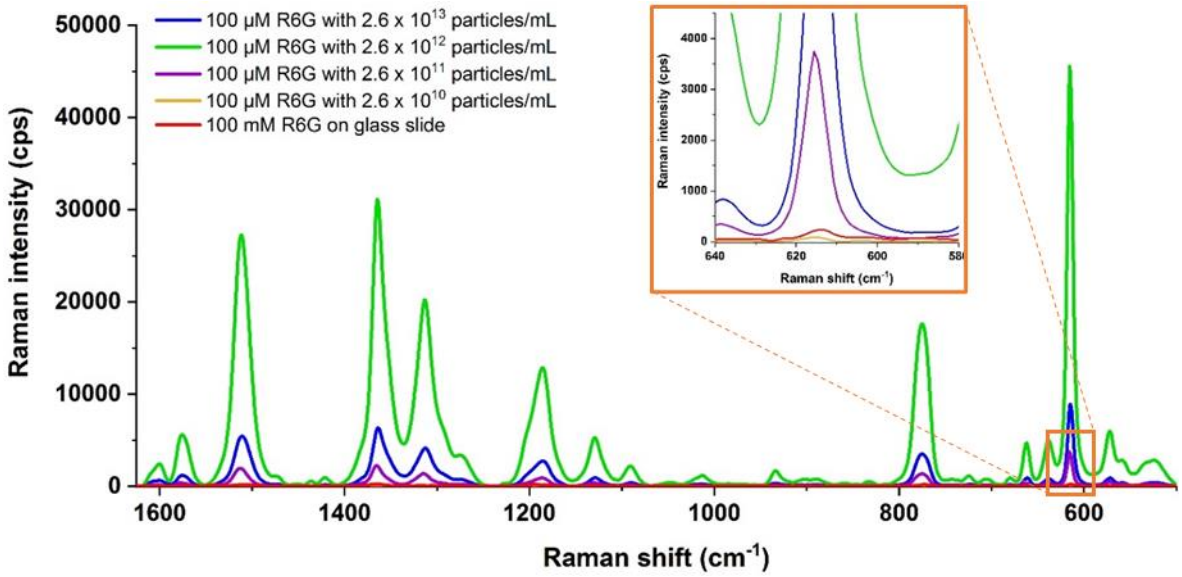

Figure 55. Effect of Au-in-Ag nanoparticle concentration on the SERS signal enhancement of Rhodamine 6G (R6G).

Additionally, other studies have shown that the distance between the nanostructures is also of great importance in the enhancement of SERS signals. Similar results were obtained with silver nanodomes such that, when nanodomes were close enough to each other for contact, the SERS signal was low, and when the distance was increased to 17 nm a much higher SERS enhancement was obtained (Choi et al., 2010). This tunneling effect, where in extreme proximity of the

nanoparticles, the charge density of the hotspots are weakening leads to lower SERS signals (Savage et al., 2012; Yan et al., 2017). In the case of 2.6×10^{13} particles/mL, the tunneling effect is thought to be responsible for the reduction in the Raman signal enhancement. Based on these results, 2.6×10^{12} nanoparticle concentration was chosen for the detection of acrylamide.

The highest SERS enhancement factor obtained with Au-in-Ag nanoparticles in the best we obtained to date for biodegradable zein based platforms (Turasan et al., 2019). The highest enhancement factor obtained with Au-in-Ag nanoparticle decorated zein nanofibers (2.49×10^{6}) is significantly higher than the enhancement factors of previously fabricated zein-based SERS sensor platforms. Gold coated inverted nanopyramid structures imprinted on zein film gave an EF of 1.3×10^{4} (Gezer et al., 2016a), gold nanoparticle decorated gold coated inverted nanopyramid structures imprinted on zein film gave an EF of 2.8×10^{4} (Jia et al., 2019b), and Au-in-Ag nanoparticle decorated gold coated inverted nanopyramid structures imprinted on zein film gave an EF of 3.36×10^{5}) (Ma et al., 2020). In addition, it is noteworthy that the higher enhancement factor was achieved in this study using less amount of metal in the fabrication of SERS platforms.

7.4.5 Testing the zein fiber-based platforms for acrylamide

The concentration of 2.6×10^{12} Au-in-Ag nanoparticles /mL were used for decoration of the zein nanofiber-based platforms to test the limit of detection (LOD) of acrylamide. The signature peaks of acrylamide can be seen in Figure 56 at the Raman shifts of 509.39 cm^{-1} (OCN bending), 619.81 cm^{-1} (NH_2 twisting), 846.53 cm^{-1} (NH_2 wagging), 962.82 cm^{-1} C-C stretching and HC=CH wagging), 1053.27 cm^{-1} (CH_2 rocking), 1148.42 cm^{-1} (NH_2 rocking), 1285.86 cm^{-1} (CN stretching), 1439.74 cm^{-1} (CH bending), 1587.76 cm^{-1} (NH_2 bending), 1639.44 cm^{-1} (C=C bending), 1686.43 cm^{-1} (C=O bending), 3033.30 cm^{-1} (CH_2 stretching), and 3103.02 cm^{-1} (CH_2 stretching) (Jonathan, 1961).

Since zein itself gives multiple Raman peaks due to its protein structure, it is important to select a peak to identify the acrylamide structure and to differentiate it from the protein structure. The characteristic peak of acrylamide at 1440-1478 cm^{-1} that does not appear in zein Raman spectra has been selected to detect acrylamide (Cheng et al., 2019; Gezer et al., 2016b). It has to be noted that the peak of acrylamide that appeared around 1440 cm^{-1} in Gezer et al.'s study was found at

1478 cm^{-1} in Cheng et al.'s study. These slightly peak shifts during SERS measurements in different SERS media has been reported before (Stacy and Van Duyne, 1983; Zhang et al., 2006). Therefore, in this study, the peak that appears at 1456 cm^{-1}, was chosen as the peak to detect acrylamide.

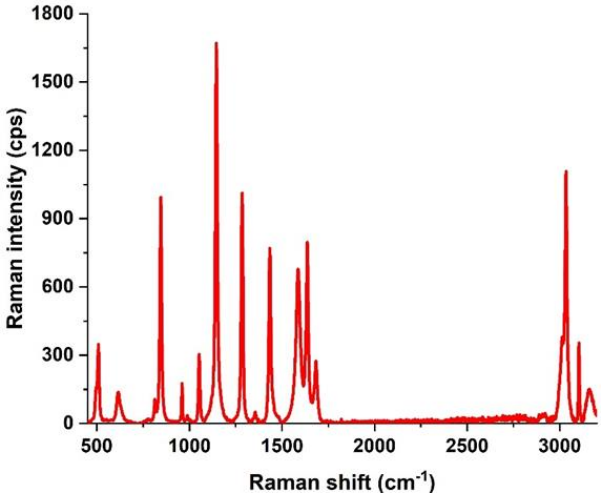

Figure 56. Raman measurement of 0.5 g/ml acrylamide on a glass slide.

SERS spectra of zein nanofibers with no nanoparticle decoration and zein nanofibers decorated with Au-in-Ag nanoparticles (2.6×10^{12}) are shown in Figure 57. Zein nanofibers without decoration did not cause any strong peak appearances, but noise was observed. Zein nanofibers with Au-in-Ag nanoparticles, showed strong Raman shifts at 1609 cm^{-1}, 1322 cm^{-1}, 1032 cm^{-1}, 1006 cm^{-1}, 864 cm^{-1}, and 397 cm^{-1} due to protein structure. No peak at 1440-1478 cm^{-1} region appeared in either non-decorated or decorated zein nanofiber platforms.

Five concentrations of acrylamide (100 μg/mL, 10 μg/mL, 1 μg/mL, 100 ng/mL and 10 ng/mL) were tested on the optimally decorated zein nanofiber mats and their SERS spectra are shown in Figure 57. Among these five concentrations, 100 μg/ml acrylamide had the highest 1456 cm^{-1} peak intensity, which decreased gradually with decreasing acrylamide concentration. Despite its lowest intensity among five concentrations, this peak was still visible at 10 ng/ml acrylamide concentration, indicating that the nanoparticle decorated zein nanofiber platforms are still capable of detecting acrylamide at a concentration of 10 ng/mL.

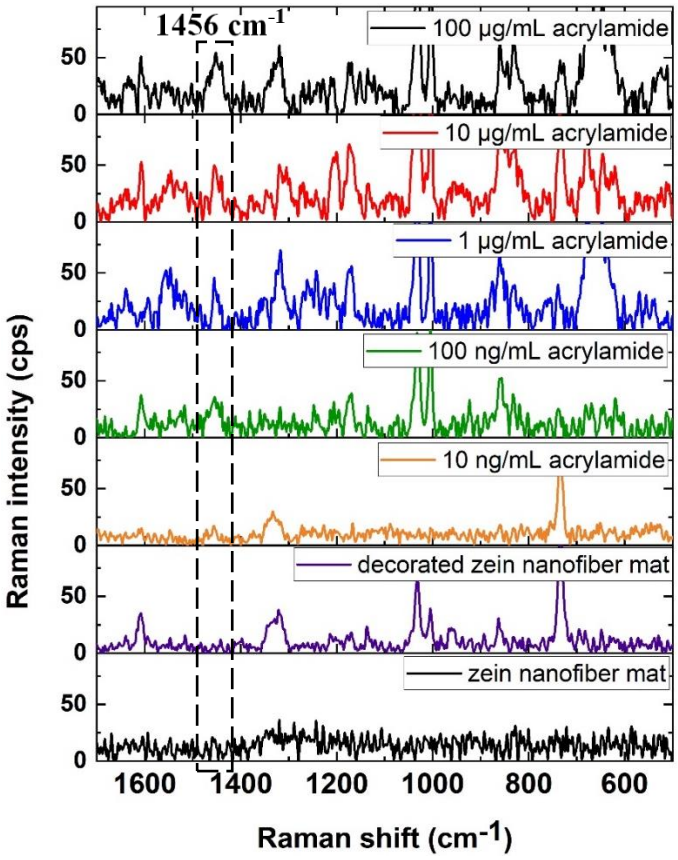

Figure 57. Detection of acrylamide on Au-in-Ag nanoparticle decorated zein nanofiber platforms.

The intensities of 1456 cm^{-1} peak compared to the acrylamide concentrations were fitted with a linear regression to determine the limit of detection quantitatively (Figure 58). The intensities gave the equation y=8.1664x+16.8358 with an R^2 of 0.91975. The limit of detection of 1.15 ng/ml was calculated using 3N/S (Ahmed et al., 2017; Jia et al., 2019b; Pang et al., 2019), where N is the standard deviation of the blank sample SERS signal and S is the slope of the standard curve. The LOD for this biodegradable platform , is approximately 10^4 times lower than the limit of detection that was achieved previously with the zein film-based SERS platform in our laboratory (10µg/mL) (Gezer et al., 2016b). This lower detection limit of the same analyte (acrylamide) is due to the higher surface area created with the nanofiber structure compared to the inverted nanopyramid structures imprinted on the zein film surface, the higher number of hotspots created on the zein nanofibers, and the higher plasmonic effect of Au-in-Ag nanoparticles.

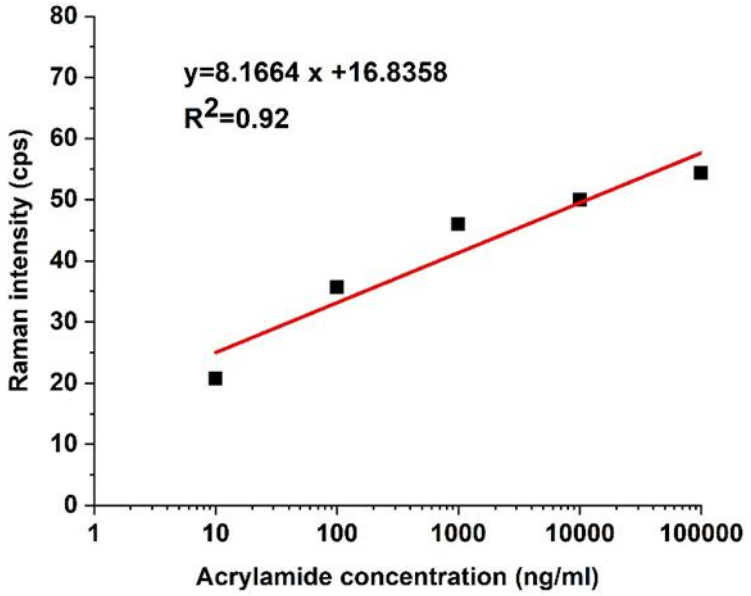

Figure 58. Calibration curve for acrylamide.

Lower limits of detection for acrylamide have been reported with non-biodegradable, synthetic polymers or graphene-based SERS platforms previously (Segal and Gedanken, 2015; Wang et al., 2017). For example, a LOD of 0.071 ng/mL was achieved using reduced graphene oxide on silicon wafer (Segal and Gedanken, 2015), raspberry-like silver nanoparticles on polydopamine spheres gave a LOD of 0.04 ng/mL (Wang et al., 2017). However, these SERS platforms are either toxic to the environment due to their graphene contents or take decades to degrade in the environment. In this study, we developed a new corn protein based renewable SERS platform that is 1000 times more sensitive than the previously fabricated protein-based platform and is reliable, biodegradable and environmentally friendly. Also, the LOD of acrylamide detected using the zein nanofiber-based SERS platform is comparable to some of the other non-biodegradable, non-renewable SERS platform LODs (Baia et al., 2011; Cheng et al., 2019). The fabrication of zein-nanofiber platforms is significantly faster than the other platforms, since it only requires electrospinning but not time-consuming lithography techniques.

The LOD found in this paper (1.15 ng/mL) is much lower than the average acrylamide values found in several foods (ranging between 6-318 ng/mL) reported by the European Union Joint Research Center (United States Environmental Protection Agency, 2010). Additionally, in a report of a joint FAO/WHO consultation, the lowest levels of GC-MS and LC-MS/MS techniques for the

detection of acrylamide were reported as 5-10 ng/mL and 20-50 ng/mL, respectively, under the assumption of 1 kg water as the basis and the LOD found in this paper is much lower than these values (World Health Organization in collaboration with the and Food and Agriculture Organization of the United Nations, 2002). These reports show the potential of zein nanofiber-based biodegradable SERS platforms of becoming alternatives to other non-biodegradable platforms to detect acrylamide.

This sensor follows the biodegradability and recovery strategies proposed in a previous study (Jia et al., 2019b). Briefly, the sensor will be immersed in 70% ethanol and the zein and the noble metal nanoparticles will be separated and recycled. The most effective dissolution of zein in 70% ethanol occurs at 65°C. The metallic nanoparticles will be harvested by filtration.

7.5 Conclusions

In this study electrospun zein nanofibers decorated with gold (Au), silver (Ag), gold+silver (Au+Ag) or silver shelled gold (Au-in-Ag) nanoparticles were fabricated and tested as a new SERS sensor platform. Au-in-Ag nanoparticles gave the highest SERS enhancement factor followed by Ag and Au+Ag, respectively. The highest SERS enhancement factor of 2.49×10^6 was achieved with 2.6×10^{12} nanoparticles/mL. The platform was tested with acrylamide, a highly toxic, carcinogenic chemical which is the by-product of frying and baking of cereal products, and gave a limit of detection of 1.15 ng/ml, 10^4 times lower than the previously achieved limit of detection with another zein-based SERS platform (Gezer et al., 2016b). The SERS enhancement factor is the highest achieved among all the zein-based SERS platforms reported (Gezer et al., 2016a; Jia et al., 2019b; Ma et al., 2020). With this new and high sensitivity, zein-based nanofiber mats have the potential to become a new green and renewable alternative for non-biodegradable SERS platforms for acrylamide detection.

7.6 References

Ahmed, J., Rahman, M. M., Siddiquey, I. A., Asiri, A. M., & Hasnat, M. A. (2017). Efficient Bisphenol-A detection based on the ternary metal oxide (TMO) composite by electrochemical approaches. *Electrochimica Acta, 246,* 597–605. https://doi.org/10.1016/j.electacta.2017.06.072

Bai, T., Lu, P., Zhang, K., Zhou, P., Liu, Y., Guo, Z., & Lu, X. (2017). Gold/Silver Bimetallic Nanocrystals: Controllable Synthesis and Biomedical Applications. *Journal of Biomedical Nanotechnology*, *13*, 1178–1209. https://doi.org/10.1166/jbn.2017.2423

Baia, M., Melinte, G., Barbu-Tudoran, L., Diamandescu, L., Iancu, V., Cosoveanu, V., Danciu, V., & Baia, L. (2011). Highly porous nanocomposites based on TiO2-noble metal particles for sensitive detection of water pollutants by SERS. *Journal of Physics: Conference Series*, *304*, 012059. https://doi.org/10.1088/1742-6596/304/1/012059

Baruah, P. K., Singh, A., Rangan, L., Sharma, A. K., & Khare, A. (2018). Optimization of copper nanoparticles synthesized by pulsed laser ablation in distilled water as a viable SERS substrate for karanjin. *Materials Chemistry and Physics*, *220*, 111–117. https://doi.org/10.1016/j.matchemphys.2018.08.064

Chang, T.-W., Gartia, M. R., Seo, S., Hsiao, A., & Liu, G. L. (2014). A wafer-scale backplane-assisted resonating nanoantenna array SERS device created by tunable thermal dewetting nanofabrication. *Nanotechnology*, *25*(14), 145304. https://doi.org/10.1088/0957-4484/25/14/145304

Cheng, J., Zhang, S., Wang, S., Wang, P., Su, X.-O., & Xie, J. (2019). Rapid and sensitive detection of acrylamide in fried food using dispersive solid-phase extraction combined with surface-enhanced Raman spectroscopy. *Food Chemistry*, *276*, 157–163. https://doi.org/10.1016/j.foodchem.2018.10.004

Choi, C. J., Xu, Z., Wu, H.-Y., Liu, G. L., & Cunningham, B. T. (2010). Surface-enhanced Raman nanodomes. *Nanotechnology*, *21*(41), 415301. https://doi.org/10.1088/0957-4484/21/41/415301

Dowgiallo, A. M., & Guenther, D. A. (2019). Determination of the Limit of Detection of Multiple Pesticides Utilizing Gold Nanoparticles and Surface-Enhanced Raman Spectroscopy. *Journal of Agricultural and Food Chemistry*. https://doi.org/10.1021/acs.jafc.9b01544

Eustis, S., & A. El-Sayed, M. (2006). Why gold nanoparticles are more precious than pretty gold: Noble metal surface plasmon resonance and its enhancement of the radiative and nonradiative properties of nanocrystals of different shapes. *Chemical Society Reviews*, *35*(3), 209–217. https://doi.org/10.1039/B514191E

Farrokhpour, H., & Ghandehari, M. (2019). Theoretical Spectroscopic Study on the Au, Ag, Au/Ag, and Ag/Au Nanosurfaces and Their Cytosine/Nanosurface Complexes: UV, IR, and Charge-Transfer SERS Spectra. *The Journal of Physical Chemistry C*, *123*(26), 16345–16358. https://doi.org/10.1021/acs.jpcc.9b00683

Gezer, P. G., Hsiao, A., Kokini, J. L., & Liu, G. L. (2016). Simultaneous transfer of noble metals and three-dimensional micro- and nanopatterns onto zein for fabrication of nanophotonic platforms. *Journal of Materials Science*, *51*(8), 3806–3816. https://doi.org/10.1007/s10853-015-9699-0

Gezer, P. G., Liu, G. L., & Kokini, J. L. (2016a). Development of a biodegradable sensor platform from gold coated zein nanophotonic films to detect peanut allergen, Ara h1, using surface enhanced raman spectroscopy. *Talanta*, *150*, 224–232. https://doi.org/10.1016/j.talanta.2015.12.034

Gezer, P. G., Liu, G. L., & Kokini, J. L. (2016b). Detection of acrylamide using a biodegradable zein-based sensor with surface enhanced Raman spectroscopy. *Food Control*, *68*, 7–13. https://doi.org/10.1016/j.foodcont.2016.03.002

Hong, S., Choi, Y., & Park, S. (2011). Shape Control of Ag Shell Growth on Au Nanodisks. *Chemistry of Materials*, *23*(24), 5375–5378. https://doi.org/10.1021/cm2021966

Jia, F., Barber, E., Turasan, H., Seo, S., Dai, R., Liu, L., Li, X., Bhunia, A. K., & Kokini, J. L. (2019). Detection of Pyocyanin Using a New Biodegradable SERS Biosensor Fabricated Using Gold Coated Zein Nanostructures Further Decorated with Gold Nanoparticles. *Journal of Agricultural and Food Chemistry*, *67*(16), 4603–4610. https://doi.org/10.1021/acs.jafc.8b07317

Jiao, A., Dong, X., Zhang, H., Xu, L., Tian, Y., Liu, X., & Chen, M. (2019). Construction of pure worm-like AuAg nanochains for ultrasensitive SERS detection of pesticide residues on apple surfaces. *Spectrochimica Acta Part A: Molecular and Biomolecular Spectroscopy*, *209*, 241–247. https://doi.org/10.1016/j.saa.2018.10.051

Jonathan, N. (1961). The infrared and Raman spectra and structure of acrylamide. *Journal of Molecular Spectroscopy*, *6*, 205–214. https://doi.org/10.1016/0022-2852(61)90243-0

Lin, L.-K., & Stanciu, L. A. (2018). Bisphenol A detection using gold nanostars in a SERS improved lateral flow immunochromatographic assay. *Sensors and Actuators B: Chemical*, *276*, 222–229. https://doi.org/10.1016/j.snb.2018.08.068

Lin, Z., & He, L. (2019). Recent advance in SERS techniques for food safety and quality analysis: a brief review. *Current Opinion in Food Science*, *28*, 82–87. https://doi.org/10.1016/j.cofs.2019.10.001

Liu, H., Du, X., Zang, Y.-X., Li, P., & Wang, S. (2017). SERS-Based Lateral Flow Strip Biosensor for Simultaneous Detection of Listeria monocytogenes and Salmonella enterica Serotype Enteritidis. *Journal of Agricultural and Food Chemistry*, *65*(47), 10290–10299. https://doi.org/10.1021/acs.jafc.7b03957

Liu, Y., Xu, S., Li, H., Jian, X., & Xu, W. (2011). Localized and propagating surface plasmon co-enhanced Raman spectroscopy based on evanescent field excitation. *Chemical Communications*, *47*(13), 3784–3786. https://doi.org/10.1039/C0CC04988C

Ma, X., Turasan, H., Jia, F., Seo, S., Wang, Z., Liu, G. L., & Kokini, J. (2020). A novel biodegradable ESERS (enhanced SERS) platform with deposition of Au, Ag and Au/Ag nanoparticles on gold coated zein nanophotonic structures for the detection of food analytes. *Journal of Vibrational Spectroscopy*.

Maruoka, K., Sugano, K., & Isono, Y. (2017). SERS detection and analysis of a single DNA oligomer using a single gold nanoparticle dimer. *2017 19th International Conference on Solid-State Sensors, Actuators and Microsystems (TRANSDUCERS)*, 468–471. https://doi.org/10.1109/TRANSDUCERS.2017.7994087

Neng, J., Li, Y., Driscoll, A. J., Wilson, W. C., & Johnson, P. A. (2018). Detection of Multiple Pathogens in Serum Using Silica-Encapsulated Nanotags in a Surface-Enhanced Raman Scattering-Based Immunoassay. *Journal of Agricultural and Food Chemistry*, *66*(22), 5707–5712. https://doi.org/10.1021/acs.jafc.8b00026

Orendorff, C., Gearheart, L., R. Jana, N., & J. Murphy, C. (2006). Aspect ratio dependence on surface enhanced Raman scattering using silver and gold nanorod substrates. *Physical Chemistry Chemical Physics*, *8*(1), 165–170. https://doi.org/10.1039/B512573A

Pande, S., Ghosh, S. K., Praharaj, S., Panigrahi, S., Basu, †, Jana, S., Pal, A., Tsukuda, T., & Pal, T. (2007). *Synthesis of Normal and Inverted Gold−Silver Core−Shell Architectures in β-Cyclodextrin and Their Applications in SERS*. https://doi.org/10.1021/jp0702393

Pang, Y., Wan, N., Shi, L., Wang, C., Sun, Z., Xiao, R., & Wang, S. (2019). Dual-recognition surface-enhanced Raman scattering(SERS)biosensor for pathogenic bacteria detection by using vancomycin-SERS tags and aptamer-Fe3O4@Au. *Analytica Chimica Acta*, *1077*, 288–296. https://doi.org/10.1016/j.aca.2019.05.059

Rycenga, M., Cobley, C. M., Zeng, J., Li, W., Moran, C. H., Zhang, Q., Qin, D., & Xia, Y. (2011). Controlling the Synthesis and Assembly of Silver Nanostructures for Plasmonic Applications. *Chemical Reviews*, *111*(6), 3669–3712. https://doi.org/10.1021/cr100275d

Sankar, S. S., Sangeetha, K., Karthick, K., Anantharaj, S., Ede, S. R., & Kundu, S. (2018). Pt nanoparticle tethered DNA assemblies for enhanced catalysis and SERS applications. *New Journal of Chemistry*, *42*(19), 15784–15792. https://doi.org/10.1039/c8nj03940b

Savage, K. J., Hawkeye, M. M., Esteban, R., Borisov, A. G., Aizpurua, J., & Baumberg, J. J. (2012). Revealing the quantum regime in tunnelling plasmonics. *Nature*, *491*(7425), 574–577. https://doi.org/10.1038/nature11653

Segal, E., & Gedanken, A. (2015). Can r-graphene oxide replace the noble metals in SERS studies: the detection of acrylamide. *Environmental Chemistry*, *13*(1), 58–67. https://doi.org/10.1071/EN14245

Seo, S., Chang, T.-W., & Liu, G. L. (2018). 3D Plasmon Coupling Assisted Sers on Nanoparticle-Nanocup Array Hybrids. *Scientific Reports*, *8*(1), 3002. https://doi.org/10.1038/s41598-018-19256-7

Shen, J., Su, J., Yan, J., Zhao, B., Wang, D., Wang, S., Li, K., Liu, M., He, Y., Mathur, S., Fan, C., & Song, S. (2015). Bimetallic nano-mushrooms with DNA-mediated interior nanogaps for high-efficiency SERS signal amplification. *Nano Research*, *8*(3), 731–742. https://doi.org/10.1007/s12274-014-0556-2

Stacy, A. A., & Van Duyne, R. P. (1983). Surface enhanced raman and resonance raman spectroscopy in a non-aqueous electrochemical environment: Tris(2,2′-bipyridine)ruthenium(II) adsorbed on silver from acetonitrile. *Chemical Physics Letters*, *102*(4), 365–370. https://doi.org/10.1016/0009-2614(83)87057-2

Tu, Q., Hickey, M. E., Yang, T., Gao, S., Zhang, Q., Qu, Y., Du, X., Wang, J., & He, L. (2019). A simple and rapid method for detecting the pesticide fipronil on egg shells and in liquid eggs by Raman microscopy. *Food Control*, *96*, 16–21. https://doi.org/10.1016/j.foodcont.2018.08.025

Turasan, H., Cakmak, M., & Kokini, J. (2019). Fabrication of zein-based electrospun nanofiber decorated with gold nanoparticles as a SERS platform. *Journal of Materials Science*, *54*(12), 8872–8891. https://doi.org/10.1007/s10853-019-03504-w

United States Environmental Protection Agency. (2010). *Toxicology review of acrylamide* (No. 79-06–1). U.S. Environmental Protection Agency. https://cfpub.epa.gov/ncea/iris/iris_documents/documents/toxreviews/0286tr.pdf

Vitos, L., Ruban, A. V., Skriver, H. L., & Kollár, J. (1998). The surface energy of metals. *Surface Science*, *411*(1), 186–202. https://doi.org/10.1016/S0039-6028(98)00363-X

Walker, C. G. H., El-Gomati, M. M., Assa'd, A. M. D., & Zadražil, M. (2008). The secondary electron emission yield for 24 solid elements excited by primary electrons in the range 250–5000 ev: a theory/experiment comparison. *Scanning*, *30*(5), 365–380. https://doi.org/10.1002/sca.20124

Wang, H., Guo, X., Fu, S., Yang, T., Wen, Y., & Yang, H. (2015). Optimized core–shell Au@Ag nanoparticles for label-free Raman determination of trace Rhodamine B with cancer risk in food product. *Food Chemistry*, *188*, 137–142. https://doi.org/10.1016/j.foodchem.2015.04.122

Wang, P., Zhou, Y., Zhou, Y., Wen, Y., Wang, F., & Yang, H. (2017). In-situ growth of raspberry-like silver composites for Raman detection of acrylamide. *Sensors and Actuators B: Chemical*, *243*, 856–862. https://doi.org/10.1016/j.snb.2016.12.056

Wijaya, W., Pang, S., Labuza, T. P., & He, L. (2014). Rapid Detection of Acetamiprid in Foods using Surface-Enhanced Raman Spectroscopy (SERS). *Journal of Food Science*, *79*(4), T743–T747. https://doi.org/10.1111/1750-3841.12391

World Health Organization in collaboration with the, & Food and Agriculture Organization of the United Nations. (2002). *Health Implications of Acrylamide in Food* [CONSULTATIONS AND WORKSHOPS]. World Health Organization - Food and Agriculture Organization of the United Nations. https://apps.who.int/iris/bitstream/handle/10665/42563/9241562188.pdf?sequence=1&isAllowed=y

Wu, H.-Y., Choi, C. J., & Cunningham, B. T. (2012). Plasmonic Nanogap-Enhanced Raman Scattering Using a Resonant Nanodome Array. *Small*, *8*(18), 2878–2885. https://doi.org/10.1002/smll.201200712

Xu, Z., Wu, H.-Y., Ali, S. U., Jiang, J., Cunningham, B. T., & Liu, L. (2011). Nanoreplicated positive and inverted submicrometer polymer pyramid array for surface-enhanced Raman spectroscopy. *Journal of Nanophotonics*, *5*(1), 053526. https://doi.org/10.1117/1.3663259

Yan, X., Li, P., Zhou, B., Tang, X., Li, X., Weng, S., Yang, L., & Liu, J. (2017). Optimal Hotspots of Dynamic Surfaced-Enhanced Raman Spectroscopy for Drugs Quantitative Detection. *Analytical Chemistry*, *89*(9), 4875–4881. https://doi.org/10.1021/acs.analchem.6b04688

Zhang, X., Shah, N. C., & Van Duyne, R. P. (2006). Sensitive and selective chem/bio sensing based on surface-enhanced Raman spectroscopy (SERS). *Vibrational Spectroscopy*, *42*(1), 2–8. https://doi.org/10.1016/j.vibspec.2006.02.001

CHAPTER 8. CONCLUSIONS

In this dissertation, different approaches were tested to improve the physical, surface and mechanical properties and the detection sensitivity of zein-based SERS platforms for the detection of food toxins. As the first step, structural changes occurring in zein with chemical crosslinking were studied. As a result a new mechanism was proposed for the first time for glutaraldehyde (GDA) crosslinking of plasticized zein films, where new bonds formed between the GDA aldehydes and amine groups of glutamine β-turns of the zein protein. This mechanism created tighter junction points in the zein matrix, leading to improved mechanical and surface properties. These improvements also increased the transfer fidelity of nanostructures onto zein film surfaces during SERS platform fabrication.

Gold layer coated nanostructured zein-film platforms were further improved in detection of analytes using surface decoration with metallic nanoparticles. Initially, surface of gold layer coated nanostructured zein films were decorated with gold nanoparticles. This increased the hotspot formation significantly, and as a result SERS enhancement factor was increased two folds ($2 * 10^4$). This platform successfully detected pyocyanin, a toxin secreted by P. aeruginosa, with a limit of detection of 0.025 μmol/ml. A comparison between gold, silver and silver-shelled-gold nanoparticles revealed that due to its bimetallic nature, silver-shelled-gold nanoparticle decoration resulted even a further SERS enhancement factor of 10^5.

In the last part of this research, a new approach was tested, where electrospun zein nanofiber mats were used as the SERS platform instead of nanostructured zein films. This approached was found to be significantly more rapid to fabricate and more cost effective in production due to its simplicity. Additionally, this higher new zein nanofiber-based platform only required a small amount of metallic nanoparticle decoration for surface decoration, which reduced the amount of metal usage significantly. The high surface area created by the nanofibers enabled a higher number of hotspot formation, which led to higher SERS enhancement factors of 10^6. Optimization of metallic nanoparticle type and concentration revealed that, silver-shelled-gold nanoparticles at a concentration of 10^{12} particles/ml gave the highest enhancement factor of $2.5 * 10^6$, which is the highest SERS enhancement factor ever reported for a biodegradable SERS platform. This newly

developed and optimized zein nanofiber-based SERS platform was tested in the detection of acrylamide, a food carcinogen, and the limit of detection (1.15 ng/ml) was found to be 10^4 times lower than the previously developed zein-film based SERS platform.

Overall, the successful fabrication and application of zein film-based or zein-nanofiber based SERS platforms presented in this dissertation show that there is a great potential for these sensors to become new green and renewable alternatives for non-biodegradable plastic-based SERS platforms.

VITA

HAZAL TURASAN, PhD

- **EDUCATIONAL HISTORY**

Aug 2014 – June 2020	**Doctor of Philosophy in Food Science** Purdue University, West Lafayette, IN Thesis Advisor: Prof. Dr. Jozef L. Kokini GPA: 3.63
Aug 2011 – Jun 2014	**Master of Science in Food Engineering** Middle East Technical University (METU), Ankara, Turkey Thesis Advisor: Prof. Dr. Serpil Sahin Thesis Co-Advisor: Prof. Dr. Gulum Sumnu GPA: 3.79
Aug 2006 – Jun 2011	**Bachelor of Science in Food Engineering** Middle East Technical University (METU), Ankara, Turkey GPA: 3.56
Feb 2010 – July 2010	**LLP Erasmus Program in Bachelor of Science, Food Technology** Wageningen University (WUR), Wageningen, The Netherlands

- **PROFESSIONAL HISTORY**

Aug 2014 – May 2020	**Research Assistant - Purdue, West Lafayette, IN** Focused on fabricating corn protein-based biodegradable and environmentally friendly biosensor Surface Enhanced Raman Spectroscopy (SERS) platforms to detect common food allergens, contaminants, and carcinogens. Protein chemistry characterization was extensively studied using many spectroscopic methods. Protein-based sensor platforms were fabricated using soft lithography or electrospinning. Zein film-based nanophotonic platforms and electrospun zein nanofiber mats were then used in the detection of various food toxins.
Aug 2016 – May 2018	**Teaching Assistant - Purdue University, West Lafayette, IN** FS-591 Advanced Food and Biological Materials Characterization Techniques: Helped the instructor with the preparation of the course material, taught some of the classes in the absence of the instructor, demonstrated the available equipment in the laboratory and helped with the grading of the exams. FS-690 Linear and Non-Linear Viscoelastic Rheology of Foods: Helped the instructor with the preparation of the course material and with the grading of the exams.
Oct 2011 – Jun 2014	**Research Assistant - METU, Ankara, TURKEY** Focused on microencapsulation of rosemary essential oil using freeze drying to increase its storage stability. Microparticulation was optimized using various coating materials, and homogenization techniques. The morphology and stability were assessed using particle sizer, SEM and GC-MS.
Oct 2011 – Jun 2014	**Teaching Assistant - METU, Ankara, TURKEY** FDE-305 Food Microbiology Laboratory: Taught the course material weekly, supervised the students during laboratory sessions that includes various microbiological tests, prepared and graded the exams.

FDE-310 Food Materials Laboratory: Taught the course material and equipment instructions weekly, supervised the students during laboratory sessions that include various chemical and physical food material characterization tests, prepared and graded the exams.
FDE-494 Special Topics in Food Engineering: Microbial Genotyping in Food Microbiology: Helped the instructor with the preparation of course material and graded exams.
FDE-224 Food Engineering Operations I (Momentum Transfer): Conducted recitation hours every week, prepared and graded problems sets and homeworks.
FDE-321 Food Engineering Operations II (Heat Transfer): Conducted recitation hours every week, prepared and graded problems sets and homeworks.
FDE-312 Food Processing: Helped the instructor to prepare the lecture presentations, prepared and graded problem sets.
FDE-324 Food Engineering Operations III (Mass Transfer): Conducted recitation hours twice every week, prepared and graded problems sets and homeworks

July 2009 – Aug 2009 **Intern** - Nestlé Quality Assurance and Product Development, Bursa, TURKEY

Aug 2010 – Aug 2010 **Intern** - Sakipaga Milk Industries Co. Quality Assurance and Product Development, Izmir, TURKEY

- **ACADEMIC ACHIEVEMENTS**

Rankings: Bachelor's degree graduation ranked as first

Scholarships: 2018 Donald Danforth Plant Science Center Fall Symposium Travel Award
2017 Purdue Agriculture Graduate Student Pathmaker Award
2014-2016 Fulbright Scholarship for Ph.D. Program in US
2011-2013 TUBITAK (The Scientific and Technological Research Council of Turkey) Graduate Scholarships for Turkish Citizens

Rolls: High Honour Roll 2007 – Fall Semester
High Honour Roll 2007 – Spring Semester
Honour Roll 2008 – Fall Semester
Honour Roll 2008 – Spring Semester
High Honour Roll 2010 – Fall Semester
Honour Roll 2010 – Spring Semester

- **LEADERSHIP ACHIEVEMENTS AND MENTORING ROLES**

- During my PhD program, I have served as the lab manager in my adviser's lab at Purdue University. My responsibilities included maintaining the order in the lab, making sure all the devices were in good condition, welcoming new students to the lab and training them for lab safety, keeping the lab safety documentations up-to-date and complete, helping new students how to follow good research practices.
- I have mentored several undergraduate students, new graduate students and visiting scholars conducting research in our lab at Purdue University. My responsibilities included helping them build lab skills, teach how to operate lab equipment, gain responsibility and experience in graduate-level projects. Additionally, I have helped my thesis adviser in the design of the projects/experiments that my mentees conducted, and I closely followed them at the beginning of their projects to guide them when necessary. Many publications came out of these collaborations with my lab mates.

- So far, I have very closely mentored 2 undergraduate students, Morgan Malm (2014-2016) and Yumi Higashiyama (2019-2020). Morgan Malm is currently pursuing her PhD degree at Purdue University which I believe is a result of research enthusiasm and curiosity she gained in our lab. My mentorship to Morgan Malm helped me receive Purdue Agriculture Graduate Student Pathmaker Award in 2017. Yumi Higashiyama joined our lab in January 2019 and recently graduated (May 2020) from the Department of Nutrition Science at Purdue. Despite to the challenges of mentoring an undergraduate student from another discipline, it was exciting to see a student from nutrition science develop skills of a food process engineer. Yumi has recently been accepted to the graduate program in the Department of Food Science at Cornell University. I have also closely mentored a visiting PhD scholar from Colombia and a new graduate student from Panama in our lab.
- As an extracurricular activity, I served as the president of the Fulbright Student Association for two years at Purdue University (2016-2018). The responsibilities included collecting information of the new incomers from various countries, contacting them to help them with the transportation to US and finding housing, furniture etc., organizing monthly board meetings with the board members to decide on the schedule of the events, bi-weekly events/coffee hours to help new student adjust to a new culture/environment and engaging all the Fulbright students to extracurricular activities, finding sponsors to fund the events we were holding.

- **REFEREED JOURNAL PUBLICATIONS**

1. Turasan, H., Cakmak, M., Kokini, J.L. (2020). Fabrication and validation of ultrasensitive biodegradable electrospun zein nanofiber-based SERS sensor for acrylamide detection. Innovative Food Science and Emerging Technologies (In preparation).
2. Higashiyama, Y., Turasan, H., Cakmak, M., Kokini J.L. (2020) Fabrication of novel pristine electrospun kafirin nanofibers loaded with thymol and carvacrol. (In preparation).
3. Turasan, H., Kokini, J.L. (2020). Non-destructive biosensors for the food industry. Annual Review of Food Science and Technology. (Invited review, submitted).
4. Yildirim Ertuk, M., Turasan, H., Kokini, J.L. (2020). The effect of the number of harmonics on reconstruction and smoothing of large amplitude oscillations and Lissajous-Bowditch curves in understanding and characterization of the LAOS behaviour of a corn starch. Journal of Rheology (Under review).
5. Ozturk, O. K. and Turasan, H. (2020). Latest developments in the application of microfluidization to modify functional properties of macromolecules. Food Hydrocolloids (Under Review).
6. Turasan, H., Bonilla, J., Bozkurt F., Maldonado L., Li, X., Yilmaz, T., Sadeghi, R., Kokini, J.L (2020). Comparison of the fabrication methods, formation dynamics, structure and delivery performance of solid nanoparticles and hollow layer-by-layer (LbL) edible/biodegradable nanodelivery systems. Journal of Food Process Engineering, 43 (5), e13413. https://doi.org/10.1111/jfpe.13413
7. Turksoy, S., Erturk, M.Y., Bonilla, J. Turasan, H., Kokini, J.L (2020). Effect of aging at different temperatures on LAOS properties and secondary protein structure of hard wheat flour dough. Journal of Cereal Science, 92, 102926.
8. Ma, X., Turasan, H., Jia, F., Seo, S., Wang, Z., Liu, G.L., Kokini, J.L. (2020). A novel biodegradable ESERS (enhanced SERS) platform with deposition of Au, Ag and Au/Ag nanoparticles on gold coated zein nanophotonic structures for the detection of food analytes. Journal of Vibrational Spectroscopy, 106, 103013.
9. Turasan, H., Cakmak, M., and Kokini, J.L. (2019). Fabrication of zein-based electrospun nanofiber decorated with gold nanoparticles as a SERS platform. Journal of Materials Science. 54 (12), 8872-8891.
10. Yilmaz, T., Maldonado, L., Turasan, H., and Kokini, J.L. (2019). Thermodynamic mechanism of particulation of sodium alginate and chitosan polyelectrolyte complexes as a function of charge ratio and order of addition. Journal of Food Engineering, 254, 42-50.

11. Fei, J., Barber, E., Turasan, H., Seo, S., Dai, R., Liu, G.L., Li, X., Bhunia, A., and Kokini, J.L. (2019). Detection of pyocyanin using a new biodegradable SERS biosensor fabricated using gold coated zein nanostructures further decorated with gold nanoparticles. Journal of Agricultural and Food Chemistry. 67 (16), 4603- 4610.
12. Barber, E.A., Turasan, H., Gezer, P.G., Devina, D., Liu, G.L. and Kokini, J.L. (2019). Effect of plasticizing and crosslinking at room temperature on microstructure replication using soft lithography on zein films. Journal of Food Engineering. 250, 55-64.
13. Turasan, H., Barber, E.A., Malm, M. & Kokini, J.L. (2018). Mechanical and spectroscopic characterization of crosslinked zein films cast from solutions of acetic acid leading to a new mechanism for the crosslinking of oleic acid plasticized zein films. Food Research International, 108, 357-367. https://doi.org/10.1016/j.foodres.2018.03.063
14. Turasan, H. and Kokini, J.L. (2017). Advances in understanding the molecular structures and functionalities of biodegradable zein-based materials using spectroscopic techniques: A review. Biomacromolecules, 18 (2), 331-354. doi: 10.1021/acs.biomac.6b01455.
15. Turasan, H., Sahin, S., & Sumnu, G. (2015). Encapsulation of rosemary essential oil. LWT-Food Science and Technology, 64(1), 112–119. http://doi.org/10.1016/j.lwt.2015.05.036

- **BOOK CHAPTERS**

1. Turasan, H., and Kokini, J.L. (2020). Enhancing the bioavailability of nutrients by nano-delivery systems. In Food Nanotechnology: Applications and Approaches. Elsevier. (In press).
2. Turasan, H. and Kokini, J.L. (2020). Chapter 6 - Delivery of bioactives using biocompatible nanodelivery technologies. In Handbook of Functionalized Nanomaterials for Industrial Applications. First edition, pp. 133-166. Elsevier.
3. Turasan, H., Bonilla J., Jia, F., Maldonado, L., Malm, M., Rouf, T.B. and Kokini, J.L. (2020). Chapter 12 - Advances in food functionality and packaging using nanotechnology. In Food Applications of Nanotechnology, First edition, pp. 271–318. CRC Press Taylor & Francis Group.

- **CONFERENCE PRESENTATIONS**

1. Yildirim, M., Turasan, H. Gao, M., Kokini, J. (2019). “The Effect of Harmonic Number on Large Amplitude Oscillatory Shear (LAOS) Testing of Starch Suspensions”. AIChE International Conference, Orlando, FL. Oral presentation.
2. Turasan, H., Cakmak, M., and Kokini, J.L. (2019). A plant protein-based SERS biosensor platform for detection of food toxins and allergens. IFT19 Annual Meeting. New Orleans, LA. Poster presentation.
3. Turasan, H., Cakmak, M., and Kokini, J.L. (2018). Creating biodegradable corn protein-based electrospun nanofiber platforms for SERS detections. Donald Danforth Plant Science Center Fall Symposium, St. Louis, MO. Oral presentation.
4. Turasan, H., Cakmak, M., Kokini, J.L. “Fabrication and decoration of zein-based electrospun nanofiber platforms for SERS detection” Birck Nanotechnology center, SMART Films Consortium Workshop, Poster Presentation, November 14th, 2018, West Lafayette, Indiana
5. Turasan, H., Cakmak, M., and Kokini, J.L. (2018). Fabrication and decoration of zein-based electrospun nanofiber platforms for SERS detection. AIChE International Conference, Pittsburgh, PA. Oral presentation
6. Yildirim, M., Turasan, H., and Kokini, J.L. (2018). The Effect of Instrumental Inertia on Large Amplitude Oscillatory Shear (LAOS) Testing of Starch Suspensions. Society of Rheology Annual Meeting, Houston, TX. Oral presentation.
7. Yildirim, M., Turasan, H., Duvarci, O. and Kokini, J.L. (2018). LAOS (Large Amplitude Oscillatory Shear) rheological characteristics of shear thickening corn starch as a model for shear thickening rheology. IFT18 Annual Meeting. Chicago, IL. Poster presentation

8. Turasan, H., Kokini, J.L. (2017). Analyzing the Effects of Time and Crosslinker Ratio on the Mechanical Properties of Biodegradable Zein Super Gels. AICHe International Conference, Minneapolis, MS. Oral presentation.
9. Turasan, H., Barber, E.A., & Kokini, J.L. (2017). Characterization of physical and chemical properties of crosslinked zein films for biodegradable platform formation. IFT17 Annual Meeting. Las Vegas, NV. Poster presentation
10. Turasan, H., Barber, E.A., Meiser, M. & Kokini, J.L. (2016). Analyzing the chemical and the physical characteristics of crosslinked zein gel films cast. AICHe International Conference, San Francisco, CA. Poster presentation.
11. Barber, E.A., Turasan, H., Devina, D. & Kokini, J.L. (2016). Optimized and tested zein film for utilization as an effective sers sensor. AICHe International Conference, San Francisco, CA. Oral presentation.
12. Barber, E.A., Turasan, H., Rouf, T. & Kokini, J.L. (2016). Characterization of engineered biodegradable zein films for sensor-based platform production. EFFoST International Conference. Vienna, Austria. Oral presentation.
13. Sahin, S., Turasan, H. & Sumnu, G. (2014). Microencapsulation of rosemary essential oil. XXII International Conference on Bioencapsulation. September 17-19. Bratislava, Slovakia, 172-173. Poster presentation

- **PROFESSIONAL ACTIVITIES**

As refereed journal reviewer:

- *Journal of Cereal Science.* Reviewed 3 manuscripts. Jun 2016, Aug 2016, Nov 2016
- *Journal of Agricultural and Food Chemistry.* Reviewed 14 manuscripts starting on Oct 2017

- **ACTIVITIES AND ORGANIZATIONS**

Purdue Fulbright Student Association President (2016-2018)
Purdue Fulbright Student Association Communications Officer (2015-2016)
Purdue Fulbright Association Membership (2014-current)
Purdue Food Science Graduate Student Association Membership (2015-current)
Purdue Turkish Student Association Membership (2015-current)
Institute of Food Technologists Student Membership (2015- current)
Phi Tau Sigma Honour Society Membership (2017- current)
Omicron Delta Kappa (ODK) Society Membership (2016 - current)
International Exchange Erasmus Student Network (2010)
METU - Food Society (2009-2014)
Union of Chambers of Turkish Engineers and Architects / Chamber of Food Engineers (2010-2011)

- **LAB SKILLS:**

Gas Chromatography-Mass Spectrometer
Fourier Transform-Raman Spectroscopy
Atomic Force Microscopy
Transmission Electron Microscopy
Texture Analyzer
Soft lithography
Encapsulation
Spin Coating
Electrospinning
Rheology
Fourier Transform Infrared Spectroscopy
Dispersive Raman Spectroscopy
Scanning Electron Microscopy
Tensiometer
Circular Dichroism Spectroscopy